# Modelling and Analysis of Asynchronous and

# Synchronous Torques

# in Split-Phase Induction Machines

Peter Scavenius Andersen

A thesis submitted to

The Department of Electronics and Electrical Engineering

University of Glasgow

for the Degree of Doctor of Philosophy

October 2007

# Abstract

In this thesis, the nature of asynchronous and synchronous torques in a split-phase induction machine is investigated and quantified.

The equivalent circuit for this type of machine is derived using the rotating field theory. It is extended to include harmonic effects. Using this model, winding harmonics and permeance harmonics may be calculated independently of each other so that the model can be used to analyse asynchronous torques from winding harmonics as well as synchronous torques from permeance harmonics. These are calculated separately. The asynchronous torques appear as perturbations in the steady-state torque-speed curve while the synchronous torques only appear at specific speeds. The synchronous torques are superimposed onto the torque-speed curves to model both effects together.

The model predictions are compared against test results using purpose-built experimental machines together with production machines. These have varying rotor bar number and skew. Different methods are used to assess the synchronous torques. It is found that measuring synchronous locking torque is not a straightforward matter; however, reasonable agreement is found between calculation and measurement.

The work highlights the need for the correct choice of stator and rotor slot numbers together with the effect skew has on reducing the synchronous and asynchronous locking torques.

# Acknowledgements

# List of symbols

Below, a list of expressions found in the main thesis is given. It is split into "variables" and "indices" since in most cases these exist in many combinations of each other. For example, the variable $\overline{F}_{irf}$ means "Magnetomotive Force of the Forward Rotor Current"

SI units and standard nomenclature used throughout.

## Variables

| Symbol | Unit | Description |
|---|---|---|
| $B$ | T | Flux density |
| $E, e$ | V | Electromotive force |
| $f$ | Hz | Frequency |
| $F$ | A | Magnetomotive force |
| $F_L$ | N | Lorentz force |
| $H$ | A/m | Field intensity |
| $I, i$ | A | Current |
| $L_{stk}$ | m | Stack length |
| $L$ | H | Inductance |
| $l_g$ | m | Radial air gap length corrected by Carter's coefficient |
| $l_{mech}$ | m | Radial air gap length as difference in rotor and stator bore radii |
| $N$ | ... | Total winding number |
| $\hat{N}$ | ... | Winding amplitude |
| $N_b$ , $N_r$ | ... | Number of rotor bars |
| $N_s$ | ... | Number of stator slots |
| $n_b$ | ... | Number of pole pairs of the flux density created by interaction of general harmonic magnetising MMF and permeance |
| $P$ | H / m$^2$ | Permeance coefficient (relevant for 2D analysis) |
| $Perm$ | H | Permeance (relevant for 3D analysis) |
| $p$ | ... | Number of pole pairs of a general harmonic magnetising MMF |
| $R$ | Ω | Resistance |
| $r$ | m | Air gap mid-radius |
| $s$ | ... | Slip, relative difference in rotor and synchronous speeds |
| $T$ | Nm | Torque |
| $x$ | ... | Number of pole pairs of a general harmonic permeance |

| $X$ | $\Omega$ | Reactance |
| $y$ | ... | The multiplum of rotor speed with which a general harmonic permeance wave rotates |
| $\alpha$ | rad | 1. General integration angle |
| | | 2. Angle of a rotor bar pitch |
| $\beta$ | ... | Winding ratio |
| $\gamma$ | rad | Phase angle of main and auxiliary flux densities of same rotational direction |
| $\theta$ | rad | General angle variable |
| $\varphi$ | rad | Phase angle of impedance |
| $\Phi$ | Wb | Magnetic flux |
| $\nu$ | Rad | Angle of rotor skew |
| $\omega$ | Rad/s | Radian frequency |
| $\Psi$ | Wb | Flux linkage |

## Indices

| Index | Description |
| --- | --- |
| $a$ | Auxiliary |
| $b$ | Backward |
| $B$ | Flux density |
| $f$ | Forward |
| $g$ | (Air) Gap |
| $I, i$ | Current |
| $m$ | 1. Main |
| | 2. Magnetising (e.g. magnetising reactance) |
| | 3. $m^{th}$ harmonic |
| $n$ | $n^{th}$ harmonic |
| $n_b$ | Harmonic order $= n_b$ |
| $p$ | Harmonic order $= p$ |
| $r$ | Rotor |
| $s$ | Stator |

# List of figures

Below, a list of figures as they appear in the main thesis is given.

# Table of contents

# Chapter 1

# Introduction

Although it was invented more than 100 years ago, the vast majority of electrical motors used in industrial and domestic applications worldwide are of the induction motor type [1]. These are in power ratings from a few tens of watts to several megawatts. The traditional advantages of this type of machine are its mechanical and thermal ruggedness as well as its ability to operate directly from an AC supply. Although it is being increasingly outperformed by permanent magnet motors in various areas, particularly in terms of energy consumption, the performance of the induction motor has been steadily improving, and it still offers a cost-effective alternative to the permanent magnet motor in areas such as pumps, fans, compressors and also in home appliances, particularly in the single-phase or split-phase configuration, the latter being a motor which runs from a single-phase supply, but which features two spatially separated windings and often featuring an auxiliary impedance. For example, the company Danfoss Compressors GmbH, Germany, has an annual production volume of around 11 million piston compressors for domestic and light commercial refrigeration, each featuring an electric motor. Around 90% of this volume uses the split-phase induction motor. Although the permanent magnet motor is also gaining volume in this field, the production of induction motors will not decrease for the foreseeable future.

Particularly in the ASEAN area, where living standards are rapidly increasing, domestic appliances using induction motors are expecting to see great growth rates.

However, the manufacturing competition in this field is very harsh. Moreover, the direct material prices of such materials as steel and copper increase rapidly. Therefore the manufacturer needs to consider the motor design at a very high level of detail in order to make the best possible use of the material, and to achieve the desired operating performance in the most rational way.

As will be investigated in this thesis, the physical distribution of the windings in an induction motor may cause considerable harmonic field effects, which, when not considered carefully, may cause undesired performance characteristics in terms of losses and starting capabilities. These are known as asynchronous torque dips.

Moreover, the choice of the combination of stator slots and rotor slots may result in additional harmonic effects, being generated from slot permeance harmonics, which manifest themselves as torque pulsations and, for certain speeds, synchronous locking torques which

tend to keep the rotor at this certain speed and therefore may impair the starting abilities of the motor.

The traditional revolving field theory for describing a single-phase motor was introduced by Morrill [2]. This method assumes ideally distributed windings and no slotting effects. Even so, description of such a machine is very mathematical [3], [4], [5]. A certain amount of literature is dedicated to the motor operating in tapped-winding configuration, e.g. [6], [7], however, very little is dedicated to harmonic torques in general and synchronous torques in particular. As for asynchronous torques, [8] introduced a model of a 3-phase induction machine with the principal winding harmonics present in a general design. The literature on the single phase motor is much less, but [9] showed a similar model, although limited to the pure single phase machine. The split-phase machine, which contains a main and auxiliary winding and is much more complex than both the 3-phase and single-phase machine in terms of number of parameters, is even more sparsely described. [10] introduced the equivalent circuit of a split-phase machine with superimposed winding harmonics. Recently, [11] described the winding harmonics using an impedance matrix method, and a similar method was proposed by [12]. Very recent work, published shortly before completion of this thesis, considers modification of the classical equivalent circuits (i.e. the revolving field model, symmetrical components model and the cross-field model) to include winding harmonics [13].

Regarding synchronous locking torques, some general considerations were first done by Kron [14]. The concept of introducing permeance harmonics was further carried out in [15], [16] and [17] and at a more detailed level in [18], which is also used in [19] for a sensorless speed estimation. Using transient finite element analysis, [20] quantified the phenomenon for a given machine. [21] – [23] brought forward some general considerations relating to harmonic effects, but did not provide any quantitative calculations. [24] and [25] described how such synchronous torques can be measured. However, it all focuses on 3-phase machines, which are, at least when operating in balanced conditions, simpler to describe than the split-phase motor. On single-phase machines, very little appear to have been published.

The aim of this thesis is to describe and quantify the above mentioned harmonic phenomena in a split-phase induction motor, and to develop a model which considers them in detail. Quantitative calculations will be shown and compared against measured data to evaluate the precision of the results.

# 1. Introduction

The approach taken in this thesis will be to describe the idealised single-phase machine and extend this analysis to cover the phenomena related to winding and permeance harmonics in order to describe them qualitatively as well as assess them quantitatively.

Chapter 2 will develop a model for the machine from first principles using rotating field theory and simple application of Maxwell's equations to establish an equivalent circuit, from which EMFs and currents and, subsequently, torques can be calculated.

In Chapter 3, spatial winding harmonics are introduced and the theory is developed to illustrate how they generate asynchronous torques.

Chapter 4 describes the effects of stator and rotor slot permeance while in Chapter 5 the theory developed in the previous chapters is brought together to develop a method for calculating the synchronous torque spikes and dips.

Throughout these theory chapters example simulations are used to illustrate the points developed. However, deeper evaluation of the simulation techniques is carried out in Chapter 6 and the results are verified experimentally. The work is assessed and discussed in Chapter 7 with brief additional conclusions and suggestions for further work put forward in Chapter 8.

# Chapter 2

# Fundamental theory of the idealised machine

Although the aim of this work is to extend the basic theory regarding single-phase induction motors, it is worthwhile to investigate the fundamental theory concerning this type of machine. This is in order to present the nomenclature and foundation for modelling, which will be used at a later stage, as well as serve as a reference chapter.

Throughout this thesis, revolving field theory is used as the modelling approach. However, other approaches, such as the cross-field or symmetrical components, as described by [26], may be equally suited for the task.

In this chapter, the origin of the rotating field components and induction are described, and the classical equivalent circuit for the single-phase squirrel cage induction motor is derived.

## *2.1. Rotating MMF*

In the following derivation, a stator with a 2-pole sinusoidal winding distribution is considered. The total number of turns is $N$ where the "winding amplitude" $\hat{N}$ is $N/2$. The number of conductors at a given angle $\theta$ is described by

$$N(\theta) = \frac{N}{2}\sin(\theta) \tag{2.1}$$

This means that a radial path through the stator is surrounded by a number of conductors described by

$$N_{surround}(\theta) = N\cos(\theta) \tag{2.2}$$

If this winding is excited by a sine-varying current, a surface MMF will be created on the stator, which pulsates in time and is sinusoidally graduated in space so that

$$F(t,\theta) = N\cos(\theta) \cdot I\cos(\omega t)$$
$$= \frac{NI}{2}\left(\cos(\omega t - \theta) + \cos(\omega t + \theta)\right) \tag{2.3}$$

This represents two rotating MMF components which are of equal magnitude but rotate in opposite directions at angular velocity $\omega$, i.e.:

$$F_f(t,\theta) = \frac{NI}{2}\cos(\omega t - \theta), \quad F_b(t,\theta) = \frac{NI}{2}\cos(\omega t + \theta) \tag{2.4}$$

The rotational speed is determined by $\omega$, the supply voltage frequency, and the number of poles. That means the stator winding can be divided into two parts: one which creates the

forward rotating field and one which creates the backwards rotating field. These are connected in series so that the current through the two windings is the same; the winding number of each winding is half the total winding number.

## 2.2. Induction

Here, the induction of the fundamental flux density component in the fundamental winding distribution is considered. The winding distribution is described in space by (2.1). Similarly, the fundamental component of air gap flux density can also be described in time and space by

$$B(t,\theta) = B\cos(\omega t - \theta) \tag{2.5}$$

To find the induced voltage in the winding, the flux linking the coils at a given spatial displacement is considered and then integrated this over the whole pole pitch. Hence, at a given displacement $\alpha$, the induced voltage is, from Faraday's law,

$$E(\alpha) = -N(\alpha) \cdot \frac{d}{dt} r L_{stk} \int_{-\alpha}^{\alpha} B(t,\theta) d\theta \tag{2.6}$$

Inserting (2.1) and (2.5) into this yields:

$$
\begin{aligned}
E(\alpha) &= -\frac{N}{2}\sin(\alpha) \cdot \frac{d}{dt} r\, L_{stk} \int_{-\alpha}^{\alpha} B(t,\theta)\, d\theta \\
&= -\frac{N}{2}\sin(\alpha) \cdot \frac{d}{dt} r\, L_{stk} \left(-2B\right)\cos(\omega t)\sin(-\alpha) \\
&= N\sin^2(\alpha)\, B\, r\, L_{stk}\, \omega \sin(\omega t)
\end{aligned}
\tag{2.7}
$$

The total voltage is then found by integrating (2.7) with respect to $\alpha$ from 0 to $\pi$.

$$
\begin{aligned}
E(t) &= \int_{0}^{\pi} E(\alpha,t) d\alpha \\
&= N\, B\, r\, L_{stk}\, \omega \sin(\omega t) \int_{0}^{\pi} \sin^2(\alpha)\, d\alpha \\
&= N\, B\, r\, L_{stk}\, \omega \sin(\omega t) \left[\frac{\alpha}{2} - \frac{\sin(2\alpha)}{4m}\right]_{0}^{\pi} \\
&= \frac{N\, B\, r\, L_{stk}\, \omega\, \pi}{2} \sin(\omega t)
\end{aligned}
\tag{2.8}
$$

It should be emphasized that in (2.8), as well as in the previous analysis, $N/2$ is the "winding amplitude" of the winding, i.e. the number of turns of the full pitch coils. (The total number of turns is $N$).

Equation (2.8), which is a sine function of time, shows that the induced voltage phasor lags the flux density phasor, (2.5), which is a cosine function of time. This would be relevant for generator action, where any induced current would be driven by this induced voltage, which would thus generate power. When the energy flow is reversed, the current is driven into this

induced voltage by an external voltage source, and the induced voltage would thus consume power, as would be the case in a motor (active power) or a passive coil (reactive power). In such cases, the so-called "sink" conversion should be applied, in which case the induced voltage would have to lead the magnetic field.

Therefore, the "sink" convention of (2.8) is

$$E(t) = -\frac{N\,B\,r\,L_{stk}\,\omega\,\pi}{2}\sin(\omega t)$$
(2.9)

## 2.3. The induced rotor current

It was stated earlier that there are forward and backward rotating flux density waves in the air-gap. Here, the induced EMFs and the resultant currents in the rotor are found. There are several derivations in standard texts; the method put forward here for determining the rotor current is based on induction principles. It will be shown later that space-harmonic components of air-gap flux density also exist in the rotor; however, for simplicity, these are ignored at this stage.

**Induced current in a solid conducting cylinder**

It is assumed that the rotor is made of two concentric cylinders. The inner cylinder is made of iron with a very high value of relative permeability, while the outer cylinder is made of a conducting material such as aluminium or copper. Fig. 2.1 shows this rotor.
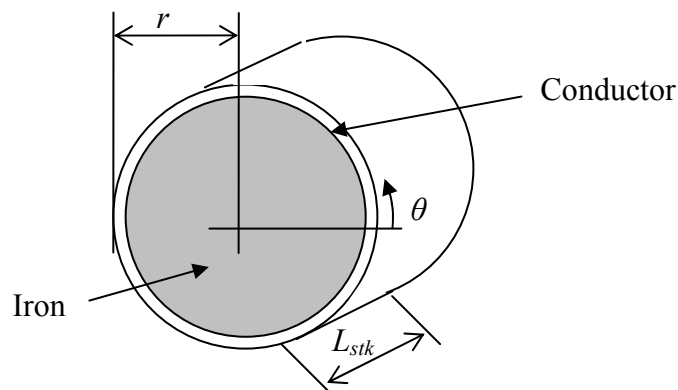


*Fig. 2.1 Machine co-ordinate representation*

This means that as well as space harmonics, MMFs and any slotting effects in the rotor are also neglected at this stage. It is described in more detail in Section 3.5.

**Forward currents**

The forward revolving flux densities can be described by

$$B_f(t,\theta) = \widehat{B}_f \cos(\omega t - \theta) \tag{2.10}$$

If the rotor is rotating in the positive direction (i.e. anti-clockwise as in fig. 2.2) at speed $\omega' = (1-s)\,\omega$, the relative rotational speed of the air gap flux density with respect to the rotor is $\omega - \omega' = s\,\omega$. The flux through an infinitesimal surface area of the rotor, defined by angle $d\theta$, is then

$$\Phi_f(t,\theta) = r\,L_{stk}\,\widehat{B}_f \cos(s\omega t - \theta)\,d\theta \tag{2.11}$$

This rotating flux wave gives rise to a circulating current at angle $\theta$ along the rotor surface area defined by $d\theta$. The current is driven by an induced voltage, acting along this path. This means, at angle $\theta$, the current is driven by voltage $e(\theta)$, acting along the length of the stack. But a similar voltage $e(\theta+d\theta)$ drives a current opposite $i(\theta)$, as shown in Fig. 2.2.
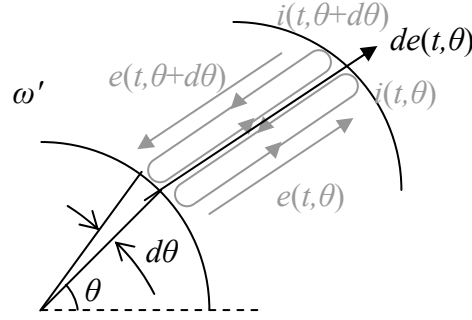


*Fig. 2.2 Air-gap electric field representation*

By Maxwell's 4th law:

$$e(t,\theta) = \frac{-\partial}{\partial t} B_f(t,\theta)\, r\, L_{stk}\, d\theta$$
$$e(t,\theta+d\theta) = \frac{-\partial}{\partial t} B_f(t,\theta+d\theta)\, r\, L_{stk}\, d\theta \tag{2.12}$$

The resulting voltage along the length of the rotor stack is the difference between the two. If the direction out of the paper plane is chosen as positive, the resulting voltage becomes

$$e_{res}(t,\theta)d\theta = e(t,\theta) - e(t,\theta+d\theta) = -de(t,\theta) \tag{2.13}$$

Inserting (2.12), the resulting voltage in the rotor conductor is

$$e_{res}(t,\theta) = \frac{-\partial e(t,\theta)}{\partial \theta} = \frac{\partial}{\partial t}\frac{\partial B_f(t,\theta)}{\partial \theta} r\, L_{stk} \tag{2.14}$$

The current at angle $\theta$ in the conducting path defined by $d\theta$ is driven by the resulting voltage and limited by the impedance, which is likewise defined by the area of the path:

## 2. Fundamental theory of the idealised machine

$$i_f(t,\theta)d\theta = \frac{e_{res}(t,\theta)}{\dfrac{\overline{Z}}{d\theta}} = \frac{e_{res}(t,\theta)d\theta}{\overline{Z}}$$

(2.15)

$$i_f(t,\theta) = \frac{e_{res}(t,\theta)}{\overline{Z}} = \frac{1}{\overline{Z}}\frac{\partial}{\partial t}\frac{\partial B_f(t,\theta)}{\partial \theta}r\,L_{stk}$$

Using complex notation, in which:

$$\frac{\partial}{\partial \theta} \rightarrow -j \quad , \quad \frac{\partial}{\partial t} \rightarrow js\omega$$

(2.16)

- then (2.15) becomes

$$\overline{I}_f = \frac{1}{\overline{Z}}j\,s\,\omega(-j)\overline{B}_f\,r\,L_{stk} = \frac{1}{\overline{Z}}s\,\omega\,r\,L_{stk}\,\overline{B}_f$$

(2.17)

From (2.17), the forward rotor current distribution is determined from the rotor impedance and the flux density. If the rotor impedance is purely resistive, the current distribution is in phase with the flux density distribution. Since the positive direction for the current is out of the paper plane, this will produce torque in the positive (CCW) direction according to the Lorentz force:

$$\overline{F} = L_{stk} \cdot \overline{I} \times \overline{B}$$

(2.18)

$\overline{Z}$ is the rotor impedance. Since $\overline{Z}$ may contain an inductive part, it will cause the current distribution to lag the flux density by an angle $\varphi$, which is given by:

$$\varphi = \arctan\left(\frac{\mathrm{Im}(\overline{Z})}{\mathrm{Re}(\overline{Z})}\right)$$

(2.19)

Rewriting (2.17), the forward rotor current distribution becomes, in time and space

$$i_f(t,\theta) = \frac{1}{|\overline{Z}|}s\,\omega\,r\,L_{stk}\,B_f\cos(\omega t - \theta - \varphi)$$

(2.20)

**Backwards currents**

Similarly, current distributions set up by the backwards revolving flux wave will also exist in the rotor. The backwards revolving flux density wave can be expressed as

$$B_b(t,\theta) = B_b\cos(\omega t + \theta)$$

(2.21)

The relative speed of the rotor with respect to the backwards field is $(1-s)\omega + \omega = (2-s)\omega$. Using the same approach as in the previous section, the backwards rotating current distribution with respect to the stator must be:

$$i_b(t,\theta) = \frac{1}{Z}(2-s)\omega\,r\,L_{stk}\,B_b\cos(\omega t + \theta + \varphi)$$

(2.22)

This current distribution rotates at negative synchronous speed. This means, that for a motor operating at any slip other than one (standstill), two different current components, at different frequencies, namely $s\omega/2\pi$ and $(2-s)\omega/2\pi$, will flow in the rotor.

**The rotor impedance**

In (2.15), $\overline{Z}/d\theta$ is the impedance of the path defined by the angle $d\theta$. This impedance can be expressed in terms of a measurable/calculable impedance of a section of the rotor, defined by the angle $\alpha$. This impedance $\overline{Z}_\alpha$ is the parallel impedance of a large number of $\overline{Z}/d\theta$ sections so that

$$\frac{1}{\overline{Z}_\alpha} = \left(\frac{d\theta}{\overline{Z}} + \frac{d\theta}{\overline{Z}} + \cdots\right) = \int_0^\alpha \frac{1}{\overline{Z}} d\theta \quad \Rightarrow$$
$$\overline{Z} = \overline{Z}_\alpha \alpha$$

(2.23)

While this is valid for the resistive part of the impedance, it is likewise assumed that the rotor slot inductance can be calculated in a "per-angle" fashion.

## 2.4. The equivalent circuit diagram

As stated in Section 2.3, when assuming two counter-rotating, sinusoidal-distributed flux density waves in the air-gap of a machine with a conducting rotor and rotating at angular velocity $(1-s)\omega$, the rotor current distribution induced by the forward field is:

$$i_{fr}(t,\theta) = \frac{1}{\overline{Z}} s\omega L_{stk} B_{fm}(t,\theta)$$

(2.24)

Likewise, the rotor current distribution induced by the backward field:

$$i_{br}(t,\theta) = \frac{1}{\overline{Z}}(2-s)\omega L_{stk} B_{bm}(t,\theta)$$

(2.25)

In this section, the rotor current, stator current and air gap flux density are linked together.

In Section 2.1, a single pulsating MMF can be resolved into two equal, but oppositely rotating MMFs of half magnitude. This can be thought of as two series-connected windings, each having half the total number of turns in series, and each creating a forward and backwards rotating MMF. In this section the forwards and backwards components are therefore considered separately.

**The forward revolving circuit**

Fig. 2.3 shows a section of the rotor, air gap and stator for the forward-revolving wave.

2. Fundamental theory of the idealised machine
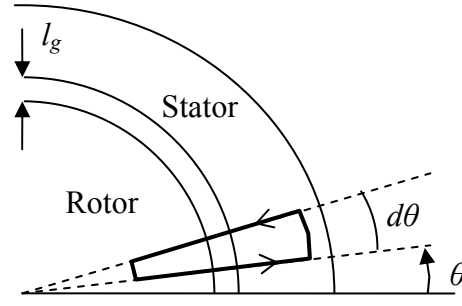


*Fig. 2.3 Closed loop used for Ampere's Law application*

The path shown in Fig. 2.3 is the closed path at which Maxwell's 3rd law (Àmpere's Law) applies. If the outward radial field direction is treated as positive:

$$\left[ H_f\left(t,\theta\right) - H_f\left(t,\theta + d\theta\right) \right] l_g = \left[ i_{fr}\left(t,\theta\right) + N_{fs}\left(\theta\right) i_s(t) \right] d\theta$$

(2.26)

Expressing this as a differential, (2.26) becomes

$$-\frac{\partial H_f\left(t,\theta\right)}{\partial\theta} = \frac{1}{l_g}\left( i_{fr}\left(t,\theta\right) + N_{fs}\left(\theta\right) i_s(t) \right)$$

(2.27)

Translation from field intensity $H$ to flux density $B$ is done by introducing $\mu_0$, the permeability of vacuum. The iron is considered infinitely permeable. The rotor current distribution $i_{fr}(t,\theta)$ is expressed in terms of the air gap flux density from (2.20). Therefore, from (2.27):

$$-\frac{\partial B_f\left(t,\theta\right)}{\partial\theta} = \frac{\mu_0}{l_g}\left( \frac{1}{Z} s\,\omega\,r\,L_{stk}\,B_f\left(t,\theta\right) + N_{fs}\left(\theta\right) i_s(t) \right)$$

(2.28)

This is an expression which is time and space dependant. For simplicity, complex notation is used. Since all functions are sine and cosine, these general rules apply:

$$\frac{\partial}{\partial\theta} \rightarrow -j \quad , \quad \frac{\partial}{\partial t} \rightarrow j\omega$$

(2.29)

Using the notation as described in (2.29), and utilising the stator winding amplitude $N/2$, further divided by 2 since only the forward rotating part of the field is considered here, (2.28) becomes

$$j\overline{B}_f = \frac{\mu_0}{l_g}\left( \frac{1}{Z} s\,\omega\,r\,L_{stk}\,\overline{B}_f + \frac{jN}{4}\overline{I}_s \right)$$

(2.30)

The $j$ in front of the winding term $N/4$ indicates where the peak of the winding number occurs, as shown in Fig. 2.4.

19

# 2. Fundamental theory of the idealised machine
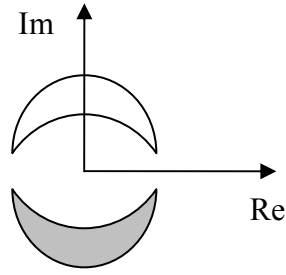


*Fig. 2.4 Winding concentration round stator surface*

Solving for $B_f$, the following expression is obtained:

$$\overline{B}_f = \frac{j\,\mu_0\,\dfrac{N}{4}}{l_g\left[j - \left(\dfrac{\mu_0}{l_g}\dfrac{1}{\overline{Z}}\,s\,\omega\,r\,L_{stk}\right)\right]} \cdot \overline{I}_s \qquad (2.31)$$

This is an expression for the forward rotating magnetic flux density in the air-gap. This revolving flux density wave induces a voltage $E_f$ into the stator winding, determined by, from (2.9)

$$\overline{E}_f = j\,\frac{N}{2}\,r\,L_{stk}\,\omega\,\pi\,\overline{B}_f \qquad (2.32)$$

Note, that in this case, $N/2$ is the winding amplitude of the complete stator winding. Inserting (2.31):

$$\overline{E}_f = j\,\frac{N}{2}\,r\,L_{stk}\,\omega\,\pi\,\frac{j\,\mu_0\,\dfrac{N}{4}}{l_g\left[j - \left(\dfrac{\mu_0}{l_g}\dfrac{1}{\overline{Z}}\,s\,\omega\,r\,L_{stk}\right)\right]} \cdot \overline{I}_s \qquad (2.33)$$

At this stage, it is worthwhile considering the rotor impedance $\overline{Z}$ in more detail. Inserting the expression from (2.23), it consists of a resistive and an inductive component. Since the current in the rotor is at slip frequency, the rotor impedance is

$$\overline{Z} = \alpha\overline{Z}_\alpha = \alpha R_\alpha + j\alpha s X_\alpha \qquad (2.34)$$

Inserting this in (2.33) and rearranging yields

## 2. Fundamental theory of the idealised machine

$$\overline{E}_f = \frac{-r L_{stk}\, \omega \pi \mu_0 \left(\dfrac{N}{4}\right)^2 2}{l_g \left[ j - \left( \dfrac{\mu_0}{l_g} \dfrac{1}{\alpha R_\alpha + j\alpha s X_\alpha} s\omega r L_{stk} \right) \right]} \cdot \overline{I}_s$$

$$= \frac{-r L_{stk}\, \omega \pi \mu_0 \left(\dfrac{N}{2}\right)^2 \dfrac{1}{2}}{l_g \left[ j - \left( \dfrac{\mu_0}{l_g} \dfrac{1}{\dfrac{\alpha R_\alpha}{s} + j\alpha X_\alpha} \omega r L_{stk} \right) \right]} \cdot \overline{I}_s$$

(2.35)

The rotor impedance term of (2.35) is expanded with $\pi$ so that

$$\overline{E}_f = \frac{-r L_{stk}\, \omega \pi \mu_0 \left(\dfrac{N}{2}\right)^2 \dfrac{1}{2}}{l_g \left[ j - \left( \dfrac{\mu_0}{l_g} \dfrac{\pi}{\dfrac{\alpha\pi R_\alpha}{s} + j\alpha\pi X_\alpha} \omega r L_{stk} \right) \right]} \cdot \overline{I}_s$$

(2.36)

The numerator and denominator of (2.36) are multiplied with the term $j[(\alpha\pi R_\alpha/s)+j\alpha\pi X_\alpha\,]$ where

$$\overline{E}_f = \frac{-j r L_{stk}\, \omega \pi \mu_0 \left(\dfrac{N}{2}\right)^2 \left( \dfrac{\alpha\pi R_\alpha}{s} + j\alpha\pi X_r \right) \dfrac{1}{2}}{l_g \left[ -\left( \dfrac{\alpha\pi R_\alpha}{s} + j\alpha\pi X_r \right) - j\left( \dfrac{\mu_0}{l_g} \pi \omega r L_{stk} \right) \right]} \cdot \overline{I}_s$$

(2.37)

Rearranging (2.37) and multiplying numerator and denominator with the term $(N/2)^2/2$ yields

$$\overline{E}_f = \frac{j\dfrac{1}{2} \dfrac{r L_{stk}\, \omega \pi \mu_0}{l_g} \left(\dfrac{N}{2}\right)^2 \dfrac{1}{2} \left( \dfrac{\alpha\pi R_\alpha}{s} + j\alpha\pi X_\alpha \right)\left(\dfrac{N}{2}\right)^2}{\dfrac{1}{2}\left( \dfrac{\alpha\pi R_\alpha}{s} + j\alpha\pi X_\alpha \right)\left(\dfrac{N}{2}\right)^2 + j\dfrac{1}{2}\left( \dfrac{\mu_0\pi \omega r L_{stk}}{l_g} \right)\left(\dfrac{N}{2}\right)^2} \cdot \overline{I}_s$$

(2.38)

This is the form of a parallel impedance, i.e. (2.38) can be rewritten as

$$\overline{E}_f = \left[ \frac{jX_m}{2} \,\|\, \frac{\dfrac{R'_r}{s} + jX'_r}{2} \right] \cdot \overline{I}_s$$

(2.39)

where

$$X_m = \frac{r L_{stk}\, \omega \pi \mu_0 \left(\dfrac{N}{2}\right)^2}{l_g}$$

(2.40)

and

$$\frac{R'_r}{s} = \frac{\alpha \pi R_\alpha}{s} \left( \frac{N}{2} \right)^2 \quad , \quad X'_r = \alpha \pi X_\alpha \left( \frac{N}{2} \right)^2 \tag{2.41}$$

with $R_\alpha$ and $X_\alpha$ being the resistance and leakage inductance of a rotor section, determined by angle $\alpha$.

**The backwards revolving circuit**

The analysis in the previous section concentrates on the air gap flux density wave which is rotating in the forwards direction (i.e. in the direction of the rotor). The analysis can be more or less repeated for the backwards rotating flux density, with the exception that

$$\frac{\partial}{\partial \theta} \to j \quad , \quad \frac{\partial}{\partial t} \to j\omega \quad , \quad \int d\theta \to -j \tag{2.42}$$

Using this notation in the previous section, the induced EMF in the stator winding by the backwards rotating field component is determined from

$$\overline{E}_b = \left[ \frac{jX_m}{2} \, \| \, \frac{\frac{R'_r}{2-s} + jX'_r}{2} \right] \cdot \overline{I}_s \tag{2.43}$$

with $R'_r$ and $X'_r$ as given by (2.41).

**The equivalent circuit diagram**

Equations (2.39) and (2.43) are expressions for the voltages induced into the stator winding by the forward and backwards rotating flux density waves. The total induced voltage must be the vector sum of the two. In both cases the EMF is determined by the stator current $I_s$.

Observing that the current is limited partly by the EMF and partly by the stator resistance and leakage inductance, the equivalent circuit diagram of the single-phase machine can be represented as Fig. 2.5.
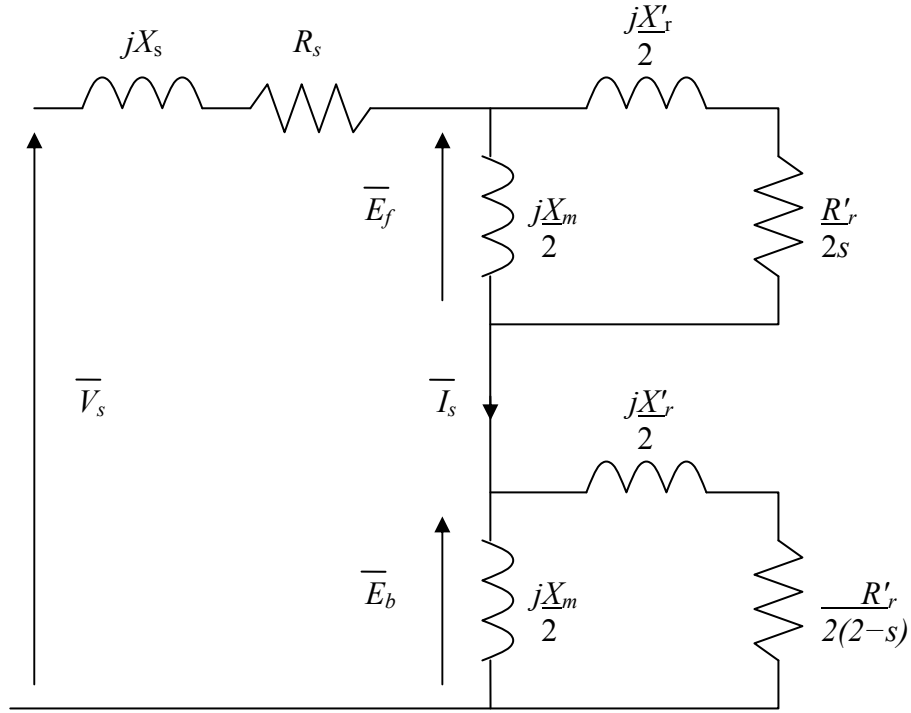
*Fig. 2.5 Equivalent circuit of single phase machine considering sinusoidal winding*

This is how the classical revolving fields equivalent circuit was introduced in [2]

## 2.5. Location of current distributions

This section studies the current distribution of the rotor and stator in space. These distributions use the phasor diagram technique shown by Miller in [28] and extended to cover both forward and backwards rotating components.

The visualization of the current distribution phasor starts with the forward air gap flux density. This is plotted in Fig. 2.6 as $\overline{B}_f$. This is generated by a (fictitious) MMF, this is the magnetizing current, $\overline{F}_{imf}$, which is in phase with $\overline{B}_f$.

In Section 2.3 it was shown that the rotor current distribution is shifted from the air gap flux density by an angle $\varphi$, which is determined by the rotor impedance. However, the impedance itself is determined by the slip. At low slip, when the rotor impedance is mostly resistive, and relatively high, the spatial displacement between flux density and current distribution (angle $\varphi$) is small. The rotor MMF is shifted by 90° (lagging) from the current itself, and plotted in Fig. 2.6 as $\overline{F}_{irf}$. Since $\overline{F}_{imf}$ is the resulting MMF, it requires that the rotor MMF is balanced by the stator. This balancing MMF is shown as $\overline{F}'_{irf}$ in Fig. 2.6. Therefore, the resulting stator MMF $\overline{F}_{isf}$ consists of two parts: a magnetizing MMF and a rotor balancing MMF.

These two MMFs are set up by the stator current, and it is these that are represented in the equivalent circuit diagram. The rotor MMF itself is not "seen" in the equivalent circuit diagram.

The phasor diagram for the backwards revolving circuit is derived from the starting point of the stator MMF $\overline{F}_{isb}$ since this must be of equal magnitude but opposite angle as the forward stator MMF. At low per-unit slip, the backwards slip (2−s) is high so that the rotor impedance is low and significantly inductive. Therefore, the rotor MMF is only a little smaller than the stator MMF, and only leading this by a small angle. From this, the remaining phasors are deduced in a similar manner to the forward circuit, and the result is given in Fig. 2.7.
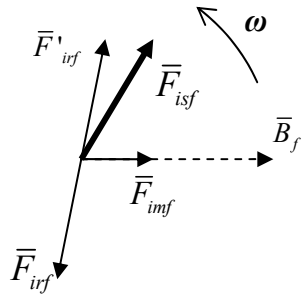


Fig. 2.6 Forward MMF phasors                    Fig. 2.7 Backward MMF phasors
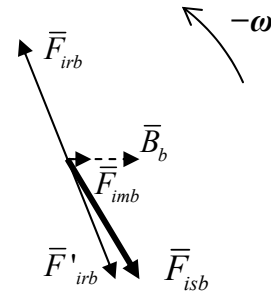
## 2.6. Force and torque

Figs. 2.6 and 2.7 explain how torque is created in a single phase machine: at slips smaller than 1, the forward flux density is greater than the backward flux density, and the rotor forward MMF, though smaller in magnitude than the backward rotor MMF, is in a better spatial position to produce force. In this section an expression for the machine torque is derived.

From Fig. 2.6, the forward flux density and rotor current distribution (not MMF) is displaced at an angle $\varphi$ with respect to each other. If in a standard Cartesian coordinate system with $x$ being from origo to right, $y$ upwards and $z$ outwards, the current and the flux density are orthogonal in the $(x, z)$ plane, the Lorenz force acting on a small segment of the rotor will be

$$dF_f = L_{stk} I_{rf} \cos\left(\omega t - \theta - \varphi_f\right) B_{rf} \cos\left(\omega t - \theta\right) d\theta \qquad (2.44)$$

Note that the flux density $B_{fr}$ is the flux density at the rotor bars, which is greater than the air gap flux density $B_f$. The total rotor force is then found by integrating (2.44) around the rotor circumference where

$$F_f = \int_0^{2\pi} L_{stk} I_{rf} \cos(\omega t - \theta - \varphi_f) B_{rf} \cos(\omega t - \theta) d\theta$$

$$= L_{stk} I_{rf} B_{rf} \cos(-\varphi_f) \pi \qquad (2.45)$$

And the rotor torque is

$$T_f = L_{stk} I_{rf} B_{rf} \cos(\varphi_f) \pi r_r \qquad (2.46)$$

This can be translated to air-gap values. The air-gap flux is equal to the flux at the rotor conductor, so (2.46) becomes

$$T_f = L_{stk} I_{rf} B_f \cos(\varphi_f) \pi r \qquad (2.47)$$

Expressing the torque in terms of equivalent circuit parameters, (2.47) can be rewritten using (2.32) so that

$$T_f = \frac{E}{\omega \left( \dfrac{N}{2} \right)} \cos(\varphi_f) I_{rf} \qquad (2.48)$$

From Fig. 2.6 it can be seen that that the rotor MMF is of equal magnitude but opposite angle to the referred rotor MMF, i.e., $\overline{F}_{irf} = -\overline{F}'_{irf}$. In terms of the current, this means:

$$\left| \overline{F}_{Irf} \right| = \int_0^{\pi} I_{rf} \sin(\theta) d\theta = 2 I_{rf} \qquad (2.49)$$

and

$$\left| \overline{F}_{I'rf} \right| = \int_0^{\pi} \frac{N}{4} I'_{rf} \sin(\theta) d\theta = \frac{N}{2} I'_{rf} \qquad (2.50)$$

so that

$$\overline{I}_{rf} = -\frac{N}{4} \overline{I}'_{rf} \quad \Rightarrow \quad I_{rf} = \frac{N}{4} I'_{rf} \qquad (2.51)$$

It should be emphasized that the rotor current and induced voltage are expressed in terms of their amplitude, i.e. peak value. Inserting (2.51) and rewriting in terms of RMS values, (2.48) becomes

$$T_f = \frac{E_{f\,rms} \sqrt{2}}{2\omega} \cos(\varphi_f) I'_{fr\,rms} \sqrt{2} = \frac{E_{f\,rms}}{\omega} \cos(\varphi_f) I'_{fr\,rms} \qquad (2.52)$$

with angle $\varphi_f$ equal to the phase angle of the forward rotor impedance $Z_r$, but also the phase angle of $I'_{fr}$ and $E_f$. Similarly, the backwards torque is

$$T_b = \frac{E_{b\,rms}}{\omega} \cos(\varphi_b) I'_{br\,rms} \qquad (2.53)$$

The shaft power is then equal to

$$P_{shaft} = \omega'\left(T_f - T_b\right) \tag{2.54}$$

**Pulsating torque**

Equations (2.53) and (2.54) are expressed in terms of the RMS values of EMF and (referred) rotor current. This means that they have no time or space dependency, and since the difference between the two is the resulting torque, this appears to be constant in time. However, (2.53) and (2.54) describe the interaction of the forward and backward flux density and current respectively. Other torque components exist due to the interaction of the forward field with the backward current and vice versa.

The force due to the forward rotating rotor current distribution and the backwards rotating flux density on an infinitesimal element of the rotor is

$$dF_{IfrBbr} = L_{stk}I_{fr}\cos\left(\omega t - \theta - \varphi_f\right)B_{br}\left(\omega t + \theta\right)d\theta \tag{2.55}$$

Integrating over the entire rotor circumference, the corresponding torque can be expressed as

$$T_{IfrBb} = L_{stk}I_{fr}B_b r\pi \cos\left(2\omega t - \varphi_f\right) \tag{2.56}$$

And similarly:

$$T_{IbrBf} = L_{stk}I_{br}B_f r\pi \cos\left(2\omega t - \varphi_b\right) \tag{2.57}$$

The sum of (2.56) and (2.57) gives the shaft torque its pulsating behaviour. This makes the shaft torque pulsate at twice line frequency, but since this component produces no average torque, (2.54) is sufficient to calculate the machine output.

## 2.7. The auxiliary winding

An inherent shortcoming of the single-phase motor is that since the forward and backward circuits are identical at standstill, the forward and backward torques will be identical and no net starting torque is produced.

When introducing an auxiliary winding, the performance of the resulting split-phase motor resembles that of a polyphase machine.

**The split-phase equivalent circuit**

An equivalent circuit derivation similar to Section 2.4 is possible; this includes the auxiliary winding, which leads the main winding in space by $\pi/2$, i.e., the phasor is displaced mechanically by $-j$ relative to the main winding. This is shown in Fig. 2.8.

## 2. Fundamental theory of the idealised machine
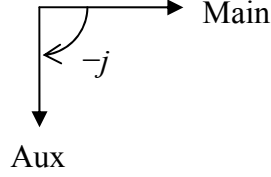


*Fig. 2.8 Main and auxiliary winding spatial relationship*

Starting with Maxwell's 3rd law, the process of coupling the stator and rotor circuits is repeated, but this time taking the auxiliary winding into account. Therefore

$$j\overline{B}_f = \frac{\mu_0}{l_g}\left(\frac{1}{\overline{\overline{Z}}}s\,\omega\,r\,L_{stk}\overline{B}_f + \frac{jN_m}{4}\overline{I}_m + \frac{N_a}{4}\overline{I}_a\right) \tag{2.58}$$

where $N_m$ and $N_a$ are the total winding turns of the (sinusoidal) main and auxiliary winding, and $\overline{I}_m$ and $\overline{I}_a$ representing the main and auxiliary current phasors.

Solving for $\overline{B}_f$, (2.58) becomes

$$\overline{B}_f = \frac{-j\mu_0\dfrac{N_m}{4}\overline{I}_m - \mu_0\dfrac{N_a}{4}\overline{I}_a}{l_g\left[j - \left(\dfrac{\mu_0}{l_g}\dfrac{1}{\overline{\overline{Z}}}s\,\omega\,r\,L_{stk}\right)\right]} \tag{2.59}$$

The induced voltage in the main and auxiliary winding from this flux density is, from (2.32):

$$\overline{E}_{fm} = j\frac{N_m}{2}r\,L_{stk}\,\omega\,\pi\,\overline{B}_f \quad , \quad \overline{E}_{fa} = jj\frac{N_a}{2}r\,L_{stk}\,\omega\,\pi\,\overline{B}_f \tag{2.60}$$

Here, it is useful to introduce the winding ratio $\beta$, which is defined by

$$\beta = \frac{N_a}{N_m} \tag{2.61}$$

Using the winding ratio, (2.60) becomes, for the main winding:

$$\overline{E}_{fm} = \frac{j\dfrac{N_m}{2}r\,L_{stk}\,\omega\,\pi\,j\mu_0\dfrac{N_m}{4}}{l_g\left[j - \left(\dfrac{\mu_0}{l_g}\dfrac{1}{\overline{\overline{Z}}}s\,\omega\,r\,L_{stk}\right)\right]}\overline{I}_m + \frac{j\dfrac{N_a}{\beta\,2}r\,L_{stk}\,\omega\,\pi\,\mu_0\dfrac{N_a}{4}}{l_g\left[j - \left(\dfrac{\mu_0}{l_g}\dfrac{1}{\overline{\overline{Z}}}s\,\omega\,r\,L_{stk}\right)\right]}\overline{I}_a \tag{2.62}$$

This can be translated into circuit parameters using the same approach as in (2.34) to (2.39):

$$\overline{E}_{fm} = \left[\frac{jX_{mm}}{2}\,\Big\|\,\frac{\dfrac{R'_{rm}}{s} + jX'_{rm}}{2}\right]\overline{I}_m + \frac{-j}{\beta}\left[\frac{jX_{ma}}{2}\,\Big\|\,\frac{\dfrac{R'_{ra}}{s} + jX'_{ra}}{2}\right]\overline{I}_a \tag{2.63}$$

Similarly, for the auxiliary winding:

$$\bar{E}_{fa} = \frac{-\dfrac{N_a}{2} r L_{stk} \,\omega\pi\,\mu_0 \dfrac{N_a}{4}}{l_g\left[ j - \left( \dfrac{\mu_0}{l_g}\dfrac{1}{Z} s\,\omega r L_{stk} \right) \right]} \bar{I}_a + \frac{-\dfrac{\beta N_m}{2} r L_{stk} \,\omega\pi\,j\mu_0 \dfrac{N_m}{4}}{l_g\left[ j - \left( \dfrac{\mu_0}{l_g}\dfrac{1}{Z} s\,\omega r L_{stk} \right) \right]} \bar{I}_m \tag{2.64}$$

which, when expressed in circuit parameters, becomes

$$\bar{E}_{fa} = \left[ \frac{jX_{ma}}{2} \,\|\, \frac{\dfrac{R'_{ra}}{s} + jX'_{ra}}{2} \right] \bar{I}_a + j\beta \left[ \frac{jX_{mm}}{2} \,\|\, \frac{\dfrac{R'_{rm}}{s} + jX'_{rm}}{2} \right] \bar{I}_m \tag{2.65}$$

The equations (2.62) to (2.65) show that the voltage in the main and auxiliary windings due to the forward component of the flux density contain components of current and impedance both from its own winding and the other winding, i.e., it can be interpreted as a pure impedance and an induced voltage.

This derivation can be repeated for the backwards component of flux density with similar results; however, since the rotation is opposite, the phases of the induced voltages from the other winding are shifted π. From this, the split-phase equivalent circuit diagram can be derived.


**Forward and backward rotating fields**

Introducing the auxiliary winding results in 2 pairs of forwards and backwards rotating components in the air-gap. The symmetry line of these are orthogonal to each other as shown in Fig. 2.9.
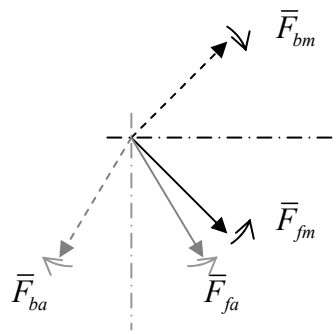


*Fig. 2.9 Forwards and backwards MMF components for main and auxiliary currents*


By correct magnitude matching and phase alignment, the forward components will add directly and the backwards components cancel each other. With this, the drawbacks related to the backwards rotating fields disappear completely: losses in backward circuit and torque pulsations.

**Force and torque**

The forward force created in the split-phase motor is found identically to (2.52) with the exception that there are contributions from both windings. As shown previously, the forward flux density is the vector sum of the main and auxiliary flux densities, spatially displaced by angle $\gamma_f$. Hence

$$dF_f = L_{stk} I_{rfm} \cos\left(\omega t - \theta - \varphi_f\right)\left[ B_{rfm} \cos\left(\omega t - \theta\right) + B_{rfa} \cos\left(\omega t - \theta + \gamma_f\right)\right]d\theta +$$
$$+L_{stk} I_{rfa} \cos\left(\left(\omega t - \theta + \gamma_f - \varphi_f\right)\right)\left[ B_{rfm} \cos\left(\omega t - \theta\right) + B_{rfa} \cos\left(\omega t - \theta + \gamma_f\right)\right]d\theta \quad (2.66)$$

where $\varphi_f$ is the (identical) angle of the rotor impedances of the main and auxiliary circuits.

The total rotor torque is found by integrating (2.66) over the rotor circumference and including the rotor radius:

$$T_f = \frac{r L_{stk} I_{rfm} B_{rfm}}{2}\left[\int_0^{2\pi} \cos\left(-\varphi_f\right)d\theta + \int_0^{2\pi} \cos\left(2\omega t - 2\theta - \varphi_f\right)d\theta\right] +$$
$$+\frac{r L_{stk} I_{rfm} B_{rfa}}{2}\left[\int_0^{2\pi} \cos\left(-\varphi_f - \gamma_f\right)d\theta + \cdots\right] + \cdots \quad (2.67)$$
$$= r L_{stk} I_{rfm}\pi\left( B_{rfm} \cos\left(-\varphi_f\right) + B_{rfa} \cos\left(-\varphi_f - \gamma_f\right)\right) +$$
$$+r L_{stk} I_{rfa}\pi\left( B_{rfm} \cos\left(-\varphi_f + \gamma_f\right) + B_{rfa} \cos\left(-\varphi_f\right)\right)$$

$\gamma_f$ is the spatial angle between the forward revolving flux densities set up by the main and the auxiliary winding. But it is also the angle between the two components of induced voltage in each winding, as shown by Fig. 2.10, where, the induced voltages lead the respective flux densities.

Main winding         Aux winding
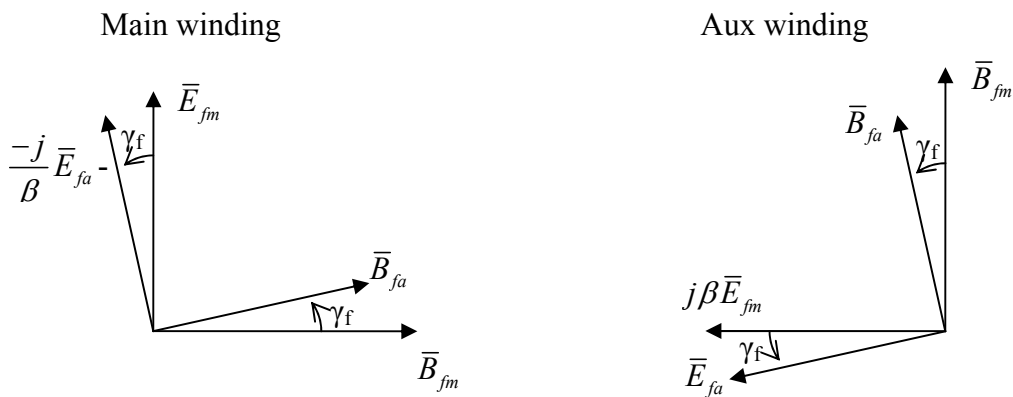


*Fig. 2.10 Main and auxiliary winding air-gap flux and electric field phasors*

Equation (2.67) is expressed in terms of induced voltages instead of flux densities, and referred rotor current instead of "direct" or "true" rotor current; analogous to (2.50) to (2.53) where

## 2. Fundamental theory of the idealised machine

$$T_f = \left[ \frac{E_{fm}}{2\omega}\cos\left(-\varphi_f\right) + \frac{\frac{1}{\beta}E_{fa}}{2\omega}\cos\left(-\varphi_f - \gamma_f\right) \right] I'_{rfm} +$$

$$+ \left[ \frac{E_{fa}}{2\omega}\cos\left(-\varphi_f\right) + \frac{\beta E_{fm}}{2\omega}\cos\left(-\varphi_f + \gamma_f\right) \right] I'_{rfa} \tag{2.68}$$

This is expressed in terms of peak values. The same expression in phasor notation (RMS values) becomes

$$T_f = \mathrm{Re}\left( \left[ \frac{\bar{E}_{fm}}{\omega} + \frac{\frac{-j}{\beta}\bar{E}_{fa}}{\omega} \right] \bar{I}'^{*}_{rfm} \right) + \mathrm{Re}\left( \left[ \frac{\bar{E}_{fa}}{\omega} + \frac{j\beta\bar{E}_{fm}}{\omega} \right] \bar{I}'^{*}_{rfa} \right) \tag{2.69}$$

The backwards torque can be expressed in a similar way so that

$$T_b = \mathrm{Re}\left( \left[ \frac{\bar{E}_{bm}}{\omega} + \frac{\frac{j}{\beta}\bar{E}_{ba}}{\omega} \right] \bar{I}'^{*}_{rbm} \right) + \mathrm{Re}\left( \left[ \frac{\bar{E}_{ba}}{\omega} + \frac{-j\beta\bar{E}_{bm}}{\omega} \right] \bar{I}'^{*}_{rba} \right) \tag{2.70}$$

As mentioned in Section 2.6, (2.69) and (2.70) are time-constant values. For the pure single-phase machine, the shaft torque will have an oscillating component at double line frequency, due to the interaction of forward and backwards flux densities and rotor current distributions. However, in the special case where the motor is perfectly balanced, these oscillating components disappear, making the shaft torque perfectly constant in time.

# Chapter 3

# The influence of winding harmonics

In the previous chapter, only the fundamental MMF is considered. Since a winding is distributed in a finite number of slots, and may not be exactly sine wound, it will be in the form of a spatial harmonic series, the magnitudes of which can be investigated mathematically.

These harmonics series of order $m$ will have $m$ times as many poles as the fundamental winding. In this chapter, their impact on the motor performance is investigated.

Since the equivalent circuit is a convenient way of determining the motor properties, the equivalent circuit diagram derived in Chapter 2 will be extended to include winding harmonics. Symmetrical main and auxiliary winding are assumed, which means that even-order harmonics are eliminated due to half-wave symmetry. Some motor configurations can result in even-order harmonics being generated due to tapped-winding connection during starting, as described in [7], however, the following analysis considers odd winding harmonics only.

## 3.1. Properties of the harmonic MMF

In the following, some basic properties of the general winding of harmonic order $m$ are derived. They will be referred to at a later stage.

**Synchronous speed of the $m^{th}$ harmonic MMF**

From (2.1) in Chapter 2, the $m^{th}$ harmonic MMF can be expressed as

$$F(t,\theta,m) = N_m \cos(m\theta) I \cos(\omega t)$$
$$= \frac{N_m I}{2} \left( \cos(\omega t - m\theta) + \cos(\omega t + m\theta) \right) \qquad (3.1)$$
$$\qquad\qquad forward \qquad\quad backward$$

The synchronous speed of the forward MMF is determined by the time it takes for the $m^{th}$ harmonic MMF to complete one *mechanical* cycle, i.e.:

$$\omega t = m\theta \ \text{ for } \theta = 2\pi$$

which gives

$$t = \frac{m2\pi}{\omega} = \frac{1}{f} = \frac{2\pi}{\omega_{sm}} \ \Rightarrow \ \omega_{sm} = \frac{\omega}{m} \qquad (3.2)$$

**Winding amplitude of the $m^{\text{th}}$ harmonic winding**

Since the harmonic MMF is given by (3.1), $N_m$ is the total winding number *of one pole pitch*.

The (fictious) winding amplitude $\hat{N}_m$ of this winding is found from

$$N_m = \int_0^{\pi/m} \hat{N}_m \sin(m\theta) \, d\theta = \frac{\hat{N}_m}{m} \left[ -\cos(m\theta) \right]_0^{\pi/m} \Rightarrow$$

$$\hat{N}_m = \frac{m N_m}{2}$$

(3.3)

## 3.2. Induction, windings and fluxes of different harmonic order

This section investigates the influence of harmonic windings and fluxes. Therefore, it is necessary to investigate the effects of flux densities and winding distributions of different harmonic order.

This is similar to the approach described in Chapter 2 - but in this case the winding and the flux density is not necessarily of the same harmonic order.

The $m^{\text{th}}$ harmonic winding can be described by (3.3) where

$$N_m(\theta) = \frac{m N_m}{2} \sin(m\,\theta)$$

(3.4)

Similarly, the $n^{\text{th}}$ harmonic component of air gap flux density can be described by

$$B_n(t,\theta) = B_n \cos(\omega t - n\,\theta)$$

(3.5)

From (2.6):

$$E_{(mn)}(\alpha) = -\frac{m N_{(m)}}{2}(m,\alpha) \frac{d}{dt} r L_{stk} \int_{-\alpha}^{\alpha} B_{(n)}(t,\theta) \, d\theta$$

(3.6)

Inserting (3.4) and (3.5) yields

$$
\begin{aligned}
E_{(mn)}(\alpha) &= -\frac{m N_m}{2} \sin(m\alpha) \frac{d}{dt} r L_{stk} \int_{-\alpha}^{\alpha} B_{(n)} \cos(\omega t - n\theta) \, d\theta \\
&= -\frac{m N_m}{2} \sin(m\alpha) \frac{d}{dt} r L_{stk} \frac{-2B_n}{n} \cos(\omega t) \sin(n\alpha) \\
&= m N_m \sin(m\alpha) \sin(n\alpha) \frac{B_n \, r \, L_{stk} \, \omega}{n} \sin(\omega t)
\end{aligned}
$$

(3.7)

The total voltage is found by integrating (3.7) with respect to $\alpha$ from 0 to $\pi$:

$$
\begin{aligned}
E_{(mn)}(t) &= \int_0^{\pi} E_{(mn)}(\alpha,t) \, d\alpha \\
&= \frac{m}{n} N_m B_n r L_{stk} \omega \sin(\omega t) \int_0^{\pi} \sin(m\alpha) \sin(n\alpha) \, d\alpha
\end{aligned}
$$

(3.8)

Using the trigonometric identity $\sin(A)\sin(B) = \frac{1}{2}[\cos(A-B) - \cos(A+B)]$, (3.8) becomes

$$E_{(mn)}(t) = \frac{m}{2n} N_m B_n r L_{stk} \omega \sin(\omega t) \left[ \int_0^\pi \cos\left(\alpha[m-n]\right) d\alpha - \int_0^\pi \cos\left(\alpha[m+n]\right) d\alpha \right]$$

$$= \frac{m}{2n} N_m B_n r L_{stk} \omega \sin(\omega t) \left[ \left[ \frac{\sin\left(\alpha[m-n]\right)}{m-n} \right]_0^\pi - \left[ \frac{\sin\left(\alpha[m+n]\right)}{m+n} \right]_0^\pi \right] \tag{3.9}$$

Since $m$ and $n$ are whole numbers, both $m-n$ and $m+n$ will be whole numbers, in which case

$$E_{(mn)}(t) = 0 \quad \text{for } m \neq n \tag{3.10}$$

This shows that only windings and fluxes of equal harmonic order induce voltages. In this case, for harmonic order $m$, (3.8) reduces to

$$E_{(m)}(t) = \int_0^\pi E_{(m)}(\alpha,t) d\alpha$$

$$= N_m B_m r L_{stk} \omega \sin(\omega t) \int_0^\pi \sin^2(m\alpha)\, d\alpha \tag{3.11}$$

$$= N_m B_m r L_{stk} \omega \sin(\omega t) \left[ \frac{\alpha}{2} - \frac{\sin(2m\alpha)}{4m} \right]_0^\pi$$

$$= \frac{N_m B_m r L_{stk} \omega}{2} \sin(\omega t)$$

Again it should be emphasized that in (3.11) $N_m$ is the harmonic winding number of the harmonic winding. The winding amplitude of this winding is described by (3.3).

## 3.3. Equivalent circuit including winding harmonics

Below, an approach similar to that described in Section 2.4 will be used to include winding harmonics in the equivalent circuit.

**Harmonic forward rotor current distributions**

The harmonic MMFs set up flux density waves in the air-gap which induce rotor EMFs and generate rotor currents similar to the fundamental. However, there are dissimilarities in terms of relative speeds. When the rotor rotates at slip speed $\omega' = (1-s)\omega$, the fundamental flux density wave will rotate with speed $s\omega$ relative to the rotor. However the $m^{th}$ harmonic flux density will rotate at synchronous speed $\omega_{sm} = \omega/m$ relative to the stator. This will rotate with a speed relative to the rotor. This speed is given by:

$$\omega_{sm} - \omega' = \frac{\omega}{m} - (1-s)\omega = \omega\left(\frac{1}{m} - 1 + s\right) \tag{3.12}$$

where $\omega$ is the radian frequency of the voltage supply. Therefore, Section 2.4 can be repeated by applying the following substitutions:

# 3. The influence of winding harmonics

$$s \;\rightarrow\; \frac{1}{m} - 1 + s \tag{3.13}$$

$$\theta \;\rightarrow\; m\theta \tag{3.14}$$

As a consequence of (3.13) and (3.14), in complex notation, this means that

$$\frac{\partial}{\partial t} \;\rightarrow\; j\left[\frac{1}{m} - 1 + s\right]\omega \quad,\quad \frac{\partial}{\partial \theta} \;\rightarrow\; -jm \tag{3.15}$$

and the induced rotor current distribution due to the $m^{th}$ harmonic forward revolving flux density wave is

$$\overline{I}_f = \frac{1}{\overline{Z}} j\left[\frac{1}{m} - 1 + s\right]\omega(-jm)\overline{B}_f r\, L_{stk} = \frac{1}{\overline{Z}}\left[1 - m + sm\right]\omega r\, L_{stk}\,\overline{B}_f \tag{3.16}$$

The frequency of the current is $(1 - m + sm)\omega$ relative to the rotor.

**Harmonic backward rotor current distributions**

As mentioned previously, the backwards MMF and subsequent backward-rotating flux density wave are also present. The speed of those relative to the rotor is

$$\omega_{sm} + \omega' = \frac{\omega}{m} + (1-s)\omega = \omega\left(\frac{1}{m} + 1 - s\right) \tag{3.17}$$

Following a similar approach, the induced rotor current distribution due to the $m^{th}$ harmonic backward-revolving flux density is

$$\overline{I}_b = \frac{1}{\overline{Z}} j\left[\frac{1}{m} + 1 - s\right]\omega(-jm)\overline{B}_b r\, L_{stk} = \frac{1}{\overline{Z}}\left[1 + m - sm\right]\omega r\, L_{stk}\,\overline{B}_b \tag{3.18}$$

**The space-harmonic rotor impedance**

In Section 2.4 the "per angle" rotor impedance was derived. Here, the $m^{th}$ harmonic current distribution is considered. Compared to the fundamental, this means that only $1/m$ of the conducting area is available to carry the current for one pole pitch of the rotor current as illustrated in Fig. 3.1, which shows a linearised rotor section.



Fundamental current distribution
3$^{rd}$ harmonic current distribution
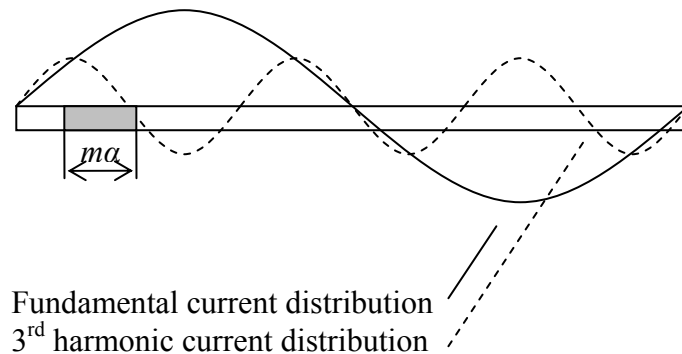
*Fig. 3.1 MMF distribution with 3$^{rd}$ harmonic*

Mathematically, this means that for the $m^{\text{th}}$ harmonic current distribution, the total rotor circumference will have the angular length of $2m\pi$. An absolute angular section of the rotor $\beta$ will have a length corresponding to $m\alpha$. Hence, the infinitesimal impedance of a rotor section $d\theta$ can be derived in a similar way to (2.23) by modifying the expression for the harmonic order, i.e.:

$$\frac{1}{\overline{Z}_\alpha} = \left( \frac{d\theta}{\overline{Z}} + \frac{d\theta}{\overline{Z}} + \cdots \right) = \int_0^{m\alpha} \frac{1}{\overline{Z}} d\theta \quad \Rightarrow$$
$$\overline{Z} = \overline{Z}_\alpha m\alpha \tag{3.19}$$

**Derivation of the equivalent circuit including winding harmonics**

In order to evaluate the effects of the winding harmonics, the theory derived from Maxwell's 3rd law in Section 2.4 for the forward-revolving components is repeated. This includes the effect of the $m^{\text{th}}$ harmonic. Only the $m^{\text{th}}$ harmonic is considered, but this covers all the winding harmonics in consideration.

From (2.28):

$$-\frac{\partial B_f(t,\theta)}{\partial \theta} = \frac{\mu_0}{l_g} \left[ \frac{1}{\overline{Z}} s \omega r L_{stk} B_f(t,\theta) + \frac{1}{\overline{Z}} [1-m+sm] \omega r L_{stk} B_{fm}(t,\theta) \right.$$
$$\left. + \left( N_{fs}(\theta) + N_{fsm}(\theta) \right) i_s(t) \right] \tag{3.20}$$

The left-hand side of (3.20) is expanded using (3.15) so that (3.20) becomes, in phasor notation:

$$j\overline{B}_f + jm\overline{B}_{fm} = \frac{\mu_0}{l_g} \left[ \frac{1}{\overline{Z}} s \omega r L_{stk} \overline{B}_f + \frac{1}{\overline{Z}} [1-m+sm] \omega r L_{stk} \overline{B}_{fm} + \left( \overline{N} + \overline{N}_m \right) \overline{I}_s \right] \tag{3.21}$$

This is a single equation with two unknown phasors $\overline{B}_f$ and $\overline{B}_{fm}$. It is split into two separate equations (3.22) and (3.23) since they have different spatial frequency (space harmonic) and therefore can not affect each other. When solved separately:

$$j\overline{B}_f = \frac{\mu_0}{l_g} \left( \frac{1}{\overline{Z}} s \omega r L_{stk} \overline{B}_f + \frac{jN}{4} \overline{I}_s \right) \tag{3.22}$$

$$jm\overline{B}_{fm} = \frac{\mu_0}{l_g} \left( \frac{1}{\overline{Z}} [1-m+sm] \omega r L_{stk} \overline{B}_{fm} + \frac{jmN_m}{4} \overline{I}_s \right) \tag{3.23}$$

where (3.22) is identical to (2.58) while (3.23) is similar but contains modification for the harmonic order and the slip. However, in (3.23) $\overline{B}_{fm}$ can be expressed according to (2.58) when substituting $j$ with $jm$ and $s$ with $[1-m+sm]$; in which case (3.23) becomes

# 3. The influence of winding harmonics

$$\bar{B}_{fm} = \frac{j\,\mu_0\,\dfrac{mN_m}{4}}{l_g\left[jm - \left(\dfrac{\mu_0}{l_g}\dfrac{1}{Z}[1-m+sm]\omega r L_{stk}\right)\right]}\bar{I}_s \qquad (3.24)$$

From (3.11):

$$\bar{E}_{fm} = j\frac{N_m}{2}r L_{stk}\,\omega\,\pi\,\bar{B}_{fm} \qquad (3.25)$$

which, when (3.24) is inserted with a slight modification to the denominator, gives

$$\bar{E}_{fm} = j\frac{N_m}{2}r L_{stk}\,\omega\,\pi\,\frac{j\dfrac{\mu_0}{l_g}\dfrac{m\,N_m}{4}}{jm - \left(\dfrac{\mu_0}{l_g}\dfrac{1}{Z}[1-m+sm]\omega r L_{stk}\right)}\bar{I}_s \qquad (3.26)$$

Inserting $Z = m\,\alpha\,R_\alpha + j\,m\,\alpha\,(1-m+sm)\,X_\alpha$ from (2.19) and expanding the impedance ratio with $\pi$, (3.26) becomes

$$\bar{E}_f = \frac{-\dfrac{\mu_0\,r L_{stk}\,\omega\,\pi\,m}{l_g}\left(\dfrac{N_m}{2}\right)^2\dfrac{1}{2}}{jm - \dfrac{\mu_0}{l_g}\dfrac{\pi}{\dfrac{m\,\alpha\,\pi\,R_\alpha}{1-m+sm}+j\,m\,\alpha\,\pi X_\alpha}\omega r L_{stk}}\bar{I}_s \qquad (3.27)$$

The numerator and denominator is expanded with the impedance expression so that

$$\bar{E}_f = \frac{-\dfrac{\mu_0 r L_{stk}\,\omega\,\pi\,m}{l_g}\left(\dfrac{N_m}{2}\right)^2\dfrac{1}{2}\left(\dfrac{m\,\alpha\,\pi\,R_\alpha}{1-m+sm}+j\,\alpha\,\pi X_\alpha\right)}{jm\left(\dfrac{m\,\alpha\,\pi\,R_\alpha}{1-m+sm}+j\,m\,\alpha\,\pi X_\alpha\right)-\dfrac{\mu_0 r L_{stk}\,\omega\,\pi}{l_g}}\bar{I}_s \qquad (3.28)$$

Rearranging and expanding with $-\tfrac{1}{2}j(N_m/2)^2$ yields

$$\bar{E}_f = \frac{j\dfrac{\mu_0 r\,L_{stk}\,\omega\,\pi}{l_g}\left(\dfrac{N_m}{2}\right)^2\dfrac{1}{2}\left(\dfrac{m^2\alpha\pi R_\alpha}{1-m+sm}+jm^2\alpha\pi X_\alpha\right)\left(\dfrac{N_m}{2}\right)^2\dfrac{1}{2}}{\left(\dfrac{m^2\alpha\,\pi R_\alpha}{1-m+sm}+jm^2\alpha\pi X_\alpha\right)\left(\dfrac{N_m}{2}\right)^2\dfrac{1}{2}+j\dfrac{\mu_0 r L_{stk}\,\omega\,\pi}{l_g}\left(\dfrac{N_m}{2}\right)^2\dfrac{1}{2}}\bar{I}_s \qquad (3.29)$$

By inspection, (3.29) is seen to consist of a parallel impedance network, i.e.:

$$\bar{E}_{fm} = \left[\frac{jX_{mm}}{2}\,\middle\|\,\frac{\dfrac{R'_{rm}}{1-m+sm}+jX'_{rm}}{2}\right]\bar{I}_s \qquad (3.30)$$

where

36

$$X_{mm} = \frac{r\,L\,\omega\,\pi\,\mu_0 \left(\dfrac{N_m}{2}\right)^2}{l_g} \tag{3.31}$$

and

$$\frac{R'_{rm}}{1-m+sm} = \frac{m^2 \alpha \pi R_\alpha}{1-m+sm}\left(\frac{N_m}{2}\right)^2 \quad,\quad X'_r = m^2 \alpha \pi X_\alpha \left(\frac{N_m}{2}\right)^2 \tag{3.32}$$

with $R_\alpha$ and $X_\alpha$ being the resistance and leakage reactance of a rotor section determined by angle $\alpha$. $N_m$ is the total winding number *of one pole pitch*, i.e. $mN_m/2$ is the winding amplitude of the $m$th harmonic winding. Similarly, for the backwards MMF:

$$\overline{E}_{bm} = \left[ \frac{jX_{mm}}{2} \,\|\, \frac{\dfrac{R'_{rm}}{1+m-sm} + jX'_{rm}}{2} \right] \overline{I}_s \tag{3.33}$$

with $R'_{rm}$ and $X'_{rm}$ obtained from (3.32).

In terms of the equivalent circuit, the sum of all EMFs and the voltage drop across the stator resistance and leakage reactance equals the supply voltage. Hence, when considering winding harmonics, this can be thought of as a series connection of harmonic "motors" as shown in Fig. 3.2.
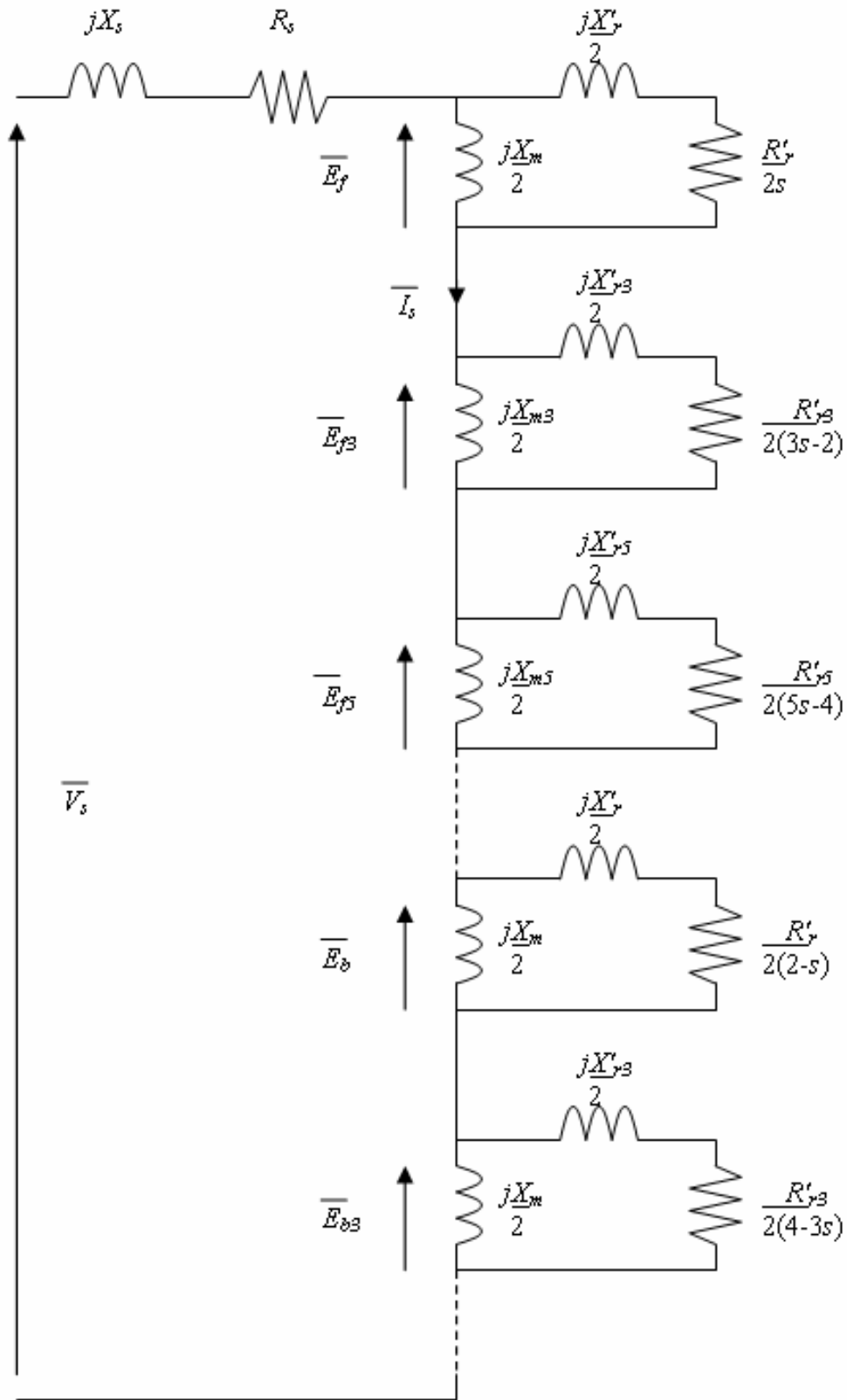
*Fig. 3.2 Equivalent circuit including MMF harmonics*

**Force and torque**

In a similar manner to Section 2.6, the force acting on an infinitesimal section of the rotor is

$$dF_{fm} = L_{stk} I_{rfm} \cos\left(\omega t - m\theta - \varphi_{fm}\right) B_{rfm} \cos\left(\omega t - m\theta\right) d\theta \qquad (3.34)$$

The total rotor force is found by integrating (3.34) over the entire rotor circumference

$$F_{fm} = \int_0^{2\pi} L_{stk} I_{rfm} \cos\left(\omega t - m\theta - \varphi_{fm}\right) B_{rfm} \cos\left(\omega t - m\theta\right) d\theta$$

$$= L_{stk} I_{rfm} B_{rfm} \cos\left(-\varphi_{fm}\right)\pi \qquad (3.35)$$

And the rotor torque is

$$T_{fm} = L_{stk} I_{rfm} B_{rfm} \cos(\varphi_{fm})\pi \, r_r \qquad (3.36)$$

This can be translated into air-gap values, since the air-gap flux is equal to the flux at the rotor conductor, so (3.36) becomes

$$T_{fm} = L_{stk} I_{rfm} B_{fm} \cos(\varphi_{fm}) \pi \, r \qquad (3.37)$$

Expressing the torque in terms of equivalent circuit parameters, (3.37) can be rewritten using (3.25):

$$T_{fm} = \frac{E_{fm}}{\omega \dfrac{N_m}{2}} \cos\left(\varphi_{fm}\right) I_{rfm} \qquad (3.38)$$

From Fig. 2.5 it can be seen that that the rotor MMF is of equal magnitude but opposite angle to the referred rotor MMF, i.e. $\bar{F}_{irf} = -\bar{F}'_{irf}$. This is also true for the harmonic MMFs. As a consequence, since the true rotor MMF is

$$\left|\bar{F}_{Irfm}\right| = \int_0^{\pi/m} I_{rfm} \sin\left(m\theta\right) d\theta = \frac{2 I_{rfm}}{m} \qquad (3.39)$$

and the referred rotor MMF is

$$\left|\bar{F}_{I'rfm}\right| = \int_0^{\pi/m} \frac{mN}{4} I'_{rfm} \sin\left(m\theta\right) d\theta = \frac{N}{2} I'_{rfm} \qquad (3.40)$$

This means that the relationship between the true and referred rotor current distribution is

$$\bar{I}_{rfm} = -m\frac{N}{4}\bar{I}'_{rf} \quad \Rightarrow \quad I_{rfm} = m\frac{N}{4} I'_{rfm} \qquad (3.41)$$

It should be emphasized that the rotor current and induced voltage are expressed in terms of their amplitude, i.e., the peak value.

Inserting (3.41) and rewriting in terms of RMS values, (3.38) becomes

$$T_{fm} = m\frac{E_{fm\,rms}\sqrt{2}}{2\omega} \cos\left(\varphi_{fm}\right) I'_{frm\,rms}\sqrt{2} = m\frac{E_{fm\,rms}}{\omega} \cos\left(\varphi_{fm}\right) I'_{fr\,rms} \qquad (3.42)$$

$\varphi_{fm}$ is the angle between the flux density and rotor current distribution, which is equal to the angle of the rotor impedance.


**Influence of the auxiliary winding**

The auxiliary winding modifies the single-phase equivalent circuit shown in Fig. 2.4. A number of voltage sources, representing the flux waves, are produced by the auxiliary winding. These flux waves set up voltages in the two windings, which differ in magnitude (and are determined by the winding ratio) and in phase by the mechanical displacement between the two. This is also the case for the harmonic fluxes. Considering the spatial displacement between harmonics of the main and the auxiliary winding yields:

$$N_{m,main}(\theta) = N_{m,main} \sin (m\,\theta) \tag{3.43}$$

$$N_{m,aux}(\theta) = N_{m,aux} \sin (m\,(\theta + \pi/2)) = N_{m,aux} \sin (m\,\theta + m\,\pi/2) \tag{3.44}$$

This shows that for $m = 1, 5, 9, 13...$ the $m^{th}$ harmonic auxiliary winding will *lead* the main winding by $\pi/2$ or $j$, whereas for $m = 3, 7, 11, 15...$the $m^{th}$ harmonic auxiliary winding will *lag* the main winding by $\pi/2$ or $j$. This is illustrated in Fig. 3.3 below for $m = 3$: If the $3^{rd}$ harmonic amplitudes of main and auxiliary windings have the same sign, the $3^{rd}$ harmonic auxiliary winding will lag the main winding. If they have different signs, the auxiliary will lead the main. The different sign could originate from a different distribution of the main and auxiliary windings. The latter is illustrated in Fig. 3.4.
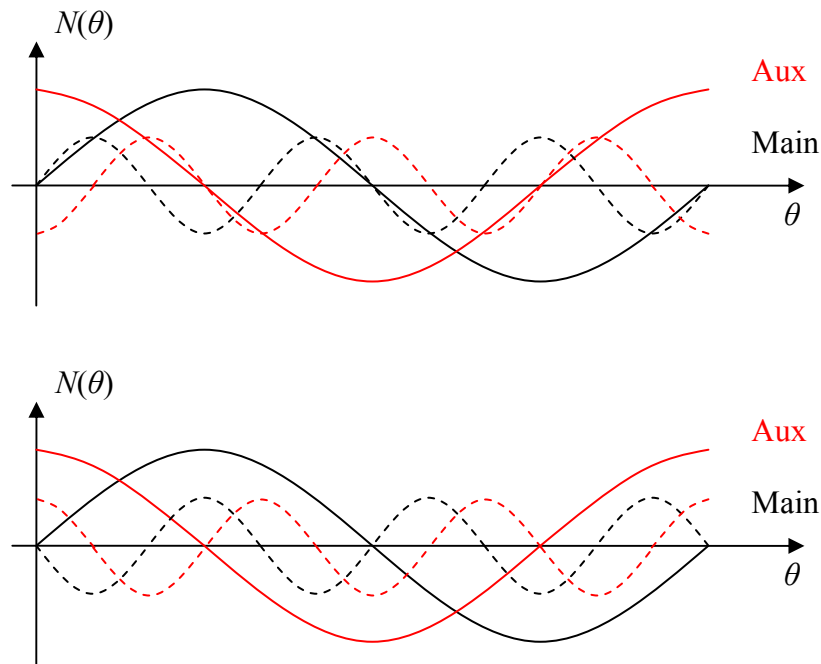


*Fig. 3.3 Main and auxiliary MMFs with $3^{rd}$ harmonics*

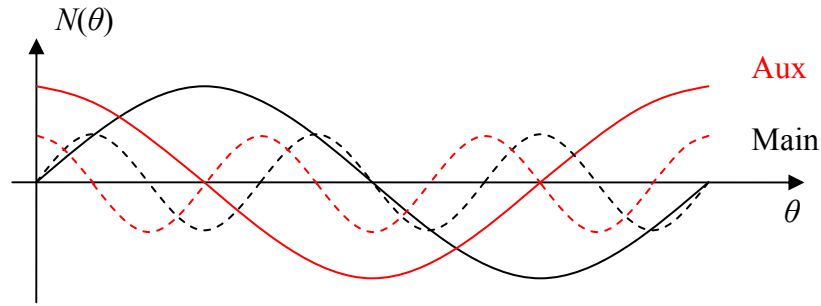# 3. The influence of winding harmonics



*Fig. 3.4 Different main and auxiliary winding distributions*

In a similar manner to Section 2.7, the equivalent circuit diagram of the split phase motor is as depicted in Fig. 3.5.
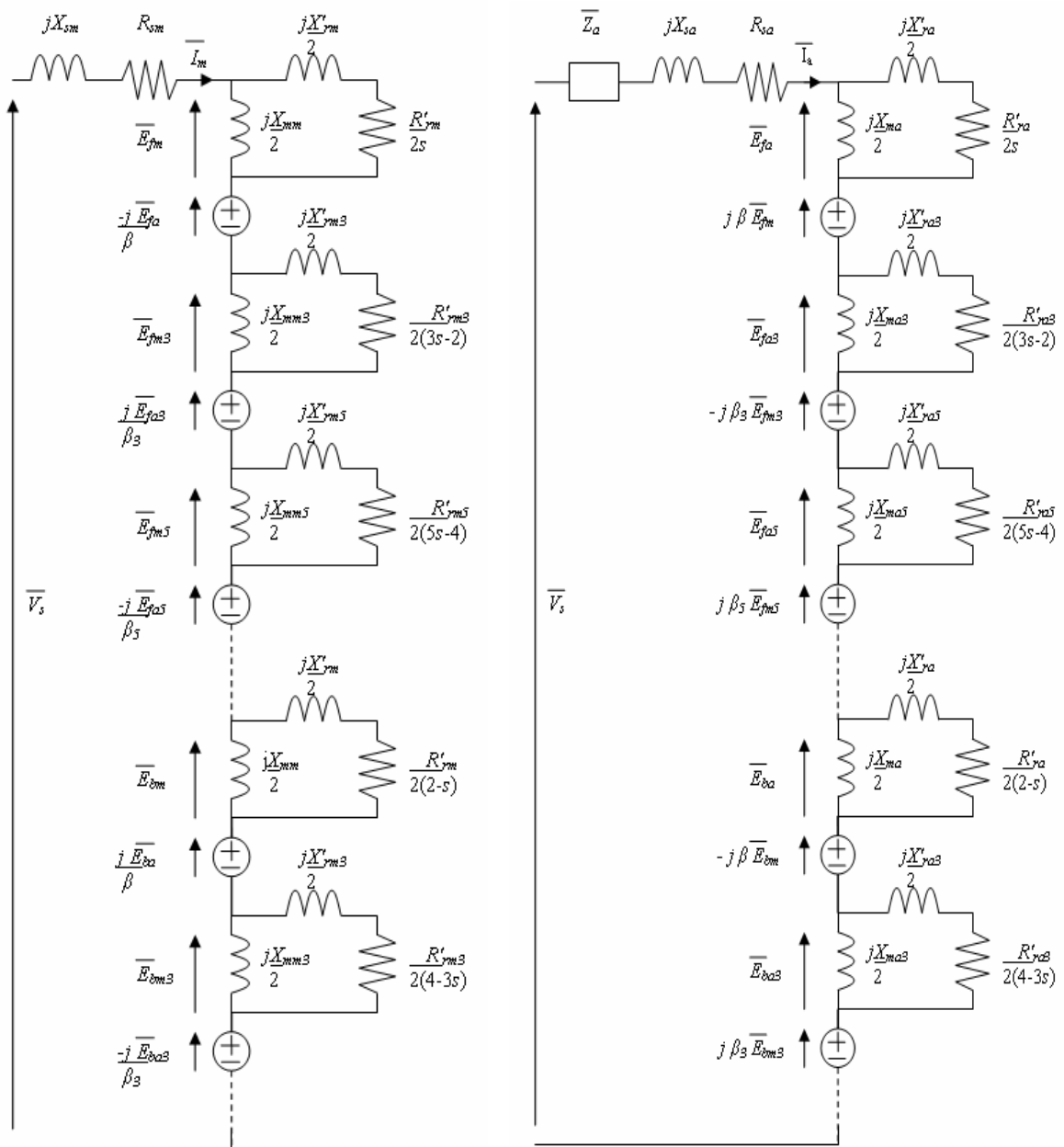


*Fig. 3.5 Main and auxiliary equivalent circuits*

3. The influence of winding harmonics

The impedance shown in the auxiliary circuit $\overline{Z}_a$ represents the auxiliary impedance for starting and/or running - i.e. a resistive or capacitive impedance.

## 3.4. Force and torque calculations

For the fundamental torque, the $m^{th}$ harmonic torque arises from the interaction of the $m^{th}$ harmonic flux density at the rotor bars and the $m^{th}$ harmonic rotor current distribution where

$$dF_{fm} = L_{stk} I_{rfMm} \cos(\omega t - m\theta - \varphi_{fm}) \left[ B_{rfMm} \cos(\omega t - m\theta) + B_{rfAm} \cos(\omega t - m\theta + \gamma_{fm}) \right] d\theta$$
$$+ L_{stk} I_{rfAm} \cos(\omega t - m\theta + \gamma_{fm} - \varphi_{fm}) \left[ B_{rfMm} \cos(\omega t - m\theta) + B_{rfAm} \cos(\omega t - m\theta + \gamma_{fm}) \right] d\theta$$

$$(3.45)$$

From (2.66), the corresponding torque can be expressed as

$$T_{fm} = \frac{r_r L_{stk} I_{rfMm} B_{rfMm}}{2} \left[ \int_0^{2\pi} \cos(-\varphi_{fm}) d\theta + \int_0^{2\pi} \cos(2\omega t - 2m\theta - \varphi_f) d\theta \right] +$$
$$+ \frac{r_r L_{stk} I_{rfAm} B_{rfAm}}{2} \left[ \int_0^{2\pi} \cos(-\varphi_f - \gamma_f) d\theta + \cdots \right] + \cdots$$

$$(3.46)$$

This is expressed in terms of the flux density at the rotor conductor $B_r$ and the corresponding mean radius of this rotor conductor $r_r$. This can be described by means of air-gap values directly, i.e., (3.46) becomes, by simplification:

$$T_{fm} = r_g \, L_{stk} \, I_{rfMm} \, \pi \left( B_{fMm} \cos(-\varphi_f) + B_{rfAm} \cos(-\varphi_f - \gamma_f) \right)$$
$$+ r_g \, L_{stk} \, I_{rfAm} \, \pi \left( B_{fMm} \cos(-\varphi_f + \gamma_f) + B_{rfAm} \cos(-\varphi_f) \right)$$

$$(3.47)$$

This is identical to (2.66) which means that the torque can be described in terms of equivalent circuit parameters, corrected for the harmonic order, according to (3.42):

$$T_{fm} = \mathrm{Re}\left( \left[ \frac{m\overline{E}_{fMm}}{\omega} + \frac{\frac{-j}{\beta_m} m\overline{E}_{fAm}}{\omega} \right] \overline{I}'_{rfMm}{}^* \right) + \mathrm{Re}\left( \left[ \frac{m\overline{E}_{fAm}}{\omega} + \frac{j\beta_m m\overline{E}_{fMm}}{\omega} \right] \overline{I}'_{rfAm}{}^* \right) \quad (3.48)$$

The backwards torque can be expressed in a similar way, i.e.:

$$T_{bm} = \mathrm{Re}\left( \left[ \frac{m\overline{E}_{bMm}}{\omega} + \frac{\frac{j}{\beta_m} m\overline{E}_{bAm}}{\omega} \right] \overline{I}'_{rbMm}{}^* \right) + \mathrm{Re}\left( \left[ \frac{m\overline{E}_{bAm}}{\omega} + \frac{-j\beta_m m\overline{E}_{bMm}}{\omega} \right] \overline{I}'_{rbAm}{}^* \right) \quad (3.49)$$

**Components of torque**

The resulting average torque of the machine will consist of contributions from harmonics of both forward and backwards rotating fields and current distributions where

$$T_{avg} = T_{f1} + T_{f3} + T_{f5} + \dots - T_{b1} - T_{b3} - T_{b5} - \dots \quad (3.50)$$

3. The influence of winding harmonics

This is illustrated in Fig. 3.6 which shows the fundamental and harmonic torques vs. speed for an arbitrary machine. For each harmonic order, the blue graph is resulting torque, the green is forwards (positive) torque and red is (negative) backwards torque. As can be seen, when the speed exceeds approximately 100 rad/s, which corresponds to the synchronous speed of the 3rd harmonic, only the fundamental forwards component produce positive torque. All other components will produce braking torque. The resulting torque curve of the machine is affected, since it displays asynchronous torque dips near the synchronous speeds of the respective harmonics.
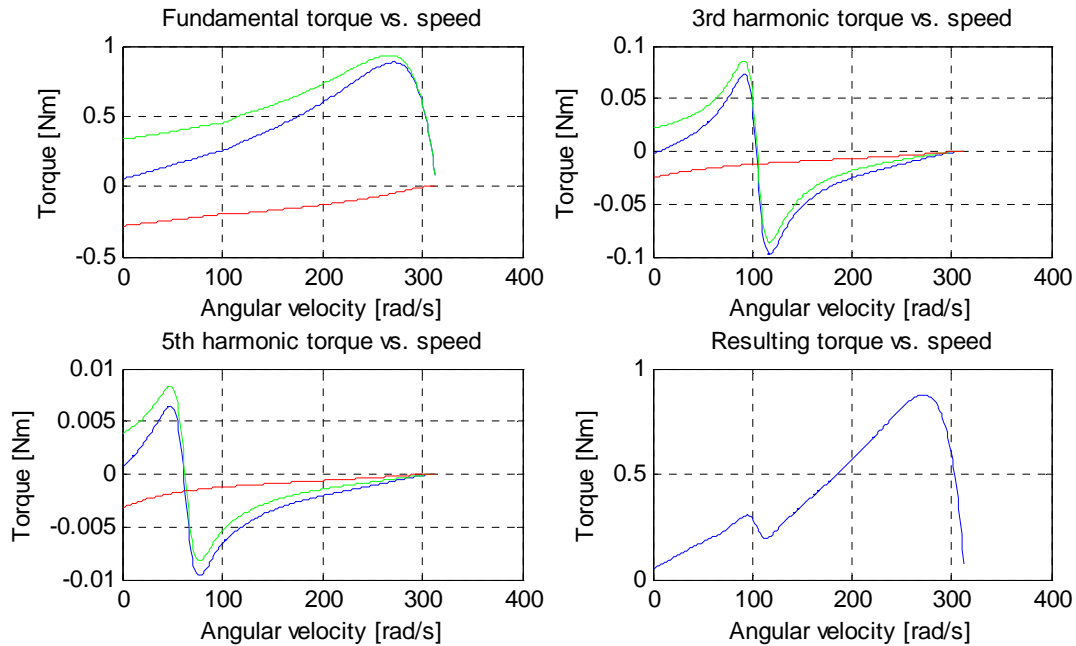


*Fig. 3.6 Simulation results from example machine*

**Torque pulsations**

In Section 2.7 the net torque is shown to be produced by the interaction of forward rotor current distribution with forward flux density as well as backward rotor current distribution with backward flux density. This is also the case for the harmonic components, since current distributions and flux densities of different harmonic order produce no average torque.

However, the harmonic components give rise to new sets of pulsating torques, as various rotor current distributions and flux densities move past each other. A detailed study of this will not be performed here, it is only emphasized that average torque will be produced only by components of rotor current and flux density of the *same harmonic order* and *same rotational direction*.

## *3.5. Rotor MMF harmonics*

In the previous analysis, the rotor circuit has been assumed consisting of a conducting cylinder and so reacts uniformly to any field imposed on it from the stator. However, having the rotor circuit confined in slots results in new sets of harmonic fields.

**Induction in discrete rotor circuit**

In the following, the voltage distribution of a rotor containing $N$ bars is derived when excited by a sinusoidal rotating flux density with $m$ pairs of poles as described by

$$B_m(t,\theta) = \hat{B}_m \cos(\omega t - m\theta) \tag{3.51}$$

This results in a pulsating flux through the loop spanned by conductors $n_1$ and $n_2$ given by

$$\Phi_{m(n_1 \to n_2)}(t,\theta) = \hat{B}_m r L_{stk} \int_{\frac{n_1 2\pi}{N}}^{\frac{n_2 2\pi}{N}} \cos(\omega t - m\theta)\, d\theta \tag{3.52}$$

$$= \frac{2\hat{B}_m r L_{stk}}{m} \sin\left(\frac{m\pi(n_2 - n_1)}{N}\right) \cos\left(\omega t - \frac{(n_2 + n_1)m\pi}{N}\right)$$

The resulting induced voltage in this loop is

$$e_{m(n_1 \to n_2)}(t,\theta) = \frac{2\omega \hat{B}_m r L_{stk}}{m} \sin\left(\frac{m\pi(n_2 - n_1)}{N}\right) \sin\left(\omega t - \frac{(n_2 + n_1)m\pi}{N}\right) \tag{3.53}$$

The voltage induced into the $n^{th}$ bar is due to contributions of flux linkages through every loop containing the $n^{th}$ bar. These flux linkages link the $n^{th}$ bar and the adjacent bars of successively longer spans, as illustrated in Fig. 3.7. This shows a fictitious 6 bar rotor circuit.
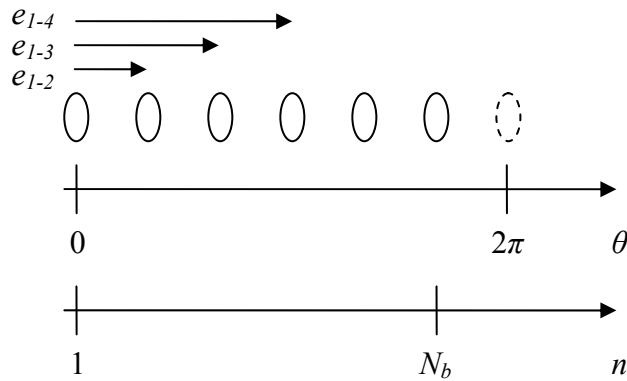


*Fig. 3.7 EMFs induced to rotor bars*

The voltage of the $n^{th}$ bar is therefore a sum of contributions from all the loop combinations in which the $n^{th}$ bar is a part. This summation should be divided by 2, since the bar voltage is assumed to be half of the loop voltage. Hence

$$e_n(t,\theta) = \frac{\omega \hat{B}_m r L_{stk}}{m} \sum_{n_2=n_1}^{N_b+n_1} \sin\left(\frac{m\pi(n_2-n_1)}{N}\right) \sin\left(\omega t - \frac{(n_2+n_1)m\pi}{N}\right) \tag{3.54}$$

As discussed in Section 2.3, the current in the $n^{th}$ bar will be similar and determined by the bar impedance $\overline{Z}_b$ :

$$i_n(t,\theta) = \frac{\omega \hat{B}_m r L_{stk}}{m \overline{Z}_b} \sum_{n_2=n_1}^{N_b+n_1} \sin\left(\frac{m\pi(n_2-n_1)}{N}\right) \sin\left(\omega t - \frac{(n_2+n_1)m\pi}{N}\right) \tag{3.55}$$

Since $\overline{Z}_b$ is determined by, amongst other things, the cross-sectional area of the bar, the bar impedance will increase proportionally with the number of bars if the bar depth and the bar pitch (or bar width/bar tooth ratio) are constant.

The rotor MMF in a given direction is given by the total bar currents, summed over an angle corresponding to $\pi/m$ so that

$$f_m(\theta) = \int_{\theta}^{\theta+\pi/m} i(\theta)\, d\theta \tag{3.56}$$

For an ideal sinusoidal current distribution, the peak MMF will be equal to twice the current amplitude. For a slotted rotor with a finite number of bars $N_b$, the MMF will vary discretely, as given by

$$f(n) = \sum_{n=n_1}^{n_1+\frac{N_b}{2}} i(n) \frac{2\pi}{N_b} \tag{3.57}$$

Figs. 3.8 and 3.9 show the induced rotor MMF (in arbitrary but comparable values) of two rotors with 16 and 30 bars. Note, that although the bar voltages (blue curves) increase with number of bars, the bar currents (red curves) are limited to the same values by the increased bar impedances. This results in MMFs (black curves) whose peak and fundamental values are similar, but whose harmonic content differ.

# 3. The influence of winding harmonics
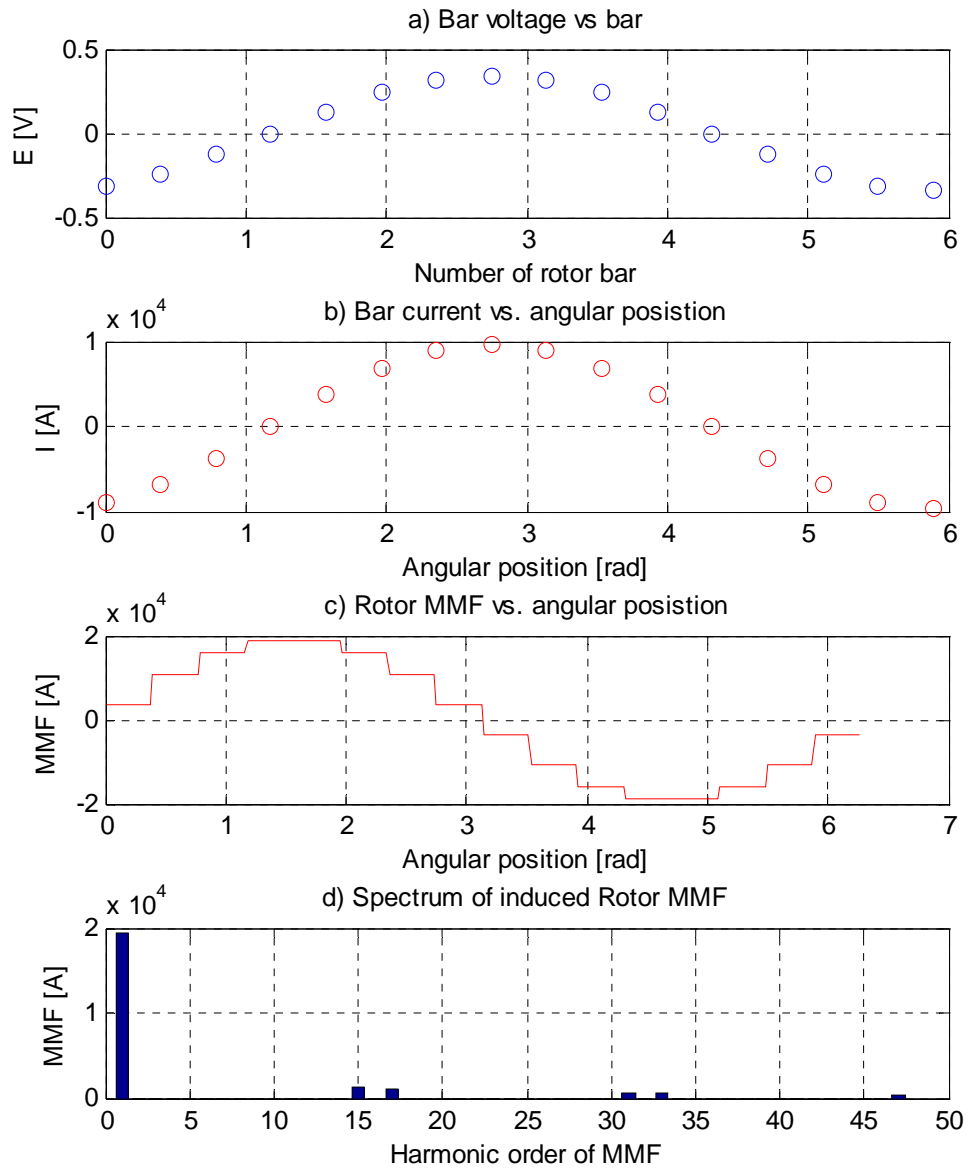


Fig. 3.8 a) Induced voltage, b) current, c) MMF and d) MMF spectrum for rotor with 16 bars

## 3. The influence of winding harmonics
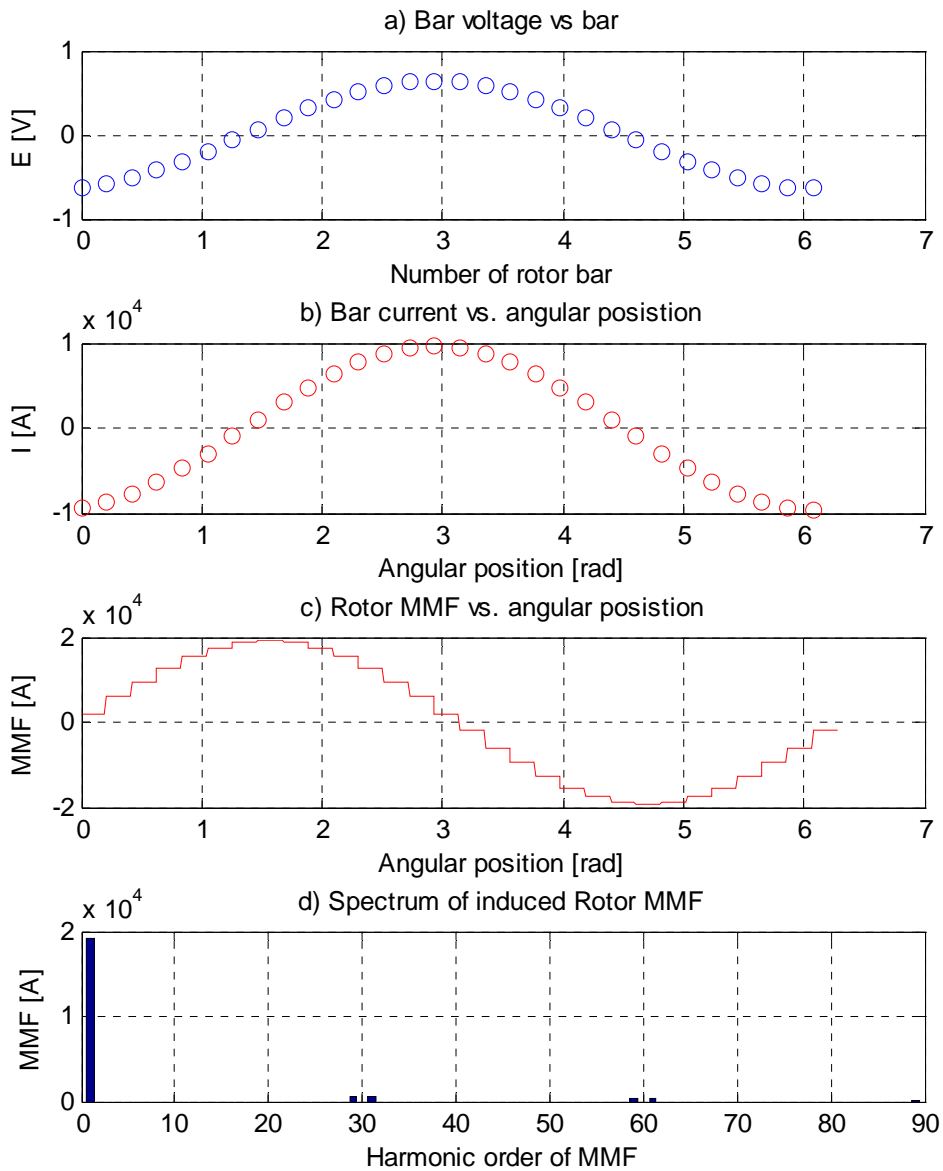


*Fig. 3.9 a) Induced voltage, b) current, c) MMF and d) MMF spectrum for rotor with 30 bars*

It is clearly seen that the principal bar harmonics of order $nN_b\pm1$ are present. However, the finite number of bars will affect the spectra for the higher harmonics. Fig. 3.10 shows the spectra of the MMFs for the 16 slot rotor. These are for the same flux density amplitude but with harmonic order $m = 1, 5, 9$ and $15$.

# 3. The influence of winding harmonics
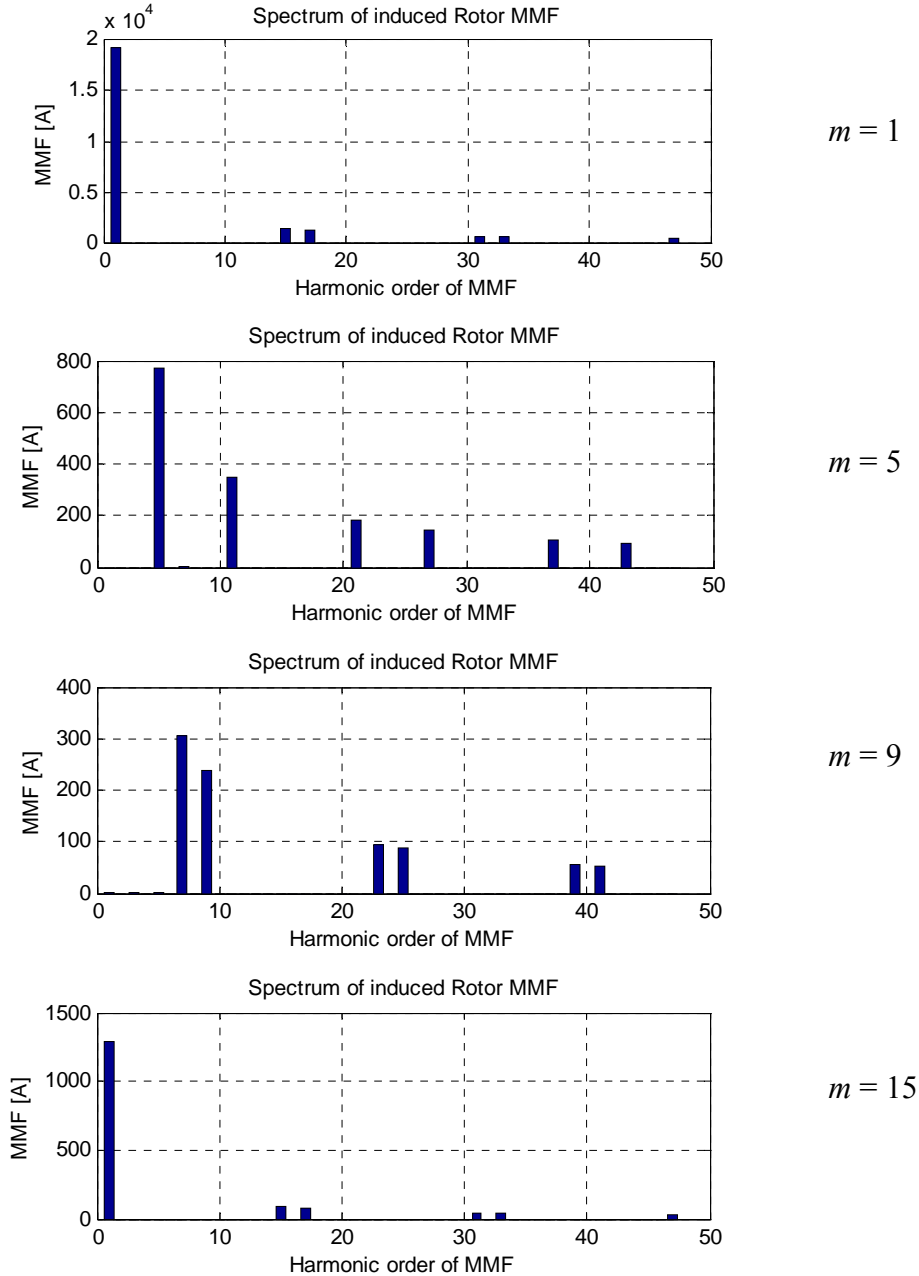


*Fig. 3.10 Spectra of rotor MMFs with 16 bar rotor*

It can be observed that for magnitudes of MMF of the same order, the exciting flux density decreases by a factor of $1/m^2$. This is consistent with the theory regarding the equivalent circuit, as described by (3.32).

These simulation results also illustrate that the induced spectra vary with the harmonic order $m$ of the exciting field. As the order increases, the order of the nearest super harmonic becomes gradually lower, and eventually, a sub harmonic will be present. For the 9th harmonic field, a sub harmonic MMF of order 7 is induced. More generally, as well as

inducing super harmonics, the flux density of order $N_b/2 +1$ creates sub harmonic MMFs, and the harmonic of order $N_b-1$ creates a sub harmonic of order 1.

To incorporate the rotor bar harmonics into the motor simulation, the referred rotor impedances can be modified. In order to do this a cross-coupling factor for each harmonic can be multiplied with the harmonic rotor impedance that it affects. It is obvious that the lower the number of rotor bars, the more pronounced this phenomenon becomes.

For the example in Fig. 3.10, the 15th harmonic field is seen to increase the fundamental rotor MMF by some 7 % if the amplitude of the 15th harmonic field is equal to that of the fundamental field.

Given the rapidly decreasing nature of the super harmonic flux densities, the impact of the (in this case) 15th harmonic field of the fundamental MMF is negligible. This means that, although the impact is somewhat greater on the higher harmonics, in the modelling performed here, the cross coupling effect is ignored altogether to simplify the simulation process. When operating with very few rotor bars, e.g., 10 or fewer, it would have to be implemented in order to correctly estimate the fundamental and harmonic rotor MMF. However, few induction motors have such few bars.

## 3.6. Model implementation and evaluation

The split-phase induction machine equivalent circuit given in Fig. 3.5 can be analysed using classical circuit analysis in order to obtain values for the currents flowing in any branch of the circuit. When analysed as a system of mesh equations using Kirchoff's Voltage Law, the corresponding set of equations can be solved using linear algebra. This produces an impedance matrix. The model can be implemented using any software capable of handling linear algebra and complex numbers. In this case, The MathWorks MATLAB® was used. Fig. 3.11 shows the central part of the coding where the impedance matrix is defined and the circuit current equation matrix is solved.

# 3. The influence of winding harmonics

```
%Impedance matrix based on mesh equations
Z = [(Rsm+j*Xsm+Rfem) (-Rfem) 0 0 0 0 0 0 0 0 0 0 0 0 0 0 0 0 0 0;
     (-Rfem) (Rfem+j*(Xmm(1)+Xmm(3)+Xmm(5)+Xmm(7))) (-j*Xmm(1)/2) (-j*Xmm(3)/2) (-j*Xmm(5)/2) (-j*Xmm(7
     0 (-j*Xmm(1)/2) (Rrm(1)/(2*s)+j*(Xmm(1)/2+Xrm(1)/2)) 0 0 0 0 0 0 0 0 0 0 0 0 0 0 0 0;
     0 (-j*Xmm(3)/2) 0 (Rrm(3)/(2*(3*s-2))+j*(Xmm(3)/2+Xrm(3)/2)) 0 0 0 0 0 0 0 0 0 0 0 0 0 0 0 0;
     0 (-j*Xmm(5)/2) 0 0 (Rrm(5)/(2*(5*s-4))+j*(Xmm(5)/2+Xrm(5)/2)) 0 0 0 0 0 0 0 0 0 0 0 0 0 0 0;
     0 (-j*Xmm(7)/2) 0 0 0 (Rrm(7)/(2*(7*s-6))+j*(Xmm(7)/2+Xrm(7)/2)) 0 0 0 0 0 0 0 0 0 0 0 0 0 0;
     0 (-j*Xmm(1)/2) 0 0 0 0 (Rrm(1)/(2*(2-s))+j*(Xmm(1)/2+Xrm(1)/2)) 0 0 0 0 0 0 0 0 0 0 0 0 0;
     0 (-j*Xmm(3)/2) 0 0 0 0 0 (Rrm(3)/(2*(4-3*s))+j*(Xmm(3)/2+Xrm(3)/2)) 0 0 0 0 0 0 0 0 0 0 0 0;
     0 (-j*Xmm(5)/2) 0 0 0 0 0 0 (Rrm(5)/(2*(6-5*s))+j*(Xmm(5)/2+Xrm(5)/2)) 0 0 0 0 0 0 0 0 0 0 0;
     0 (-j*Xmm(7)/2) 0 0 0 0 0 0 0 (Rrm(7)/(2*(8-7*s))+j*(Xmm(7)/2+Xrm(7)/2)) 0 0 0 0 0 0 0 0 0 0;
     0 0 0 0 0 0 0 0 0 0 (Zaux+Rsa+j*(Xsa)+Rfea) (-Rfea) 0 0 0 0 0 0 0 0;
     0 0 (beta(1)*Xmm(1)/2) (-beta(3)*Xmm(3)/2) (beta(5)*Xmm(5)/2) (-beta(7)*Xmm(7)/2) (-beta(1)*Xmm(1)
     0 0 0 0 0 0 0 0 0 0 (-j*Xma(1)/2) (Rra(1)/(2*s)+j*(Xma(1)/2+Xra(1)/2)) 0 0 0 0 0 0 0;
     0 0 0 0 0 0 0 0 0 0 (-j*Xma(3)/2) 0 (Rra(3)/(2*(3*s-2))+j*(Xma(3)/2+Xra(3)/2)) 0 0 0 0 0 0;
     0 0 0 0 0 0 0 0 0 0 (-j*Xma(5)/2) 0 0 (Rra(5)/(2*(5*s-4))+j*(Xma(5)/2+Xra(5)/2)) 0 0 0 0 0;
     0 0 0 0 0 0 0 0 0 0 (-j*Xma(7)/2) 0 0 0 (Rra(7)/(2*(7*s-6))+j*(Xma(7)/2+Xra(7)/2)) 0 0 0 0;
     0 0 0 0 0 0 0 0 0 0 (-j*Xma(1)/2) 0 0 0 0 (Rra(1)/(2*(2-s))+j*(Xma(1)/2+Xra(1)/2)) 0 0 0;
     0 0 0 0 0 0 0 0 0 0 (-j*Xma(3)/2) 0 0 0 0 0 (Rra(3)/(2*(4-3*s))+j*(Xma(3)/2+Xra(3)/2)) 0 0;
     0 0 0 0 0 0 0 0 0 0 (-j*Xma(5)/2) 0 0 0 0 0 0 (Rra(5)/(2*(6-5*s))+j*(Xma(5)/2+Xra(5)/2)) 0;
     0 0 0 0 0 0 0 0 0 0 (-j*Xma(7)/2) 0 0 0 0 0 0 0 (Rra(7)/(2*(8-7*s))+j*(Xma(7)/2+Xra(7)/2))];

% Now, current vector is calculated from Gaussian elimination of matrix
% ('Left divide')

I = Z\V; % similar to I = inv(Z)*V but faster
```

*Fig. 3.11 Representation of impedance matrix in MATLAB*

In order to obtain realistic results, the values of the various circuit parameters must be accurately estimated. In Appendix 1, the derivation of every circuit parameter is described.

**Model evaluation**

When implementing the model as shown in Fig. 3.11, the steady-state behaviour of any split-phase motor can be predicted. In order to asses the level of accuracy, a number of different motors were simulated and their performance characteristics were compared with measurements. Two 2-pole motors were used with one having more harmonic winding content than the other. Both machines have 24 slots and the winding layouts for the first six slots are shown in Table 3.1. Further details of the two motors can be found in Appendix 3.

For the 115V motor, the auxiliary winding contains bifilar windings in slots 1 and 2. This means that some of the turns are wound oppositely to the rest of the winding, which reduces the net winding number. This is done to increase resistance for auxiliary winding, and for two reasons: to have sufficient starting torque and to limit the starting current, without having to add an additional in-line resistance with the auxiliary winding.

Both motors are calculated in run mode.

## 3. The influence of winding harmonics

| ↓ Motor          Slot No. → | 1 | 2 | 3 | 4 | 5 | 6 |
|---|---|---|---|---|---|---|
| 220V Motor: | | | | | | |
| Main winding | 0 | 46 | 76 | 100 | 118 | 118 |
| Aux winding | 85 | 85 | 79 | 65 | 0 | 0 |
| 115V Motor: | | | | | | |
| Main winding | 0 | 0 | 33 | 53 | 55 | 55 |
| Aux winding (net) | 25 | 25 | 31 | 0 | 0 | 0 |
| Aux winding (abs) | 40 | 40 | 31 | 0 | 0 | 0 |

*Table 3.1 Machine winding layouts*

### 1. 220V 50Hz RSCR motor

Fig. 3.12 shows the measured (red) and simulated (blue) torque vs. speed in the entire speed range, whereas fig. 3.13 shows the current and efficiency vs. load torque in the operating range.

This is a resistor-start capacitor-run (RSCR) machine so that there is a resistor in series with the auxiliary when starting which is switched out when running close to full-load speed, when a run capacitor is switched into the auxiliary circuit.

The simulated pull-out torque appears to be correctly estimated although the speed at which it occurs is a little too high. This could be because the rotor resistance is slightly underestimated. The line current simulation is close to the measured, whereas it appears from the efficiency curves that the copper losses are underestimated, resulting in discrepancy between simulated and measured efficiency at high load. This is consistent with the torque curves. The iron loss, which dominates at light load, appears to be correctly estimated, since the calculated efficiency agrees well to the measured one.

The stator windings are quasi-sine wound over 5 out of 6 slots for a quarter winding, resulting in relatively small MMF harmonics. Hence the resulting torque curve is seen to contain practically no harmonic influence during run-up.

### Torque vs. speed: running condition
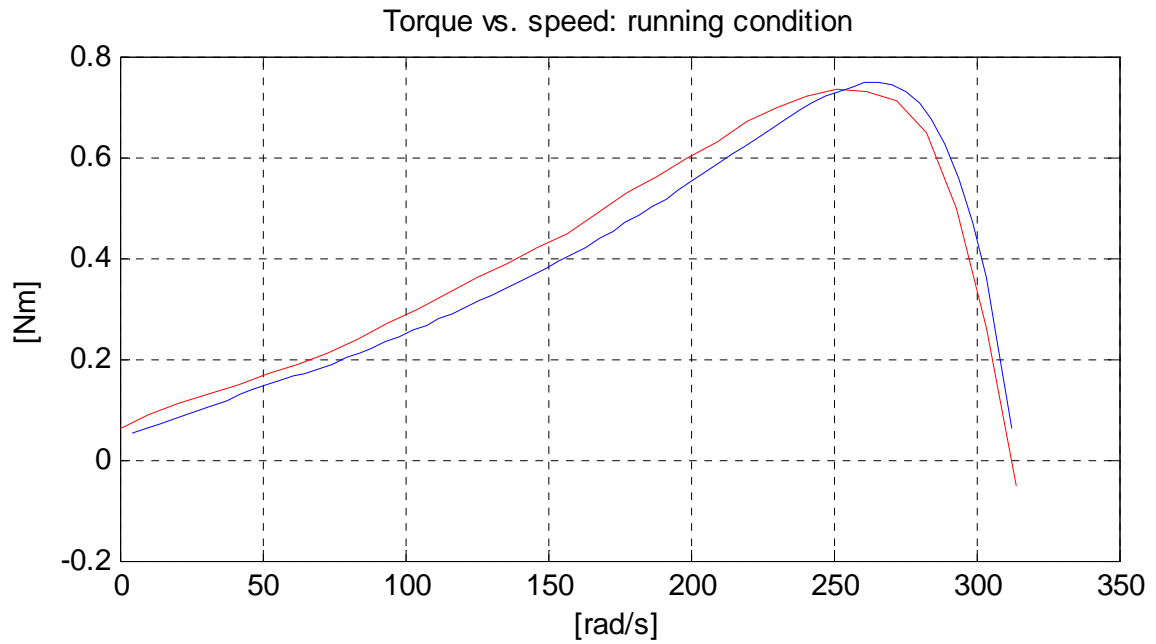


*Fig. 3.12 Comparison of measured (red) and simulated (blue) torque for 220 V motor*

### Current vs. torque

### Efficiency vs. torque
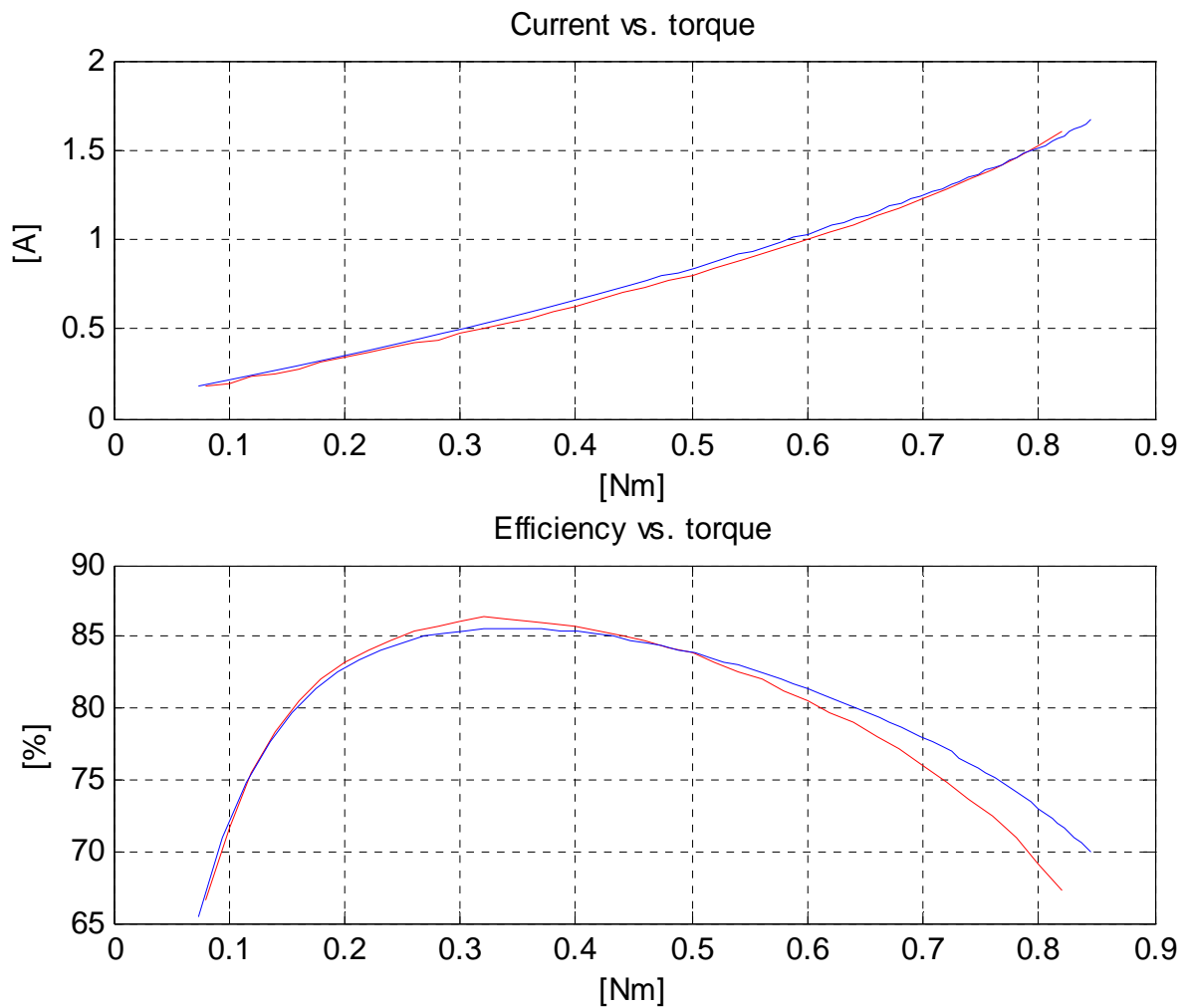


*Fig. 3.13 Comparison of measured (red) and simulated (blue) values for 220 V motor*

*2. 115V 60Hz RSIR motor*

This machine is a resistor-start induction-run (RSIR) motor. This means that when the motor approaches full-load speed, the auxiliary winding is switched out and it runs as a single phase machine.

Fig. 3.14 shows the measured (red) and simulated (blue) torque vs. speed in the entire speed range, whereas fig. 3.15 shows the current and efficiency vs. load torque in the operating range.

The winding is distributed in 4 out of 6 slots for a quarter winding and contains significantly more space harmonics than the previous example. The influence of the winding harmonics is seen in the torque vs. speed curve, where the harmonic torque dips due to the $3^{rd}$ and $5^{th}$ harmonics are clearly visible. The harmonic torque dips seem to be correctly estimated by the simulation. The simulated machine efficiency is a few points higher than the measured and could be due to an underestimation of the iron losses. As with the previous example, the slightly higher pull-out torque and speed could indicate an underestimated rotor resistance.

It should be noted, that the modelled performance shown in Figs. 3.12 to 3.15 are obtained with the direct use of the machine geometry and material properties without any adjustment factors. In practice, some adjustment is nearly always necessary, due to imperfections in production, in particular in the rotor casting, but also in terms of machining tolerances, etc. Tuning a few of the parameters in the simulated curves shown here would improve the predicted motor performance further.
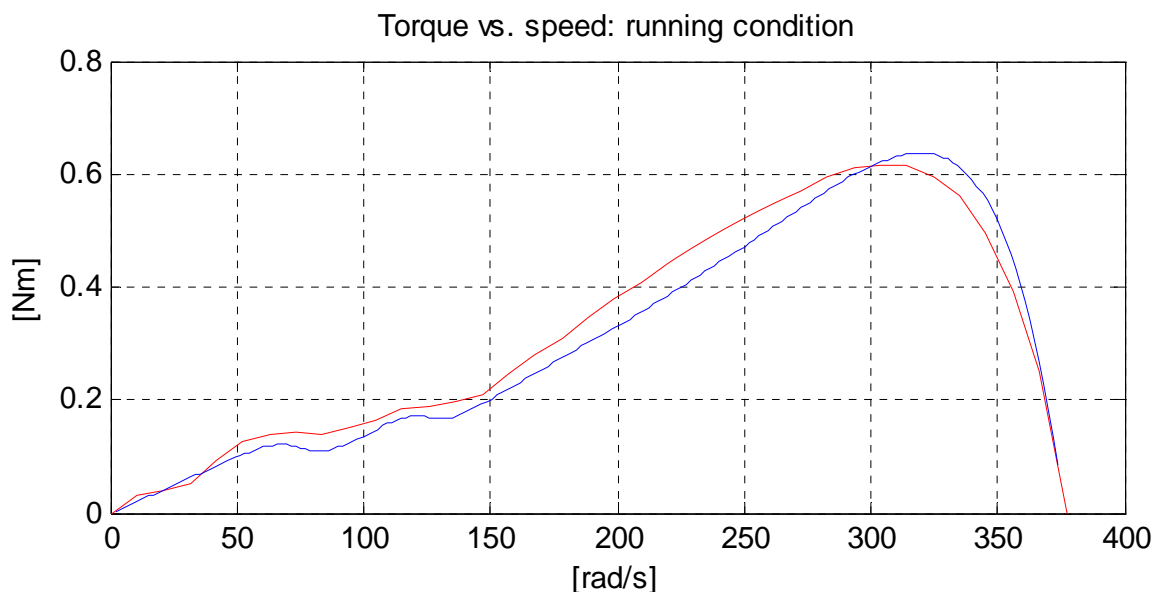


*Fig. 3.14 Comparison of measured (red) and simulated (blue) torque for 115 V motor*

## Current vs. torque
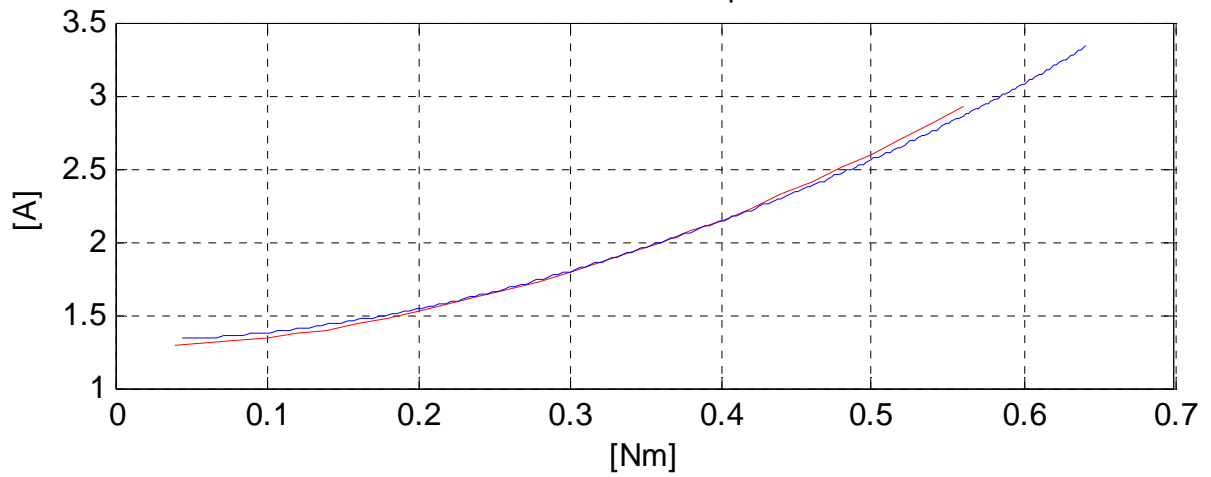


## Efficiency vs. torque
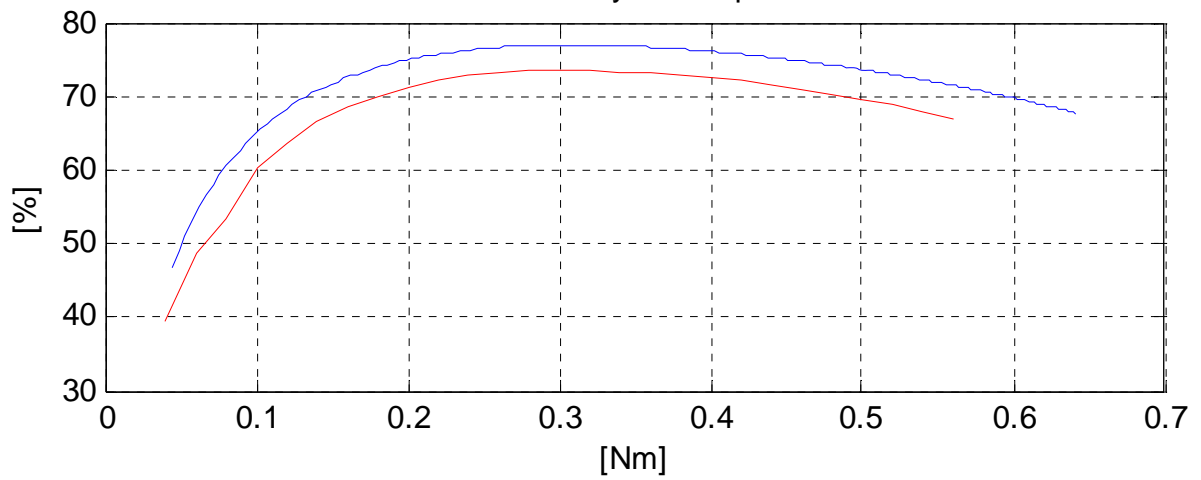
*Fig. 3.15 Comparison of measured (red) and simulated (blue) values for 115 V motor*

# Chapter 4

# Stator and rotor permeance

So far, the air-gap has been assumed to be ideal, being treated as the gap between two smooth concentric cylinders. The existence of slots on both stator and rotor surfaces, however, introduces harmonic effects in the motor performance. This is partly due to the discrete location of conductors in the slots, which gives rise to harmonic asynchronous torques already described in Chapter 3, and partly by introducing harmonics in the air gap permeance (as described in this chapter).

## *4.1. Air-gap length harmonics*

F.W. Carter described a relationship between the mechanical air-gap and the equivalent air gap which takes stator and rotor slots into account [29], [30]. This is an adjustment of the mechanical constant value. Here, the air-gap as seen by the electromagnetic field is investigated in a little more detail.

In order to asses the variation of the air-gap magnetic field, a 2D finite element model is created which has an actual stator geometry but assumes a non-slotted rotor. This is shown in Fig. 4.1. The red slots carry a uniform current density of opposite magnitude, whereas the grey slots carry no current. Hence, a quasi-square wave MMF is created.
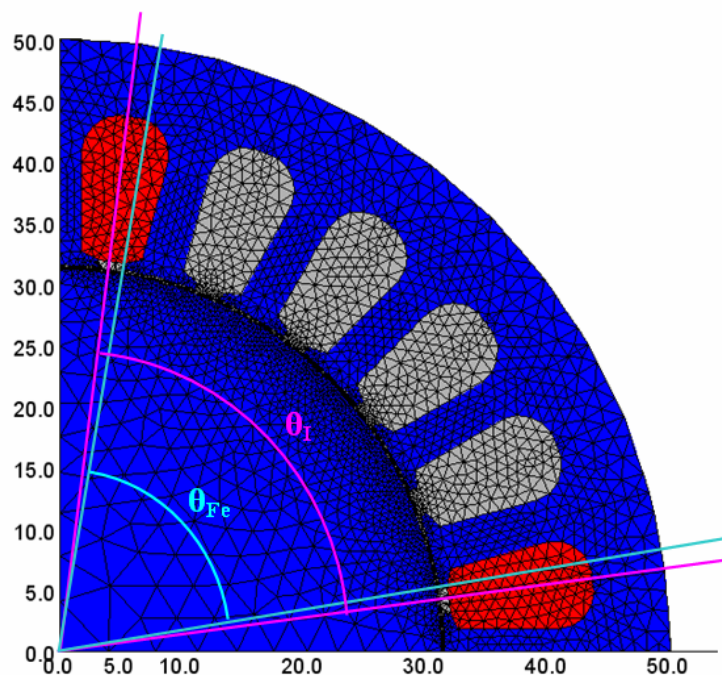


*Fig. 4.1 2D finite element analysis of machine with smooth rotor*

## 4. Stator and rotor permeance

A static analysis of this model results in an air gap flux density versus angle for a single tooth pitch as given in Fig. 4.2.
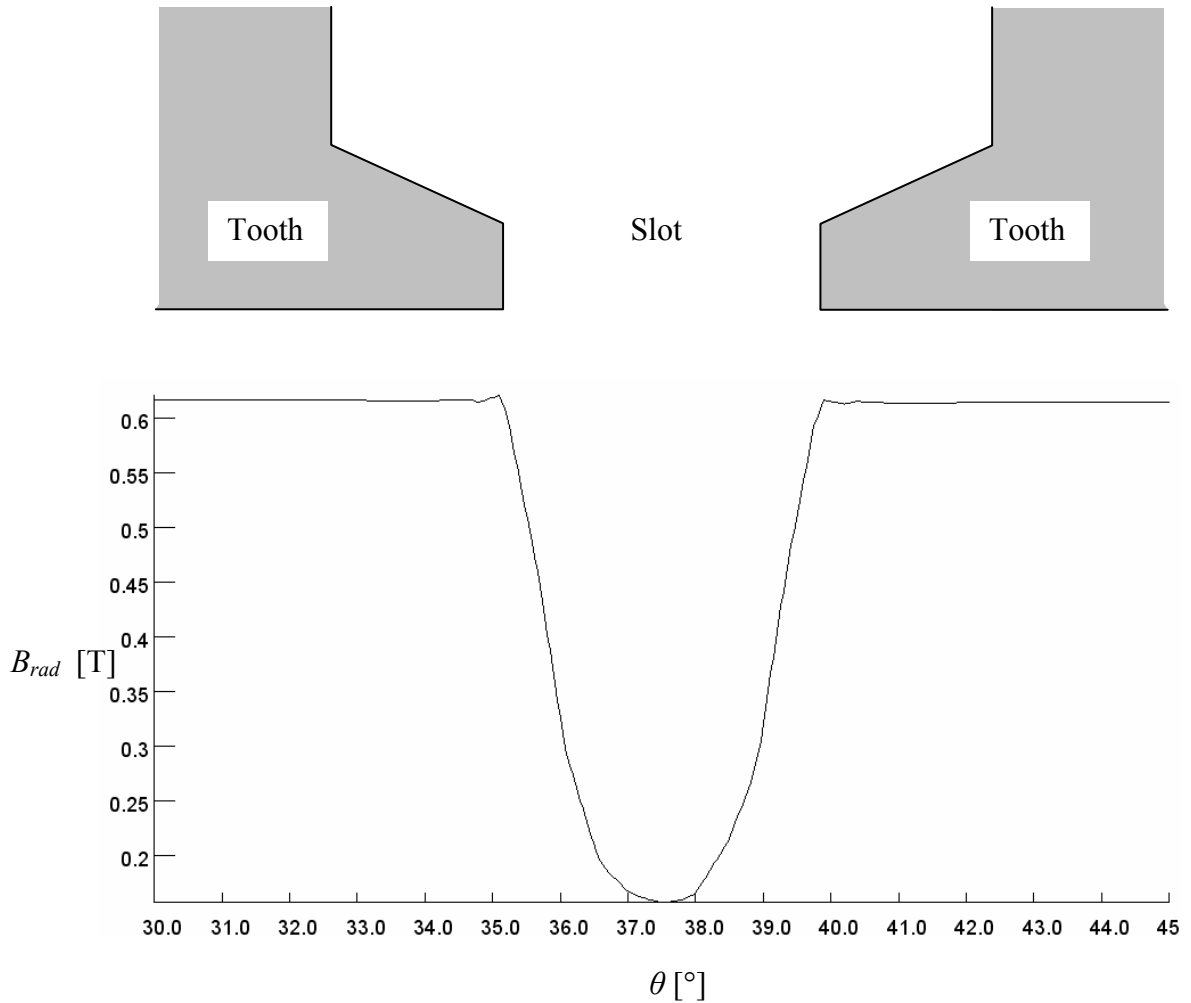


*Fig. 4.2 Radial component of air gap flux density distribution from finite element analysis*

From this flux density variation, the radial air gap length can be extracted from Ámpere's law using this expression

$$l_g(\theta) = \frac{\theta_I}{\theta_{Fe}} \frac{\mu_0 I_{tot}}{2 B_g(\theta)}$$  (4.1)

The angles $\theta_I$ and $\theta_{Fe}$ are defined in Fig. 4.1 and the ratio takes into account the concentration of flux due to the slotting, since the angular span of the MMF is larger than the span of the flux due to the slot openings.

Extracting the corresponding air-gap length from Fig. 4.2 and performing a harmonic analysis of the resulting function results in a spectrum of harmonic air-gap lengths as given by Fig. 4.3.
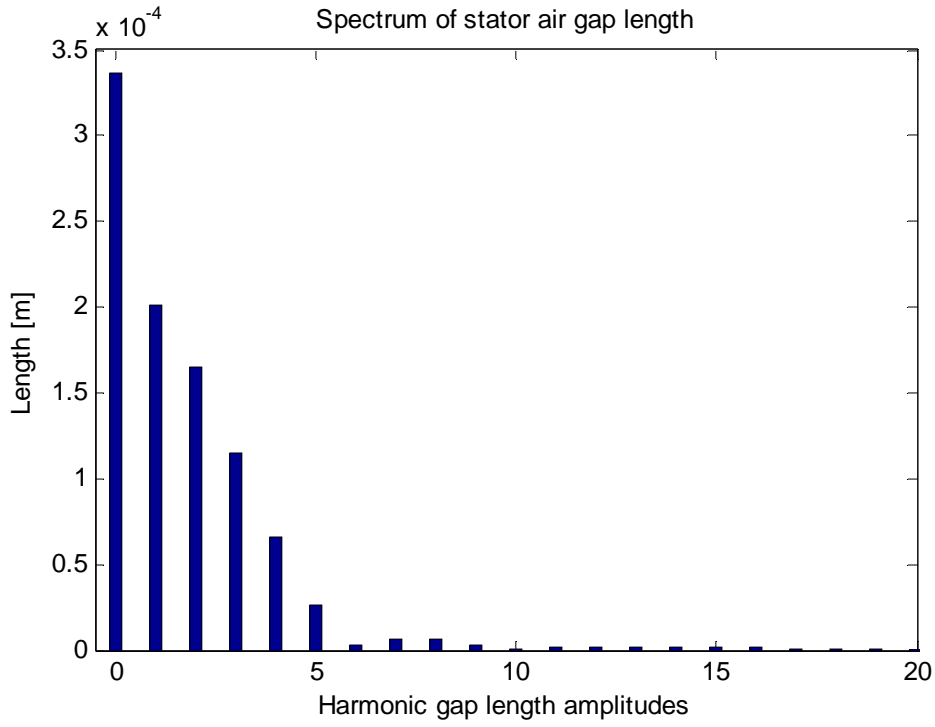
*Fig. 4.3 Harmonic air-gap lengths*

For the following analysis, it is necessary to express the air-gap length variation mathematically. From Fig. 4.2, a suitable approximation is indicated by the dotted blue line in Fig. 4.4.
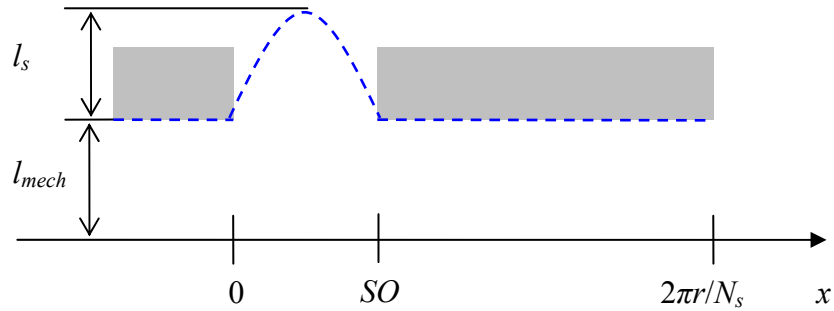


*Fig. 4.4 Air gap length approximation*

A suitable mathematic expression over the span $0 < x < SO$ is

$$f(x) \quad = \quad l_{mech} + l_s \, \sin\!\left(\frac{\pi}{SO} x\right) \tag{4.2}$$

And for $SO \le x \le 2\pi r/N_s$:

$$f(x) \quad = \quad l_{mech} \tag{4.3}$$

where $l_{mech}$ is the mechanical air-gap and $l_s$ is the effective air gap as determined using the Carter factor. This actually corresponds to a constant term, i.e., the zero order harmonic of Fig. 4.3.

Performing a Fourier analysis of the periodic function described by (4.2) and (4.3) will result in a spectrum which can be directly compared with the one in Fig. 4.3 (as obtained from the finite element analysis). Any general magnitude deviation can be accounted for by multiplying the harmonic lengths with a correction factor. In Fig. 4.5, blue graph shows the spectrum of the series defined by (4.2) and (4.3) directly, whereas the red graph shows the same spectrum, but where the harmonic coefficients have been multiplied with by a factor of 1.3.
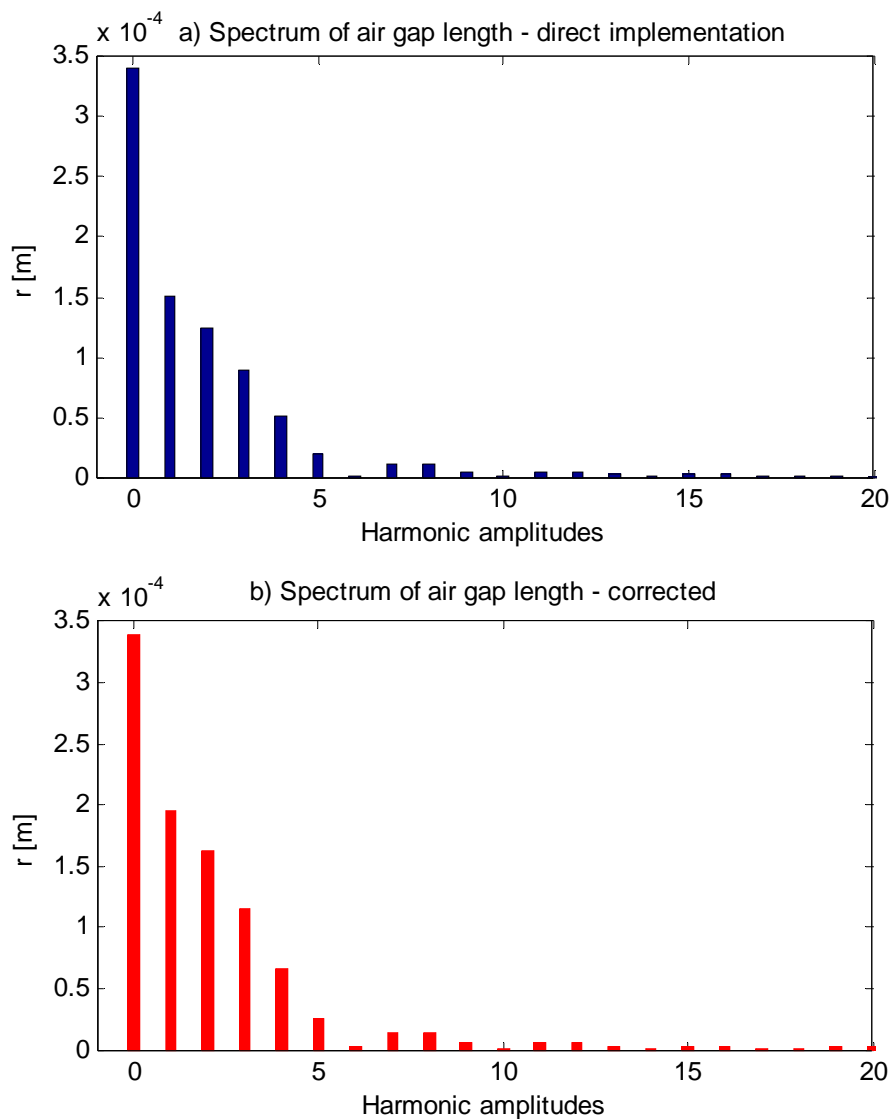


*Fig. 4.5 Comparison of harmonic air-gap lengths with adjustments (blue is the original harmonic magnitude and red multiplies the harmonic lengths by a factor of 1.3)*

It is seen that the corrected spectrum (red graph) is in good agreement with the reference spectrum in Fig. 4.3. Therefore, the mathematical functions in (4.2) and (4.3) for describing the air-gap length variation will be used in the following analysis, though this may not be the case with different geometry.

Generally, it can be observed from the spectra that both even and odd harmonics are present. For the lower harmonics the magnitudes are significant.

Since the spectra show the length variation over one tooth pitch, the fundamental value corresponds to the $N_s^{th}$ harmonic when observing the entire air-gap where $N_s$ is the number of stator slots. Hence, for the entire air-gap, the order of the harmonic is $N_s$ times higher than shown in Fig 4.5.

## 4.2. Air-gap permeance

The reluctance variation of the air-gap is proportional to the air-gap length. The permeance is proportional to the inverse of the reluctance – a detailed definition is carried out in Section 5.2. It will have a spectrum similar to that of the reluctance, as shown in Fig. 4.5. This spectrum is for an air-gap section corresponding to one tooth pitch. For an air-gap around the whole motor air-gap circumference, the harmonic series has a fundamental of order $N_s$ (the number of stator slots) rather that unity. This is shown in Fig. 4.6, which shows the air-gap permeance coefficient (a two-dimensional term proportional with the 3-dimensional permeance) and the corresponding spectrum for an air-gap with 24 slots.
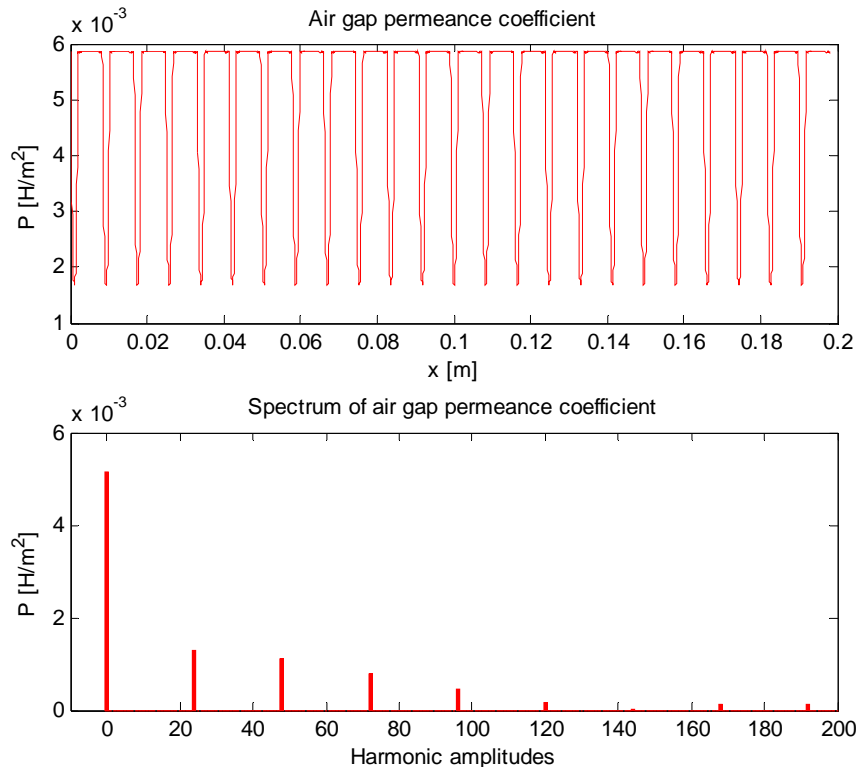


*Fig. 4.6 Air-gap permeance coefficient with harmonic decomposition*

A similar spectrum will exist for the rotor, with a fundamental corresponding to the number of bar slots, and the fundamental and harmonics will rotate with the rotor itself.

## *4.3. Representation of permeance harmonics*

In the following derivation, the combined effects of stator and rotor permeance are described analytically. The approach developed by [15] is used and extended. The total air-gap reluctance is a series connection of independent reluctance terms,. However, for the total air-gap permeance, or, in this case, the permeance coefficient, the inversion process means that the stator slot, rotor slot and average permeance coefficient terms may be described by a parallel connection of individual permeance coefficients, i.e.,:

$$P = \left( \frac{1}{P_r} + \frac{1}{P_s} + \frac{1}{P_g} \right)^{-1}$$

$$= \frac{P_r P_s P_g}{P_s P_g + P_r P_g + P_r P_s} \tag{4.4}$$

This type of air-gap harmonic inversion was also studied by [17] and[18]. By substitution, and for the moment ignoring higher slot harmonics:

$$P_s = P_{0s} + P_{ms} \cos\left(mN_s\theta\right) \tag{4.5}$$

and

$$P_r = P_{0r} + P_{mr} \cos\left(mN_r\theta - \omega_r t\right) \tag{4.6}$$

Therefore the resulting air-gap permeance coefficient will be

$$P = \frac{\left(P_{0r} + P_{mr}\cos\left(mN_r\theta - \omega_r t\right)\right)\left(P_{0s} + P_{ms}\cos\left(mN_s\theta\right)\right)P_g}{\left\{ \begin{array}{l} \left[\left(P_{0s} + P_{ms}\cos\left(mN_s\theta\right)\right)P_g + \left(P_{0r} + P_{mr}\cos\left(mN_r\theta - \omega_r t\right)\right)P_g\right] \\ + \left(P_{0r} + P_{mr}\cos\left(mN_r\theta - \omega_r t\right)\right)\left(P_{0s} + P_{ms}\cos\left(mN_s\theta\right)\right) \end{array} \right\}}$$

$$= \frac{\left\{ \begin{array}{l} P_{0r}P_{0s}P_g + P_g P_{0s}P_{mr}\cos\left(mN_r\theta - \omega_r t\right) \\ + P_g P_{0r}P_{ms}\cos\left(mN_s\theta\right) + P_{mr}\cos\left(mN_r\theta - \omega_r t\right)P_{ms}\cos\left(mN_s\theta\right) \end{array} \right\}}{\left\{ \begin{array}{l} P_{0s}P_g + P_{0r}P_g + P_{0r}P_{0s} + \left(P_{0r} + P_g\right)P_{ms}\cos\left(mN_s\theta\right) \\ + \left(P_g + P_{0s}\right)P_{mr}\cos\left(mN_r\theta - \omega_r t\right) + P_{mr}\cos\left(mN_r\theta - \omega_r t\right)P_{ms}\cos\left(mN_s\theta\right) \end{array} \right\}} \tag{4.7}$$

Both the numerator and denominator of (4.7) contain contributions of constant and time-space-varying permeance coefficient terms. For the denominator, however, the time-space-varying permeance coefficient terms are small compared to the constant terms and are therefore ignored in the following analysis. Hence, the combined-effect air-gap permeance coefficient can be written as

## 4. Stator and rotor permeance

$$P = P_0 \left[ 1 + \sum_{m=1}^{M} \frac{P_{Sm}}{P_0} \cos\left( mN_S\theta \right) \right] \times \left[ 1 + \sum_{m=1}^{M} \frac{P_{Rm}}{P_0} \cos\left( mN_R\left(\theta - \omega_r t\right) \right) \right] \tag{4.8}$$

The terms belonging to the stator are fixed in space, whereas the rotor terms will rotate with rotor speed. This gives rise to several terms of permeance coefficients where

$$
\begin{aligned}
P = {} & P_0 + P_{S1}\cos\left(N_S\theta\right) + P_{S2}\cos\left(2N_S\theta\right) + P_{S3}\cos\left(3N_S\theta\right) + \cdots \\
& + P_{R1}\cos\left(N_R\left(\theta - \omega_r t\right)\right) + P_{R2}\cos\left(2N_R\left(\theta - \omega_r t\right)\right) + P_{R3}\cos\left(3N_R\left(\theta - \omega_r t\right)\right) + \cdots \\
& + \frac{P_{S1}P_{R1}}{P_0}\cos\left(N_S\theta\right)\cos\left(N_R\left(\theta - \omega_r t\right)\right) + \frac{P_{S2}P_{R2}}{P_0}\cos\left(2N_S\theta\right)\cos\left(2N_R\left(\theta - \omega_r t\right)\right) + \cdots \\
& + \frac{P_{S1}P_{R2}}{P_0}\cos\left(N_S\theta\right)\cos\left(2N_R\left(\theta - \omega_r t\right)\right) + \frac{P_{S1}P_{R3}}{P_0}\cos\left(N_S\theta\right)\cos\left(3N_R\left(\theta - \omega_r t\right)\right) + \cdots \\
& + \frac{P_{S2}P_{R1}}{P_0}\cos\left(2N_S\theta\right)\cos\left(N_R\left(\theta - \omega_r t\right)\right) + \frac{P_{S2}P_{R3}}{P_0}\cos\left(2N_S\theta\right)\cos\left(3N_R\left(\theta - \omega_r t\right)\right) + \cdots \\
& + \frac{P_{S3}P_{R1}}{P_0}\cos\left(3N_S\theta\right)\cos\left(N_R\left(\theta - \omega_r t\right)\right) + \frac{P_{S3}P_{R2}}{P_0}\cos\left(3N_S\theta\right)\cos\left(2N_R\left(\theta - \omega_r t\right)\right) + \cdots \\
& + \frac{P_{S4}P_{R1}}{P_0}\cdot\cdot
\end{aligned}
\tag{4.9}
$$

The combined-effects terms can be rewritten using the general formula
cos $A$ cos $B = 0.5 \cos(A{-}B) + 0.5 \cos(A{+}B)$ so that

$$P_{m,n} = \frac{P_{Sm}P_{Rn}}{2P_0}\cos\left(\left[mN_S - nN_R\right]\theta + nN_R\omega_r t\right) + \frac{P_{Sm}P_{Rn}}{2P_0}\cos\left(\left[mN_S + nN_R\right]\theta - nN_R\omega_r t\right) \tag{4.10}$$

where $m$ and $n$ are stator and rotor slot harmonics. Altogether, the total air-gap permeance coefficient can be written using the following five terms:

$$
\begin{aligned}
P = {} & P_0 + \sum_{m=1}^{M} P_{Sm}\cos\left(mN_S\theta\right) + \sum_{n=1}^{N} P_{Rn}\cos\left(nN_R\left(\theta - \omega_r t\right)\right) \\
& + \sum_{m=1}^{M}\sum_{n=1}^{N} \frac{P_{Sm}P_{Rn}}{2P_0}\left[\cos\left(\left[mN_S - nN_R\right]\theta + nN_R\,\omega_r t\right) + \cos\left(\left[mN_S + nN_R\right]\theta - nN_R\,\omega_r t\right)\right]
\end{aligned}
\tag{4.11}
$$

The permeance will behave identically but includes consideration of the axial dimension, whereas only the cross-sectional geometry has been considered so far. The correlation between permeance and permeance coefficient will be investigated further in section 5.2.

(4.11) is identical to the derivations of other authors, e.g. [18], although (4.11) includes the higher slot harmonics. The first term corresponds to the average air-gap permeance, calculated using the Carter factor. This is the only term which has a non-zero mean value. The second and third terms correspond to stator and rotor slot harmonics. These will have $mN_S$ and $nN_R$ pole-pairs. The fourth and fifth terms contain combinations of the stator and

rotor harmonic permeances. These are permeance waves consisting of waves of $|mN_S + nN_R|$ pole pairs for the fourth term and $|mN_S - nN_R|$ pole pairs for the fifth term.

**Rotational speed of harmonic permeance waves**

The rotational speed of the various harmonics will vary. The permeance harmonics related to the stator, i.e. the second term of (4.11), will be stationary, i.e. their rotational speed will be 0. For the other terms of (4.11), the rotational speed can be determined by the time it takes for them to complete a full mechanical cycle, i.e.

$$\theta = 2\pi \text{ for } t = \frac{1}{f} = \frac{2\pi}{\omega_p} \tag{4.12}$$

So, for the general permeance coefficient term

$$P_{gen}(\theta,t) = P_x \cos(x\theta - y\omega_r t) \tag{4.13}$$

the rotational speed can be found by substituting $\theta$ with $2\pi$ and $t$ with $2\pi/\omega_p$ and equating 0. Therefore

$$\omega_p = \frac{y}{x}\omega_r \tag{4.14}$$

For the rotor permeance harmonics of order $n$, the rotational speed will be

$$\omega_p = \frac{nN_R}{nN_R}\omega_r = \omega_r \tag{4.15}$$

For the combined-effect permeance of order $m$ and $n$ together, the rotational speed will be

$$\omega_{p1} = \frac{-nN_R}{mN_S - nN_R}\omega_r \tag{4.16}$$

and

$$\omega_{p2} = \frac{nN_R}{mN_S + nN_R}\omega_r \tag{4.17}$$

$\omega_{p1}$ will rotate in the forwards direction, i.e., in the same direction of the rotor, for $mN_S < nN_R$, and in the backwards direction for $mN_S > nN_R$; whereas $\omega_{p2}$ will rotate in the forwards direction for either slot combination.

## *4.4. Skewing*

Most small induction motors have rotor skew. This reduces the effects of MMF harmonics and also slotting. Appendix 1 shows how skewing of the rotor bars affects the $R/X$ ratio of the rotor circuit. The normal degree of skew is usually somewhere between one rotor slot and one stator slot. When skewing the rotor bar through a certain angle, the rotor permeance variation

is affected. This is investigated in more detail here. Fig. 4.7 shows a linearised view of a stator placed axially above a skewed rotor.
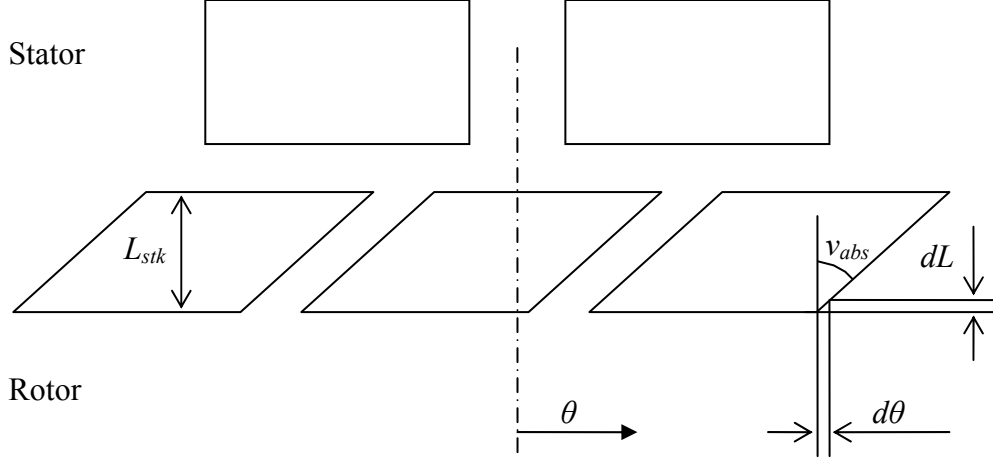


*Fig. 4.7 Skew representation*

It is shown in Fig. 4.3 how the varying air gap length can be decomposed in a series of harmonics. When averaging over the rotor stack length $L_{stk}$, the harmonic mean gap lengths can be represented by

$$l_{m\,\text{mean}}(\theta) = l_{g0} + \frac{1}{L_{stk}} \int_0^{L_{stk}} l_m(y,\theta)\, dy$$

$$= l_{g0} + \frac{-l_m}{L_{stk} \tan(v_{abs})} \left[ \sin\left( mN_r\left( \theta - \omega_r t - \frac{y}{r}\tan(v_{abs}) \right) \right) \right]_0^{L_{stk}}$$

$$= l_{g0} + \frac{r\, l_m}{mN_r L_{stk} \tan(v_{abs})} 2\cos\left( mN_r\left( \theta - \omega_r t - \frac{L_{stk}}{r}\tan(v_{abs}) \right) \right) \sin\left( \frac{mN_r L_{stk} \tan(v)}{2r} \right)$$

(4.18)

where $l_{g0}$ is the mechanical (constant) gap length and $l_m$ is the amplitude of the $m^{\text{th}}$ harmonic gap length. For constant value of $l_g$, the varying term must vanish, i.e.:

$$\sin\left( \frac{mN_r L_{stk} \tan(v_{abs})}{2r} \right) = 0 \quad \Rightarrow$$

$$\frac{mN_r L_{stk} \tan(v_{abs})}{2r} = (0),\ \pi,\ 2\pi\ ...$$

(4.19)

where 0 is not a valid value since it would mean that the denominator of (4.18) would also become 0. Hence, the smallest value of skewing resulting in zero $m^{\text{th}}$ harmonic permeance variation can be found from

$$\tan\left(\nu_{abs}\right) = \frac{2\pi r}{mN_r L_{stk}} \tag{4.20}$$

Hence, skewing the rotor stack by one rotor slot eliminates the fundamental as well as all other slot harmonics due to the periodicity of (4.19); this gives

$$\tan\left(\nu_{abs}\right) = \frac{2\pi r}{mN_r L_{stk}}\left(1, 2, 3 \ldots\right) \tag{4.21}$$

In Fig. 4.8, an illustration of the fundamental, 2<sup>nd</sup> and 3<sup>rd</sup> harmonic amplitude for the mean air-gap length variation plotted against skewing angle is shown. The rotor has 18 slots, the rotor stack length is 41 mm and radius is 31.2 mm.
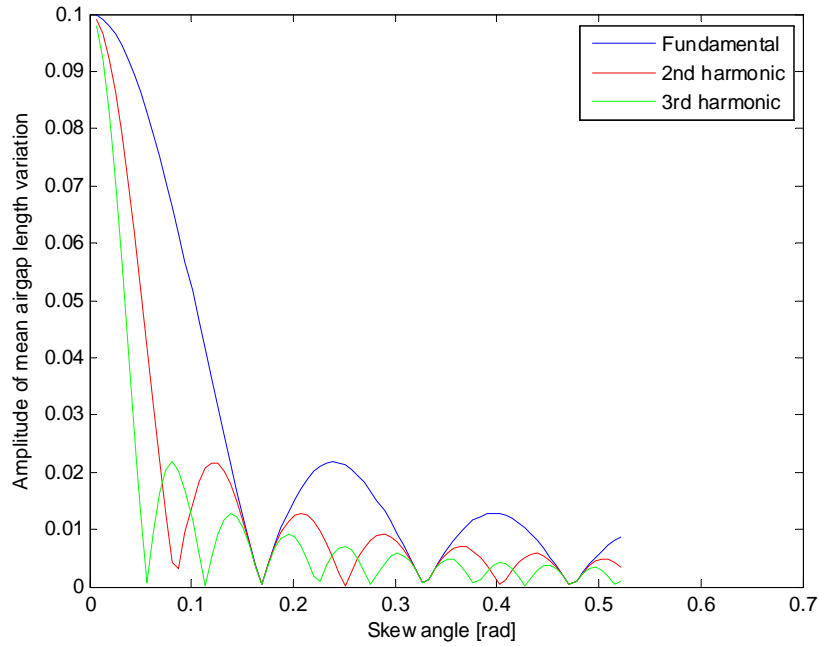


*Fig. 4.8 Harmonic amplitudes of air-gap lengths versus skew angle*

It appears that the higher the order of the harmonic, the smaller the required skew angle which is required to eliminate the harmonic. The smallest skew angle eliminating all fundamental and harmonic variation is

$$\nu = \arctan\left(\frac{2\pi \times 31.2}{28 \times 41}\right) = 0.17 \text{ rad} = 9.8° \tag{4.22}$$

For a rotor with the given dimensions, this corresponds to one rotor slot. This would mean that in (4.6), the rotor permeance would become a constant value, effectively eliminating the third, fourth and fifth terms in (4.11). The remaining permeance variation would be due to the stator only.

This is somewhat in contradiction to the findings in the literature. In [15], it is stated that "It appears at first glance that skewing the rotor one stator slot pitch should completely eliminate locking." Skewing the rotor through one stator slot pitch eliminates MMFs of harmonic order

$N_s$. For a balanced 3-phase machine, this represents the major MMF harmonics, including the 5th, 7th, 11th and so on. For single-phase machines, however, all uneven harmonics are present. Reference [17] considers an example of a 4-pole motor with 24 stator and 28 rotor slots and it finds that the optimal skew angle to be between $2\pi/18$ and $2\pi/13$. This angle is considerably larger than the angle corresponding to either one stator or one rotor slot skew.

# Chapter 5

# Synchronous locking torques

In the previous chapter, the various harmonic air-gap fields due to the air-gap permeance variation were considered and a harmonic representation developed. Here, an analysis is developed that considers the way the permeance harmonics interact with the various harmonic rotor MMFs to create torque.

## *5.1 Harmonic air-gap fields*

Figs. 2.6 and 2.7 show how the fundamental forwards- and backwards-rotating components of flux density are calculated from the MMF and air-gap permeance coefficient, although the specific term permeance coefficient in not used there; in Chapter 2 only a constant air-gap is considered. Here, the various terms of air-gap permeance coefficients are also considered. In general:

$$B = MMF_{res} \cdot P \tag{5.1}$$

The MMF of order $m$ is itself rotating with rotational speed $\pm\, \omega/m$. The product of the general permeance coefficient term as given by (4.13) and the $p^{th}$ forward-rotating harmonic component of MMF is

$$
\begin{aligned}
B(t,\theta) &= MMF_{fp} \cos(\omega t - p\theta) \times P_x \cos(x\,\theta - y\omega_r t) \\
&= \frac{MMF_{fp}\, P_x}{2}\Big[\cos\big((\omega + y\omega_r)t - (p+x)\theta\big) + \cos\big((\omega - y\omega_r)t - (p-x)\theta\big)\Big]
\end{aligned}
\tag{5.2}
$$

Bearing in mind that $y$ and $x$ have different values as given by the terms in (4.11), i.e.:

Term 1:    $y = 0$        $x = 0$

Term 2:    $y = 0$        $x = mN_s$

Term 3:    $y = nN_r$        $x = nN_r$    (5.3)

Term 4:    $y = -nN_r$        $x = mN_s - nN_r$

Term 5:    $y = nN_r$        $x = mN_s + nN_r$

Equation (5.2) is composed of two rotating fields, whose pole-pair number and rotational speed are given by

$$
\begin{aligned}
&n_{b1} = p + x \qquad\qquad n_{b2} = p - x \\
&\omega_{b1} = \frac{\omega + y\omega_r}{p + x} \qquad\quad \omega_{b2} = \frac{\omega - y\omega_r}{p - x}
\end{aligned}
\tag{5.4}
$$

## 5. Synchronous locking torques

For a negative pole-pair number, this corresponds to the reverse direction and $\omega_{b1}$ and $\omega_{b2}$ are the rotational speeds of the fields. They create net torque when reacting with rotor MMFs of the same pole number when their speeds coincide, i.e., when

$$\omega_{r1} = \frac{\omega_{b1}(p+x) - \omega}{y} \quad \text{with} \quad \omega_{b1} = \pm\frac{\omega}{n_{b1}} \tag{5.5}$$

Note that (5.5) takes into account the fact that the rotor may rotate in both directions, i.e. the slip can be both smaller than 1 (normal operation) and greater than 1 (reverse rotation).

For example, the first field component will interact with the forwards-rotating rotor MMF at a rotor speed of

$$\omega_{r1f} = \frac{\dfrac{\omega}{p+x}(p+x) - \omega}{y} = 0 \tag{5.6}$$

and with the backwards-rotating rotor MMF at a rotor speed of

$$\omega_{r1b} = \frac{\dfrac{-\omega}{p+x}(p+x) - \omega}{y} = \frac{-2\omega}{y} \tag{5.7}$$

Similarly, the interaction of the $p^{\text{th}}$ backwards-rotating harmonic MMF with the various permeance coefficient terms will result in a field where

$$
\begin{aligned}
B(t,\theta) &= MMF_{bp}\cos(\omega t + p\,\theta)\cdot P_x \cos(x\,\theta - y\,\omega_r t) \\
&= \frac{MMF_{bp}\,P_x}{2}\Big[\cos\big((\omega + y\,\omega_r)t + (p-x)\theta\big) + \cos\big((\omega - y\,\omega_r)t + (p+x)\theta\big)\Big]
\end{aligned}
\tag{5.8}
$$

which is also composed of two rotating fields whose pole-pair number and rotational speed are given by

$$
\begin{array}{ll}
n_{b3} = p - x & n_{b4} = p + x \\[2mm]
\omega_{b3} = -\dfrac{\omega + y\omega_r}{p - x} = \dfrac{\omega + y\omega_r}{x - p} & \omega_{b4} = \dfrac{\omega - y\omega_r}{-x - p}
\end{array}
\tag{5.9}
$$

with $p$ = harmonic of the MMF under consideration and $x$ and $y$ as given by (5.3). A short summary of the process is perhaps appropriate:

1.  The forwards- and backwards-rotating magnetizing MMF with $p$ pole-pairs each interacts with the general permeance coefficient term with $x$ pole pairs. (In total, 2 MMFs per harmonic $p$)

2.  For each interaction, two counter-rotating flux densities with $n_b = (p+x)$ or $(p-x)$ pole-pairs are created. (In total, 4 flux densities per harmonic $p,m,n$)

3.  The rotational speed of each flux density is determined by the rotor speed. Each flux density may therefore produce average torque with either the forwards- or the

backwards-rotating rotor MMF of the same pole number when their speeds coincide, i.e., at either positive or negative synchronous speed of the rotor MMF. (In total, 8 speeds per harmonic *p,m,n*)

This means that for each harmonic component of winding MMF, stator permeance and rotor permeance, 8 components of synchronous locking torque need to be considered.

**Current harmonics**

Although not the focus of this project, it should be mentioned that the harmonic components of air-gap flux density generated by the permeance coefficient harmonics differ from those generated by winding harmonic because the have different rotational speeds. Those originating from winding harmonics always rotate with a speed equal to the synchronous speed of the harmonic under consideration; however, the flux densities waves originating from the permeance harmonics rotate at different speeds, which are partly determined by the rotor speed. They will therefore induce voltages into the harmonic windings of same pole-pair number which have a varying frequency. Consequently, when in the equivalent circuit diagram in Fig. 3.5, additional voltage sources of a frequency different from supply frequency will exist and give rise to a harmonic series of line currents. In [19], this phenomenon is utilised in an attempt to implement a speed control of an asynchronous machine by determining the line current spectrum in real-time.

The harmonic currents create no useful torque and merely contribute to small torque pulsations and losses. The harmonic content of the current is generally very low since the machine acts as a low-pass filter by being generally inductive.

**A note on stator permeance**

Before proceeding further, the standstill stator permeance coefficient, in (5.3), as described in term 2, should be investigated. The rotational speed coefficient is 0, which implies it is stationary regardless of rotor speed. From (5.4), the rotational speed of the resulting field is always

$$\omega_b = \frac{\omega}{\pm(p+x)} \quad \text{or} \quad \omega_b = \frac{\omega}{\pm(p-x)} \tag{5.10}$$

and this interacts with the rotor MMF of same pole number at all rotor speeds. Hence it behaves more like an asynchronous torque, although not entirely so. It is not considered in the following analysis.

## *5.2. MMF, permeance and torque*

As is the case with the production of useful machine torque, the synchronous locking torque components arise from a combination of MMFs interacting with flux densities of various harmonic orders. In order to calculate the magnitude of the torque components, a detailed knowledge of the harmonic magnetizing, as well as the rotor MMFs and permeances, are required.

**Magnetizing MMF of the $p^{th}$ harmonic winding**

It should be underlined, that the MMF in consideration is the *resulting* MMF, i.e. the (fictious) vector sum of the two physical MMFs of stator and rotor. This MMF is in fact created by the magnetizing currents of each of the harmonic circuits in the equivalent circuit diagram. The magnitude of the forwards-rotating $p^{th}$ harmonic magnetizing (or resulting) MMF can be calculated from (2.39) and (2.40) when considering the $p^{th}$ magnetizing currents, i.e.

$$
\begin{aligned}
MMF_{\mathrm{mag}\,p} &= \int_{0}^{\pi/p} \left\{ \frac{pN_{p\,main}}{4} \sqrt{2}\,\overline{I}_{\mathrm{mag}\,p\,main} \right\} \sin(p\theta)\,d\theta \\
&\quad + \int_{0}^{\pi/p} \left\{ \frac{pN_{p\,main}}{4} \frac{-j\beta_p}{\sin\left(\dfrac{p\pi}{2}\right)} \sqrt{2}\,\overline{I}_{\mathrm{mag}\,p\,aux} \right\} \sin(p\theta)\,d\theta \\
&= \left| \frac{N_{p\,main}}{\sqrt{2}} \left( \overline{I}_{\mathrm{mag}\,p\,main} + \frac{-j\beta_p}{\sin\left(\dfrac{p\pi}{2}\right)} \overline{I}_{\mathrm{mag}\,p\,aux} \right) \right|
\end{aligned}
\tag{5.11}
$$

where $pN/4$ is the winding amplitude of HALF of the $p^{th}$ harmonic winding. It is perhaps appropriate to remind of the relations between total pole pitch winding number $N_p$ and winding amplitude $\hat{N}_p = p\,N_p/2$ as given by (3.3). $\overline{I}_{mag\,p}$ is the rms value of the $p^{th}$ harmonic magnetising current.

(5.11) perhaps requires some explanation. It is necessary to determine the resulting MMF, consisting of both main and auxiliary winding contributions. The MMF contains the vector sum of the main and auxiliary magnetising currents, the auxiliary component winding number is modified using the ratio $\beta$ (the winding ratio) and its spatial phase is rotated using the expression $-j/\sin(p\pi/2)$. This ensures that the auxiliary winding leads the main winding

for $p = 1, 5, 9...$ and lags the main winding for $p = 3, 7, 11...$ The square root of two calculates the MMF as a peak value. The expression for the backwards-rotating MMFs is similar but contains the expression $+j / \sin(p\pi/2)$.

Having established an expression for the resulting MMFs (5.11), the flux density component (with $p \pm x$ pole-pairs) can be calculated from the permeance coefficients using (5.1). Therefore an expression for the actual permeance needs to be developed.

**Permeance and permeance coefficient**

The air-gap permeance is commonly defined by the gap cross section divided by gap length but in order to obtain a precise expression, particularly for a sinusoidally-varying flux, two different expressions of the same flux need to be considered, and by comparing these expressions, the permeance is derived.

Initially, the air-gap flux for one pole pitch from the $p^{th}$ harmonic winding is considered. Firstly, this can be expressed by magnetizing MMF and the air-gap permeance *Perm* so that

$$\Phi_p = \frac{2}{\pi} MMF_p \cdot Perm$$

$$= \frac{2I}{\pi} \int_0^{\pi/p} \hat{N}_p \sin(p\,\theta)d\theta \cdot Perm \qquad (5.12)$$

$$= \frac{4I\hat{N}_p}{\pi p} \cdot Perm$$

where $\hat{N}_p$ is the winding amplitude of the $p^{th}$ harmonic winding. The factor $2/\pi$ takes into account the sinusoidal distribution of the flux, since it represents the ratio between the areas of a sine function and a rectangular function of equal amplitude.

Secondly, a relationship between the flux linkage and the total flux of one pole pitch of the $p^{th}$ harmonic winding must be found. Fig. 5.1 shows a pole pitch of a $p^{th}$ harmonic sinusoidally-distributed winding. At an angle $\theta$, the shaded area of the coil is linked by a number of flux lines (shown in red).

## 5. Synchronous locking torques
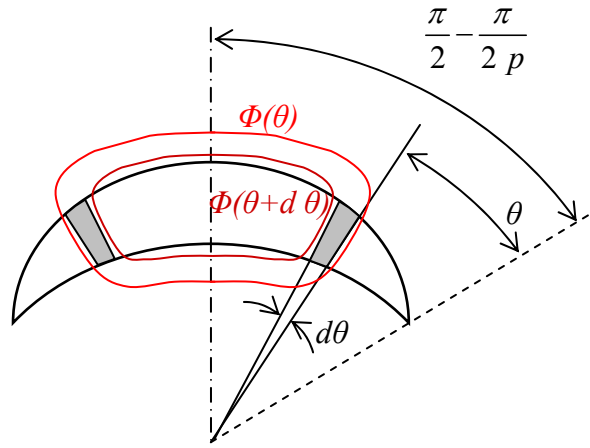


*Fig. 5.1 Pole pitch angular definitions*

At an angle $\theta$ the winding number is

$$N(\theta) = \hat{N}_p \sin(p\,\theta) \tag{5.13}$$

and the total flux is

$$\Phi(\theta) = \Phi_p \sin(p\,\theta) \tag{5.14}$$

Considering an infinitesimal radial section of width $d\theta$ at an angle $\theta$, the flux linkage is

$$
\begin{aligned}
d\Psi(\theta) &= 2\,N(\theta)\big[\Phi(\theta) - \Phi(\theta + d\theta)\big] \\
&= 2\,N(\theta)\frac{-d\Phi(\theta)}{d\theta}\cdot d\theta \\
&= -2\,\hat{N}_p \sin(p\,\theta)\, p\,\Phi_p \cos(p\,\theta)
\end{aligned}
\tag{5.15}
$$

From this, the total flux linkage of one pole pitch can be found by integrating over the entire pole pitch so that

$$
\begin{aligned}
\Psi_p &= \int_{\frac{\pi}{2}-\frac{\pi}{p2}}^{\frac{\pi}{2}} d\Psi(\theta) = -2p\hat{N}_p\Phi_p \int_{\frac{\pi}{2}-\frac{\pi}{p2}}^{\frac{\pi}{2}} \sin(p\theta)\cos(p\theta)\,d\theta \\
&= -p\hat{N}_p\Phi_p \int_{\frac{\pi}{2}-\frac{\pi}{p2}}^{\frac{\pi}{2}} \sin(2p\theta)\,d\theta = \frac{\hat{N}_p\Phi_p}{2}\big[\cos(p\pi) - \cos(p\pi - \pi)\big] \\
&= \frac{\hat{N}_p\Phi_p}{2}\left[2\sin\left(\pi\left(\frac{2p-1}{2}\right)\right)\sin\left(-\frac{\pi}{2}\right)\right] = \hat{N}_p\Phi_p
\end{aligned}
\tag{5.16}
$$

Solving for the pitch flux, and introducing a relationship between flux linkage, current and inductance gives

$$\Phi_p = \frac{\Psi_p}{\hat{N}_p} = \frac{1}{\hat{N}_p} I \frac{X_{p,mag}}{\omega} = \frac{I}{\hat{N}_p} \frac{r\, L_{stk}\, \pi\, \mu_0 \left(\dfrac{\hat{N}_p}{p}\right)^2}{l_{gap}} \tag{5.17}$$

This is obtained from (3.3) and (3.31). Equating (5.12) and (5.17) and solving for *Perm* yields

$$\frac{4I\hat{N}_p}{p\pi} \cdot Perm = I \frac{rL_{stk}\pi\mu_0\hat{N}_p}{p^2\, l_{gap}} \quad \Rightarrow$$

$$Perm = \frac{rL_{stk}\pi^2\mu_0}{4pl_{gap}} \tag{5.18}$$

This expression relates to the flux rather than the flux density, which is required here. However, the relationship between permeance and permeance coefficient is the same as that between flux and flux density *for one pole pitch*, therefore:

$$\frac{\Phi}{p} = \int B\, dA = r\, L_{stk} \int_0^{\pi/p} B \sin(p\,\theta)\, d\theta = \frac{2rL_{stk}B}{p} = \alpha B \tag{5.19}$$

So in order to obtain an expression for the permeance coefficient, the following comparisons are made. The flux is given by

$$\Phi_p = MMF \cdot Perm = \alpha B \tag{5.20}$$

and the flux density is given by

$$B_p = MMF \cdot P \tag{5.21}$$

Dividing (5.20) with (5.21) yields

$$\frac{\Phi_p}{B_p} = \frac{Perm}{P} = \alpha \tag{5.22}$$

From which, by combining (5.18) and (5.19):

$$P = \frac{Perm}{\alpha} = \frac{\pi^2\mu_0}{8l_{gap}} \tag{5.23}$$

where $l_{gap}$ is the amplitude of the harmonic gap lengths and $p$ is the pole-pair number of the harmonic flux density.

**Rotor MMF calculation**

The rotor MMF can be expressed in terms of its referred value, since only referred currents are present in the equivalent circuit diagram. Hence

# 5. Synchronous locking torques

$$MMF_{R\,n_b} = \int_0^{\pi/n_b} \frac{n_b N_{n_b\,main}}{4} \sqrt{2}\, \overline{I}\,'_{R\,n_b\,main} \sin(n_b\theta)\, d\theta$$

$$+ \int_0^{\pi/n_b} \frac{p N_{n_b\,main}}{4} \frac{-j\beta n_b}{\sin\left(\dfrac{n_b\pi}{2}\right)} \sqrt{2}\, \overline{I}\,'_{R\,n_b\,aux} \sin(n_b\theta)\, d\theta \qquad (5.24)$$

$$= \left| \frac{N_{n_b\,main}}{\sqrt{2}} \left( \overline{I}\,'_{R\,n_b\,main} + \frac{-j\beta_{n_b}}{\sin\left(\dfrac{n_b\pi}{2}\right)} \overline{I}\,'_{R\,n_b\,aux} \right) \right|$$

The relationship between the MMF and current distribution amplitude is given by (3.39), i.e.:

$$\hat{I}_{R\,n_b} = \frac{n_b MMF_{R\,n_b}}{2} = \left| \frac{n_b N_{n_b\,main}}{2\sqrt{2}} \left( \overline{I}_{R\,n_b\,main} + \frac{-j\beta_{n_b}}{\sin\left(\dfrac{n_b\pi}{2}\right)} \overline{I}_{R\,n_b\,aux} \right) \right| \qquad (5.25)$$

$N_{n_b\,main}$ is the total winding number of one pole pitch of the $n_b{}^{th}$ harmonic winding.

## Torque calculation

From (5.25) and (5.1) the magnitudes of the locking torques can be determined. The maximum value of locking torque occurs when the flux density and the current distribution are in phase, and the minimum value occurs when they are in anti-phase. The magnitude is given by

$$T_{sync\,p} = \pm r\, L \int_0^{2\pi} \hat{I}_{Rp} \sin(p\theta) \hat{B}_p \sin(p\theta)\, d\theta$$

$$= \pm r L\, \hat{I}_{Rp} \hat{B}_p \pi \qquad (5.26)$$

## Comparison with a 3-phase motor

Before proceeding to calculate the actual values of the synchronous locking torques, it is worthwhile considering the differences between a split-phase motor and a balanced 3-phase motor.

Generally, in the 3-phase motor fewer winding harmonics exist. Firstly, all winding harmonics which are multiples of 3 are not present for a Y- or Δ-connected balanced three phase motor. Secondly, at the remaining harmonics (1, 5, 7, 11....) only one of the two counter-rotating MMFs are present due to the 3-phase balancing ($5^{th}$, $11^{th}$, etc, rotate backwards while the $7^{th}$, $13^{th}$, etc, rotate forwards).

For the single phase motor, all winding harmonics of uneven order are present, and for each order, both the forward and the backwards rotating component exist. Since the synchronous

locking torques are created by the interaction of harmonic magnetizing MMFs, permeance components and harmonic rotor MMFs, there are more than twice as many sources for synchronous locking torques in the single phase motor compared to the 3 phase motor. Hence single-phase motors should be sine wound wherever possible.

## *5.3. Calculating synchronous locking torques*

As mentioned in previous sections, there are several independent synchronous locking torques which can be calculated for the $p^{th}$ magnetizing MMF. This interacts with each permeance coefficient term to create flux density waves of harmonic order $n_b$. The torque arises from their interaction with a rotor MMF of the same harmonic order $n_b$. The accurate calculation of the torque requires the magnitudes of the various flux densities and MMFs to be known. Therefore it is necessary to obtain realistic values for these.

**Implementation of model**

To obtain values for the various flux density waves and MMFs, the equivalent circuit which includes winding harmonics is used. This also includes 4 separate winding harmonics for both the forwards and backwards-rotating waves. This gives a system of 20 equations when considering both the main and auxiliary windings.

The fundamental and third winding harmonic variables are always considered, since these, or at least the fundamental, will determine the line current drawn from the supply. The third harmonic tends to be the most significant harmonic.

In addition, the winding harmonics of order $p$ (which are the ones that interacts with the permeance harmonic to produce flux) and $n_b$ (which is the winding harmonic of the same order as the resulting flux) are considered in order to obtain the values needed for torque calculation. If $p$ or $n_b$ is of an order already present in the equivalent circuit then they are set to 5 and 7 respectively. Otherwise, the currents would be wrongly calculated.

In other words, the fundamental and third harmonic variables are used to bias the equivalent circuit, and the two additional harmonic variables are used to calculate the magnitude of synchronous locking torques.

This is illustrated in Fig. 5.2, which shows the sub-circuit representing the 4 forwards-rotating harmonic windings of the main winding. In the actual circuit, as used and implemented for the calculations here, the 4 backwards-rotating windings together with the auxiliary circuits are considered.
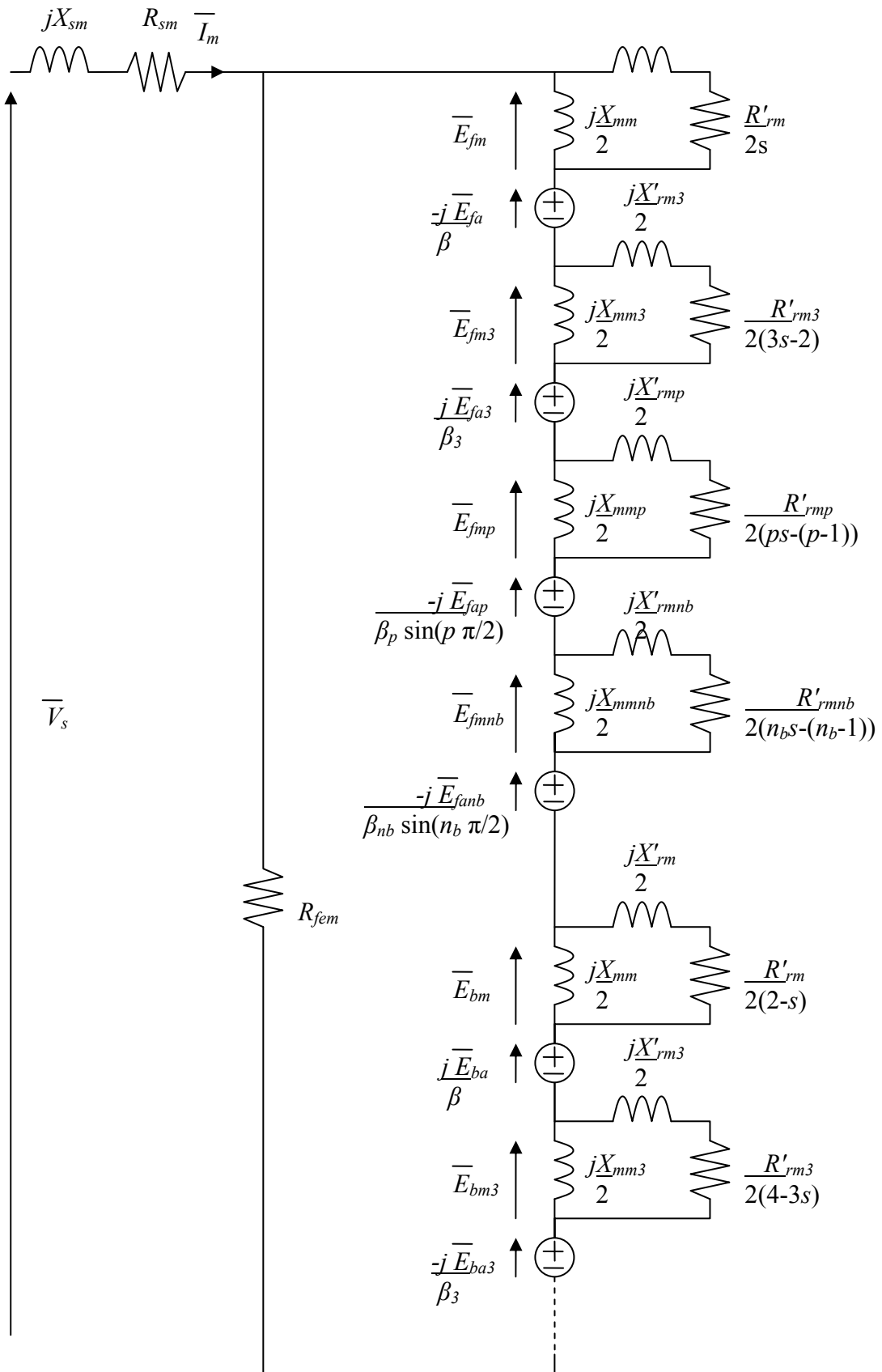
*Fig. 5.2 Harmonic sub-equivalent circuit for main forwards-rotating harmonics*

## 5. Synchronous locking torques

As mentioned previously, there are several components of synchronous locking torque that need to be considered. The calculation is performed by considering one component at a time, in a manner which can be best described in the flowchart in Fig. 5.3.

For each stator permeance harmonic $m$:

For each rotor permeance harmonic $n$:

For each permeance term $(x,y)^*$:

For each value of harmonic winding MMF ($p$):

Determine the number of poles ($n_b$) of the resulting flux densities

Determine the 8 rotor speeds ($\omega_r$) at which locking occurs

For each rotor speed ($\omega_r$):

Solve the equivalent circuit equations
Obtain values for $p^{th}$ harmonic magnetizing MMF and $n_b{}^{th}$ harmonic rotor MMF

Calculate the value of synchronous locking torque.

Create ($\omega_r$, $T$) table

Accumulate ($\omega_r$, $T$) table

Accumulate ($\omega_r$, $T$) table

Accumulate ($\omega_r$, $T$) table

Accumulate ($\omega_r$, $T$) table

Accumulate ($\omega_r$, $T$) table

*)Additionally, modifications must be made so that term 3 is only included once per rotor permeance harmonic

*Fig. 5.3 Calculation flowchart for synchronous locking torque*

# 5. Synchronous locking torques

**Calculation example**

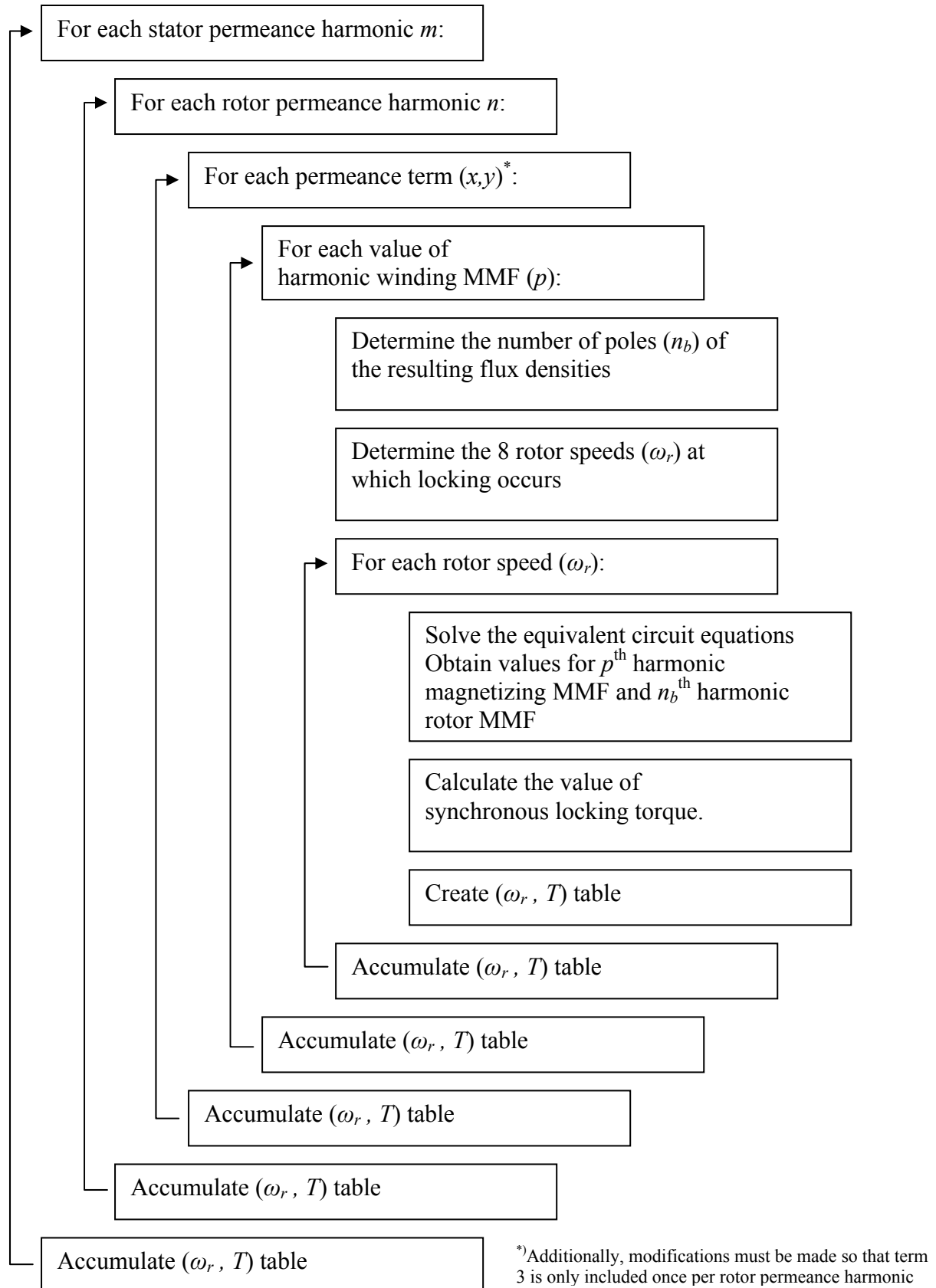An example of the innermost loop calculation, resulting in 8 separate torque components, is given in Fig. 5.4 in the upper graph. It appears that many of the components occur at the same rotor speeds, so the lower graph shows the accumulated torques at each occurring rotor speed.
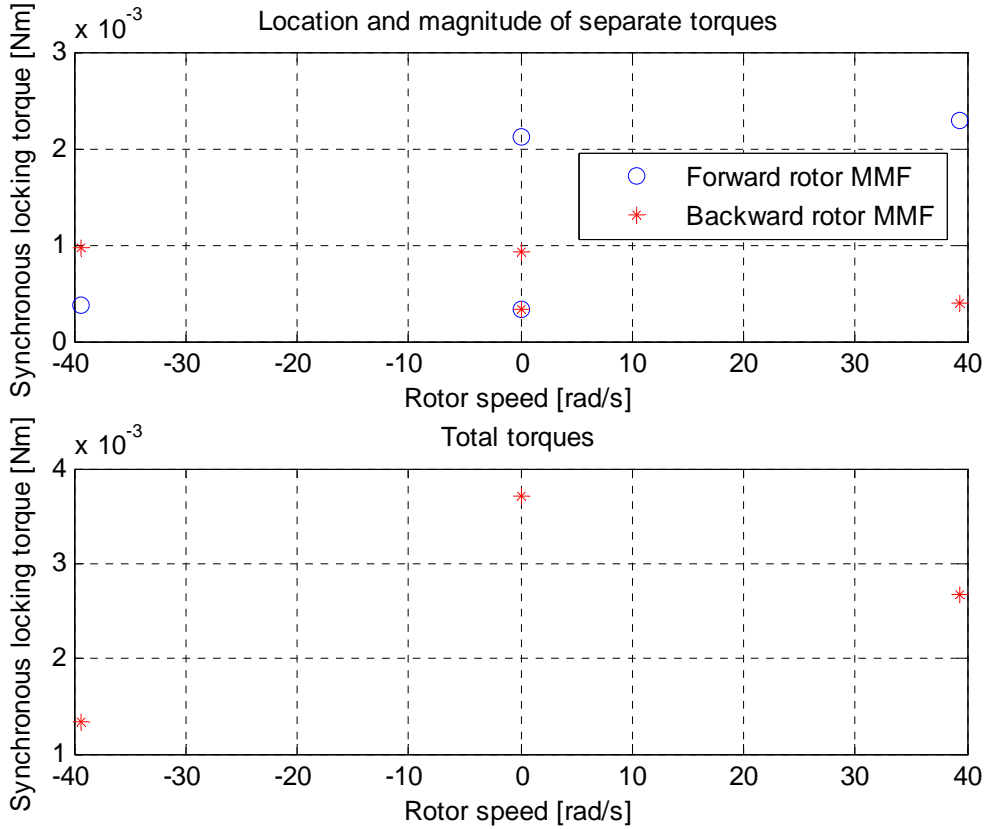


*Fig. 5.4 Synchronous torque points – top: individual points; bottom: combined points*

In order to clarify the origin of the torques illustrated in Fig. 5.4, they are here treated separately.

The example shown in Fig. 5.3 is for the case of 24 stator slots, 16 rotor slots, fundamental magnetising MMF, $24^{th}$ stator permeance harmonic, $16^{th}$ rotor permeance harmonic and third permeance term. Therefore, from (5.3)

$$y = 16 \qquad\qquad x = 16 \qquad\qquad (5.27)$$

Since the fundamental magnetising MMF is considered then $p = 1$ and the pole-pair number of the resulting fields caused by the forward magnetising MMF are, from (5.4):

$$n_{b1} = 17 \qquad\qquad n_{b2} = -15 \qquad\qquad (5.28)$$

with rotational speeds:

$$\omega_{b1} = \frac{\omega + 16\,\omega_r}{17} \qquad\qquad \omega_{b2} = \frac{\omega - 16\,\omega_r}{-15} \qquad\qquad (5.29)$$

## 5. Synchronous locking torques

These interact with the forwards-rotating rotor MMF of same pole-pair number, i.e., 17 and 15 pole-pairs respectively, at speeds as given by (5.6) and (5.7), so that

$$\omega_{r1f} = 0 \qquad\qquad \omega_{r2f} = 0 \tag{5.30}$$

They also interact with the backwards-rotating rotor MMF at speeds

$$\omega_{r1b} = \frac{-2\omega}{16} \qquad\qquad \omega_{r2b} = \frac{2\omega}{16} \tag{5.31}$$

Similarly, the backwards-rotating magnetising MMF of order $p$ creates fields with pole-pair numbers as given by (5.9):

$$n_{b3} = -15 \qquad\qquad n_{b4} = 17 \tag{5.32}$$

with rotational speeds

$$\omega_{b3} = \frac{\omega + 16\,\omega_r}{15} \qquad\qquad \omega_{b4} = \frac{\omega - 16\,\omega_r}{-17} \tag{5.33}$$

These interact with the forwards-rotating rotor MMF of same pole-pair number at speeds

$$\omega_{r3f} = \frac{-2\omega}{16} \qquad\qquad \omega_{r4f} = \frac{2\omega}{16} \tag{5.34}$$

and with the backwards-rotating rotor MMF at speeds

$$\omega_{r3b} = 0 \qquad\qquad \omega_{r4f} = 0 \tag{5.35}$$

This explains the appearance of the uppermost graph in Fig. 5.3. The torques are calculated from the current values, which are determined from the equivalent circuit for each value of rotor speed.


**Evaluation of stator and rotor slot combinations**

Implementing the algorithms as shown in Fig 5.3 and further adding an outer loop which steps through a range of rotor slots for a fixed stator slot number, it is possible to evaluate which slot number combinations give rise to the highest and lowest values of synchronous locking torque. In the following sections, three motors of approximately the same starting and pull-out torque values are considered. They are all modelled in start mode, i.e., with the value of auxiliary impedance corresponding to the starting properties of the motor. This is because the synchronous locking torques occur during the transient run-up at lower speeds, where the motor is accelerating towards operating speed.

The specifications for the machines are given in Appendix 3. These machines do not have any skew in order to emphasise the effects of the winding harmonics on the synchronous and asynchronous torques.

## 1. 220V motor designed for optimum efficiency

This motor is designed for capacitor-run operation. Fig. 5.5 shows the spectra for the main and auxiliary windings, indicating very limited harmonic effects, particularly for the main winding. Note that in the lower graphs, showing the magnitude of the higher harmonic MMFs, the fundamental value has been omitted to clarify the magnitude of the harmonics. The fundamental is shown in red in the upper graphs.
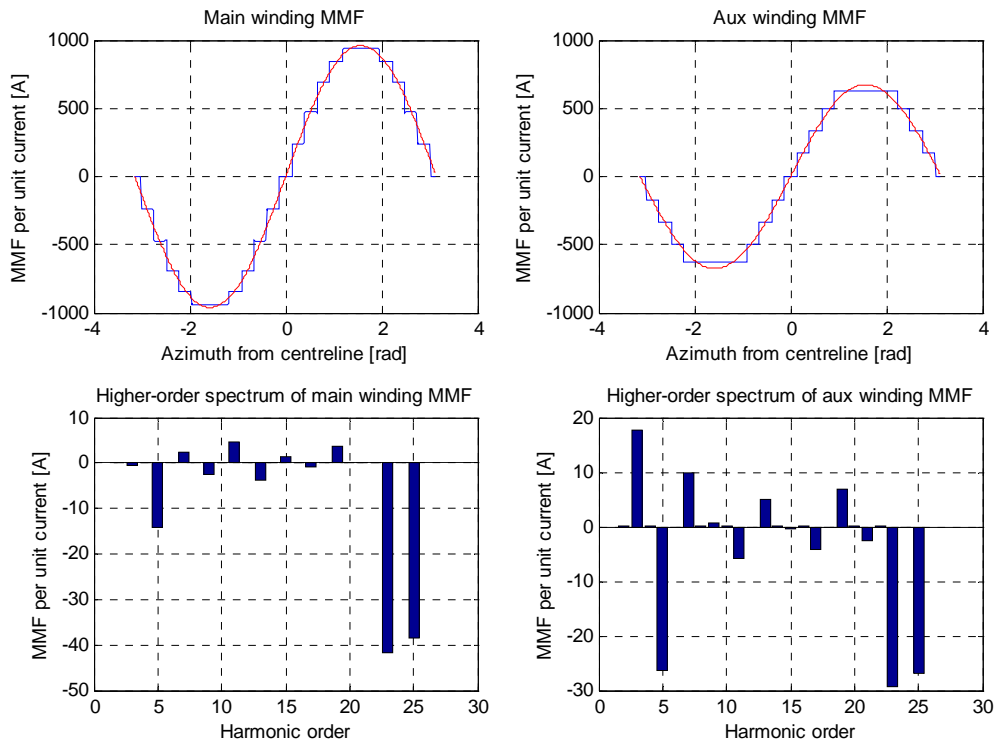


*Fig. 5.5 Winding harmonics - 220 V machine*

Fig. 5.6 shows the magnitude of the synchronous locking torque versus rotor speed and rotor slot number as a space plot in the upper graph as well as projected plots on the middle and lower graphs. The number of stator slots is 24 and the mechanical air-gap is 0.28 mm. For clarity, the data values are given by dots instead of bars, which is the normal case for plotting discrete values. However, the dot visualisation is more clear when having multiple values at the same variable. Moreover, the dots are connected by a line to indicate which values belong to the same series. Of course, the lines should not be interpreted as a continuous function; they are merely a means for clarifying the identity of the data series. For example, the red dots connected by red lines in the middle plot in fig. 5.6 all belong to the data series describing a 24 slot rotor.

# 5. Synchronous locking torques
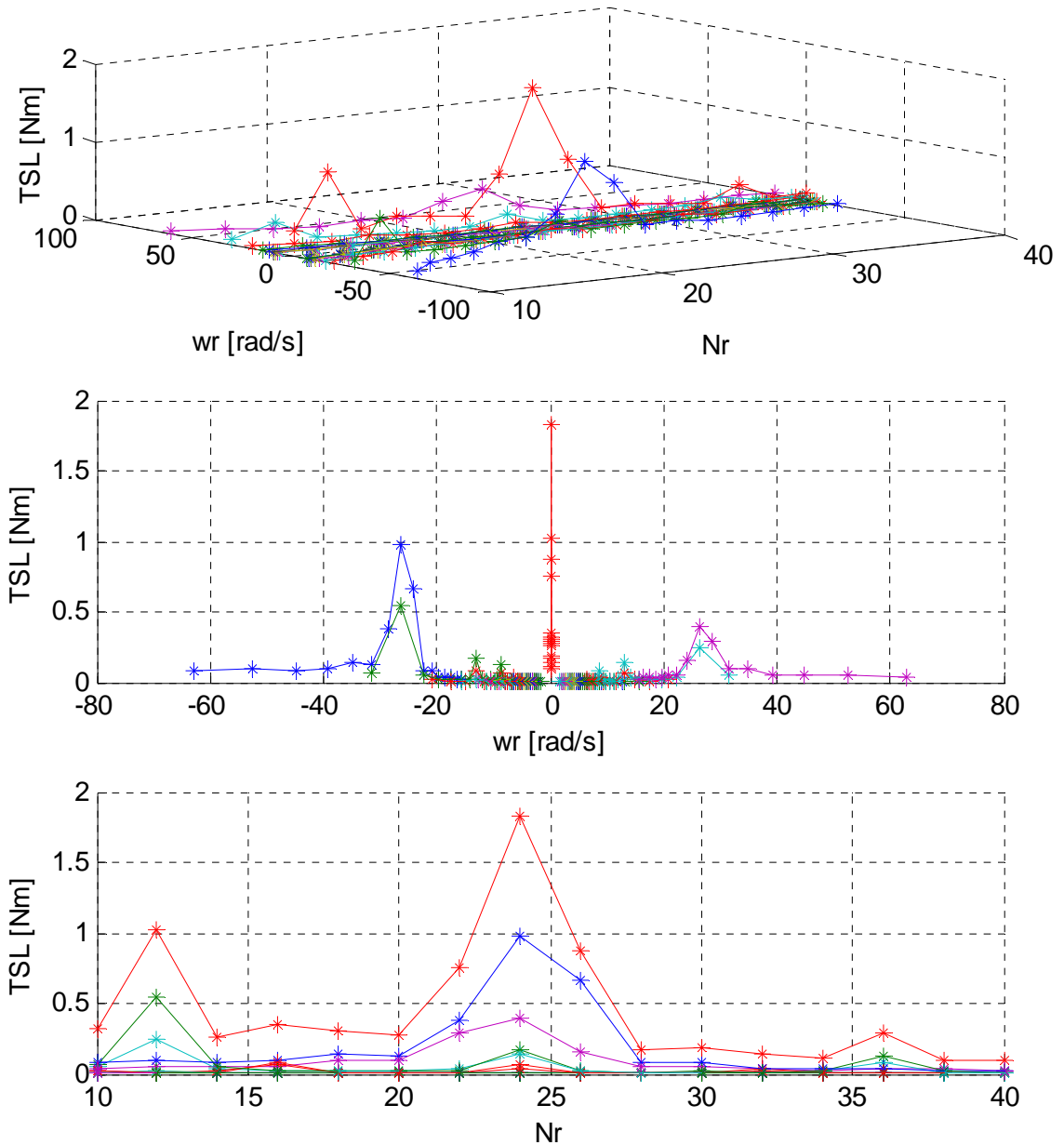


*Fig. 5.6 Magnitude and location of synchronous locking torques - 220 V machine*

Fig. 5.7 shows the synchronous locking torques superimposed on the steady state torque vs. speed curves for 20 rotor slots, which results in limited synchronous locking torque, as well as for 24 rotor slots (equal to stator slot number) which results in severe locking at standstill. Negative speeds have been included to illustrate that synchronous locking takes place at reverse rotation as well.

# 5. Synchronous locking torques

Steady state torque with superimposed sync. locking torques



Steady state torque with superimposed sync. locking torques



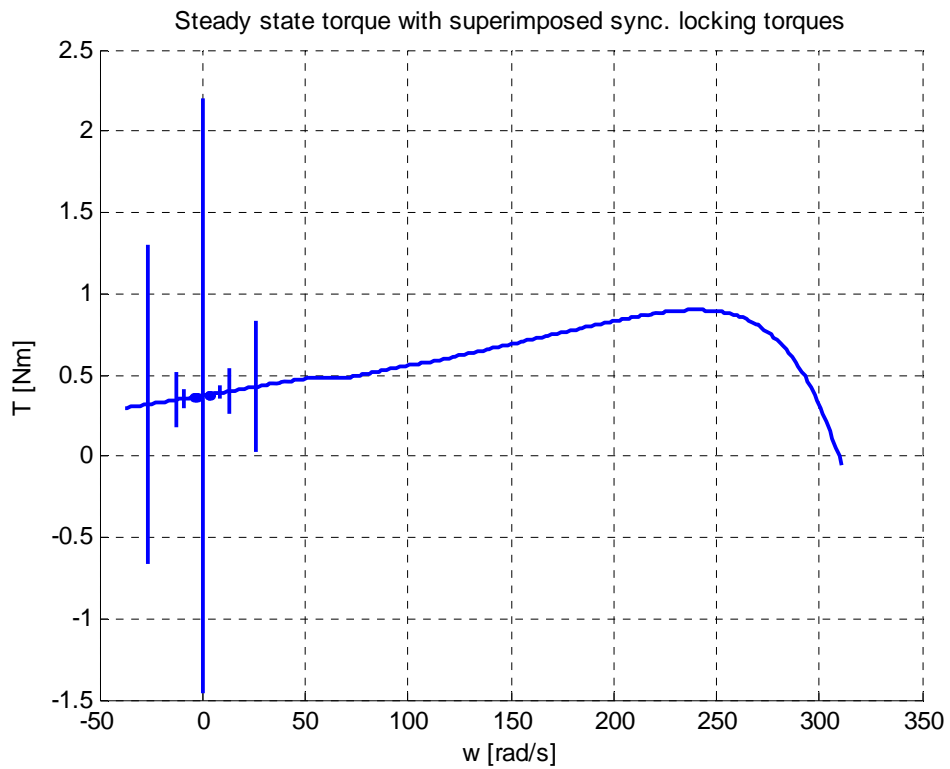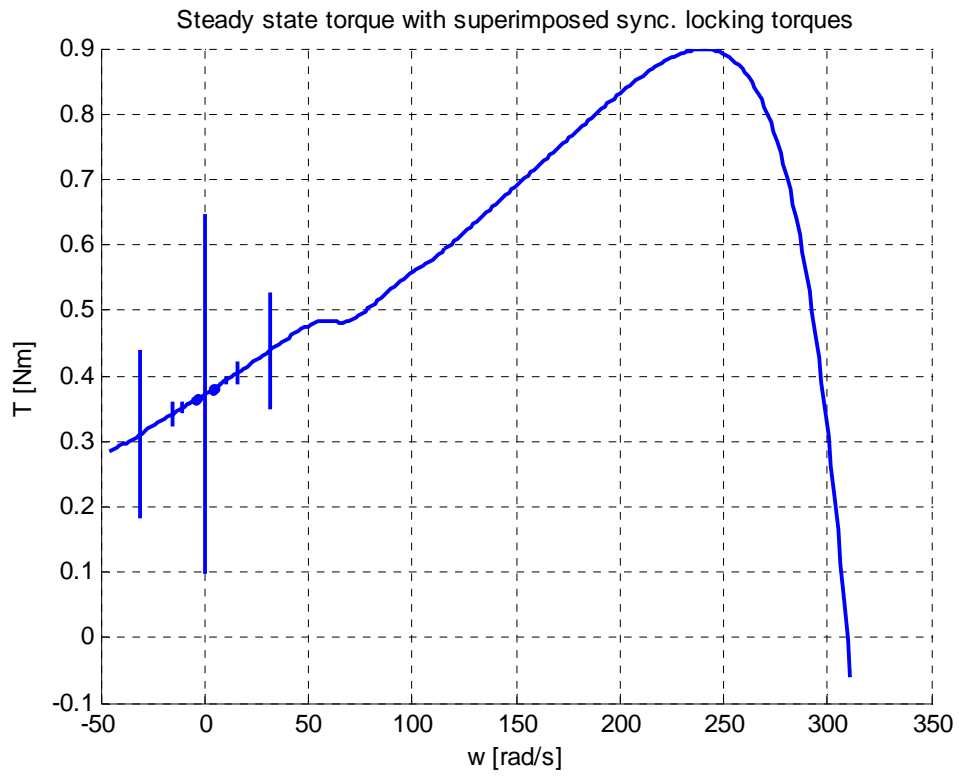*Fig. 5.7 Torque-speed curves of motor with $N_r$ = 20 and 24 slots respectively - 220 V*

*machine*

## 2. 115V motor designed for low cost and low efficiency

This motor is a 115V motor designed for single phase operation. Fig. 5.8 shows the spectra of the main and auxiliary windings, indicating considerable $3^{rd}$ and $5^{th}$ harmonics.
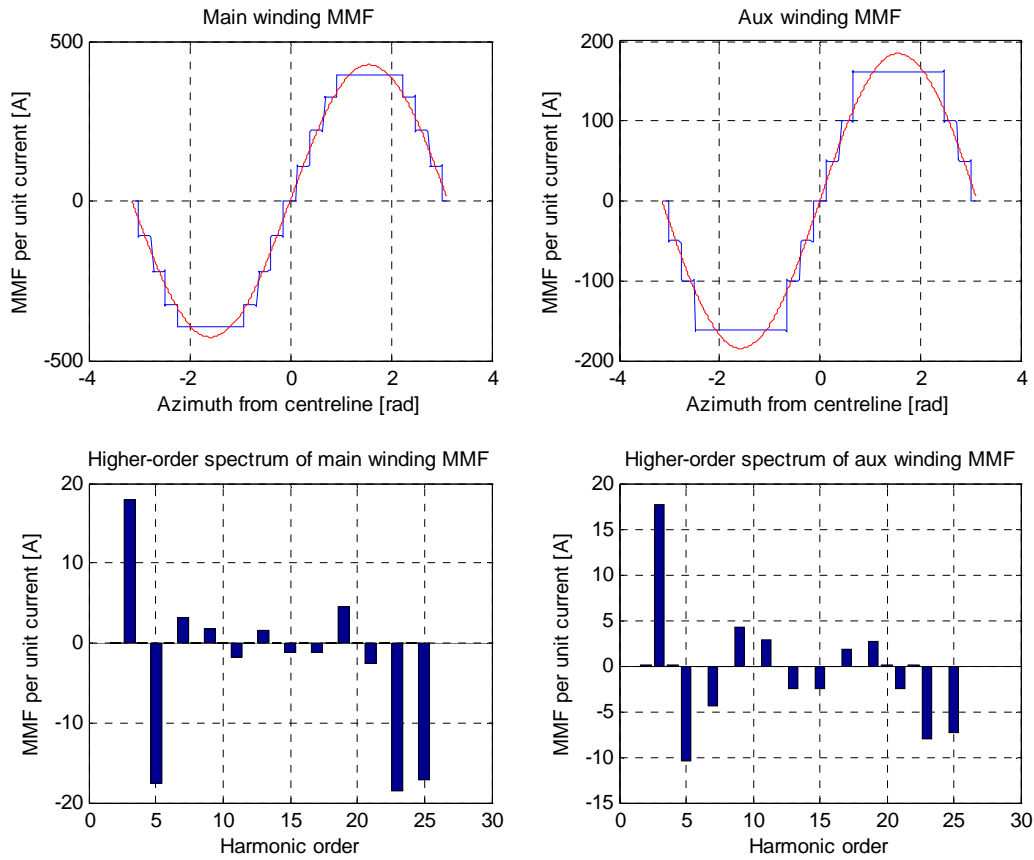


*Fig. 5.8 Winding harmonics - 115 V machine*

Fig. 5.9 shows the magnitude of the synchronous locking torque versus rotor speed and rotor slot number as a space plot in the upper graph and as projected plots in the middle and lower graphs in a similar manner to the 220 V machine. The number of stator slots is 24 and the mechanical air gap is 0.36 mm.

*Fig. 5.9 Magnitude and location of synchronous locking torques - 115 V machine*

Fig. 5.10 shows the synchronous locking torques superimposed on the steady state torque vs. speed curves for 18 rotor slots, which results in considerable synchronous locking torque, as well as for 24 rotor slots (equal to stator slot number) which results in severe locking at standstill. The steady-state torques themselves show considerable asynchronous torque dips.

# 5. Synchronous locking torques



**Steady state torque with superimposed sync. locking torques**



**Steady state torque with superimposed sync. locking torques**
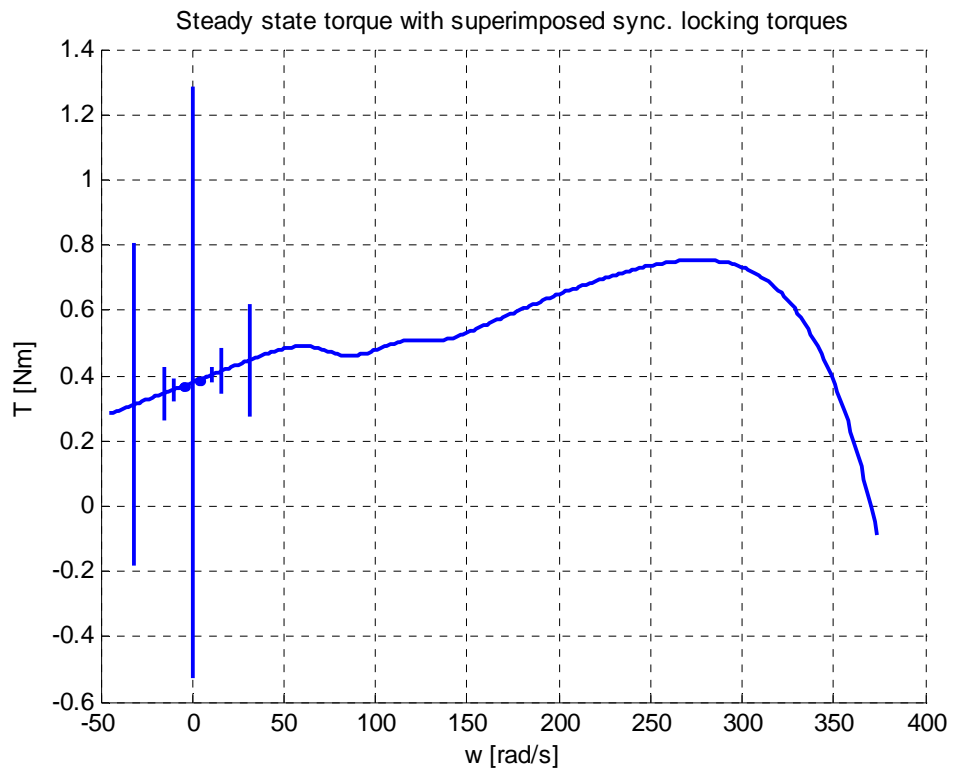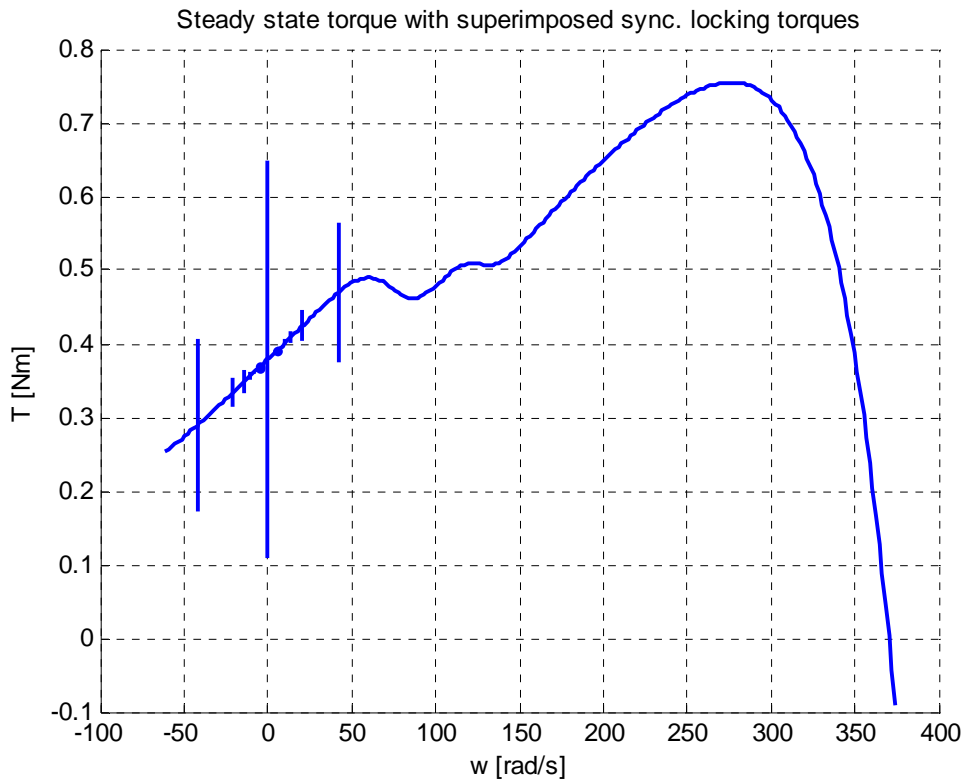
*Fig. 5.10 Torque-speed curves of motor with $N_r$ =18 and 24 slots respectively - 115 V machine*

84

**3. A 220V variant of example 1**.

This machine is based on the 220 V machine in example 1 but with a redesigned stator which has a less distributed winding. Fig. 5.11 shows the spectra of the main and auxiliary windings, indicating considerable 3$^{rd}$ and 5$^{th}$ harmonics in a similar manner to the 115 V machine in the previous example.
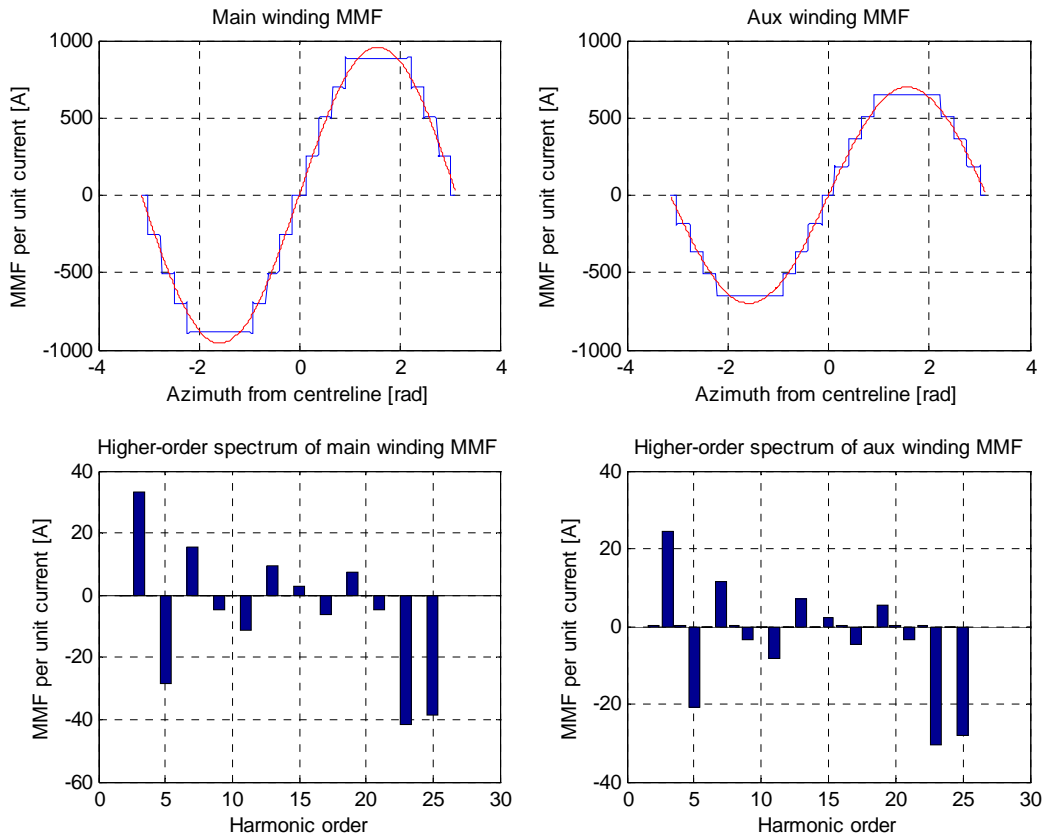


*Fig. 5.11 Winding harmonics – modified 220 V machine*

Fig. 5.12 shows the magnitude of the synchronous locking torque versus rotor speed and rotor slot number with a space plot in the upper graph and projected plots in the middle and lower graphs. The number of stator slots is 24 and the mechanical air gap is 0.28 mm.
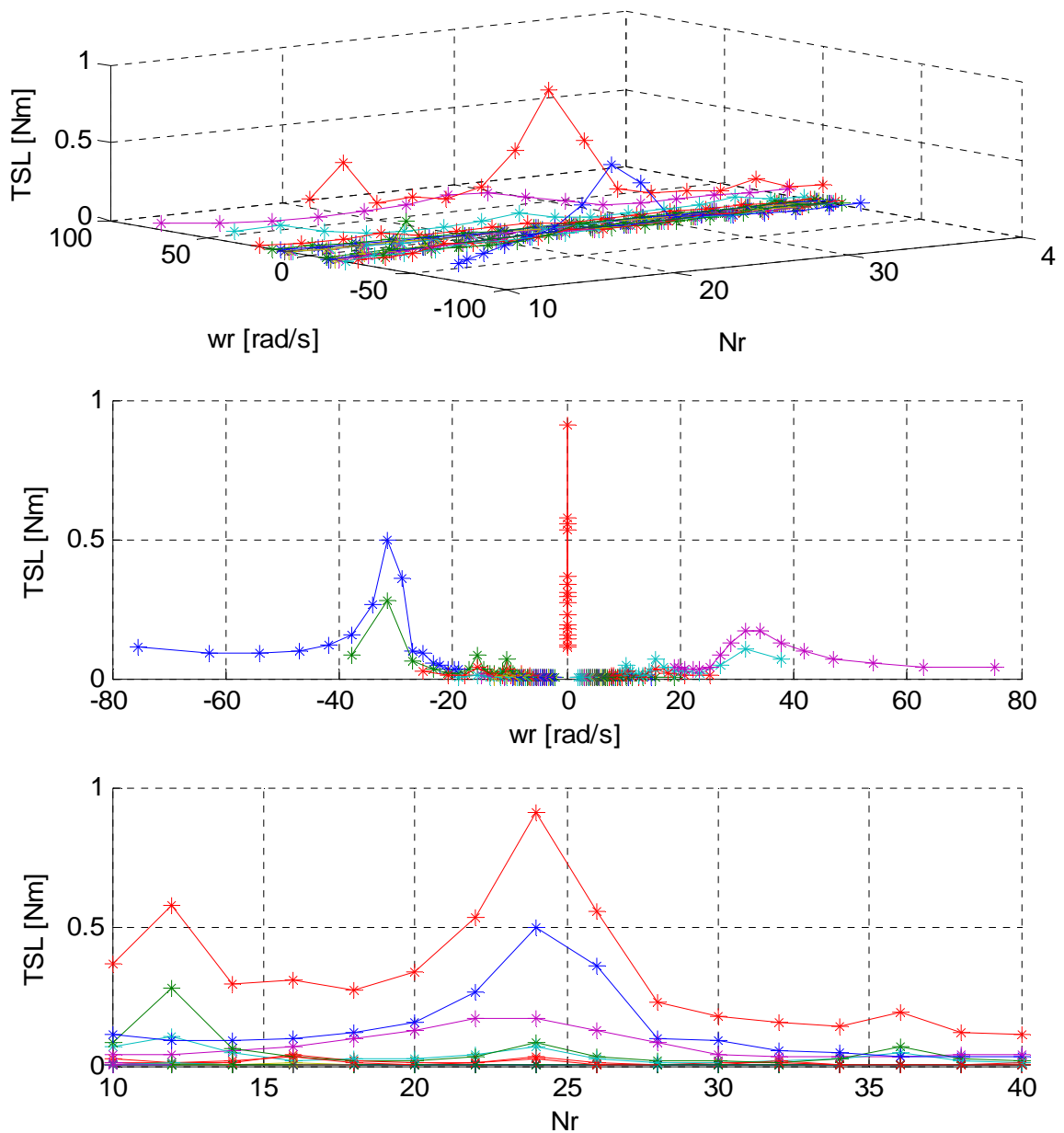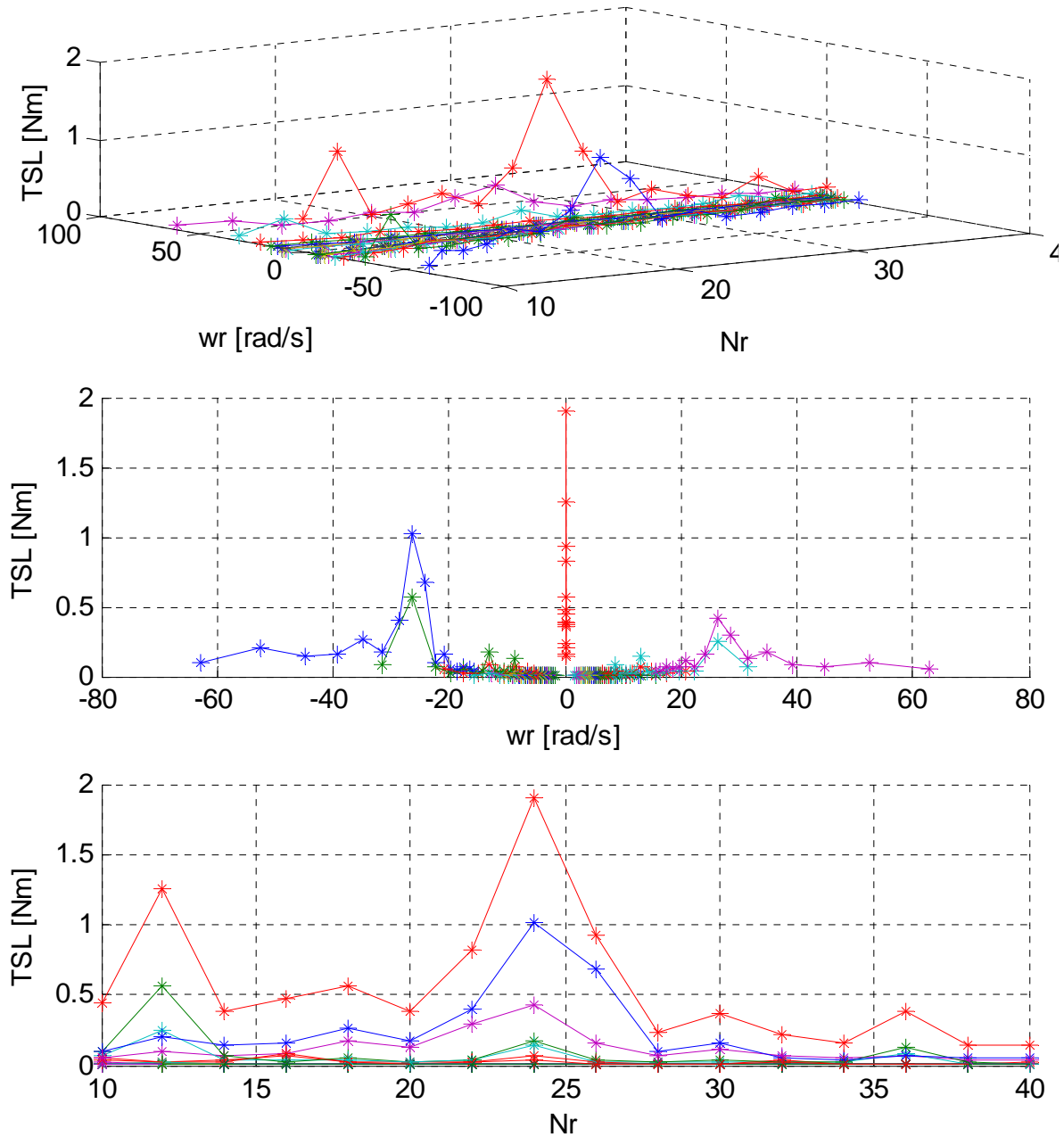
*Fig. 5.12 Magnitude and location of synchronous locking torques – modified 220 V machine*

Fig. 5.13 shows the synchronous locking torques superimposed on the steady state torque vs. speed curves for 20 rotor slots, which results in limited synchronous locking torque, as well as for 24 rotor slots (equal to stator slot number) which results in severe locking at standstill. Again, these are similar to the previous two examples in terms of the 24 slot rotor.

Steady state torque with superimposed sync. locking torques

Steady state torque with superimposed sync. locking torques
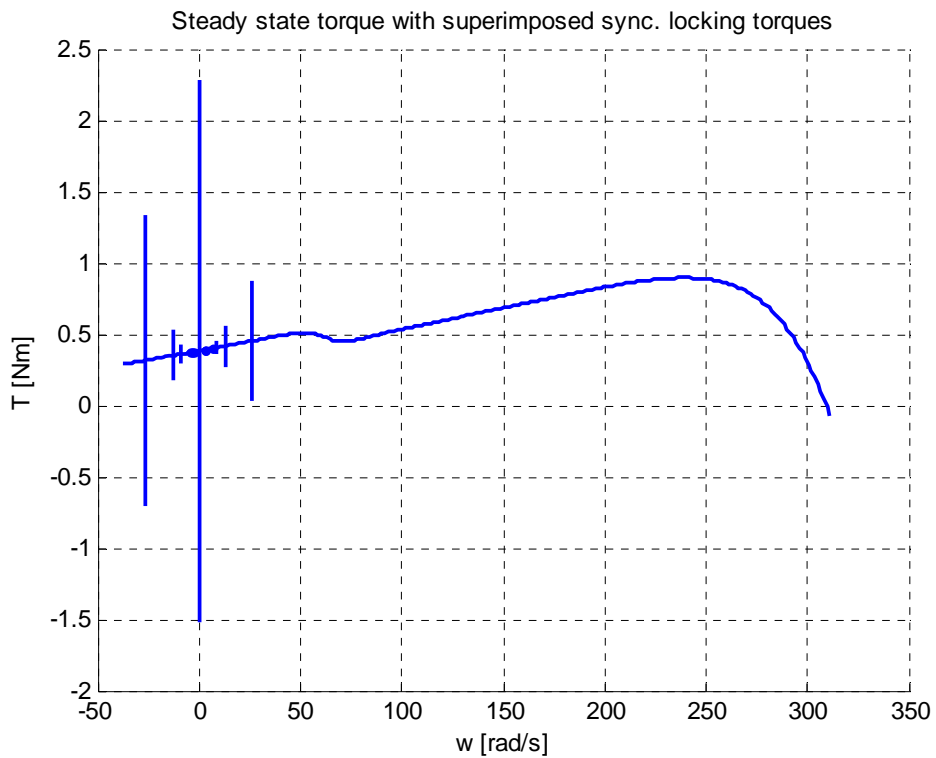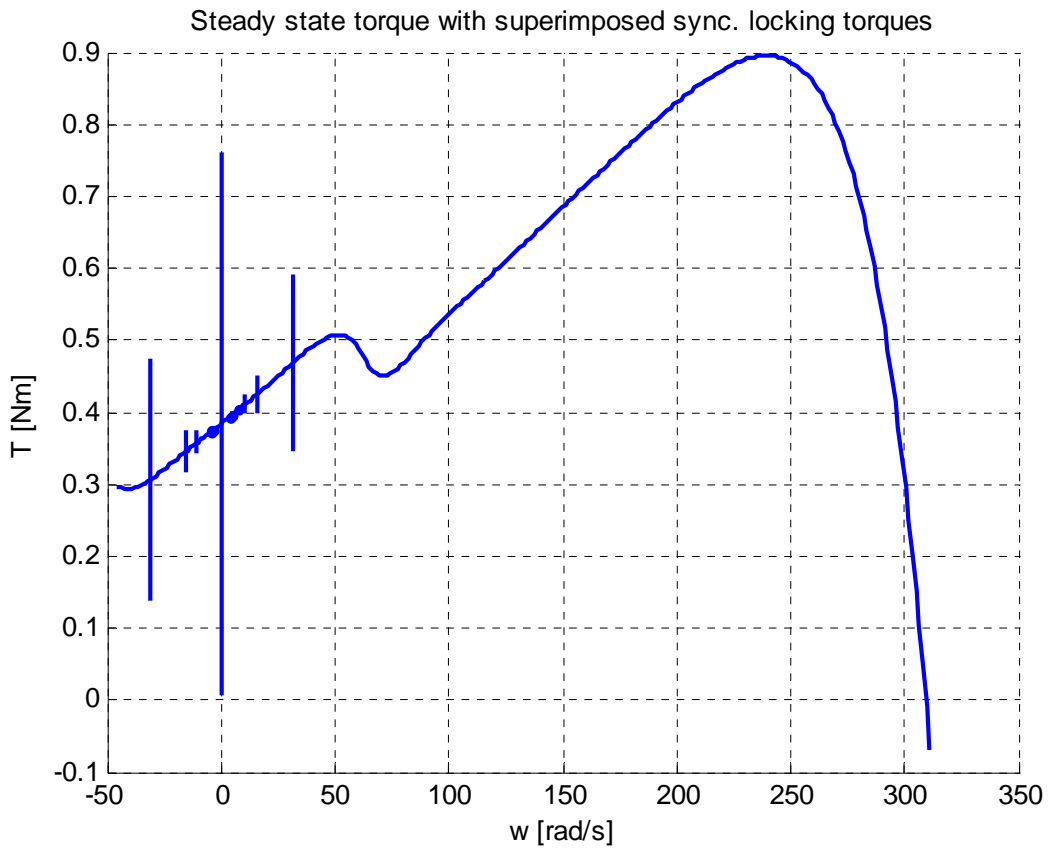
*Fig. 5.13 Torque-speed curves of motor with $N_r$ =20 and 24 slots respectively – modified 220 V machine*

## 5. Synchronous locking torques

In general, the number of stator slots is nearly always limited to a certain range of numbers. For motors in the hundred W to few kW range, the most common stator slot number is 24 or 36, being even numbers which are multiples of 3 and thus suited for both single-phase and 3-phase windings. The number of rotor bars, however, does not have the same restrictions, at least for squirrel-cage rotors, where the rotor circuit is one short-circuited winding. But specifically regarding synchronous locking torques, care must be taken in the choice of number of rotor bars. By considering the results displayed in Figs 5.8 to 5.13, it is possible to draw some preliminary conclusions from the modelling of synchronous locking torques performed in the foregoing:

*1. Winding harmonics increase the magnitude of synchronous locking torque*

This is seen by comparing the graphs of examples 1 and 3. With the same mechanical properties, the increased winding harmonics of the motor in example 3 causes the magnitude of the synchronous locking torque at all speeds and slot combinations to increase

*2. Larger air-gap decrease the magnitude of synchronous locking torque*

By comparing the graphs of examples 2 and 3, it is seen that where example 2 exhibits a larger degree of winding harmonic, the greater mechanical air-gap of example 2 causes the synchronous locking torques to be relatively lower than for the motor in example 3.

*3. Certain slot combinations result in high magnitudes of synchronous locking torque*

While the number of rotor slots resulting in the smallest values of synchronous locking torque varies, it is seen that combinations having $N_r = N_s$ or $N_s/2$ result in large values of locking in all cases. Even $N_r = 3N_s/2$ (in this case 36) results in slightly increased levels when compared to adjacent numbers.

*4. Optimal slot combination varies*

There appears to be a general tendency for the magnitude of the synchronous locking torque to decrease with increasing slot number, owing to the nature of decreasing harmonic field magnitudes as the harmonic order increases. Also, as pointed out in section 3.5, the harmonic content of rotor MMF will decrease with increasing number of bars.

However, for practical reasons, it is often desirable to have a relatively low number of rotor slots, since this enables a better casting and hence a better conductivity of the rotor. Moreover, fewer rotor slots allows a more simple stamping tool with a longer life time because of less severe demands to corner radii.

Thus, from an academic point of view, it would be desirable to have many rotor bars, whereas from a practical point of view, the rotor bars should be few.

If a low number of rotor slots are desirable, the optimal number may be unique for the individual stator with its individual MMF spectrum. In the examples, where a 24 slot stator is considered, a rotor slot number of 18 or 20 appear to be the optimal.

These conclusions are thought to be in good agreement with existing literature on the topic, although the literature mostly covers 3-phase machines. However, as to the most suitable choice of rotor slots when having a 24 slot stator, some divergence exists in the literature. For instance, [17] finds an 18 slot rotor to be "very suitable for operation", whereas in [28] it is not included in the table of suitable combinations. Moreover, it is exactly the other way around for a 16 slot rotor. Reference [28] also stresses the divergence between the work of various authors and preferences of different manufacturers.

## *5.4. Influence of eccentricity*

So far, the source of synchronous locking torques has been considered as being due to permeance harmonics, creating harmonic flux densities in the air-gap which produce torque when reacting with rotor MMFs of the same pole-pair number. In this section, it is described how air-gap eccentricity and non-alignment contribute to the creation of synchronous locking torques.

Fig. 5.14 shows 4 different cases of air-gap imperfection. The upper left diagram shows rotor eccentricity where the geometrical centre of the rotor is shifted by $x_r$ with respect to the axis of rotation.

The upper right diagram shows the case were the centre of the stator does not correspond to the axis of rotation. The lower left diagram illustrates an example where the rotor axial symmetry line is angled with respect to the axis of rotation, and finally, the lower right diagram is the case were the stator symmetry line is angled with respect to the axis of rotation.

As illustrated in the figure, the case of rotor non-alignment is similar to one of rotor eccentricity, and stator non-alignment corresponds to stator eccentricity. Hence, when attempting to describe the cases mathematically, it is sufficient to investigate the two situations of rotor and stator eccentricity.
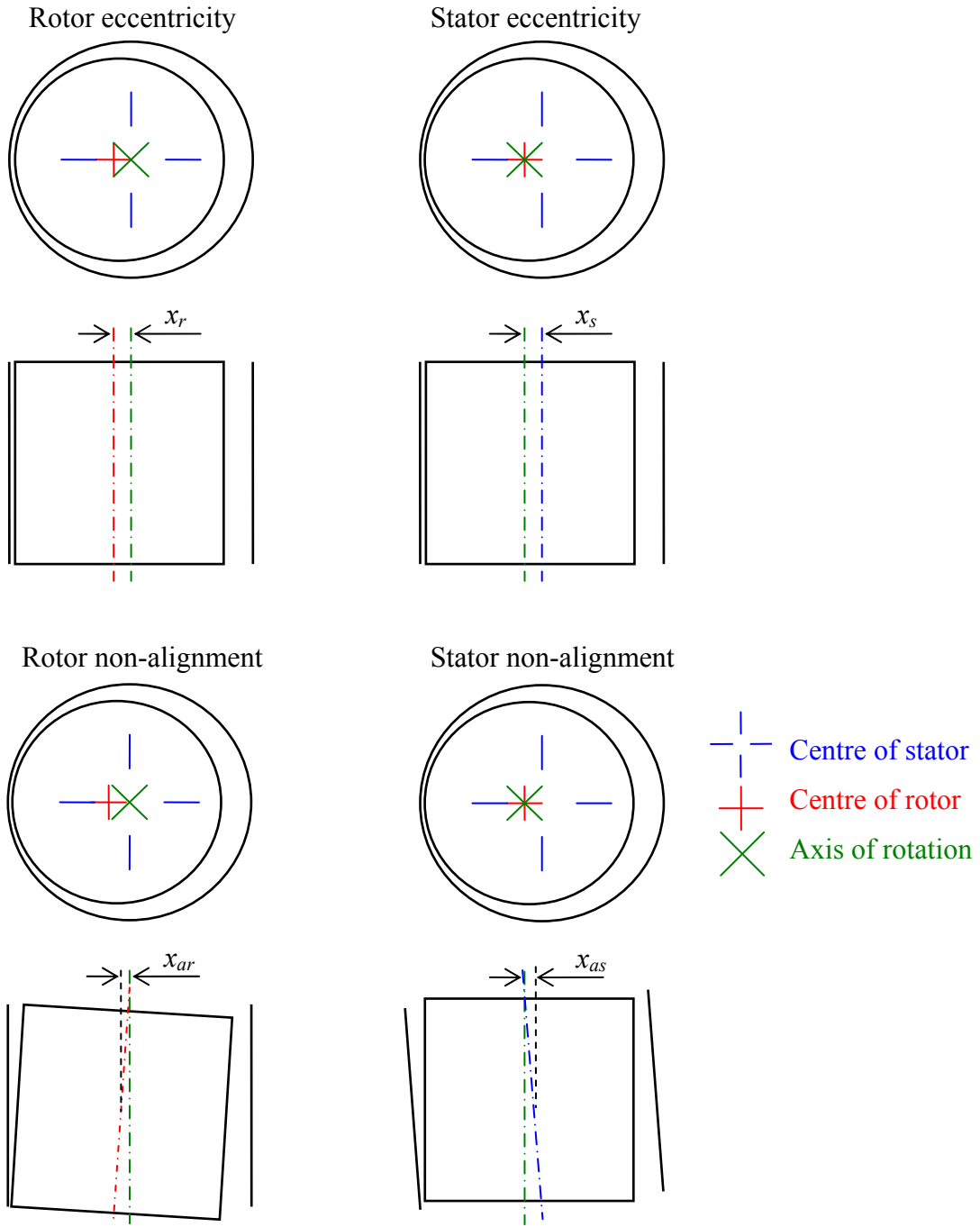
*Fig. 5.14 Cases of eccentricity*

Considering rotor eccentricity, the air-gap length $l_g$ at a given angle $\theta$ with rotor offset $x_r$ can be approximated by

$$l_g(\theta) = l_{g,nom} + x_r \sin(\theta - \omega_r t) \tag{5.36}$$

where $l_{g,nom}$ is the nominal, or average, air-gap length. For the case of stator eccentricity $x_s$, the air-gap length is independent of rotor speed, i.e.:

$$l_g(\theta) = l_{g,nom} + x_s \sin(\theta) \tag{5.37}$$

## 5. Synchronous locking torques

In both cases, the air-gap variation results in a corresponding permeance variation as shown in Fig. 5.15 for an air-gap of 0.37 mm nominal value, assuming 0.1 mm stator eccentricity.
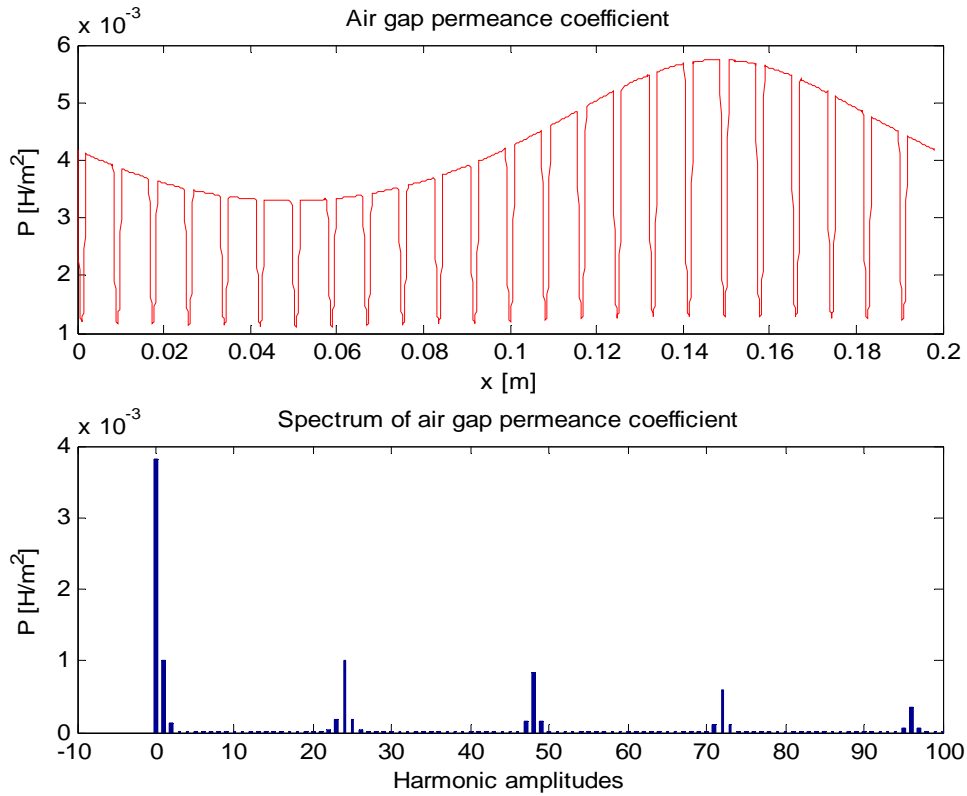


*Fig. 5.15 Air gap permeance with eccentricity*

The eccentricity is seen to "contaminate" the permeance coefficient spectrum with a fundamental value of similar magnitude to the first slot harmonic. In addition, a second harmonic permeance term is generated, although with smaller amplitude. By referring to the expressions relating to air-gap permeance variation caused by slotting, (5.36) and (5.37) are similar to rotor and stator slot permeance harmonics, respectively, although with fundamental harmonic; whereas the slot harmonics are of order $nN_r$ and $mN_s$ respectively.

However, as a source of synchronous locking torque, it is important to remember that an air-gap permeance term of uneven harmonic order would interact with harmonic MMFs of uneven order and thus create air-gap flux densities of even order. Ideally, for a two-pole motor there are no rotor current distributions of even order, and so no synchronous locking torque is created. The second order eccentricity harmonic, on the other hand, will be a source of synchronous locking torques in a similar manner to the slot harmonics.

Although the influence of eccentricity is similar to those of slot permeance harmonics, eccentricity has not been included in the model. A detailed calculation of the influence of eccentricity is not the main scope of this work; however it has been shown that eccentricity may impact the values of synchronous locking torque and can be the focus of future work.

# Chapter 6

# Evaluation of the model

In the previous sections, a model describing and predicting the synchronous locking torques was developed. In this section, a comparison of the predicted results is made with finite element analysis calculations and measurements on actual motors.

## *6.1 Calibration of steady-state model*

Since the magnitudes of the synchronous locking torques are determined from the equivalent circuit parameters, in this section a calibration of these parameters is carried out using actual motor measurements. The motor under consideration is an RSCR motor for 230V, 50Hz use. Figs 6.1 to 6.3 show comparisons between the modelled and measured run torque, line current and efficiency, respectively. These were performed at 198 V line voltage, with a line impedance of −0 V/A.

**Torque vs speed**
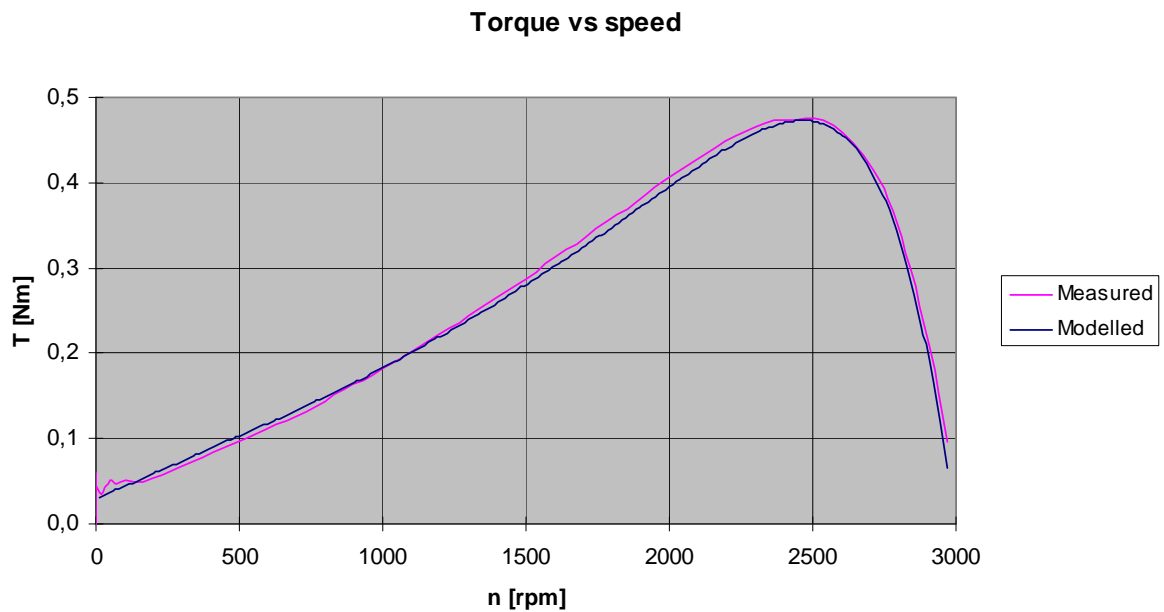


Fig. 6.1 Torque-speed curve at 198 V for the 230 V motor

**Line current vs torque**
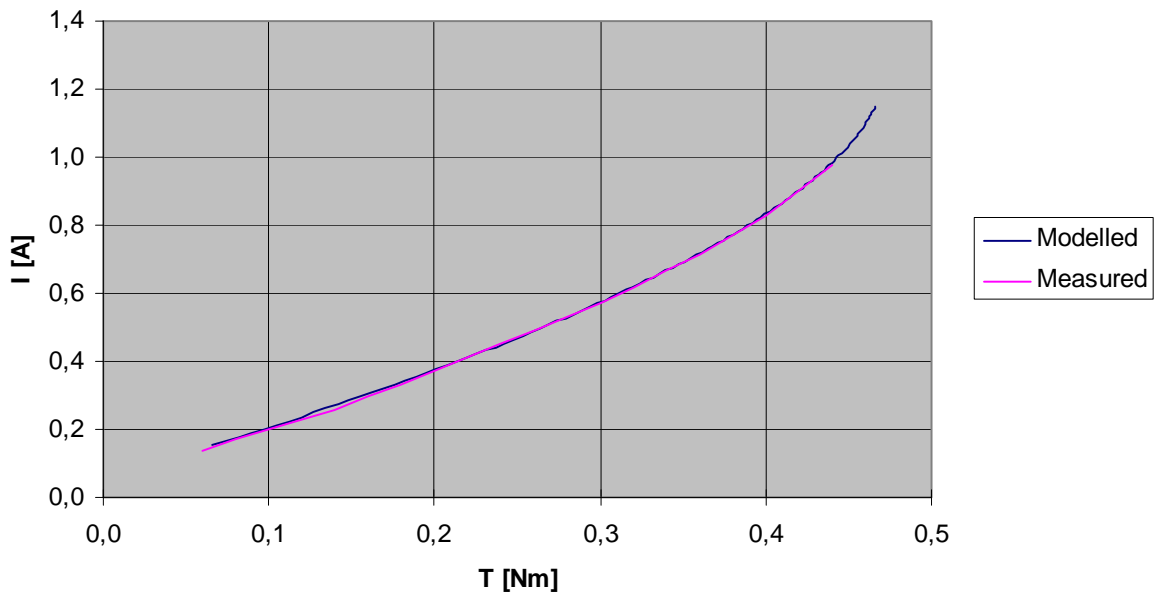


*Fig. 6.2 Current-torque curves for 230 V motor*

**Efficiency vs torque**
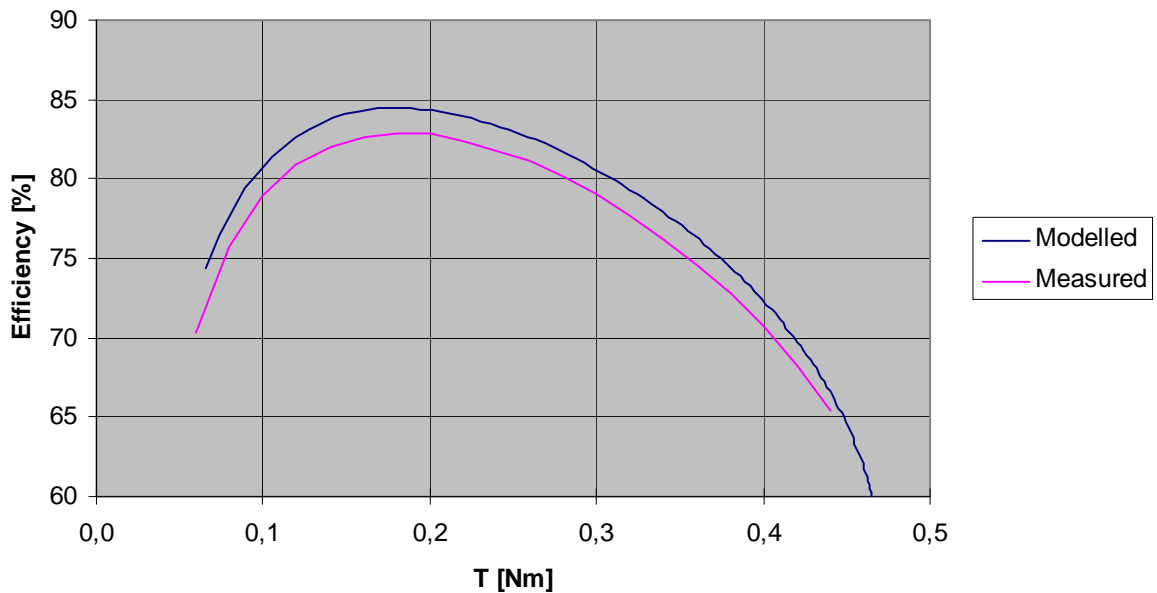


*Fig. 6.3 Efficiency-torque curves for 230 V motor*

The curves show reasonable agreement. The deviation between measured and calculated efficiency as appearing in fig. 6.3, may owe to the fact that the rotor temperature rises during the test, which is not taken into account in the model, where the temperatures are fixed. Thus

the model may have under predicted the rotor resistance simply by assuming a lower temperature than was the case. The deviation in efficiency only corresponds to app. 2-3W.

## 6.2 Modelling of synchronous locking torque

Having established a degree of confidence in the calculated parameters of the equivalent circuit, the model is used to find the speed and magnitude of the synchronous locking torques for this particular machine as a function of the number of rotor slots (assuming that the rotors are unskewed) with the same fundamental MMF rotor resistance, i.e., the same amount of aluminium and the same total slot area.

The motor is modelled in start mode, i.e., with a 25 Ω PTC resistor in parallel with the run capacitor. The location (speed) and magnitude of locking torque is shown as a 3D plot as well as projected curves in Fig 6.4.
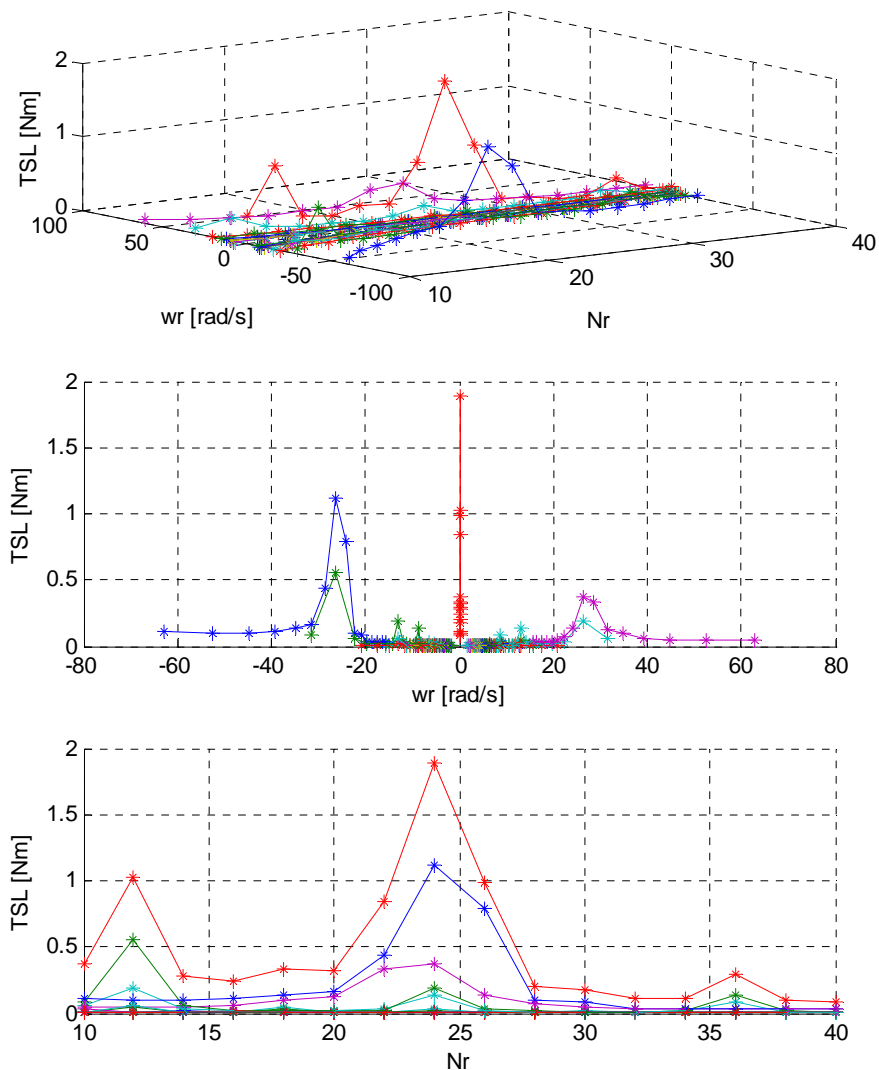


*Fig. 6.4 Synchronous locking torque characteristics for 230 V motor with varying rotor slot number ($N_r$)*

# 6. Evaluation of the model

Each line colour represents the same speed component of locking torque for each rotor slot number. For example, the red one represents torque that occurs at a rotor speed of zero.

From these results, two combinations are considered interesting:

- 24 rotor slots (i.e. the same number as stator slots) which results in severe locking, particularly at standstill and at negative speed (approximately –27rad/s)
- 18 slots, which results in a low magnitude of standstill locking when the number of rotor slots is smaller than the number of stator slots

The corresponding steady-state speed and torque are shown in Figs. 6.5 and 6.6, with their respective components of synchronous locking torque superimposed.
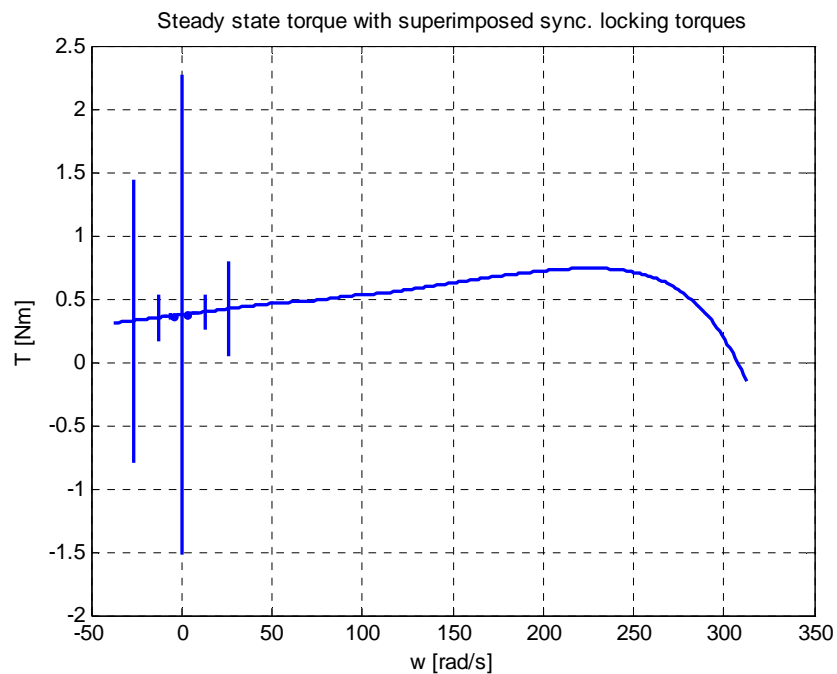


*Fig. 6.5 Steady-state torque-speed curve with synchronous locking torques superimposed for 230 V motor and 24 rotor slots*

*Fig. 6.6 Steady-state torque-speed curve with synchronous locking torques superimposed for 230 V motor and 18 rotor slots*

The nature of synchronous torques is such that they only occur at a certain speed as a constant value. At all other speeds, they will oscillate with a mean value of zero. The synchronous torque oscillation frequency reduces as the rotor speed closes in on the synchronous torque speed.

## 6.3 Start-up transients using Finite Element Analysis

The resulting torque vs. speed curves shown in Figs. 6.5 and 6.6 suggest that the starting performance may be impaired by the large locking torques at zero speed, particularly in the case of the 24 slot rotor in Fig. 6.5. These tendencies can be verified using two dimensional finite element analysis - the axial dimension can be ignored since the rotors are not skewed. The geometries for the models are shown in Figs. 6.7 and 6.8 for the 24 and 18 slot rotor arrangements.
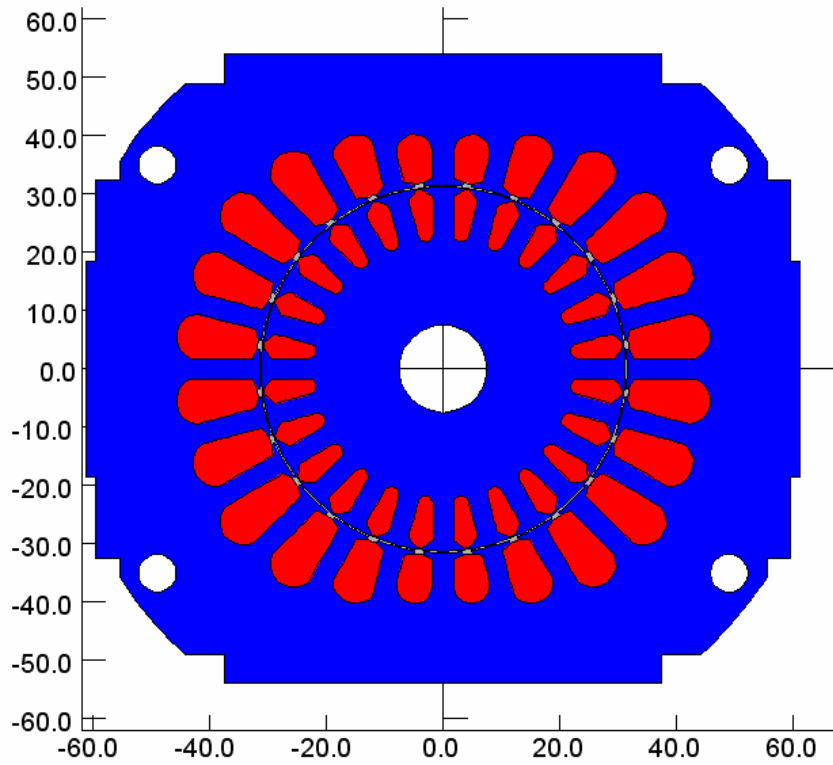
*Fig. 6.7 Finite element model geometry for 24 rotor bar model*
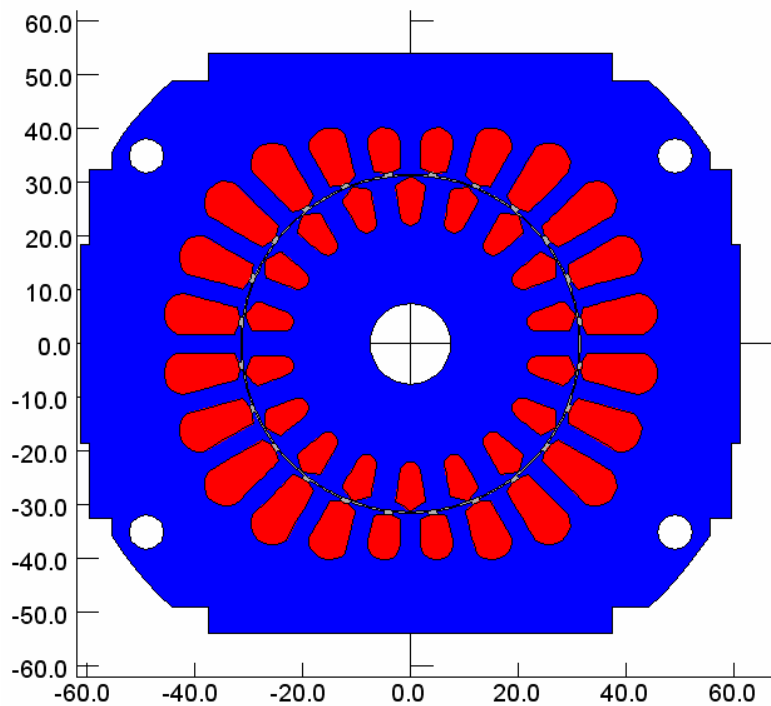


*Fig. 6.8 Finite element model geometry for18 rotor bar model*

The rotor slots are designed in such a way as to maintain constant total rotor slot area, i.e., constant rotor resistance. With the same stator, the motor should have same steady-state performance.

# 6. Evaluation of the model

A transient time-stepped finite element analysis was performed in each case, letting the motor accelerate from standstill using a 25 Ω resistor as the auxiliary impedance. In the calculation, the motor was loaded by a constant shaft torque of 0.2 Nm. Figs. 6.9 and 6.10 show the calculated values of the current (green = total, blue = main, red = auxiliary), torque, rotor angle for both rotor slot combinations. While the 24 slot rotor exhibits large torque pulsations and a reluctance to accelerate, the 18 slot rotor accelerates to an average speed of approximately 300 rad/s within 0.07 seconds.
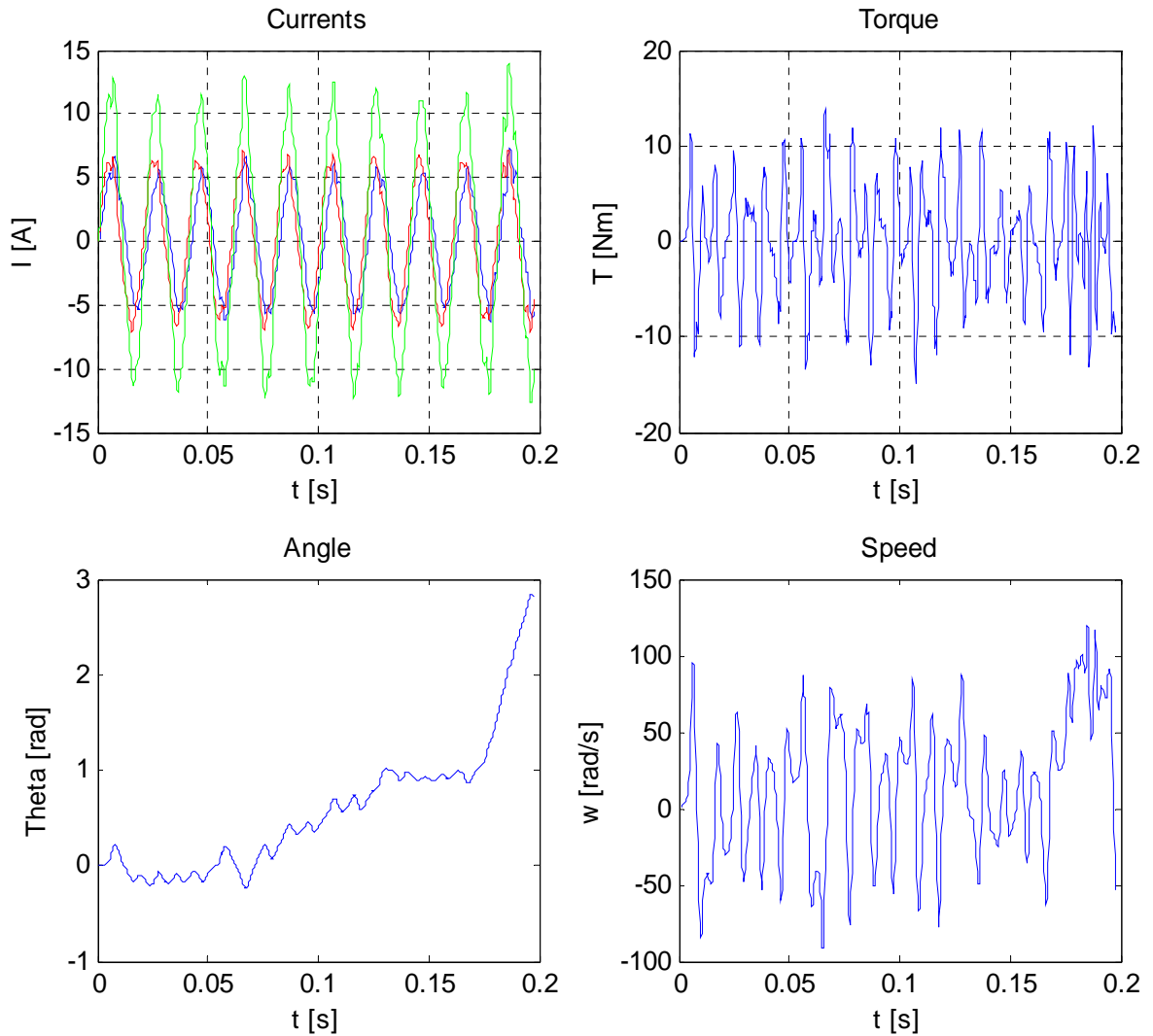


*Fig. 6.9 Performance produced from transient finite element analysis with 24 bar rotor*
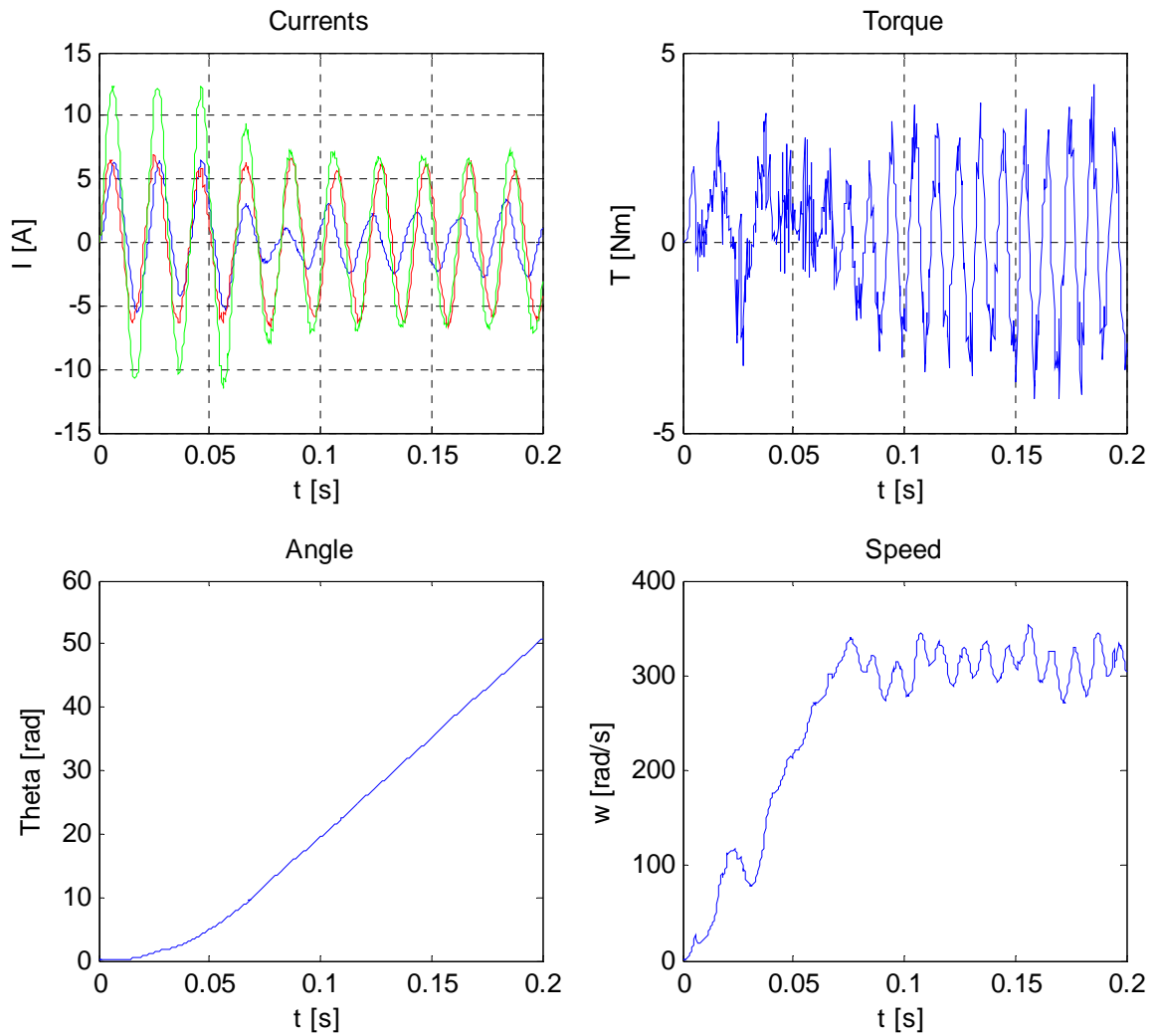
*Fig. 6.10 Performance produced from transient finite element analysis with 18 bar rotor*

As a further comparison, the results from simulations of a 22 slot rotor in combination with a 24 slot stator (As illustrated in Fig. 6.11) are shown in Fig. 12. This machine exhibits large values of synchronous locking torques, although not as severe as for the 24 slot rotor. The analysis results in Fig. 6.4 suggest that the locking torques for a 22 slot rotor should be somewhere in between those for an 18 and a 24 slot rotor, which was also found to be the case in the finite element analysis in Fig. 6.11.

From Fig. 6.12 it is appears, that the 22 rotor slot motor accelerates to near-synchronous speed (316 rad/sec) within 0.17 seconds which is considerably slower and less smooth than for the 18 slot rotor counterpart.
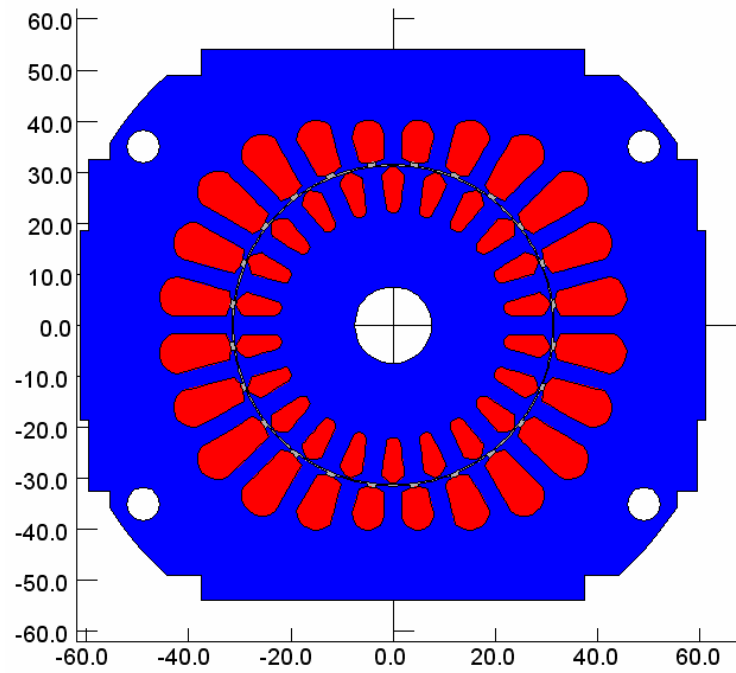
*Fig. 6.11 Finite element model geometry for 22 rotor bar model*
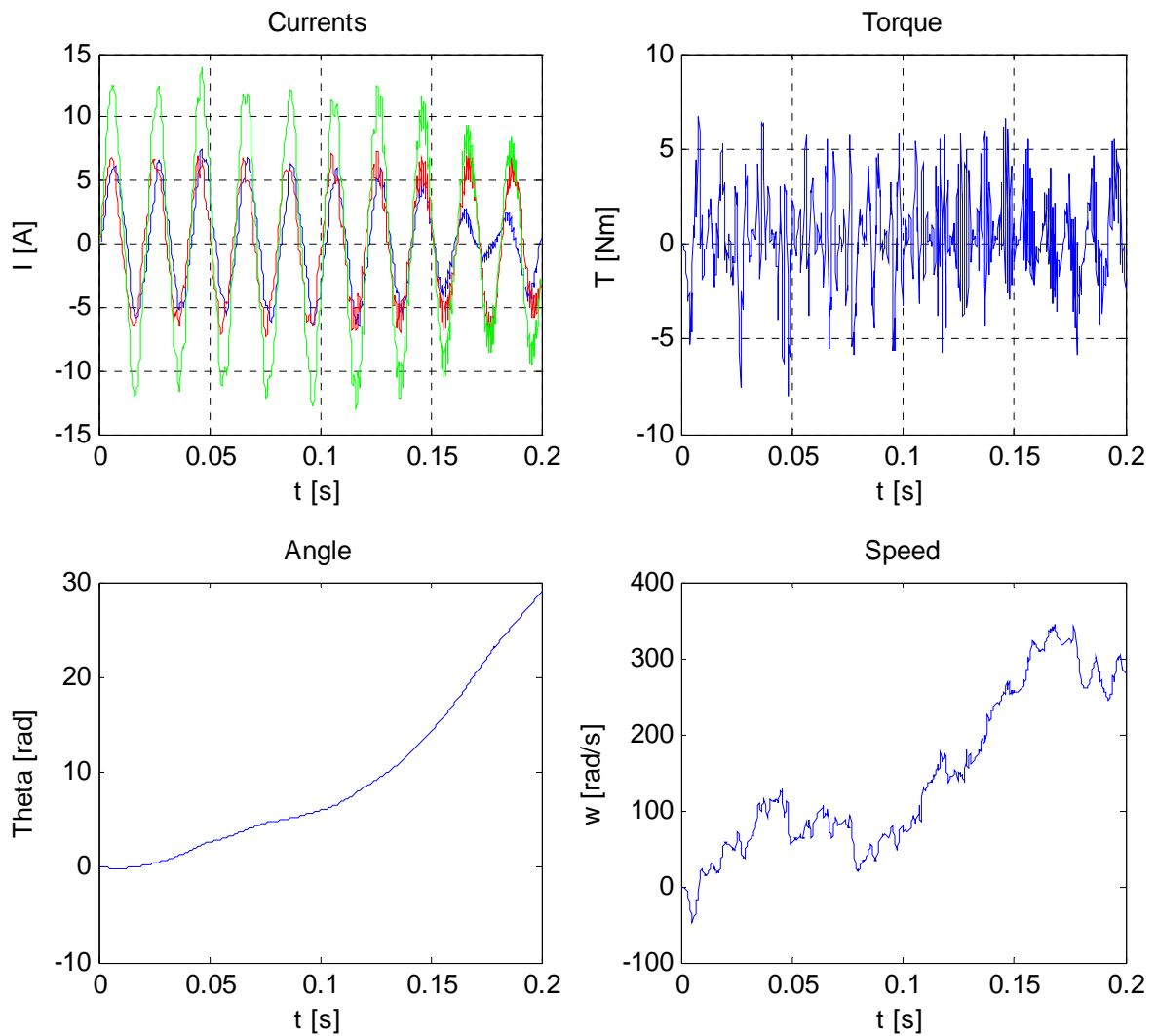


*Fig. 6.12 Performance produced from transient finite element analysis with 22 bar rotor*

The finite element analysis results appear to be in good agreement with the results obtained from the analytical method developed and described previously. However, they do not give any quantitative results for the various synchronous locking torques as they appear at different speeds. They could be extracted by a procedure described in [31]. Instead, in the following section, experimental verification is used to validate the results.

## 6.4 Verification by measurements

In order to verify the simulated results obtained in Figs. 6.5 and 6.6, the two rotors were manufactured and tested and compared with a 28 slot reference rotor, which was skewed. A detailed description of the tests carried out can be found in Appendix 2. The rotor laminations for the two rotors experimental rotors were laser cut from plate steel and the rotors fabricated.
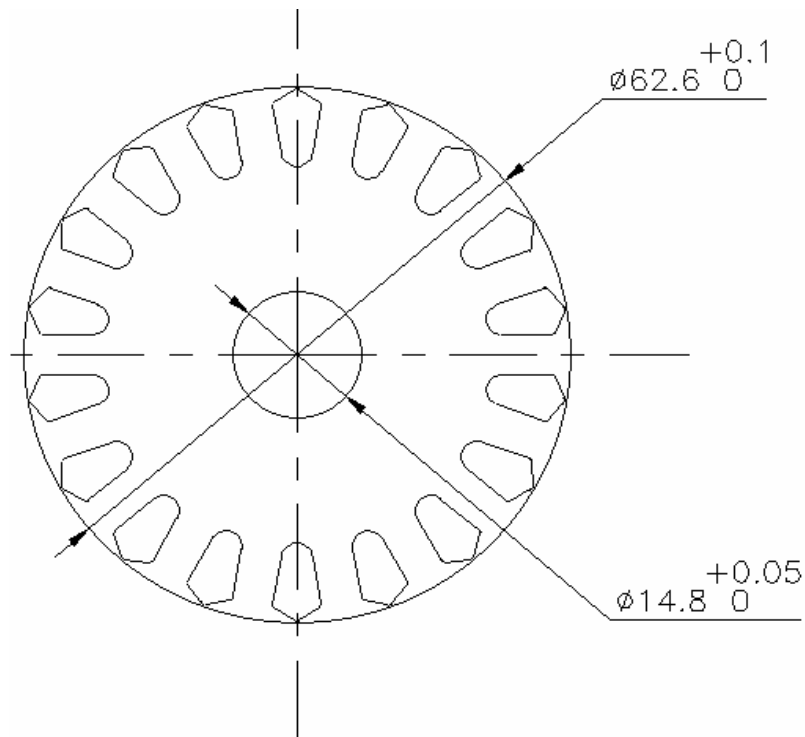


*Fig. 6.13 Geometry of 18 bar rotor*
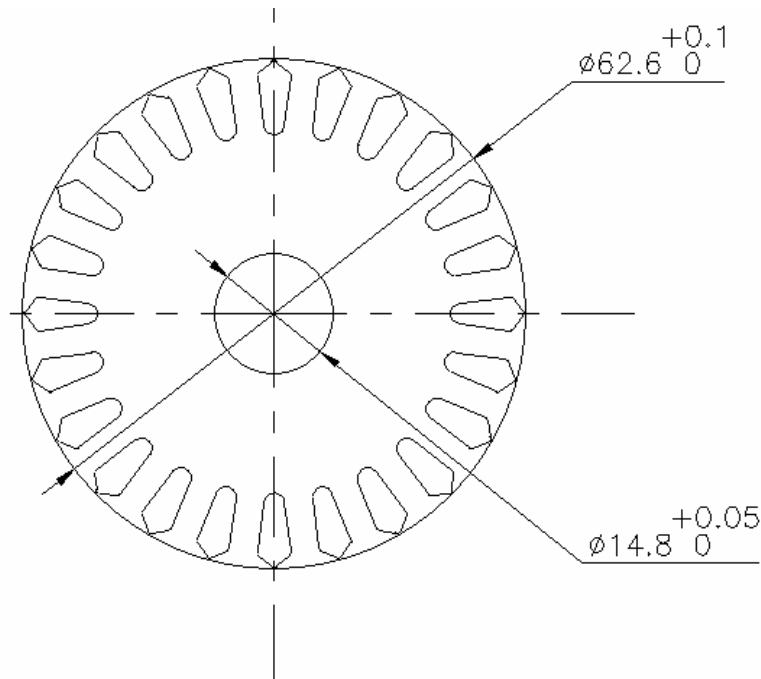
*Fig. 6.14 Geometry of 24 bar rotor*

It is described in Appendix 2 how both steady-state torque-speed and efficiency curves, as well as the magnitudes of synchronous locking torques, were obtained. The resulting steady-state torque and efficiency were obtained during run mode operation (i.e., with a 3.5 μF capacitor in series with the auxiliary) and are shown in Fig. 6.15 and 6.16. The reason for using run mode rather than start mode (as in the simulations) was to assess the steady-state operation of the machines. The rotors have identical total bar cross section and contain the same amount of aluminium. However, the reference rotor is skewed, whereas the test rotors are not.

To compare the results, Fig. 6.15 shows that the unskewed rotors result in a slightly increased maximum torque, regardless of bar number, when comparing to the reference rotors. Fig. 6.16 shows comparable efficiency of the three rotor types; however, the skewed rotor appears result in slightly increased efficiency.
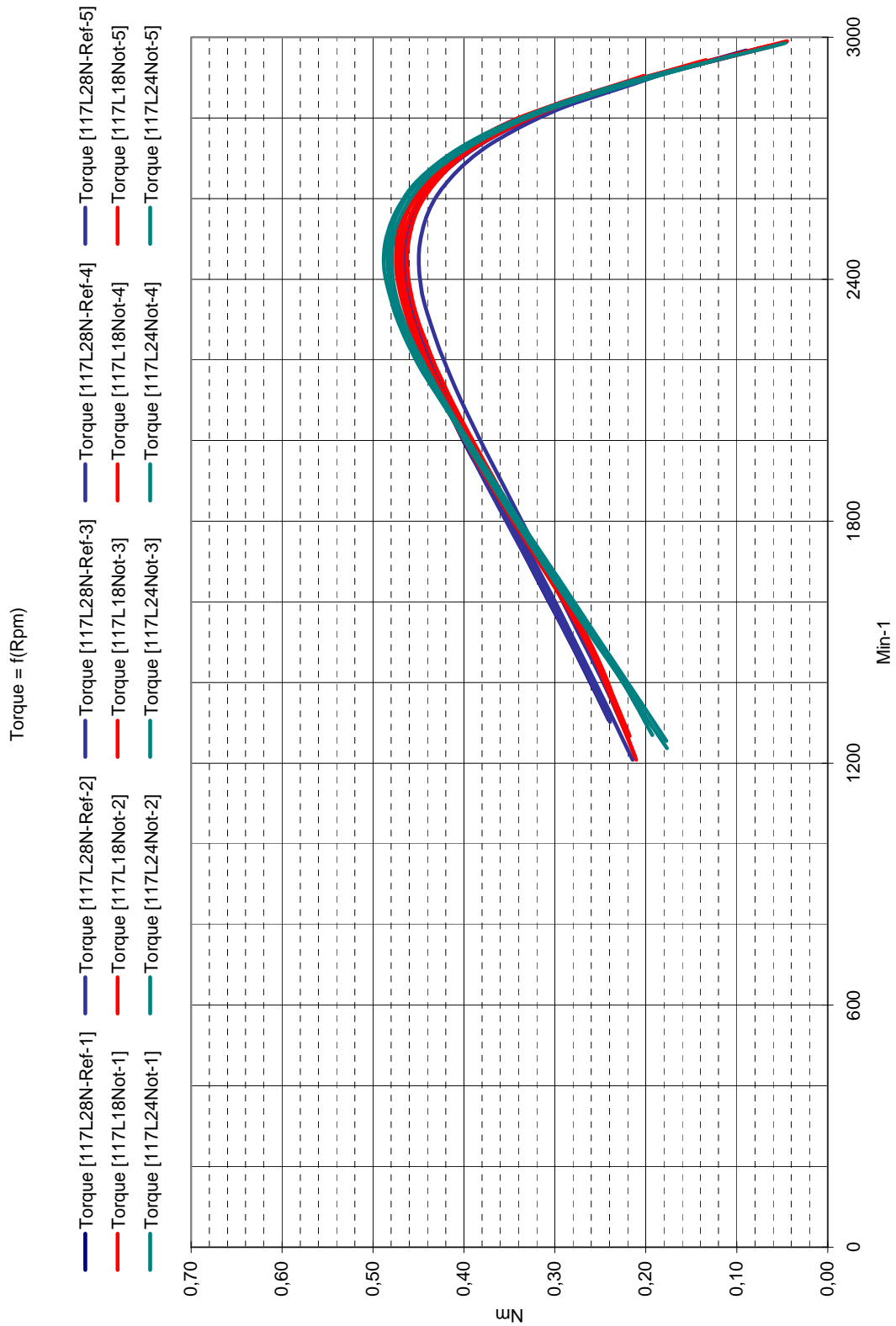
*Fig. 6.15 Comparisons of measured torque for 28, 24 and 18 rotor bar machines*

*(5 examples for each)*
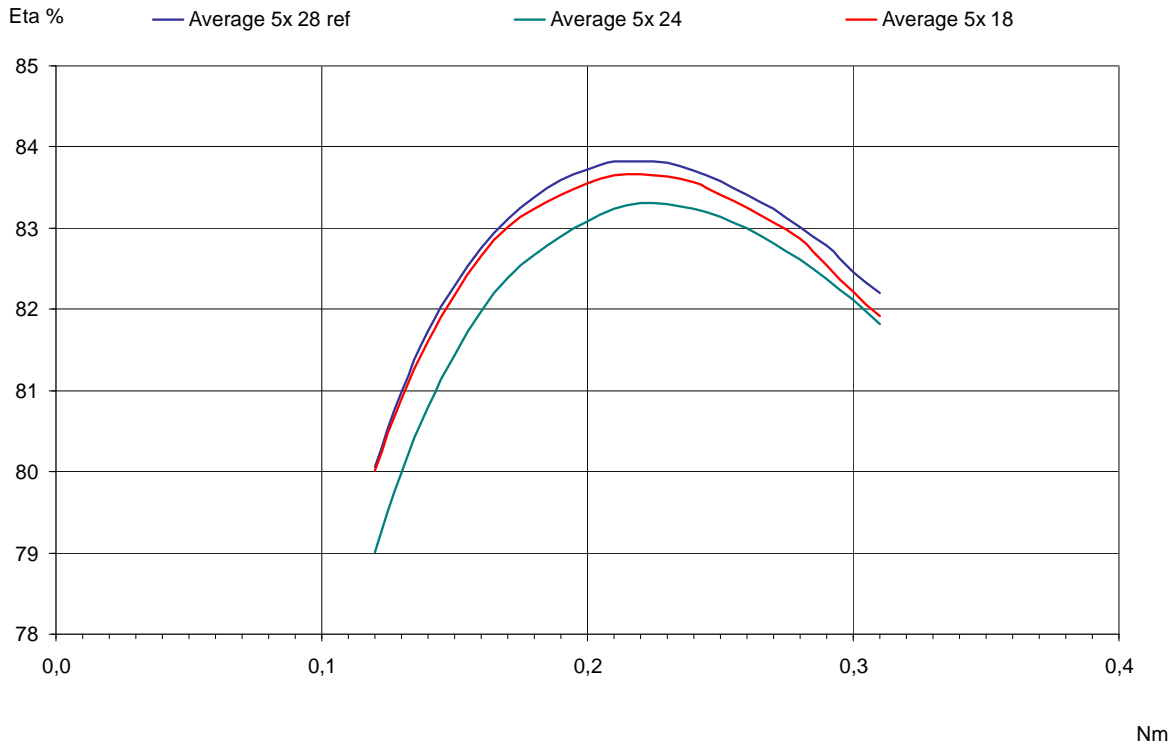
*Fig. 6.16 Comparisons of measured efficiency for 28, 24 and 18 rotor bar machines during run mode*

To obtain further experimental results in start mode a set of deceleration tests were carried out. These allowed comparison to the analytical and finite element analyses simulations which were put forward earlier. Appendix 2 describes how the deceleration tests were performed in order to investigate the locking torques at low speed with the motors in start mode, i.e., with a 25 Ω resistor in series with the auxiliary winding. Figs. 6.17 and 6.18 show the deceleration curves for the 18 slot rotor, 24 slot rotor and 28 slot rotor (skewed reference), respectively. The yellow boxes illustrate where a locking tendency occurs and the x-axis is in rpm.

For the 18 slot rotor, a locking tendency is seen at around 335 rpm, whereas for the 24 slot rotor it occurs at around 240 rpm. Even the 28 slot skewed rotor has a locking torque characteristic (although it is quite small) at 220 rpm.
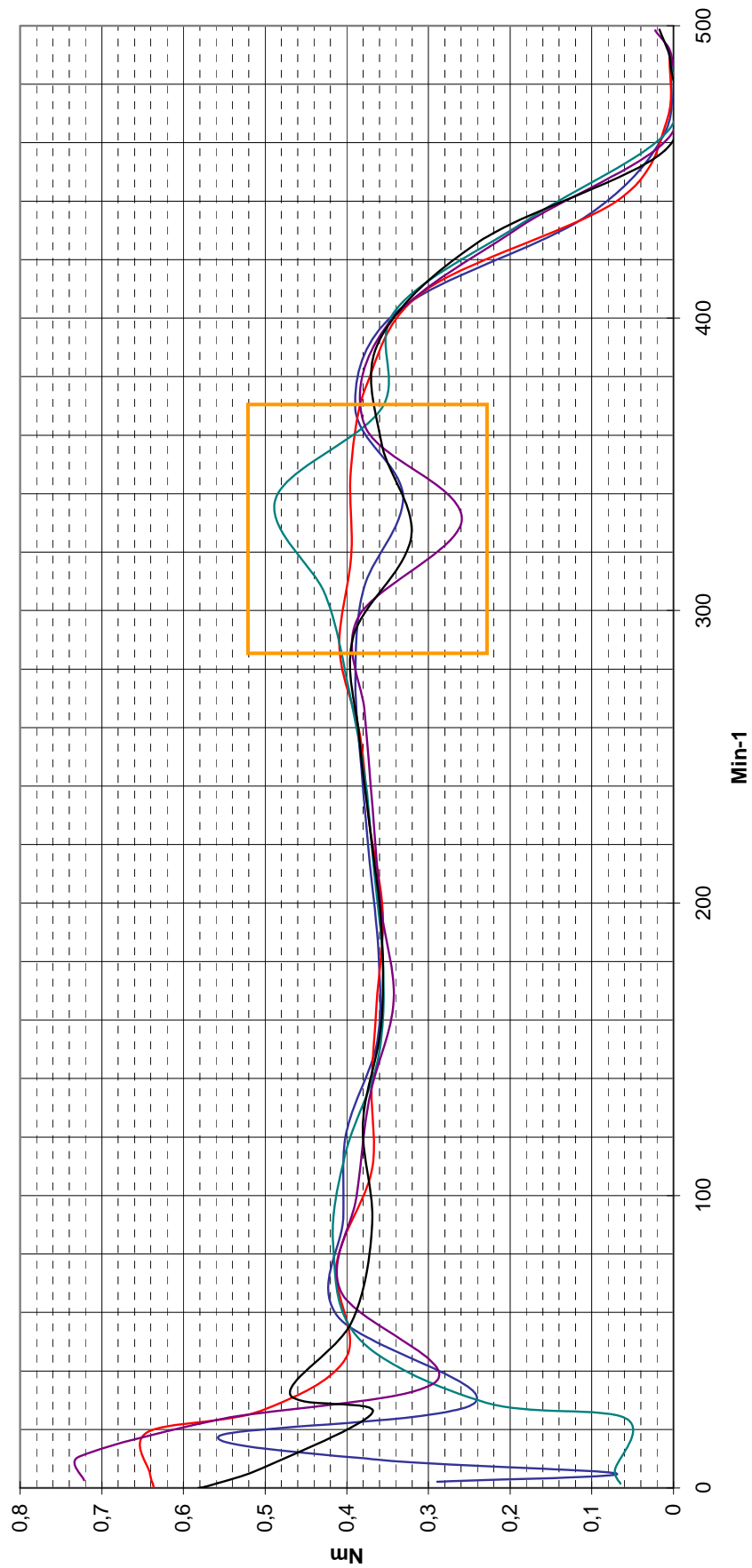
*Fig. 6.17 Deceleration curve (torque-speed) for 18 rotor bar rotor machine*

*Fig. 6.18 Deceleration curve for 24 rotor bar rotor machine*

*Fig. 6.19 Deceleration curve for 28 rotor bar rotor machine*

## 6. Evaluation of the model

Appendix 2 also describes how the peak-to-peak values of the synchronous locking torques at standstill can be found from the band width of the scatter plots of the torque values, obtained at slow speed. These scatter plots are shown in Figs. 6.20 to 6.22 for the 18 slot rotor, 24 slot rotor and 28 slot rotor (skewed) , respectively.

It is possible to compare the modelled and measured values of synchronous locking torque directly. This is done by obtaining the peak to peak values from Figs. 6.5 and 6.6 and comparing them with the ones shown in Figs. 6.17 and 6.18 for the low-speed locking torque, and with Figs. 6.20 and 6.21 for the standstill locking torque.

**18 slots**
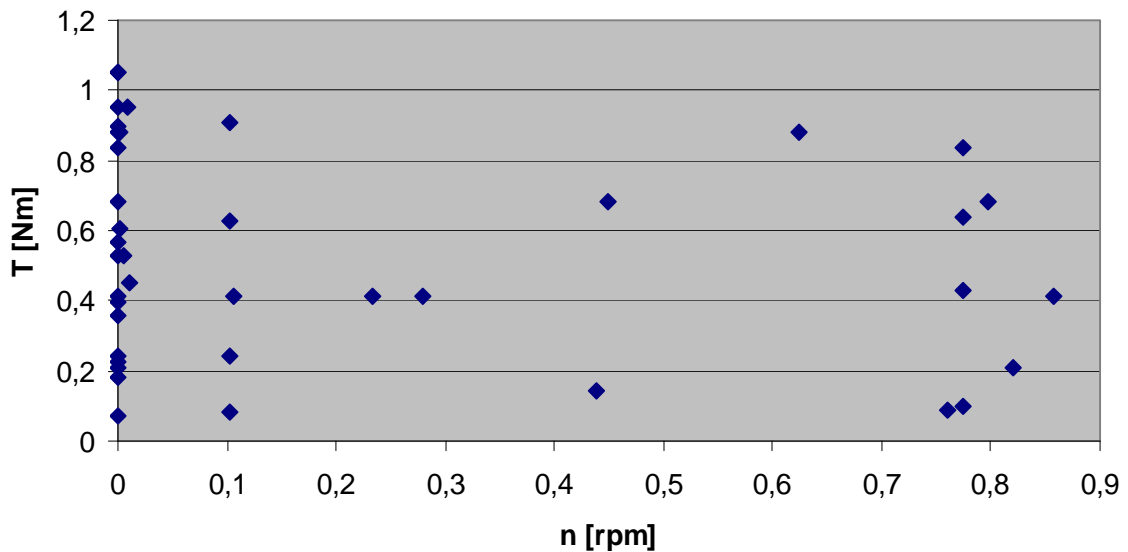


*Fig. 6.20 Synchronous torques for 18 bar rotor machine*

**24 slots**
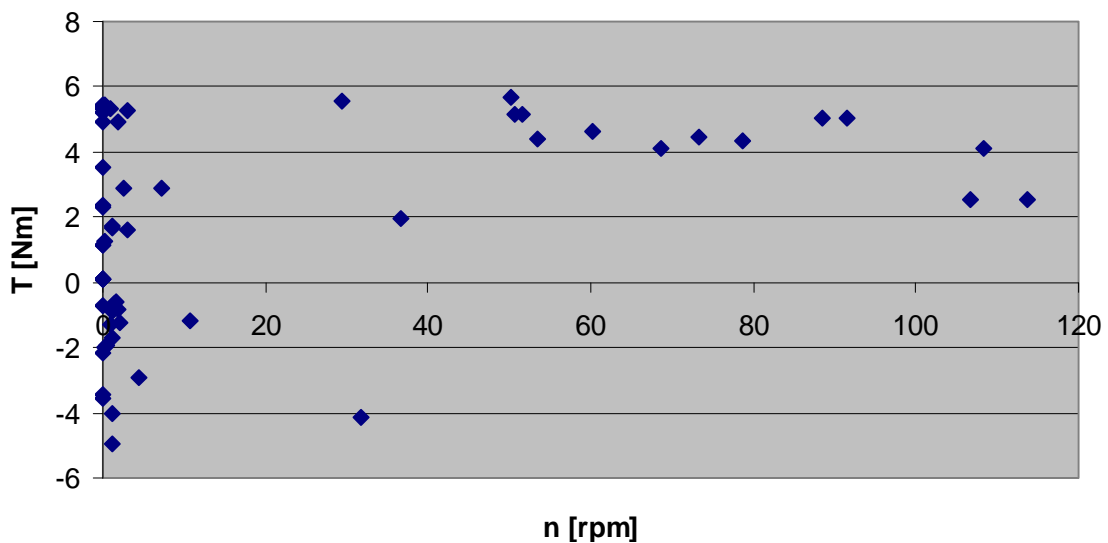


*Fig. 6.21 Synchronous torques for 24 bar rotor machine*

**28 slots skewed (ref)**



*Fig. 6.22 Synchronous torques for 28 bar rotor machine*

Fig. 6.23 shows the modelled and measured peak-to peak values of the synchronous locking vs. the speed at which they occur. Note that the steady-state motor torque has been removed to more clearly illustrate the location of the synchronous locking torques. The 28 slot skewed rotor is not included in the comparison, since it has not been calculated.
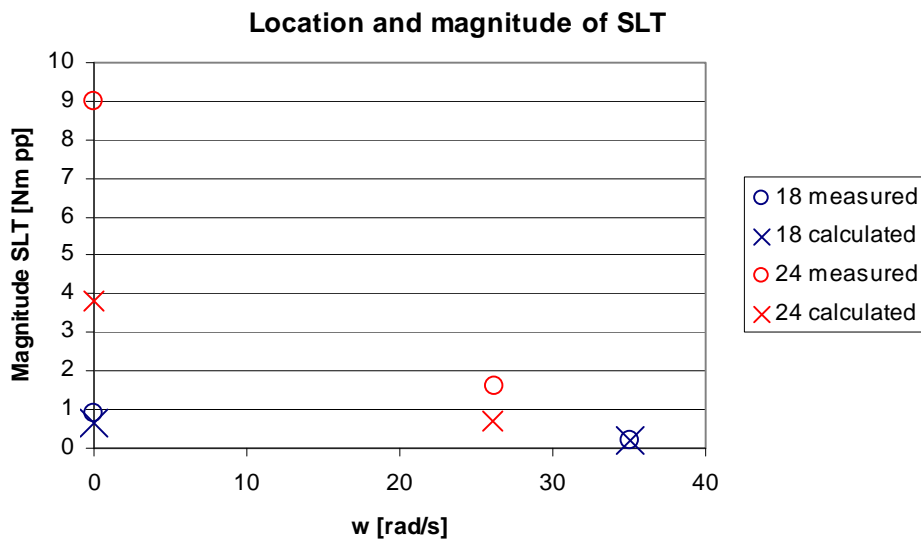


*Fig. 6.23 Synchronous locking torque comparison for 18 and 24 bar rotor machines*

While the speeds of the synchronous locking torque appear to have been correctly modelled for both rotors, the magnitudes of the torques are generally under predicted, particularly for the 24 slot rotor. Fig. 6.24 shows a plot of the deviations between modelled and measured values of synchronous locking torque. However, from the tests described here and also in

Appendix 2, it can be concluded that measuring synchronous torque is not straightforward so that precise measurements are difficult to obtain.

**Deviation, modelled to measured magnitude of SLT at different speeds**
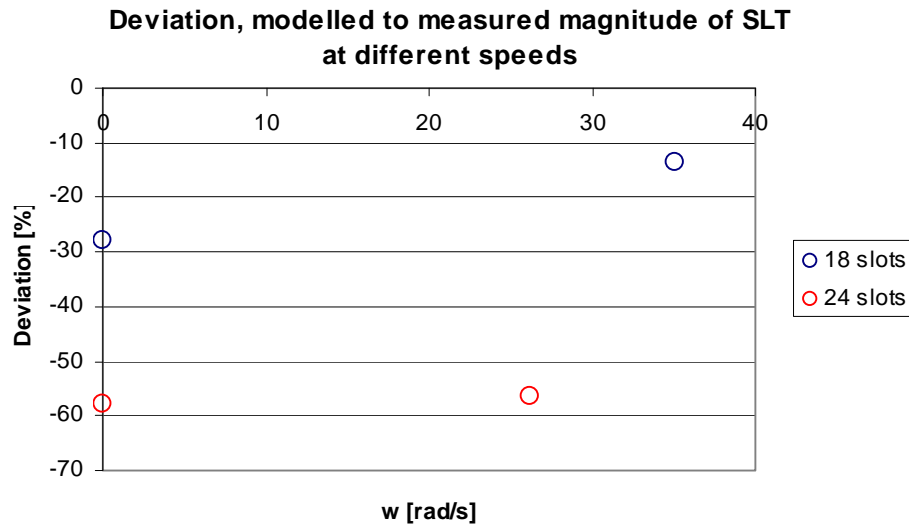


*Fig. 6.24 Synchronous locking torque deviation comparison for 18 and 24 bar rotor machines*

## 6.5 Discussion of results

The model appears to correctly identify the speed at which synchronous locking torques occur. The calculated magnitudes of the synchronous locking torque are generally under predicted, which is, however, expected to a certain degree, since air-gap imperfections in form of eccentricity and non-alignment are not considered in the model. Given the construction of the motor fixture, which facilitates a single-sided bearing of the rotor, a certain degree of eccentricity will certainly have been present during tests. Radial forces acting on the rotor during test will tend to amplify this eccentricity, further increasing this source of error. Altogether, accurate measurement of the synchronous locking torques is not straightforward. Hence, it is reasonable to suggest that in addition to the under-prediction of the synchronous locking torques, the motor fixture and measuring techniques may lead to higher measured values. The differences between modelled and measured results displayed in Fig. 6.24 are therefore high, particularly for the 24 bar rotor at zero speed. This is, however, the situation where the largest value of synchronous locking torque occurs, and it would be safe to suggest that any measurement imperfections are also mostly pronounced here, leading to large deviations between calculated and measured values as clearly illustrated in fig. 6.24.

 Chapter 8 suggests how the model can be improved further to account for additional sources of synchronous locking torques.

# Chapter 7

# Summary of modelling and results

This chapter serves as a brief overview of the modelling and results obtained in the previous chapters. For detailed description of how the modelling was derived, reference should be made to the relevant sections.

## 7.1 Asynchronous torques from winding harmonics

If the winding distribution of a machine is not sinusoidal then stator MMF harmonics are produced. These harmonics lead to harmonic air-gap flux waves which link the rotor cage, inducing EMFs and generating further rotor harmonic MMFs. Because the coils are discretely confined in slots, stepwise variations of the stator and rotor MMFs are generated which also produce MMF harmonics of a higher order. Analysing each winding harmonic separately and modelling an induction motor as a series connection of harmonic fields leads to the development of an extended equivalent circuit. In addition, since the main and auxiliary windings have different harmonic content, they are treated individually. This is described in Chapter 3. By solving the circuit equations associated with each harmonic circuit, the currents and torques due to the forwards- and backwards-rotating harmonic fields can be obtained. The net machine torque is obtained by superimposing the harmonic torques. An example of a torque vs. speed curve for a 60 Hz motor is shown in fig. 7.1. It appears that this machine has considerable $3^{rd}$ and $5^{th}$ space harmonic winding content. This model was verified experimentally since the red curve shows the measured torque and blue curve shows the simulated curve for the same motor.
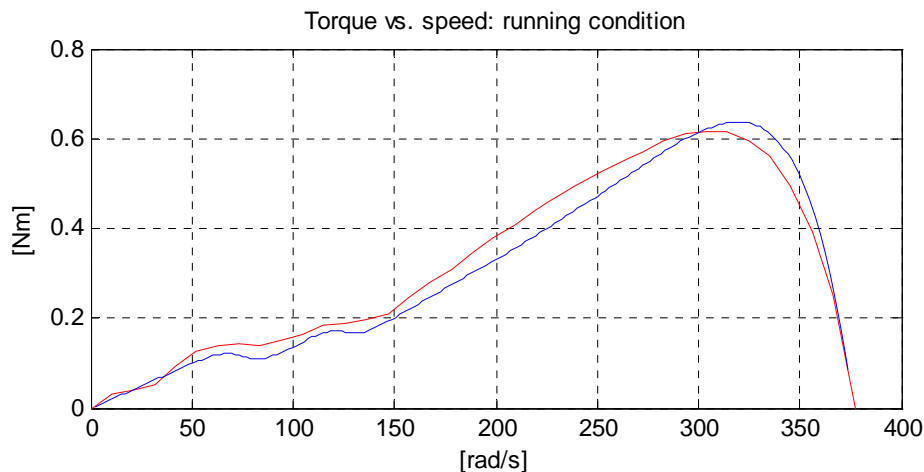


*Fig. 7.1 Comparison of simulated and measured torque*

111

The estimation of the machine performance requires simulation of the equivalent circuit parameters in terms of the fundamental and harmonic components of resistance and reactance. This is described in Appendix 1. It should be noted that the simulated torque curve in fig. 7.1 is arrived at by direct use of machine geometry using the formulae in Appendndix 1. Tuning a few of the parameters, e.g. iron losses and rotor resistivity, would improve agreement further.

## 7.2 Synchronous locking torques from permeance harmonics

The slotted stator and the slotted (or effectively slotted rotor due to saturation of the rotor bridges) combine to introduce several components of permeance harmonic in the air-gap. This is described in Chapter 4. Each permeance harmonic generates additional flux density harmonics of higher order in the air-gap. These flux density waves interact with rotor MMFs of the same harmonic order to produce torque. Prediction of these torques require knowledge of the magnitudes of the magnetising MMFs, permeances and rotor MMFs of various harmonic orders. For this purpose, the equivalent circuit described in Chapter 6.1 can be used iteratively, keeping the fundamental components constant and solving the harmonic components. The total sum of the synchronous locking torques at specific speeds from the various harmonic components can finally be obtained. A detailed description of the derivation and implementation of this model can be found in Chapter 5.

Fig. 7.2 shows the magnitudes of the locking torques as well as the speeds at which they occur for a particular 24 slot stator with various rotors having from 10 to 36 slots.

From Fig. 7.2 it is seen that certain slot combinations result in large magnitudes of synchronous locking torque, whereas other result in limited magnitudes. In order to evaluate the model derived in Chapter 5, a number of test rotors were made, and measurements were performed in order to identify the locking torque characteristics. This test is described in detail in Appendix 2.

Fig. 7.3 shows the modelled torque vs. speed curve for a given 50 Hz motor design including synchronous locking torques shown in blue; the measured values of synchronous locking torques are superimposed and are shown in red.
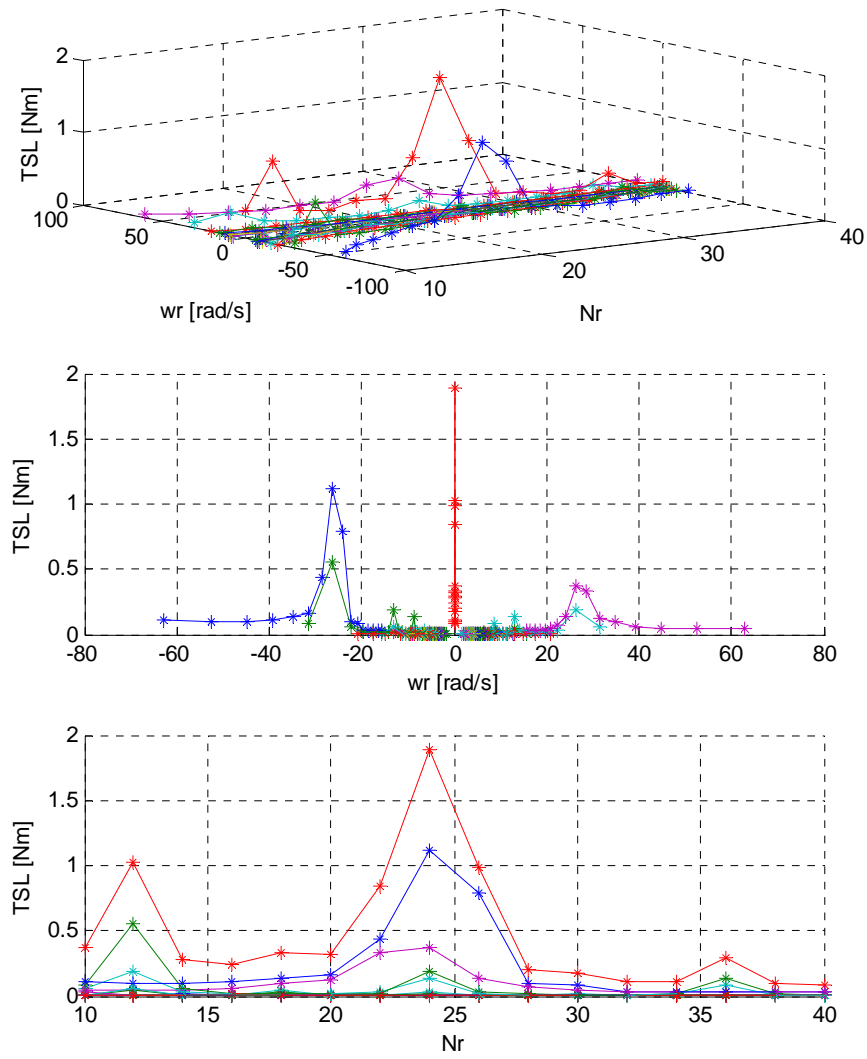
*Fig. 7.2 Variation of synchronous locking torque with rotor bar number ($N_r$)*
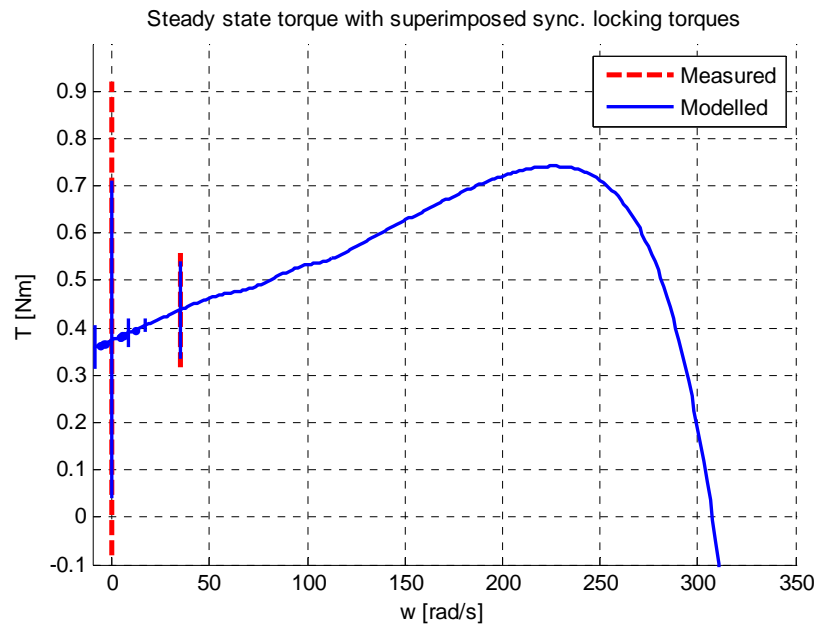


*Fig. 7.3 Comparison of simulated and measured torque including synchronous torques*

*for an 18 bar rotor*

113

## 7. Summary of modelling and results

As discussed in Section 6.5, the true deviation between measured and simulated values may be substantially smaller than indicated in fig. 7.3. A certain degree of stator-rotor eccentricity has been present during test; according to Section 5.4 this is a further source of synchronous locking. Since the model does not take this into account, the measured values of synchronous locking torque are somewhat exaggerated. The certain speeds at which the torques occur, however, appear to have been correctly identified.

# Chapter 8

# Conclusions and suggestions for further work

The results summarised in the previous chapter validate the models developed for the prediction of harmonic asynchronous and synchronous torques. While there have been some studies addressing asynchronous torques in split-phase machines (e.g., [11]), very little has been published on synchronous harmonic torques. Machine manufactures rely on the use of a set of preferred stator/rotor slot combinations and rotor skew to reduce them to acceptable levels [28]. Also, distributing the windings as sinusoidal as possible reduces magnitude of synchronous torques. However, from time-to-time design prototypes are produced that appear to exhibit synchronous locking torques.

While the deviation between modelled and measured steady-state performance is in the region of 5 %, even without parameter adjustment or fine tuning and including the asynchronous torques, the deviation is much larger for the prediction of the magnitudes of synchronous locking torques. The reasons for this were discussed. However, the speeds at which the synchronous locking torques occur appear to be correctly predicted. This leads to the overall evaluation of the model and it is concluded that the theory is sufficiently detailed to predict the effects of asynchronous and synchronous locking torques in a split-phase induction motor.

Further work could be carried out to refine and improve the simulation accuracy and these suggestions are described below.

**Stator and rotor eccentricity**

Section 5.4 describes how air-gap eccentricity gives rise to additional components of air gap permeance harmonics and creates synchronous locking torques in a similar manner to the slot permeance waves. Synchronous locking torques due to eccentricity can be predicted and quantified in the same way, but require a dedicated approach to further the analysis. It is believed that inclusion of eccentricity would increase the magnitudes of synchronous locking torques calculated in Chapters 4 and 5.

**Magnetic nonlinearity**

The model does not take magnetic nonlinearity and saturation of the steel core into account. For the asynchronous torques, this approach can be justified so long as the motor operates at

115

relatively low flux density levels, e.g., in the region of 1.2 T. However, in normal operation, this flux level is quite low; and the large line current during starting may cause the leakage inductances to saturate, resulting in low-order air gap permeance harmonics due to saturated tooth tips. As a consequence, additional components of synchronous locking torque occur, particularly at standstill. Skewing of the rotor also leads to increased saturation in the axial directions which may well affect the synchronous locking torques.

**Rotor cross-coupling**

In the model derived here, the rotor is assumed ideal and its slotting effects are solely included in the permeance calculation. However, Section 3.5 describe how a single harmonic component of rotating air-gap flux density results in a spectrum of induced rotor current distributions. Thus, when considering the rotor current distribution of order $n_b$, it is assumed induced by the rotating stator MMF of same pole number. In fact, an additional source would be a lower harmonic MMF as shown in Fig. 3.10.

Allowing for harmonic cross-coupling would affect the magnitudes of the rotor current distributions and, consequently, the magnitude of synchronous locking torques.

**Parameter accuracy**

When determining the synchronous locking torques, the model is biased by the fundamental and third harmonic parameters in the equivalent circuit diagram. The variables relevant to the calculation of the synchronous locking torques are likewise determined by the higher-order parameters. An accurately predicted value is thus important in order to obtain a precise result. While it is relatively easy to assess the parameter estimation based on steady-state measurement, the higher order parameters are more difficult to estimate since their influence on the steady-state performance is damped by the fundamental and lower order harmonics. It is likely that a more rigorous approach of determining the equivalent circuit parameters (described in Appendix 1) would result in improved model accuracy.

Altogether, it seems that the estimation of synchronous locking torques is more sensitive to error than asynchronous locking torques due to the required precision of higher-order harmonic parameters as well as eccentricity. It can be concluded that the model presented here is sufficiently precise, but improvements in the accuracy of the synchronous locking torque predictions would be possible if the effects described above were taken into account.

# References

[1] B. C. Mecrow, A. G. Jack, *Efficiency Trends in Electric Machines and Drives,* University of Newcastle Upon Tyne , October 2006
http://www.foresight.gov.uk/Energy/Reports/Mini_Energy_Reports/PDF/Efficiency_trends_in_mahines_and_drives.pdf

[2] W. J. Morrill, *The Revolving Field Theory of the Capacitor Motor,* Trans. AIEE, April 1929

[3] E. F. Fuchs, A. J. Vandenput, J. Höll, J. C. White, *Design Analysis of Capacitor-Start, Capacitor-Run Single Phase Inductions Motors,* IEEE Transactions on Energy Conversion, Vol. 5, No. 2, June 1992

[4] I. Boldea, T. Dumitrescu, S. A. Nasar, *Unified Analysis of 1-Phase AC Motors Having Capacitors in Auxiliary Windings,* IEEE Transactions on Energy Conversion, Vol. 14, No. 3, September 1999

[5] S. D. Umans, *Steady-State, Lumped-Parameter Model for Capacitor-Run, Single Phase Induction Motors,* IEEE Transactions on Industry Applications, Vol 32, No. 1, January/February 1996

[6] B. S. Guru, *Revolving-Field Analysis of T- and L-connected Capacitor Motors with Arbitrarily Displaced Windings,* IEEE Transactions on Power Apparatus and Systems, Vol. PAS-98, No. 4, July/August 1979

[7] C. G. Veinott, *Performance Calculations of L- and T-connected Tapped-Winding Capacitor Motors,* IEEE Transactions on Power Apparatus and Systems, Vol. PAS-96, No. 4, July/August 1977

[8] Philip L. Alger, *Induction Machines*, 2nd edition, Gordon and Breach Science Publishers Inc, 1970

[9] J. Stepina, *Single-phase induction motors* (English edition), Magna Physics Publishing 2004

[10] L. W. Buchanan, *An Equivalent Circuit for a Single-Phase Motor Having Space Harmonics in its Magnetic Field,* IEEE Transactions on Power Apparatus and Systems, Vol. PAS-84, No. 11, November 1965

[11] D. G. Dorrell, *Analysis of Split-phase Induction Motor Using an Impedance Matrix*, IEEE Conference on Power Electronics, Machines and Drives, Edinburgh, 31 March - 2 April 2004

References

[12] J. H. Davis and D. W. Novotny, *Equivalent Circuits for Single-Phase Squirrel Cage Induction Machines with both Odd and Even Order MMF Harmonics*, IEEE Transactions on Power Apparatus and Systems, Vol. PAS-88, No. 7, July 1969

[13] M. Popescu, C. B. Rasmussen, T. J. E. Miller, M. McGilp, *Effect of MMF Harmonics on Single-Phase Induction Motor Performace – A Unified Approach,* IEEE 42nd Industry Applications Conference, 23-27 September 2007

[14] Gabriel Kron, *Induction Motor Slot Combinations,* No. 31-46, AIEE Winter Convention New York, N.Y. Jan. 1931

[15] Philip L. Alger, *Induction Machines*, 2nd edition, Gordon and Breach Science Publishers Inc, 1970

[16] R. A. Heartz, R. M. Saunders, *Harmonics due to Slots in Electric Machines,* Paper 54-191, AIEE North Eastern District Meeting, Schenectady, N.Y., May 1954

[17] B. Heller and V. Hamata, *Harmonic Field Effects in Induction Machines*, Elsevier Scientific Publishing Company, 1977

[18] S. J. Yang, *Low-noise Electrical Motors*, Oxford University Press, 1981, ISBN 0-19-859332-5

[19] S. Nandi, *Modelling of Induction Machines Including Stator and Rotor Slot Effects*, IEEE Transactions on Industry Appliacations, Vol. 40, No. 4, July/August 2004

[20] H. D. Gersem, K. D. Brabandere, R. J. M. Belmans, K. Hameyer, *Motional Time-Harmonic Simulation of Slotted Single-Phase Induction Machines*, IEEE Transactions on Energy Conversion, Vol. 17, No. 3, Septermber 2002

[21] H. R. Fudeh and C. M. Ong, *Modelling and Analysis of Induction Machines Containing Space Harmonics - Part I: Modelling and Transformation*, IEEE Transactions on Power Apparatus and Systems, Vol. PAS-102, No. 8, August 1983

[22] H. R. Fudeh and C. M. Ong, *Modelling and Analysis of Induction Machines Containing Space Harmonics - Part II: Analysis of Asynchronous and Synchronous Actions*, IEEE Transactions on Power Apparatus and Systems, Vol. PAS-102, No. 8, August 1983

[23] H. R. Fudeh and C. M. Ong, *Modelling and Analysis of Induction Machines Containing Space Harmonics - Part III:Three-Phase Cage Rotor Induction Machines*, IEEE Transactions on Power Apparatus and Systems, Vol. PAS-102, No. 8, August 1983

[24] K. J. Binns, *Cogging torques in Induction Machines,* Paper 5662 P, Proceedings of IEE, Vol. 115, No. 12, December 1968

[25] K. J. Binns, M. Dye, *Effects of Slot Skew and Iron Saturation on Cogging Torques in Induction Machines,* Paper 6185 P, Proceedings of IEE, Vol. 117, No. 7, July 1970

References

[26] Cyril G. Veinott, *Theory and Design of Small Induction Motors*, McGraw-Hill Book Company, 1959

[27] C. B. Rasmussen and TJE Miller, *Revolving-Field Polygon Technique for Performance Prediction of Single-Phase Induction Motors*, IEEE Transactions on Industry Applications, Vol. 39, No. 5, September/October 2003

[28] TJE Miller, *SPEED's Electric Motors*, University of Glasgow, 2002 – 2004

[29] F. W. Carter, *A Note on Airgap and Interpolar Induction*, JIEE, No. 29, pp 925, 1900

[30] F. W. Carter, *The Magnetic Field of the Dynamo-Electric Machine*, JIEE, No. 64, pp 100, 1926

[31] L. Golebiowski and D. Mazur, *The Effect of Strong Parasitic Synchronous and Asynchronous Torques in Induction Machines with Rotor Eccentricity*, 10th Mediterranean Electrotechnical Conference, MEleCon 2000, Vol III

[32] A. A. Jimoh, O. Omozusi, O. Ojo, *Parameter estimation of Single-Phase Induction Machines,* IEEE 0-7803-5293-9, 1999

[33] C and F S van der Merwe, *A Study of Methods to Measure the Parameters of Single-Phase Induction Motors,* IEEE Transactions on Energy Conversion, Vol. 10, No. 2, June 1995

[34] M. R. Spiegel, *Mathematical Handbook of Formulas and Table*, McGraw-Hill, Inc, 1968

[35] D. G. Dorrell, *Calculation and Effects of End-ring Impedance in Cage Induction Motors*, IEEE Transactions on Magnetics, March 2005, pp 1176 – 1183

[36] P. J. Holik, D. G. Dorrell, P. Lombard, H. Thougaard and F. Jensen, *A Multi-Sliced Finite Element Model for Induction Machines Incorporating Inter-Bar Current*, IAS Conference Paper, October 2006

[37] D. Lin, T. Batan, E. F. Fuchs and W. M. Grady, *Harmonic Losses of Single-Phase Induction Motors under Nonsinusoidal Voltages*, IEEE Transactions on Energy Conversion, Vol. 11, No. 2, June 1996

# Appendix 1

# Equivalent circuit parameters

In order to predict the performance of a given motor design, the parameters of the corresponding equivalent circuit are required to be correctly estimated. In the literature, there are various approaches for deriving these. Methods and the complexity of these methods differ, and in many cases the expressions for the various parameters contain empirical corrections, particularly in methods developed before finite element software was available. Most of the following derivations are based on [8], [9] and [26]. Reference [32] and [33] put forward methods to test the validity of such estimations against measurements.

In this appendix, expressions for each equivalent circuit parameter are derived. In some cases the expression is taken directly from the literature, and in other cases they are derived from first principles.

## *A1.1. Stator resistance*

Perhaps the simplest parameter of the equivalent circuit is the stator resistance since it is determined from the length, wire size and resistivity of the stator coil. It is also the easiest to test. However, its estimation does require knowledge of how the coils are wound by the winding equipment for correct estimation of the end winding resistance.

Assuming that each coil loop consists of two straight sections with a certain length plus two arc sections each with a length determined by the pitch of the coil and the radius of the slots in which the coil is placed, the stator resistance $R_s$ can be determined from

$$R_s = \rho \sum_{i=1}^{N_{slots}} \frac{N_i 2 \left( L + 2 L_{ext} + p_i \pi \, r_i \right)}{A_{wire}} \qquad \text{(A1.1)}$$

- where $\rho$ is the resistivity of the material, $N_i$ is the number of turns of the coil in the $i^{th}$ slot, $L$ is the stator length, $L_{ext}$ is the winding extension in each end of the stack, $p_i$ is the pitch of the $i^{th}$ slot, and $r_i$ is the radius from stator centre to the mid point of the $i^{th}$ slot.

The stator resistance is temperature dependant since the resistivity varies with temperature $T$ so that

$$\rho(T) = \rho_0 \left( 1 + \frac{T - T_0}{\dfrac{1}{\alpha_0} + T - T_0} \right) \tag{A1.2}$$

where $\rho_0$ is the resistivity and $\alpha_0$ the temperature coefficient at the temperature $T_0$.

## A1.2 Rotor resistance

In Chapters 1 and 2, the rotor resistance was treated as a differential value, that is, a value representing an infinitesimal section of the rotor. Here, the actual resistances are determined. Fig. A1.1 shows an angular section of an example a bar of a rotor with a span of $m\alpha$, $m$ being the harmonic order of the induced current distribution in consideration. It consists of two end-ring sections where the current flows in a circumferential direction and a bar section where the current direction is axial.
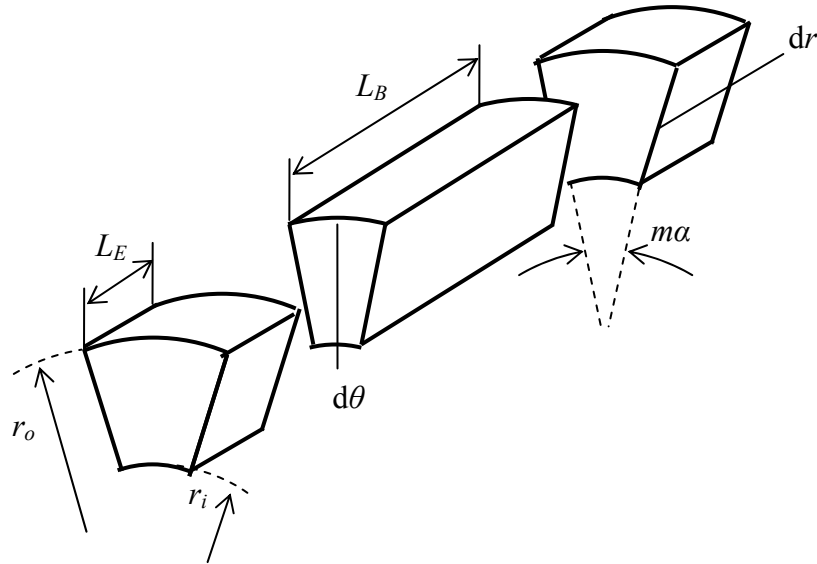


*Fig. A1.1 Bar section representation*

Therefore, since the effective cross sections are aligned circumferentially for the end-ring component and axially for the bar component, they behave differently when analysed over an infinitesimal angle $d\theta$.

From Fig. A1.1, the resistance $R_{B\alpha}$ of an angular section $\alpha$ of the rotor consists of the parallel connection of the bar components $R_{Bd}$ of an angular segment $d\theta$, i.e.:

$$R_{B\alpha} = \frac{R_{Bd}}{d\theta} \,\|\, \frac{R_{Bd}}{d\theta} \,\|\, \ldots = \left( \int_0^{m\alpha} \frac{1}{R_{Bd}} d\theta \right)^{-1} = \frac{R_{Bd}}{m\alpha} \tag{A1.3}$$

from which

$$R_{Bd} = m\alpha R_{\alpha B} \tag{A1.4}$$

For comparison, the end-ring resistance $R_{E\alpha}$ of the section $\alpha$ consists of a series connection of infinitesimal resistance segments $R_{Ed}$, which means that

$$R_{Ed} = \frac{R_{E\alpha}}{m\alpha} \tag{A1.5}$$

But each end-ring resistance segment itself is a parallel connection of radial segments with thickness d$r$, determined by the inner and outer radii of the end ring. This can be interpreted as

$$R_{E\alpha} = \frac{R_{E\alpha}(r1)}{dr} \parallel \frac{R_{E\alpha}(r1)}{dr} \parallel \ldots = \left( \int_{r_i}^{r_o} \frac{1}{\rho \dfrac{m\alpha r}{L_E dr}} \right)^{-1} = \left( \int_{r_i}^{r_o} \frac{L_E dr}{\rho m\alpha r} \right)^{-1}$$

$$= \frac{\rho m\alpha}{L_E} \left( \frac{1}{\ln(r_o) - \ln(r_i)} \right) \tag{A1.6}$$

in which case, from (A1.5)

$$R_{Ed} = \frac{R_{E\alpha}}{m\alpha} = \frac{\rho}{L_E} \left( \frac{1}{\ln(r_o) - \ln(r_i)} \right) \tag{A1.7}$$

The total resistance of an angular section d$\theta$ is the sum of the bar component and two end ring components and is thus

$$R_d = R_{Bd} + 2R_{Ed} = m\alpha\rho \frac{L_B}{A_B(\alpha)} + 2\frac{\rho}{L_E} \left( \frac{1}{\ln(r_o) - \ln(r_i)} \right) \tag{A1.8}$$

where the term $A_B(\alpha)$ is the area of the bar section determined by angle $\alpha$. Often the end-ring does not have a rectangular cross section. In this case, equivalent values for $r_o$ and $r_i$ must be used.

[26] uses power balancing methods to calculate the referred resistance of the rotor.

## A1.3 Magnetizing reactance

An expression for the magnetizing reactance of the $m^{th}$ harmonic winding is already given in (3.31). However, in previous sections, it was assumed that the iron of stator and rotor is infinitely permeable. Likewise, additional factors such as the slotting of stator and rotor were not considered. When taking these into account, it means that the magnetizing reactance must be modified for slotting and for finite (and varying) iron permeability.

**The effective air-gap**

When both stator and rotor windings are confined to slots which are open then the electromagnetic air-gap is no longer the same as the mechanical air-gap. F.W. Carter [29][30] performed analysis on how to obtain an equivalent air-gap length when taking slotting into account. This used conformal transformations. A suitable expression is given by [26] where

$$K_s = \frac{\lambda_s \left(5g + x_{sos}\right)}{\lambda_s \left(5g + x_{sos}\right) - x_{sos}^2} \quad , \quad K_r = \frac{\lambda_r \left(5g + x_{sor}\right)}{\lambda_r \left(5g + x_{sor}\right) - x_{sor}^2} \tag{A1.9}$$

and the corresponding air-gap correctional factor (Carter factor) is

$$K_c = K_s \, K_r \tag{A1.10}$$

with dimensions as given in Fig. A1.2.
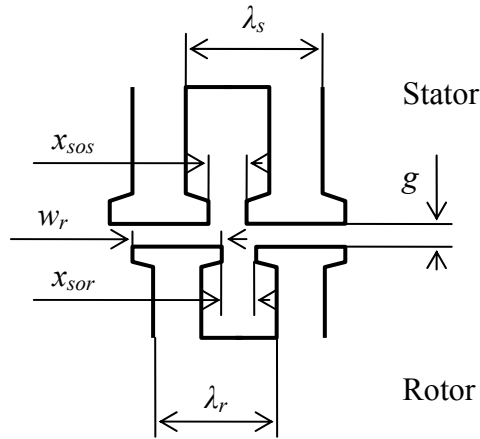


*Fig. A1.2 Stator and rotor slot geometries*

Fig. A1.2 shows an open-slot rotor. In cases where the rotor has closed slots, the Carter factor will be very close to unity; but not quite, as a result of tooth tip saturation.

**Stator and rotor permeability**

It was assumed earlier that the laminated iron cores of the stator and rotor were infinitely permeable, in which case it is effectively the machine air-gap that determines the magnetic reluctance and hence the flux density in the machine. This assumption is generally valid as long as the flux level results in the main flux paths do not saturate the magnetic steel to a great extent. However, the highly nonlinear magnetic behaviour of magnetic steel means that the relative permeability gradually reduces towards unity so the iron enters saturation. The knee of the steel B/H curve is typically at about 1.7 T.

## A1.4. Stator leakage reactance

**Slot leakage**

The slot leakage reactance is determined by the flux that links the coils in the slot only.

In most single-phase motors, the slots contain coils from both the main and auxiliary windings, so it is necessary to consider the physical location of the windings in the slots. However, as will be shown later, there is no mutual coupling between the two windings, if they are orthogonal. The following analysis is based on a method given in [8].

Fig. A1.3 shows a simplified, rectangular slot, containing coils from two windings, situated in the upper (index *u*) and lower (index *l*) part of the slot.
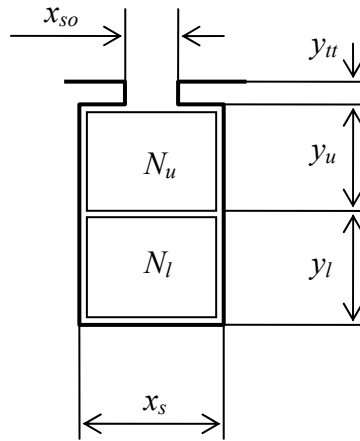


*Fig. A1.3 Rotor slot leakage calculation – required parameters*

When determining the slot leakage, it is assumed that the iron is infinitely permeable, and that the conductors are evenly distributed within their respective areas. At a given height *y*, the field intensity is, from Ámpere's Law

$$H(y) = N_l \frac{y}{y_l} \frac{I}{x_s} \tag{A1.11}$$

The flux through an infinitely thin area at height *y* is thus

$$d\Phi = \mu_0 H(y) L dy \tag{A1.12}$$

*L* is the axial length of the slot and should not be confused with the symbol for inductance. This flux links a number of coils, which is likewise determined from *y*, i.e.:

$$d\Psi = N_l \frac{y}{y_l} d\Phi \tag{A1.13}$$

The total flux linkage is found by integrating (A1.13) with respect to y from 0 to $y_l$

$$\Psi_l = \int_0^{y_l} \frac{N_l^2 I L_{stk} \mu_0 y^2}{x_s y_l^2} dy = \frac{N_l^2 I L_{stk} \mu_0 y_l}{3x_s} \tag{A1.14}$$

Other components of flux linkage exist for the sections $y_u$ and $y_{tt}$, so that

$$\Psi_u = \frac{N_l^2 I L_{stk} \mu_0 y_u}{x_s} \tag{A1.15}$$

and

$$\Psi_{tt} = \frac{N_l^2 I L_{stk} \mu_0 y_{tt}}{x_{so}} \tag{A1.16}$$

Since, in general, inductance is defined as flux linkage per unit current, this means that the total leakage inductance of the lower coil in the slot depicted in Fig. A1.3 will be

$$L_l = N_l^2 L_{stk} \mu_0 \left( \frac{y_l}{3x_s} + \frac{y_u}{x_s} + \frac{y_{tt}}{x_{so}} \right) \tag{A1.17}$$

Using the same approach for the upper winding, the leakage inductance of the upper coils in the same slot will be

$$L_u = N_u^2 L_{stk} \mu_0 \left( \frac{y_u}{3x_s} + \frac{y_{tt}}{x_{so}} \right) \tag{A1.18}$$

It appears that the inductance of the upper coil has a component less than that of the lower coil. It would seem that the leakage inductance therefore depends on the physical location of the windings in the slot. Suppose that the conductors of the upper and lower phase were mixed and evenly distributed over the entire slot area - in this case the leakage inductance of either coil in the slot would be

$$L_{u,l} = N_{u,l}^2 L_{stk} \mu_0 \left( \frac{y_u + y_l}{3x_s} + \frac{y_{tt}}{x_{so}} \right) \tag{A1.19}$$

The expression in parentheses is often referred to as the slot constant, since it is determined only by the geometry of the slot and the arrangement of conductors. The slot constant of (A1.19) is quite simple due to the simple geometry of a rectangular slot. When the slot shape is not rectangular, the slot constant becomes more complicated. In [26], a general expression for slot constants for various slot shapes can be found.

The derivation of the slot constants were performed in a similar manner to the above method. Section A1.5, which deals with the rotor slot leakage, shows how much more complex the calculation becomes when the shapes differ from the very simple rectangular shape. Even so, this method is applicable as long as the slot geometry is relatively simple; however, complex slot shapes as found in e.g. double-cage rotors may require a different approach.

**Leakage in orthogonal split phase windings**

Fig. A1.3 shows a slot containing conductors from more than one phase. Therefore, the leakage flux set up by one of the windings links the other winding, thus giving rise to a mutual inductance term. However, if the windings are orthogonal and concentric, the mutual flux will be eliminated. This is perhaps best shown graphically in Fig. A1.4.
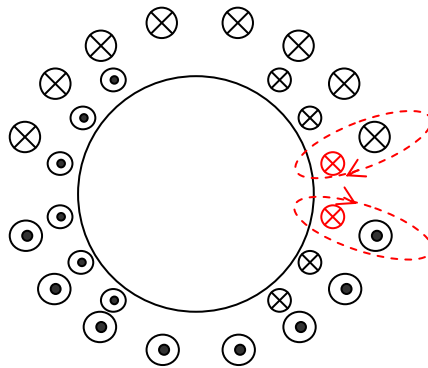


*Fig. A1.4 Main and auxiliary slot leakage linkage*

The red paths illustrate the leakage flux set up by the two coils of the innermost winding. These fluxes link the coils in the outermost windings; however the two outermost coils go in different directions; therefore the fluxes linking them will be of opposite sign and cancelling each other. This means there will be a net zero voltage induced into the outer winding. When calculating leakage flux for a split phase motor with orthogonal windings, it suffices to analyse the isolated contributions from main and auxiliary windings respectively.

**End-turn leakage**

According to the literature, in particular [8] and [26], end-turn inductance is subject to a high degree of uncertainty, since the end turns generate magnetic fields with a complex shape in three dimensions. A generally well-proven expression for end-turn leakage is given in [26] and it is repeated here:

$$X_{end} = K_x \left( \frac{\pi D_e ACT}{S_1 P} \right)$$  (A1.20)

where $K_x = 2 \pi f (C k_w)^2 \, 10^{-8}$, $D_e$ = diameter of mid-slots, $ACT$ = weighted average coil throw, $S_1$ = number of slots and $P$ = number of poles.

Note that the terminology in [26] uses winding factors to describe the fundamental winding component - this terminology is not quite identical here, where harmonic winding amplitudes are used. Further, [26] works with imperial units whereas SI-units are used here. Translating (A1.20) to the terminology and unit system used here and introducing an expression for the weighted average coil throw gives

$$L_e = N^2 \mu_0 \frac{\pi D_e}{S_1 P} \frac{\displaystyle\sum_{s=1}^{S_1/4} N_s \left( \frac{S_1}{2} - 1 - 2(s-1) \right)}{\dfrac{N}{2}} \tag{A1.21}$$

where $N$ is the total winding number of the winding.

## A1.5 Rotor leakage reactance

**Rotor slot leakage reactance**

The rotor slot leakage inductance approach used in Section A1.4.1 is repeated here but it should be noted that here the winding number is unity. It is assumed that the current density $J$ is evenly distributed over the entire slot area, thus ignoring any deep bar effect that may occur. This is quite valid for the small machines studied in this work. Treating the slot as a rectangular shape would be an over-simplification. Instead it is assumed to consist of two trapezoidal shapes as depicted in Fig. A1.4.
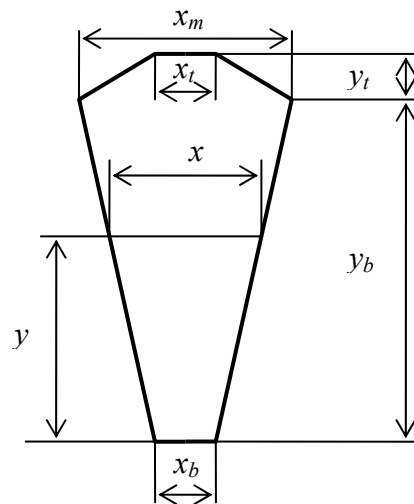


*Fig. A1.4 Rotor bar co-ordinates*

In order to calculate the slot parameters, it is necessary to establish a connection between the slot width $x$ as a function of the height at which it is measured. A similar connection must be

made for the slot area. At a given height $y$ from the slot bottom, which is taken as reference, the width of the slot is

$$x(y) = x_b + \frac{y}{y_b}(x_m - x_b), \quad 0 \le y \le y_b$$

$$= x_m + \frac{y - y_b}{y_t}(x_t - x_m), \quad y_b \le y \le y_b + y_t \tag{A1.22}$$

and the area of the slot section is

$$A(y) = \frac{y}{2}(x_b + x(y)), \quad 0 \le y \le y_b$$

$$= \frac{y - y_b}{2}(x_m + x(y)), \quad y_b \le y \le y_b + y_t \tag{A1.23}$$

If the total current in the slot is $I$, the current density $J$ is obtained from

$$J = \frac{I}{A_b + A_t} = \frac{2I}{y_b(x_b + x_m) + y_t(x_m + x_t)} \tag{A1.24}$$

As previously shown, the inductance is calculated from Ámpere's law. When calculating the inductance, the slot in Fig. A1.4 is considered separately for the bottom slot section and top slot section. For the bottom section, the inductance is determined solely from the current density in the bottom section; whereas for the top section, it is determined by the current density in the top section PLUS a constant contribution from the bottom section.

That is, for the bottom section, assuming homogeneous current density, at a given height $y$:

$$H_b(y) = \frac{JA(y)}{x(y)} \quad \Rightarrow \quad B_b(y) = \frac{\mu_0 JA(y)}{x(y)} \tag{A1.25}$$

At height $y$, the flux through an infinitesimal section of height $dy$ is

$$d\Phi = B_b(y) L_{stk} \, dy \tag{A1.26}$$

since the winding number is unity over the entire slot, $d\Phi = d\Psi$ in which case

$$\Psi_b = L_{stk} \int_0^{y_t} B_b(y) \, dy = L_{stk} \int_0^{y_b} \frac{\mu_0 \, JA(y)}{x(y)} \, dy \tag{A1.27}$$

Inserting expressions for $x(y)$ and $A(y)$ yields, when separating the integrals:

$$\Psi_b = L_{stk} \int_0^{y_b} \frac{\mu_0 J \frac{y}{2}\left(x_b + x_b + \frac{y}{y_b}(x_m - x_b)\right)}{x_b + \frac{y}{y_b}(x_m - x_b)} \, dy$$

$$= L_{stk} \mu_0 J \left( \int_0^{y_b} y \, dy - \int_0^{y_b} \frac{\frac{y^2}{2y_b}(x_m - x_b)}{x_b + \frac{y}{y_b}(x_m - x_b)} \, dy \right) \tag{A1.28}$$

From [34], mathematically, this reduces to

$$\Psi_b = L_{stk}\,\mu_0\,J\left(\left[\frac{y^2}{2}\right]_0^{y_b} - \frac{x_m - x_b}{2y_b}\left[\frac{\left(x_b + \dfrac{y}{y_b}(x_m - x_b)\right)^2}{2\left(\dfrac{x_m - x_b}{y_b}\right)^3} - \frac{2x_b\left(x_b + \dfrac{y}{y_b}(x_m - x_b)\right)}{\left(\dfrac{x_m - x_b}{y_b}\right)^3} + \frac{x_b^{\,2}}{\left(\dfrac{x_m - x_b}{y_b}\right)^3}\ln\left(x_b + \frac{y}{y_b}(x_m - x_b)\right)\right]_0^{y_b}\right) \tag{A1.29}$$

It should be noted how much more complex the slot factor becomes when changing the geometry from rectangular to trapezoid. In fact, only the $y^2/2$ term represents the rectangular section - the rest is a correction for the trapezoidal shape.

For the top section, the approach is similar, but there is an additional constant contribution from the bottom section, which means

$$H_t(y) = \frac{J\,A(y)}{x(y)} + \frac{J\,A_b}{x(y)} \quad \Rightarrow \quad B_t(y) = \frac{\mu_0\,J\left(A(y) + A_b\right)}{x(y)} \tag{A1.30}$$

$$\Psi_t = L_{stk}\int_{y_b}^{y_b + y_t} B_t(y)\,dy = L_{stk}\int_0^{y_t} \frac{\mu_0 J\left(A(y) + A_b\right)}{x(y)}\,dy \tag{A1.31}$$

Inserting expressions for $x(y)$, $A(y)$ and $A_b$ yields

$$\Psi_t = L_{stk}\int_0^{y_t}\left(\frac{\mu_0\,J\,\dfrac{y}{2}\left(x_m + x_t + \dfrac{y}{y_t}(x_t - x_m)\right)}{x_m + \dfrac{y}{y_t}(x_t - x_m)} + \frac{\dfrac{y_b}{2}(x_b + x_m)}{x_m + \dfrac{y}{y_t}(x_t - x_m)}\right)dy \tag{A1.32}$$

In a similar manner to (A1.28), (A1.32) is split into separate integrals, i.e.

$$\Psi_t = L_{stk}\mu_0 J\left(\int_0^{y_t} y\,dy - \int_0^{y_t}\frac{\dfrac{y^2}{2y_b}(x_m - x_b)}{x_m + \dfrac{y}{y_t}(x_t - x_m)}\,dy + \int_0^{y_t}\frac{\dfrac{y_b}{2}(x_b + x_m)}{x_m + \dfrac{y}{y_t}(x_t - x_m)}\,dy\right) \tag{A1.33}$$

The solution of (A1.33) is similar to (A1.29) but contains an additional expression for the bottom part, therefore:

Appendix 1: Equivalent circuit parameters

$$\Psi_t = L_{stk}\,\mu_0\,J\left[\frac{y^2}{2}\right]_0^{y_t} - L_{stk}\,\mu_0\,J\frac{x_t-x_m}{2y_t}\left[\frac{\left(x_m+\dfrac{y}{y_t}(x_t-x_m)\right)^2}{2\left(\dfrac{x_t-x_m}{y_t}\right)^3} - \frac{2x_m\left(x_m+\dfrac{y}{y_t}(x_t-x_m)\right)}{\left(\dfrac{x_t-x_m}{y_t}\right)^3} + \frac{x_m{}^2}{\left(\dfrac{x_t-x_m}{y_t}\right)^3}\ln\left(x_m+\frac{y}{y_t}(x_t-x_m)\right)\right]_0^{y_t}$$

$$+\,L_{stk}\,\mu_0\,J\frac{y_b(x_b+x_m)}{2}\left[\frac{1}{\dfrac{x_t-x_m}{y_t}}\ln\left(x_m+\frac{y}{y_t}(x_t-x_m)\right)\right]_0^{y_t}$$

(A1.34)

Finally, there is a leakage inductance contribution due to the geometry above the rotor slot. This may be either open or closed. If the rotor slots are open, the inductance is defined similarly to (A1.16) where

$$\Psi_{ttr} = \frac{JA_r L_{stk}\mu_0 y_{ttr}}{x_{sor}} = \frac{IL_{stk}\mu_0 y_{ttr}}{x_{sor}}$$

(A1.35)

from which it follows that

$$L_{ttr} = \frac{L_{stk}\mu_0 y_{ttr}}{x_{sor}}$$

(A1.36)

If the slot is closed, the assumption that the iron part has infinite permeability will cause the inductance of this bridge section to be infinitely large. However, the bridge quickly saturates, causing the incremental relative permeability to be unity.

Therefore, the expression for the bridge section of the closed section will be similar to (A1.36), i.e.

$$L_{br} = \frac{L_{stk}\mu_0 y_{br}}{x_{br}}$$

(A1.37)

in which case the height of the bridge $y_{br}$ and the length of the bridge $x_{br}$ are equivalent values. The bridge is often treated as a constant voltage source in the equivalent circuit [28].

Altogether, the (un-referred) rotor slot inductance is the sum of the expressions (A1.29), (A1.34) (when calculating the equivalent inductance) and (A1.37). Hence

$$L_r = L_{stk}\ \mu_0\ \frac{1}{y_b(x_b + x_m) + y_t(x_m + x_t)} \left( y_b^{\ 2} - \frac{\dfrac{x_m^{\ 2}}{2} - 2x_b x_m + x_b^{\ 2}\ln(x_m)}{\left(\dfrac{x_m - x_b}{y_b}\right)^2} + \frac{\dfrac{x_b^{\ 2}}{2} - 2x_b^{\ 2} + x_b^{\ 2}\ln(x_b)}{\left(\dfrac{x_m - x_b}{y_b}\right)^2} \right)$$

$$+ L_{stk}\ \mu_0\ \frac{1}{y_b(x_b + x_m) + y_t(x_m + x_t)} \left( y_t^{\ 2} - \frac{\dfrac{x_t^{\ 2}}{2} - 2x_m x_t + x_m^{\ 2}\ln(x_t)}{\left(\dfrac{x_t - x_m}{y_t}\right)^2} + \frac{\dfrac{x_m^{\ 2}}{2} - 2x_m^{\ 2} + x_m^{\ 2}\ln(x_m)}{\left(\dfrac{x_t - x_m}{y_t}\right)^2} \right)$$

$$+ L_{stk}\ \mu_0\ \frac{\dfrac{y_b}{2}(x_b + x_m)}{y_b(x_b + x_m) + y_t(x_m + x_t)}\ \frac{\ln\left(\dfrac{x_t}{x_m}\right)}{\dfrac{x_t - x_m}{y_t}} + \frac{L_{stk}\mu_0 y_{br}}{x_{br}}$$

$$\text{(A1.38)}$$

It can be seen that the resulting expression is made up of four terms that are added together. The first two are the self-inductances of the bottom and top slot sections respectively, the third is the mutual inductance between the bottom section and the top section, and the fourth is the bridge (or slot opening) component.


**End ring leakage reactance**

Estimation of the end-ring inductances require analysis of magnetic fields acting in three dimensions. An analytical approach is therefore very complex although it is possible to use two dimensional methods [35].

Instead, an expression for the un-referred end-ring inductance is derived which is based upon the expression for the stator end windings. This is possible because of the fact that the stator has uniform conductor current density, but varying winding number, whereas the rotor has varying conductor current density but uniform winding number. Thus, the ampere-turns have a similar distribution in the stator end-windings and rotor end-rings when analysed radially. Therefore an expression for the un-referred end ring reactance is

$$X_{end,r} = X_{end} \frac{D_{er}}{D_e \pi \left( \frac{N_{(1)}}{2} \right)^2}$$

(A1.39)

## *A1.6. Differential leakage components*

The term differential leakage relates to the fact that a flux linking either or both the stator windings and the rotor cage may exist, even though this flux does not induce any net voltage in the other conductor set and thus is not a part of the magnetizing reactance (i.e. it is a leakage inductance rather than a mutual inductance). In [26], several components of the leakage inductance when combined are referred to as the differential leakage, these are belt, zig-zag and skew reactances - these expressions are purely empirical.

In general terms, Ámpere's Law can be applied to any closed path encircling a net ampere-turn winding; and this may therefore describe either a magnetizing or a leakage reactance. In the following sections, an attempted is made to derive expressions for the belt and the zig-zag reactance from Ampere's Law. Thus, the general concept of differential reactance is abandoned since is it split up into its separate components. This may be subject to discussion, however comparison between modelled and measured motor performance has shown to give reasonable agreement when using the expressions derived in the following sections in a similar manner to [8].

**Stator belt leakage reactance**

Belt leakage is due to the flux created by the phase belt of a winding. It can be compared to the slot leakage, but consists of contribution from several slots as shown in Fig. A1.5. The flux paths are shown in the figure.
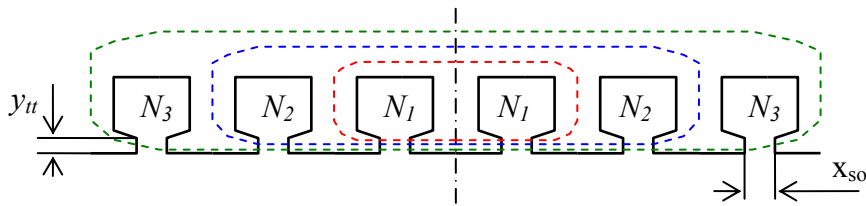


*Fig. A1.5 Belt leakage flux paths*

Neglecting the flux crossing through the slots themselves, and therefore only considering the flux crossing the slot openings, the flux linkage of the innermost group is shown in Fig. A1.5 (together with the other belt leakage fluxes). The belt leakage flux due to the two slots which contain $N_1$ conductors each is

$$\Psi_{b1} = \frac{I\left(2N_1\right)^2 \mu_0 L_{stk} y_{tt}}{2x_{so}}$$ (A1.40)

When considering the additional groups spanning further slots, successively more conductors are linked, until the outermost slots in the phase belt are reached. Hence, an expression for the total belt leakage inductance can be described by a summation:

$$L_b = 2\sum_{s=1}^{S} \frac{\left(2\sum_{s=1}^{S} N_s\right)^2 \mu_0 L_{stk} y_{tt}}{2sx_{so}}$$ (A1.41)

where $S$ is the number of slots in HALF a phase belt. The first factor 2 is used to cover both phase belts of a 2-pole winding.

It could be argued that similar leakage flux paths exist for coil groups away from the symmetry line, e.g. the right side group consisting of $N_1$ and $N_2$ or $N_1$, $N_2$ and $N_3$. However, it could likewise be argued that the contributions from these coil groups are cancelled by symmetry. However, the non-symmetric groups are not considered here.

**Zig zag leakage**

Zig-zag leakage inductance is similar to belt leakage, but here the leakage flux crosses back and forth between rotor and stator surfaces in a zig-zag fashion as shown in Fig. A1.6.
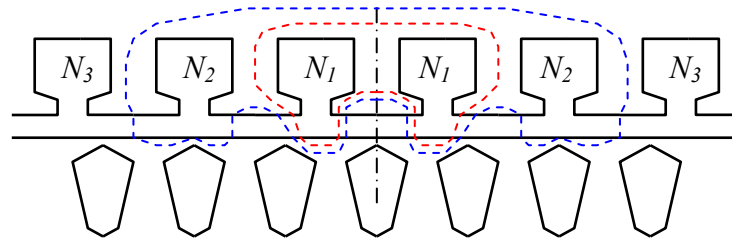


*Fig. A1.6 Zig-zag leakage flux paths*

When determining the zig-zag leakage inductance, the reluctance of the magnetic path from stator tooth across the air gap to the rotor and back to the adjacent tooth needs to be found. Here, it is necessary to consider two positions of rotor teeth, as these can be both overlapping and non-overlapping the stator tooth pair in consideration. The following derivation is similar to the one described in [26].

Stator slot
centre line



Rotor slot
centre line
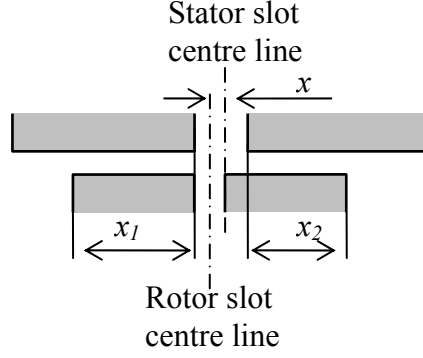
*Fig. A1.7 Stator-rotor slot relative overlaps*

Using the dimensions given in Fig. A1.2, and the further parameters shown in Fig. A1.7, the overlapping lengths $x_1$ and $x_2$ are

$$x_1(x) = w_r - \frac{x_{sos}}{2} - x, \qquad x_2(x) = w_r - \frac{x_{sos}}{2} + x, \quad -\frac{x_{sos}}{2} < x < \frac{x_{sos}}{2} \tag{A1.42}$$

In this interval, the reluctance is

$$\mathfrak{R}_1(x) = \frac{g}{L_{stk} x_1} + \frac{g}{L_{stk} x_2} + \frac{x_{sor}}{L_{stk} y_{ttr}} = \frac{g}{L_{stk}}\left(\frac{x_1+x_2}{x_1 x_2}\right) + \frac{x_{sor}}{L_{stk} y_{ttr}}$$

$$= \frac{g}{L_{stk}}\left(\frac{2w_r - x_{sos}}{\left(w_r - \frac{x_{sos}}{2}\right)^2 - x^2}\right) + \frac{x_{sor}}{L_{stk} y_{ttr}} \tag{A1.43}$$

This reluctance has a mean value

$$\mathfrak{R}_1 = \frac{1}{x_{sos}}\int_{-\frac{x_{sos}}{2}}^{\frac{x_{sos}}{2}} \frac{g}{L_{stk}}\left(\frac{2w_r - x_{sos}}{\left(w_r - \frac{x_{sos}}{2}\right)^2 - x^2}\right) dx + \frac{x_{sor}}{L_{stk} y_{ttr}} \tag{A1.44}$$

which is a standard integral that simplifies to

$$\mathfrak{R}_1 = \frac{g\,(2w_r - x_{sos})}{L_{stk}\,x_{sos}}\left[\frac{1}{2w_r - x_{sos}}\ln\left(\frac{w_r - \frac{x_{sos}}{2} + x}{w_r - \frac{x_{sos}}{2} - x}\right)\right]_{-\frac{x_{sos}}{2}}^{\frac{x_{sos}}{2}} + \frac{x_{sor}}{L_{stk} y_{ttr}}$$

$$= \frac{g}{L_{stk}\,x_{sos}} 2\ln\left(\frac{w_r}{w_r - x_{sos}}\right) + \frac{x_{sor}}{L_{stk} y_{ttr}} \tag{A1.45}$$

In the case were an underlying rotor tooth is overlapping the gap between to stator teeth, as shown in Fig. A1.8, the overlapping lengths $x_1$ and $x_2$ are

$$x_1(x) = \frac{w_r}{2} - \frac{x_{sos}}{2} - x, \quad x_2(x) = \frac{w_r}{2} - \frac{x_{sos}}{2} + x, \quad -\frac{w_r - x_{sos}}{2} < x < \frac{w_r - x_{sos}}{2} \tag{A1.46}$$

Stator slot
centre line



$x$

$x_1$

$x_2$

Rotor tooth
centre line
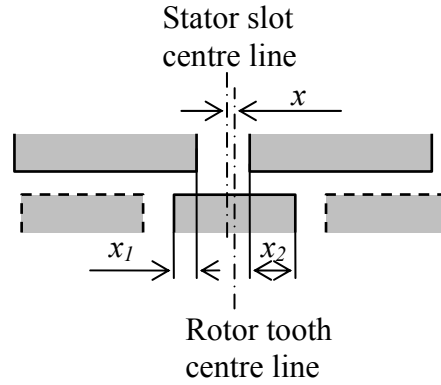
*Fig. A1.8 Stator-rotor alternative co-ordinates*

In this interval, the reluctance is

$$\mathfrak{R}_2(x) = \frac{g}{L_{stk} x_1} + \frac{g}{L_{stk} x_2} = \frac{g}{L_{stk}} \left( \frac{x_1 + x_2}{x_1 x_2} \right) = \frac{g}{L_{stk}} \left( \frac{w_r + x_{sos}}{\left( \frac{w_r - x_{sos}}{2} \right)^2 - x^2} \right) \tag{A1.47}$$

and outside this interval, the reluctance is infinity. Therefore, in order to obtain the total equivalent reluctance between two stator teeth then a parallel combination of reluctances is used which consists of a constant $\mathfrak{R}_1$ (representing the non-overlapping position) and the periodic reluctance $\mathfrak{R}_2$ which only occurs in the interval as given by (A1.46). This is depicted in Fig. A1.9.
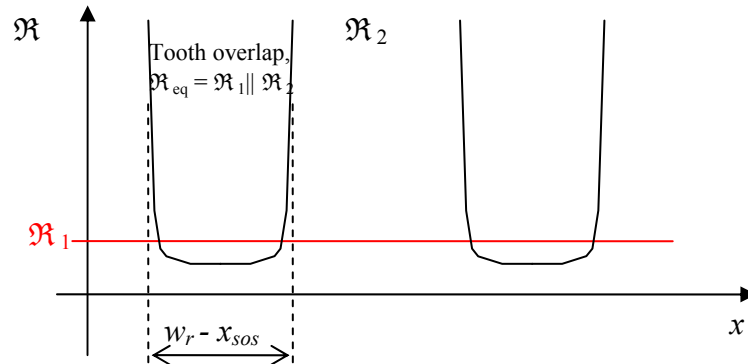


*Fig. A1.9 Reluctance variation*

Appendix 1: Equivalent circuit parameters

The mathematically correct approach would be to find, by integration, the resulting "product divided by sum" expression over the entire interval. However, given the uncertainties and simplifications in the geometry, this is probably not worthwhile.

Instead, the value of $\mathfrak{R}_2$ which represents the case where the centre of a rotor tooth is aligned with the centre of a stator tooth (a symmetric overlap) is calculated; this represents the value of $\mathfrak{R}_2$ in the whole interval $w_r - x_{sos}$. In this interval, the equivalent reluctance is the parallel reluctance combination of $\mathfrak{R}_1$ and $\mathfrak{R}_2$ while outside the interval it is equal to $\mathfrak{R}_1$.

The total equivalent reluctance is then the weighted average of the two. Therefore the value of $\mathfrak{R}_2$ representing a symmetric overlap is, from (A1.47):

$$\mathfrak{R}_2 = \frac{g}{L_{stk}\left(\dfrac{w_r - x_{sos}}{2}\right)} + \frac{g}{L_{stk}\left(\dfrac{w_r - x_{sos}}{2}\right)} = \frac{4g}{L_{stk}\left(w_r - x_{sos}\right)}$$

(A1.48)

and the parallel reluctance in the interval $w_r - x_{sos}$ is

$$\mathfrak{R}_p = \frac{\dfrac{4g}{L_{stk}\left(w_r - x_{sos}\right)}\left(\dfrac{g}{L_{stk}\,x_{sos}}\,2\ln\left(\dfrac{w_r}{w_r - x_{sos}}\right) + \dfrac{x_{sor}}{L_{stk}\,y_{ttr}}\right)}{\dfrac{4g}{L_{stk}\left(w_r - x_{sos}\right)} + \dfrac{g}{L_{stk}\,x_{sos}}\,2\ln\left(\dfrac{w_r}{w_r - x_{sos}}\right) + \dfrac{x_{sor}}{L_{stk}\,y_{ttr}}}$$

(A1.49)

and finally, the equivalent reluctance between to adjacent stator teeth is

$$\mathfrak{R}_{eq} = \frac{\lambda_r - (w_r - x_{sos})}{\lambda_r}\,\mathfrak{R}_1 + \frac{w_r - x_{sos}}{\lambda_r}\,\mathfrak{R}_p$$

(A1.50)

As stated initially in this section, zig-zag leakage is similar to belt leakage; the difference being the reluctance of their respective air-gaps. When comparing with expression (A1.41), it is noted that the expression $...L_{stk}\,y_{tt} / x_{sos}...$ is the *permeance*, or the *inverse of the reluctance*, of the slot opening geometry. Hence, an expression for zig-zag leakage inductance can be found by inserting the equivalent reluctance (A1.50) in (A1.41), i.e.:

$$L_{zz} = 4\sum_{s=1}^{S_1} \frac{N_s^2 \mu_0}{\mathfrak{R}_{eq}}$$

(A1.51)

Belt and zig-zag leakage also occur in the rotor with similar expressions to those derived in the above.

**The skew factor**

As investigated in Chapter 4, the slot harmonic effects are reduced by skewing the rotor by a certain angle over its length. This will cause the induced voltage in the rotor to be phase

shifted with respect to the field that sets it up, as well as affecting its magnitude. Skewing also affects rotor impedance since the bars become longer and their cross sections smaller. In addition, part of the developed electromagnetic torque is transferred into an axial force component. All these effects will be investigated in the following sections. Fig. A1.10 shows a rotor bar which is skewed at a certain angle $v$.
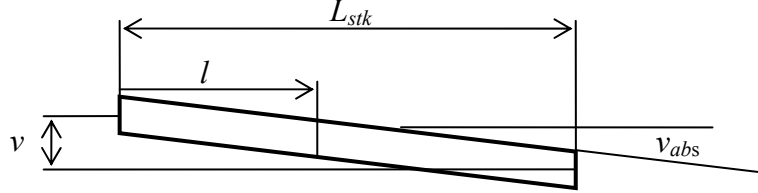


*Fig. A1.10 Bar skew representation*

In the following analysis, the induced voltage due to the $m^{th}$ harmonic field component is investigated in order to investigate the impact of skewing on the equivalent circuit parameters. If the skew is assumed uniformly distributed over the axial length of the rotor, the induced voltage in a bar section of length $dl$, axially situated at distance $l$ from either end of the rotor, is

$$de(l) = \frac{\partial}{\partial t} \frac{\partial}{\partial \theta} B_{fm} \, r \cos\left(\left[\frac{1}{m} - 1 + s\right]\omega t - m\left(\theta + l\frac{v}{L_{stk}}\right)\right) dl \tag{A1.52}$$

which means that the voltage induced into one bar is

$$
\begin{aligned}
e_b &= \int_0^{L_{stk}} \frac{\partial}{\partial t} \frac{\partial}{\partial \theta} B_{fm} \, r \cos\left(\left[\frac{1}{m} - 1 + s\right]\omega t - m\left(\theta + l\frac{v}{L_{stk}}\right)\right) dl \\
&= \frac{(1 - m + sm)\omega \, B_{fm} r \, L_{stk}}{mv}\left[-\sin\left(\left[\frac{1}{m} - 1 + s\right]\omega t - m\left(\theta - l\frac{v}{L_{stk}}\right)\right)\right]_0^{L_{stk}} \\
&= (1 - m + sm)\omega \, B_{fm} r \, L_{stk} \frac{2\sin\left(\frac{mv}{2}\right)}{mv} \cos\left(\left[\frac{1}{m} - 1 + s\right]\omega t - m\left(\theta - \frac{v}{2}\right)\right)
\end{aligned}
\tag{A1.53}
$$

        *skew factor*           *skew angle*

This expression is similar to the ones found in [8] and [9].

Hence, skewing reduces the magnitude of the induced rotor voltage, and displaces the rotor MMF relative to the air-gap flux density from which it was generated. In order to implement this in the calculations, the rotor impedance magnitude and argument are modified:

$$\bar{Z}_{sk} = \left|\bar{Z}\right| \frac{mv}{2\sin\left(\dfrac{mv}{2}\right)} \angle\left(\arg\left(\bar{Z}\right) + \frac{v}{2}\right)$$

(A1.54)

Only modifications to the rotor circuit are necessary, since the induced stator voltage remains the same as when the stator is not skewed. It is true that the magnitude of the air-gap flux density is affected by skewing, but since the air gap flux density is influenced by the rotor reactance, this is inherently accounted for. Furthermore, skewing affects the pure "per angle" reactance through dimension distortion, making the bars longer and narrower. This can be taken into account when calculating the absolute skew angle, as shown in Fig. 9.9. Where it is often common practice to have a fixed value of skew angle, e.g., corresponding to a stator tooth pitch, the absolute skew angle varies with the stack length. It can be calculated from

$$v_{abs} = \tan^{-1}\left(\frac{r\,v}{L_{stk}}\right)$$

(A1.55)

where $r$ is the rotor radius and $L_{stk}$ the length of the rotor stack. Therefore the effective bar area orthogonal to the bar current has been distorted by a factor $\cos(v_{abs})$, and its length has increased by a factor $1/\cos(v_{abs})$. The bar components of the original unskewed impedance $Z_{unsk}$ must be modified by

$$Z_{bar} = \frac{Z_{bar,unsk}}{\cos^2\left(v_{abs}\right)}$$

(A1.56)

Likewise, since the current is no longer orthogonal to the flux density, an axial force arises. This means that part of the output torque is being replaced by an axial force, which, when the rotor is fixed in axial direction, performs no work and therefore has an efficiency of 0. Its magnitude can be calculated from the rotational torque,

$$F_a = \frac{T_r}{r}\sin(v_{abs})$$

(A1.57)

where $T_r$ may be any component of rotational torque.

Equations (A1.56) and (A1.57) indicate that for a rotor with a given radius and skew angle (measured in slot pitches), the impact is greater for shorter rotor stack length.

A further undesired effect of rotor skewing may be the promotion of inter-bar rotor currents as described in [36]

## A1.7. Iron losses

Correct estimation of the iron losses requires an accurate knowledge of flux density in the main sections of the motor as well as loss data for the steel. This section aims to derive expressions for the iron losses in the equivalent circuit. The method was derived as part of

this project. However, a later literature survey revealed a similar approach which was described in [27]. The method described here is limited to the consideration of the fundamental flux density wave only. While this is a simplification, it should be stressed that iron loss estimation is not a main focus of this work. Superposition of the iron losses from harmonic flux densities waves is a tempting approach to include; this would, however, require the loss properties of the steel losses to be linear, which is not the case, as pointed out in the discussion section of [37].

**Epstein measurements versus motor characteristics**

The most common way of obtaining loss parameters for given steel samples is the Epstein square measurement, where a frame of steel sheets is sinusiodally magnetized at a specific frequency and peak flux density, typically 50 Hz and 1.5 T respectively. From this measurement the specific loss, in watts per kilogram, is obtained.

It should be underlined that in the Epstein square measurement every portion of the frame experiences the same instantaneous flux density and the magnitude of which varies sinusoidally over time. In a motor, the instantaneous flux density in the steel varies with position relative to the stator MMFs. If perfectly rotating MMFs are assumed (producing a single rotating flux wave), and the stator exerts a high degree of rotation symmetry (i.e., in a balanced 3-phase machine), the situation is similar to that of the Epstein measurement, although the peak flux density varies sinusoidally both in space and time. In this case, each infinitesimal section of the stator experiences a flux density which varies sinusoidally in time in a similar manner to the Epstein measurement. Therefore, for a balanced polyphase machine, the iron losses can easily be estimated when the flux density in the main flux paths are predicted with the iron losses slit into tooth losses and yoke losses [28].

However, in a single-phase motor, balanced operation can not be assumed due to the presence of backwards-rotating fields, which will distort the locus of the rotating MMF from a circle into an ellipse so that the peak flux density in the teeth and yoke has to be considered around the whole motor.

**The Steinmetz equation**

From [28] a model for obtaining iron the specific losses at a certain frequency and flux density is the Steinmetz equation which is defined as

$$p = C_h f B^n + C_e f^2 B^2 \qquad\qquad (A1.58)$$

with

$$C_h = \frac{h \, P_{base}}{\hat{B}_{base}^n \, f_{base}} \quad , \quad C_e = \frac{(1-h) \, P_{base}}{\hat{B}_{base}^n \, f_{base}^2} \tag{A1.59}$$

where $P_{base}$ are the measured specific iron losses at th base values of peak flux density and frequency, typically 1.5 T and 50 Hz respectively. Also $h$ is the ratio of hysteresis losses to total losses and $n$ is an empirical constant of value 1.6 – 1.8.

**Ellipsoid magnetisation**

For any operating point of a split-phase or single-phase machine, the magnetisation is determined by the forwards- and backwards-rotating fields, each of which is a constant-value field. When moving past each other, the resulting flux density will, at certain positions in the stator, be the sum of their values; and at other positions it will be the difference. As a result, an infinitesimal section of the stator will experience a flux density that oscillates in time - and the amplitude of which varies with position. This is shown in Fig. A1.11 for the fundamental field components.
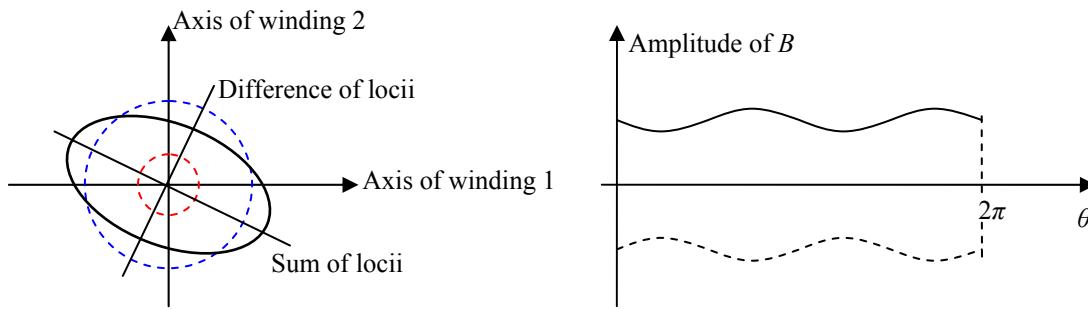


*Fig. A1.11 Effects of elliptical air gap flux rotation*

If the harmonic field components are taken into account as well, a series of higher harmonic ripples will be superimposed on to the oscillation as shown in Fig. A1.11. These will complicate the iron loss calculation greatly.

When calculating the iron losses, it is therefore necessary to predict the locus of the resulting ellipse. If the stator geometry is assumed symmetrical (i.e., round), the orientation of the ellipse is not important. From (2.32), the forwards-rotating flux density can be expressed by the main winding terms where

$$\bar{E}_{fm} = j \frac{N_m}{2} r \, L_{stk} \, \omega \, \pi \, \bar{B}_f \quad \Rightarrow$$

$$\bar{B}_f = \frac{-j \, 2 \, \bar{E}_{fm}}{N_m \, r \, L_{stk} \, \omega \, \pi} \tag{A1.60}$$

Likewise, the backwards flux density is

$$\bar{B}_b = \frac{-j\,2\bar{E}_{bm}}{N_m r L_{stk} \omega \pi} \tag{A1.61}$$

where both the forwards- and backwards-rotating field components are the resulting fields set up bothby main and auxiliary components. Since the peak flux density is used in the Steinmetz equation, (A1.60) and (A1.61) must be multiplied by $\sqrt{2}$.

As mentioned earlier, the minimum and maximum absolute values of the flux density are determined form the difference and the sum of the forwards- and backwards-rotating field components, respectively. These are

$$\hat{B}_{\min,g} = \frac{2\left(\hat{E}_{fm} - \hat{E}_{bm}\right)}{N_m r L_{stk} \omega \pi} \quad , \quad \hat{B}_{\max,g} = \frac{2\left(\hat{E}_{fm} + \hat{E}_{bm}\right)}{N_m r L_{stk} \omega \pi} \tag{A1.62}$$

An expression for the amplitude variation over the entire stator is therefore

$$\hat{B}_g(\theta) = \frac{\hat{B}_{\min,g} + \hat{B}_{\max,g}}{2} + \left(\frac{\hat{B}_{\max,g} - \hat{B}_{\min,g}}{2}\right)\sin(2\theta) \tag{A1.63}$$

The index $g$ indicates that these field values exist in the air-gap. When moving into the teeth and yoke regions, modifications will be necessary, since 1) the field will be discretised in the finite number of teeth, and 2) the flux density will change direction from radial to circumferential.

**Stator teeth losses**

Since the stator is slotted, the teeth will have to carry all the air-gap flux. In the following description, the amplitude of the oscillating flux density in each tooth will be derived together with the iron losses in each tooth. As a consequence of electromagnetic unbalance and the fact that tooth lengths may vary in some machines, the loss per tooth is not identical throughout the stator, as indicated in Fig. A1.12. However, here, it is assumed that the stator teeth are identical - otherwise the orientation of the ellipsoidal magnetization locus would have to be determined relative to the teeth lengths.
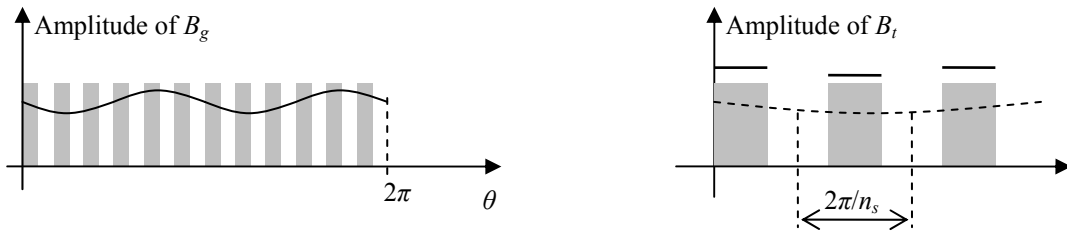


*Fig. A1.12 Effect of stator slotting on elliptical air gap flux*

In the following derivation, the $a^{th}$ tooth is considered. The flux density in the $a^{th}$ tooth is

$$B_{ta} = \frac{\Phi_a}{A_t} = \frac{L_{stk} r \displaystyle\int_{a\frac{2\pi}{n_s}}^{\frac{2\pi}{n_s}(1+a)} \hat{B}_g(\theta) d\theta}{L_{stk} w_t}$$

$$= \frac{r \, 2\pi}{n_s w_t} \frac{\hat{B}_{min,g} + \hat{B}_{max,g}}{2} + \frac{r}{w_t} \int_{a\frac{2\pi}{n_s}}^{\frac{2\pi}{n_s}(1+a)} \left( \frac{\hat{B}_{max,g} - \hat{B}_{min,g}}{2} \right) \sin(2\theta) \, d\theta \tag{A1.64}$$

$$= \frac{r\pi \left( \hat{B}_{min,g} + \hat{B}_{max,g} \right)}{n_s w_t} - \frac{r}{2 w_t} \left( \frac{\hat{B}_{max,g} - \hat{B}_{min,g}}{2} \right) \left[ \cos(2\theta) \right]_{a\frac{2\pi}{n_s}}^{\frac{2\pi}{n_s}(1+a)}$$

$$= \frac{r\pi \left( \hat{B}_{min,g} + \hat{B}_{max,g} \right)}{n_s w_t} - \frac{r}{2 w_t} \left( \frac{\hat{B}_{max,g} - \hat{B}_{min,g}}{2} \right) 2 \sin\left( \frac{2\pi(1+2a)}{n_s} \right) \sin\left( \frac{-2\pi}{n_s} \right)$$

From the Steinmetz equation (A1.59), the specific iron losses (in Watts per kilogram) in the $a^{th}$ tooth is

$$P_{ta} = C_h f B_{ta}^{\ n} + C_e \, f^2 B_{ta}^{\ 2} \tag{A1.65}$$

and since the tooth flux density is assumed uniform, the tooth loss for the $a^{th}$ tooth is

$$W_{ta} = P_{ta} \rho_{fe} w_t h_{t,avg} L_{stk} \tag{A1.66}$$

Finally, the total stator tooth losses may be found by summing (A1.66) for all the teeth:

$$W_{ta,tot} = \sum_{a=1}^{n_s} P_{ta} \rho_{fe} w_t h_{t,avg} L_{stk} \tag{A1.67}$$

It should be noted that (A1.67) assumes rectangular teeth of width $w_t$ and radial "height" $h_{ta}$, the latter of which may vary in some machines. The tooth tips can be analysed in a similar way, however these will experience additional flux density due to the leakage flux, and would therefore require extended analysis.

**Stator yoke losses**

The air-gap flux, which is sinusoidally distributed, but whose amplitude changes with position, is shown in Fig. A1.11. This is also present in the yoke where it changes direction from radial to circumferential. The yoke flux fundamental component is time-dependant and also sinusoidally distributed, with amplitude that varies with position (in the same way as for the air-gap flux). The total air gap flux is

$$\Phi_g = \int_0^\pi r L_{stk} \hat{B}_g \sin(\theta) \, d\theta = 2 r L_{stk} \hat{B}_g \tag{A1.68}$$

with $\hat{B}_g = \hat{B}_g(\theta)$ as given in (A1.63). This flux must return through the stator yoke, also creating a yoke flux density, which is sinusoidally distributed in space and whose amplitude is given by

$$\hat{B}_{sy}(\theta) = \frac{\dfrac{\Phi_g}{2}}{A_{sy}} = \frac{rL_{stk}\hat{B}_g(\theta)}{L_{stk}\, l_{sy}} \tag{A1.69}$$

At this stage, it is necessary to make the following assumptions: 1) the cross section of the yoke is constant, and 2) the stator outer geometry is approximated to a circle. Otherwise the yoke (asymmetric) geometry would have to be orientated relative to the ellipsoidal varying air-gap flux density. Although possible, it was found that these inclusions would complicate matters greatly. Given these assumptions, the yoke losses are found using Fig. A1.13; where an infinitesimal section of the circular yoke is considered.
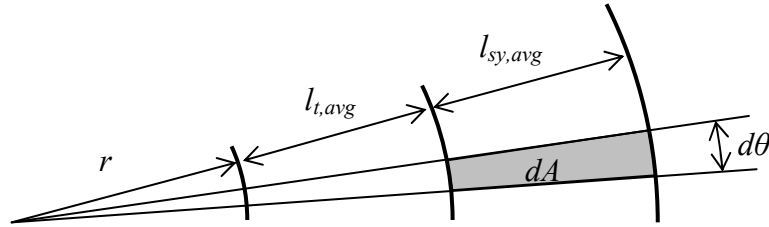


*Fig. A1.13 Yoke and tooth parameters*

The specific iron losses of the area *dA* are given by (A1.59), i.e.:

$$P_{sy}(\theta) = C_h f \hat{B}_{sy}(\theta)^n + C_e f^2 \hat{B}_{sy}(\theta)^2 \tag{A1.70}$$

and the corresponding iron loss over the whole section is

$$dW_{sy}(\theta) = P_{sy}(\theta)\, dm = P_{sy}(\theta)\, \rho_{fe} L_{stk}\, dA$$

$$= \left[ C_h f \hat{B}_{sy}(\theta)^n + C_e f^2 \hat{B}_{sy}(\theta)^2 \right] \rho_{fe} L_{stk} \left[ \frac{\left(r + l_{t,avg} + l_{sy}\right)^2 - \left(r + l_{t,avg}\right)^2}{2} \right] d\theta \tag{A1.71}$$

The total stator yoke losses can be obtained by integrating (A1.71) over the entire stator circumference when inserting the expression for $\hat{B}_g(\theta)$ as given in (9.65). This can be modified using the yoke flux density in (A1.69). Hence

$$W_{sy} = \rho_{fe} L_{stk} \left[ \frac{\left(r + l_{t,avg} + l_{sy}\right)^2 - \left(r + l_{t,avg}\right)^2}{2} \right] \int_0^{2\pi} \left[ C_h \, f\hat{B}_{sy}(\theta)^n + C_e \, f^2 \, \hat{B}_{sy}(\theta)^2 \right] d\theta$$

$$= \rho_{fe} L_{stk} \left[ \frac{\left(r + l_{t,avg} + l_{sy}\right)^2 - \left(r + l_{t,avg}\right)^2}{2} \right] C_h f \frac{r^n}{l_{sy}{}^n} \int_0^{2\pi} \left[ \frac{\dfrac{\hat{B}_{min,g} + \hat{B}_{max,g}}{2}}{+ \left( \dfrac{\hat{B}_{max,g} - \hat{B}_{min,g}}{2} \right) \sin(2\theta)} \right]^n d\theta +$$

$$+ \rho_{fe} L_{stk} \left[ \frac{\left(r + l_{t,avg} + l_{sy}\right)^2 - \left(r + l_{t,avg}\right)^2}{2} \right] C_e \frac{f^2 r^2}{l_{sy}{}^2} \int_0^{2\pi} \left[ \frac{\dfrac{\hat{B}_{min,g} + \hat{B}_{max,g}}{2}}{+ \left( \dfrac{\hat{B}_{max,g} - \hat{B}_{min,g}}{2} \right) \sin(2\theta)} \right]^2 d\theta$$

$$(A1.72)$$

There is no standard integral solution to (A1.72) but use of mathematical software Wolfram Research Mathematica® shows that (A1.72) has an exact solution containing four hyper geometric functions. Given the assumptions already made, an exact mathematical solution to (A1.72) is not considered worthwhile. Instead the integrals are solved discretely in a fixed number of steps, i.e.:

$$W_{sy} = \rho_{fe} L_{stk} \left[ \frac{\left(r + l_{t,avg} + l_{sy}\right)^2 - \left(r + l_{t,avg}\right)^2}{2} \right] C_h f \frac{r^n}{l_{sy}{}^n} \sum_{k=1}^{K} \left[ \frac{\dfrac{\hat{B}_{min,g} + \hat{B}_{max,g}}{2}}{+ \left( \dfrac{\hat{B}_{max,g} - \hat{B}_{min,g}}{2} \right) \sin\left( 2\frac{k \, 2\pi}{K} \right)} \right]^n \frac{2\pi}{K} +$$

$$+ \rho_{fe} L_{stk} \left[ \frac{\left(r + l_{t,avg} + l_{sy}\right)^2 - \left(r + l_{t,avg}\right)^2}{2} \right] C_e \frac{f^2 r^2}{l_{sy}{}^2} \sum_{k=1}^{K} \left[ \frac{\dfrac{\hat{B}_{min,g} + \hat{B}_{max,g}}{2}}{+ \left( \dfrac{\hat{B}_{max,g} - \hat{B}_{min,g}}{2} \right) \sin\left( 2\frac{k \, 2\pi}{K} \right)} \right]^2 \frac{2\pi}{K}$$

$$(A1.73)$$

where $K$ is the number of steps. The greater the value of $K$, the smaller the discretization error becomes. The sum of (A1.67) and (A1.73) gives a value for the stator iron losses due to the fundamental field components which link stator and rotor.


**Rotor losses**

For the normal operating range of a motor, the rotor iron losses are far lower than for the stator losses for two obvious reasons: 1) The forward revolving flux density rotates at a very

low frequency of only a few Hz with respect to the rotor, 2) The backward rotating flux density, although at almost twice line frequency, is small in magnitude.

However, during acceleration and at standstill, the rotor losses are substantial and therefore need to be analysed.

The approach applied to the derivation of stator teeth and yoke losses may be repeated; however a simplification must be made: the rotor rotates at $(1-s)\omega$, which means that the ellipsoidal magnetization locus actually rotates relative to the rotor at $s\omega$. This means that every small section of the rotor experiences the flux density corresponding to the maximum value of stator MMF, which is the numerical sum of the forward and backward MMF. However, the variation of the flux density is not sinusoidal, since it contains a second-order harmonic, which is not taken into account in the Steinmetz equation. Here, the 2$^{nd}$ order component is ignored and only the fundamental is considered. In this case (A1.67) and (A1.72) can be modified for rotor use. Assuming constant flux density over a section of air-gap corresponding to the width of a rotor tooth, the maximum rotor tooth flux density is

$$
\begin{aligned}
B_{ta} = \frac{\Phi_a}{A_{tr}} &= \frac{L_{stk} r \displaystyle\int_{a\frac{2\pi}{n_r}}^{\frac{2\pi}{n_r}(1+a)} \hat{B}_g(\theta)d\theta}{L_{stk}\, w_{tr}} \\[2mm]
&= \frac{r\, 2\,\pi}{n_r w_{tr}}\frac{\hat{B}_{min,g}+\hat{B}_{max,g}}{2} + \frac{r}{w_{tr}}\int_{a\frac{2\pi}{n_r}}^{\frac{2\pi}{n_r}(1+a)}\left(\frac{\hat{B}_{max,g}-\hat{B}_{min,g}}{2}\right)\sin(2\theta)\,d\theta \\[2mm]
&= \frac{r\,\pi\left(\hat{B}_{min,g}+\hat{B}_{max,g}\right)}{n_r w_{tr}} - \frac{r}{2\,w_{tr}}\left(\frac{\hat{B}_{max,g}-\hat{B}_{min,g}}{2}\right)\left[\cos(2\theta)\right]_{a\frac{2\pi}{n_r}}^{\frac{2\pi}{n_r}(1+a)} \\[2mm]
&= \frac{r\,\pi\left(\hat{B}_{min,g}+\hat{B}_{max,g}\right)}{n_r w_{tr}} - \frac{r}{2\,w_{tr}}\left(\frac{\hat{B}_{max,g}-\hat{B}_{min,g}}{2}\right)2\sin\left(\frac{2\pi(1+2a)}{n_r}\right)\sin\left(\frac{-2\pi}{n_r}\right)
\end{aligned}
\tag{A1.74}
$$

The corresponding specific iron loss becomes

$$
P_{tr} = C_h\,(1-s)f B_{ta}{}^n + C_e(1-s)^2 f^2 B_{ta}{}^2
\tag{A1.75}
$$

from which the total rotor teeth loss is

$$
W_{tr} = n_{tr} P_{tr} \rho_{fe} w_{tr} h_{tr} L_{stk}
\tag{A1.76}
$$

Similarly, from (A1.73) the rotor yoke losses can be found when modifying for the slip frequency, i.e.:

Appendix 1: Equivalent circuit parameters

$$W_{ry} = \rho_{fe}L_{stk}\left[\frac{(r-l_{tr})^2-(r-l_{tr}-l_{yr})^2}{2}\right]C_h\,(1-s)f\frac{r^n}{l_{ry}{}^n}\sum_{k=1}^{K}\left[\begin{array}{c}\frac{\hat{B}_{min,g}+\hat{B}_{max,g}}{2}\\+\left(\frac{\hat{B}_{max,g}-\hat{B}_{min,g}}{2}\right)\sin(2\frac{k\,2\,\pi}{K})\end{array}\right]^n\frac{2\,\pi}{K}+$$

$$+\rho_{fe}L_{stk}\left[\frac{(r-l_{tr})^2-(r-l_{tr}-l_{yr})^2}{2}\right]C_e\frac{(1-s)^2f^2r^2}{l_{ry}{}^2}\sum_{k=1}^{K}\left[\begin{array}{c}\frac{\hat{B}_{min,g}+\hat{B}_{max,g}}{2}\\+\left(\frac{\hat{B}_{max,g}-\hat{B}_{min,g}}{2}\right)\sin(2\frac{k\,2\,\pi}{K})\end{array}\right]^2\frac{2\,\pi}{K}$$

(A1.77)

**Leakage flux losses**

The losses described previously all relate to the main flux, i.e., the flux that crosses the air-gap and flows into the teeth and yokes of stator and rotor. Other components of flux exist, these being the leakage fluxes. The nature of leakage flux is complex; and the resulting losses even more so. Here, a simplified approach is nevertheless carried out.

The leakage flux losses in this section are assumed to be the total leakage inductance minus the end winding components. The total leakage losses are the sum of main and auxiliary winding leakage losses and these are added to the main field losses to give the total iron loss in the machine. This is a somewhat coarse simplification since the iron losses are due to the combination for the main and leakage fields together rather than consideration of different terms individually. Since the iron loss is generally a power-function of the amplitude, superposition is therefore thought to underestimate the true loss. However, it nevertheless represents the general tendency of the iron loss over the operating range. Fig. A1.14 shows the distribution of the leakage flux in the stator yoke.
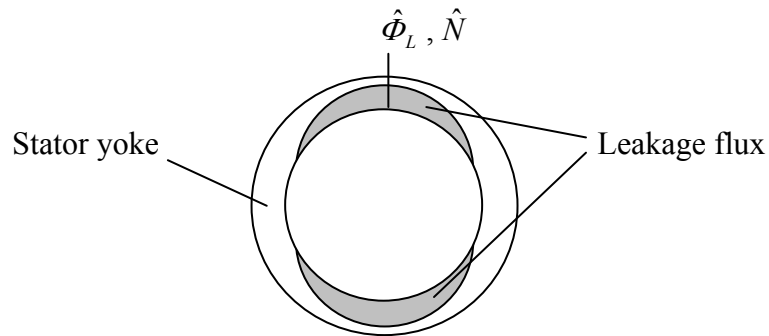


*Fig. A1.14 Stator leakage flux distribution*

Appendix 1: Equivalent circuit parameters

The peak value of leakage flux and therefore the leakage flux density are sought. Since inductance is defined as the flux linkage per unit current the yoke flux due to the axial components of leakage inductance can be obtained from

$$
\begin{aligned}
L_L - L_{end} &= \int_0^{2\pi} \frac{\frac{N}{2}\sin(\theta)\,\hat{\Phi}\,\sin(\theta)}{\hat{I}}\,d\theta \\
&= \frac{N\hat{\Phi}}{2\sqrt{2}\,I}\left[\frac{\theta}{2} - \frac{\sin(2\theta)}{4}\right]_0^{2\pi} \\
&= \frac{\pi N\hat{\Phi}}{2\sqrt{2}\,I}
\end{aligned}
\tag{A1.78}
$$

from which it follows that

$$
\hat{\Phi} = \frac{2\sqrt{2}\,I(L_L - L_{end})}{\pi N}
\tag{A1.79}
$$

and

$$
B_L(\theta) = \hat{B}_L\sin(\theta) = \frac{2\sqrt{2}\,I(L_L - L_{end})}{\pi N}\frac{1}{L\,h_{SY}}\sin(\theta)
\tag{A1.80}
$$

From (A1.59) the specific iron losses in the yoke are therefore:

$$
P_L(\theta) = C_h f B_L(\theta)^n + C_e f^2 B_L(\theta)^2
\tag{A1.81}
$$

and the infinitesimal iron losses of yoke section $d\theta$ are

$$
dW_L = P_L(\theta)\,\rho_{fe}\,L_{stk}\,\frac{\pi\left(r + l_{slot} + h_{sy}\right)^2 - \pi\left(r + l_{slot}\right)^2}{2\pi}\,d\theta
\tag{A1.82}
$$

The total stator yoke leakage loss is the integral of $dW_L$. Like (A1.72) there is no simple solution to this integral, which is therefore solved discretely, so

$$
\begin{aligned}
W_{sy} &= \rho_{fe}L_{stk}\left[\frac{\left(r + l_{t,avg} + l_{sy}\right)^2 - \left(r + l_{t,avg}\right)^2}{2}\right]C_h f\left(\frac{2\sqrt{2}\,I\left(L_L - L_{end}\right)}{N\,\pi\,L\,h_{sy}}\right)^n \sum_{k=1}^{K}\left[\sin\left(\frac{k\,2\,\pi}{K}\right)\right]^n\frac{2\,\pi}{K} + \\
&\quad + \rho_{fe}L_{stk}\left[\frac{\left(r + l_{t,avg} + l_{sy}\right)^2 - \left(r + l_{t,avg}\right)^2}{2}\right]C_e f^2\left(\frac{2\sqrt{2}\,I\left(L_L - L_{end}\right)}{N\,\pi\,L\,h_{sy}}\right)^2 \sum_{k=1}^{K}\left[\sin\left(\frac{k\,2\,\pi}{K}\right)\right]^2\frac{2\,\pi}{K}
\end{aligned}
\tag{A1.83}
$$

where $I$, $L_L$, $L_{end}$ and $N$ are the components of the winding under consideration.

So far the analysis has considered the stator yoke only, however, it is also applicable to the rotor yoke. This is done by separating into forwards- and backwards-rotating components and modifying for the rotational frequency, i.e., exchanging $f$ with $sf$ and $(2-s)\,f$ respectively.

Equation (A1.83) only represents the yoke leakage losses. Since part of this leakage flux flows through the slots, i.e. in air, the teeth leakage losses are smaller and are thus disregarded.

**Representation of iron losses**

In order to include the iron losses in the motor performance calculated from the equivalent circuit it is necessary to include a resistance whose value is determined from the calculated iron losses. Since both the main and auxiliary windings contribute to the iron losses it would make sense to include a resistance in both circuits, and let each represent the same fraction of total iron loss. This is obtained from a ratio of the induced voltages due to each field component, i.e.:

$$\frac{W_{fe,main}}{W_{fe,aux}} = \frac{\left|\overline{E}_{fm}\right| + \left|\overline{E}_{bm}\right|}{\left|\dfrac{-j}{\beta}\overline{E}_{fa}\right| + \left|\dfrac{j}{\beta}\overline{E}_{ba}\right|} \tag{A1.84}$$

and since $W_{fe,tot} = W_{fe,main} + W_{fe,aux}$ it follows that

$$W_{fe,aux} = \frac{W_{fe,tot}}{\dfrac{\left|\overline{E}_{fm}\right| + \left|\overline{E}_{bm}\right|}{\left|\frac{-j}{\beta}\overline{E}_{fa}\right| + \left|\frac{j}{\beta}\overline{E}_{ba}\right|} + 1} \quad , \quad W_{fe,main} = W_{fe,tot}\left(1 - \frac{1}{\dfrac{\left|\overline{E}_{fm}\right| + \left|\overline{E}_{bm}\right|}{\left|\frac{-j}{\beta}\overline{E}_{fa}\right| + \left|\frac{j}{\beta}\overline{E}_{ba}\right|} + 1}\right) \tag{A1.85}$$

In order to feed the iron losses through to the stator windings, the iron loss resistances are placed in parallel with the magnetizing branch of the respective winding, as illustrated in Fig. A1.15 for the main winding circuit:
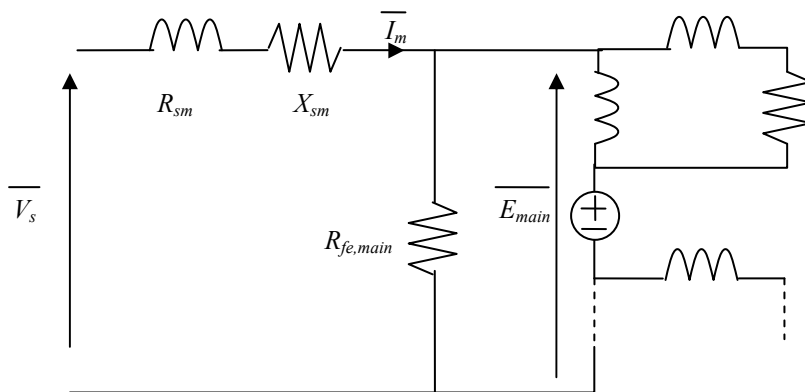


*Fig. A1.15 Equivalent circuit including iron loss resistance*

When placed here, the power dissipated in the resistance is determined from the magnitude of the resulting induced voltage due to all the component of flux densities. Therefore

$$R_{fe,main} = \frac{E_{main}^2}{W_{fe,main}} \quad , \quad R_{fe,aux} = \frac{E_{aux}^2}{W_{fe,aux}} \tag{A1.86}$$

with

$$E_{main} = \left| \overline{V}_s - \overline{I}_m \left( R_{sm} + jX_{sm} \right) \right| \quad , \quad E_{aux} = \left| \overline{V}_s - \overline{I}_a \left( \overline{Z}_{aux} + R_{sm} + jX_{sm} \right) \right| \tag{A1.87}$$

Fig. A1.16 show the variation of the different iron loss components over the speed range from standstill to near-synchronous speed for an arbitrary machine when using the iron loss model developed here.
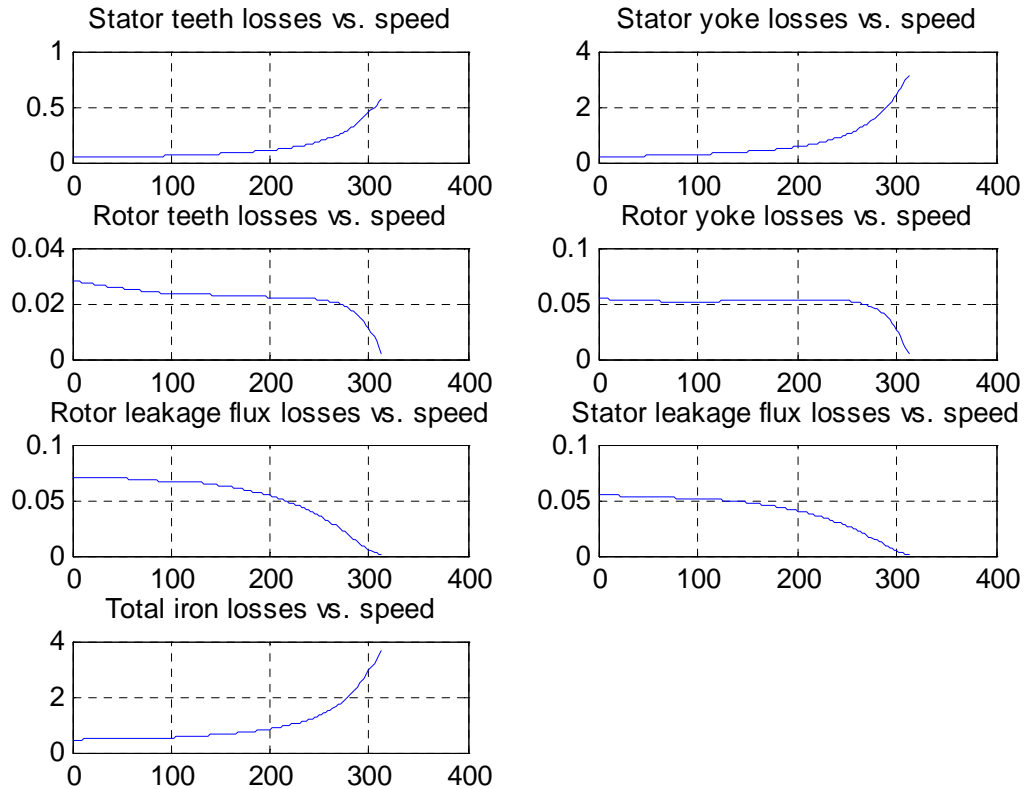


*Fig. A1.16 Variation of losses (W) with speed (rad/s)*

In Section 3.6, the predicted performances of several machines were put forward. These simulations used models whose parameters were calculated using the expressions derived in this appendix. These results were compared with actual measurements and reasonable correlation was found.

# Appendix 2

# Quasi-steady-state torque measurement

This appendix describes the tests that were carried out in relation to Section 5.4

## A2.1 Background

In order to compare the performances of the skewed and unskewed rotors used in Section 5.4, two unskewed rotors were fabricated: an 18 slot rotor, which was thought to result in the smallest magnitudes of synchronous locking torque, and a 24 slot rotor, thought to result in the most severe case of synchronous locking torque. These were tested together with a 28 slot rotor skewed by one stator slot.

**Test rotors**

Figs. A2.1, A2.2 and A2.3 show the cross sections of the three rotor types.
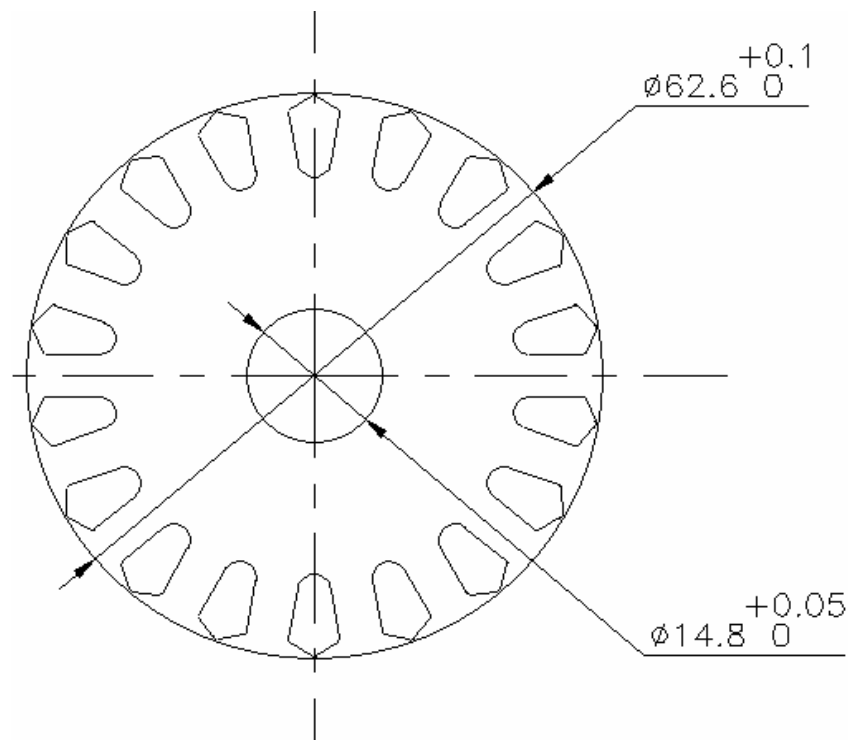


*Fig. A2.1 Cross-section of 18 bar rotor (unskewed rotor)*
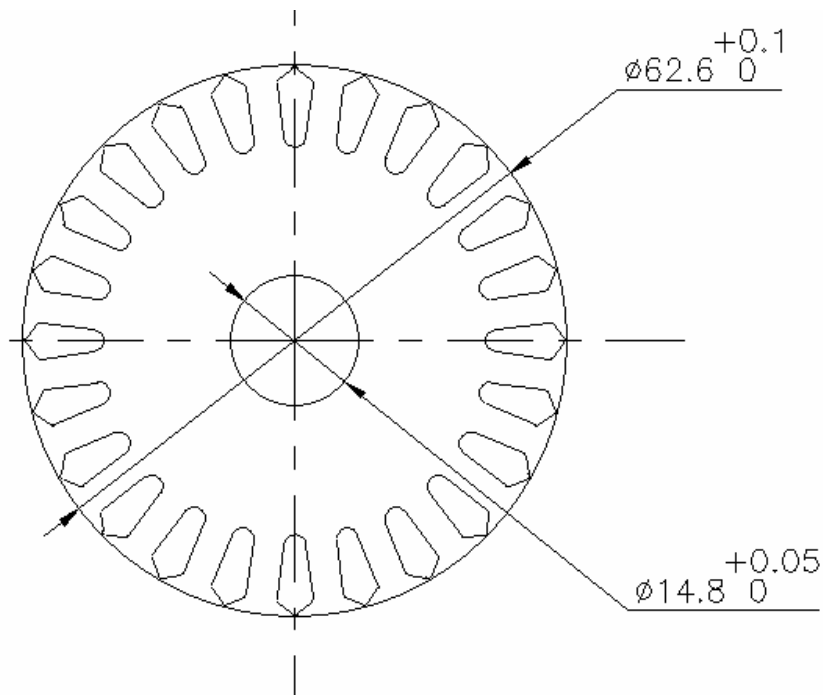
*Fig. A2.2 Cross-section of 24 bar rotor (unskewed rotor)*
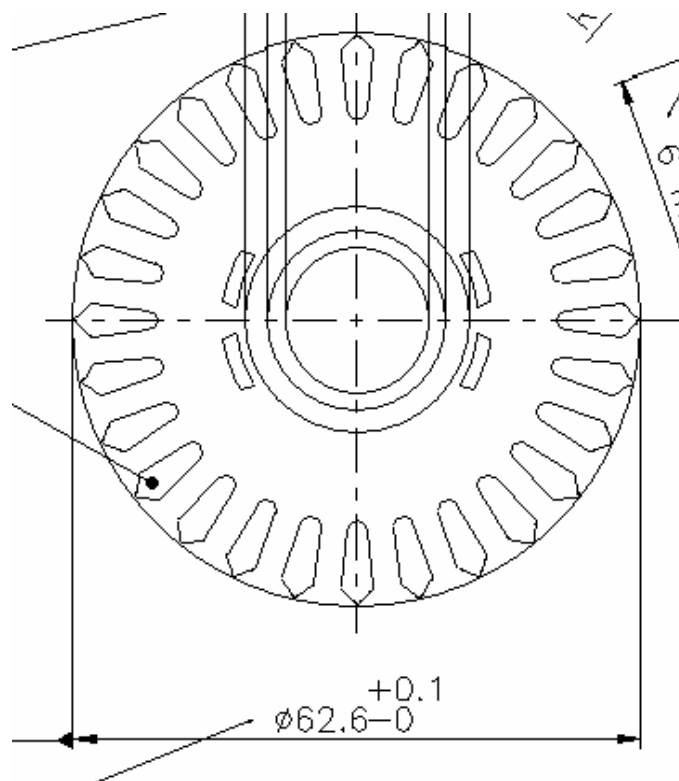


*Fig. A2.3 Cross-section of 28 bar rotor (skewed rotor)*

The rotors were so designed so that the total aluminium was constant. It should be noted that the given dimensions are cutting dimensions. Final rotor outside diameter was machined down to Ø 62.45 mm. The rotor laminations shown in Figs. A2.1 and A2.2 were laser cut from plate steel, whereas the rotor shown in Fig. A2.3 is a standard production rotor, which

was stamped. All 3 rotor types had identical end rings, shown in Fig. A2.4. Fig. A2.5 illustrates one of the test rotors, after stacking, casting and machining. For each rotor type, five rotors were made, resulting in fifteen rotors.
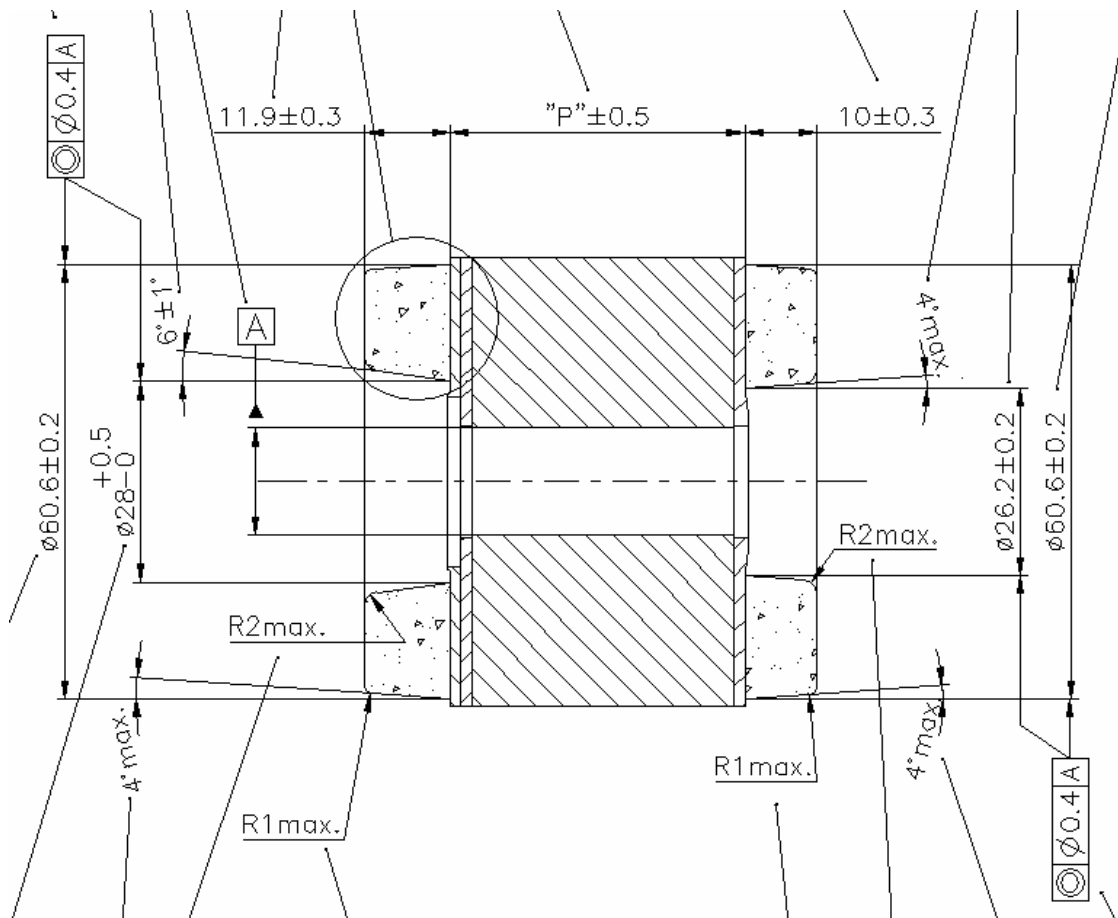


*Fig. A2.4 Drawings of rotor axial section for all three rotors*



*Fig. A2.5 Manufactured cast rotor*

## A2.2 Test setup

The tests were split in four parts:

**1      Efficiency curves over a limited operating range**

This would display the differences in efficiency obtained at steady-state for the three rotor types

**2      Torque-speed curves from synchronous to zero speed (run condition)**

This would displays the differences in pull-out torque at steady state for the thee rotor types

**3       Slow deceleration from 500rpm to 0 rpm (start condition)**

This would indicate the occurrence of any synchronous locking torque at low speed. The rate of speed change is relatively small, limiting the influence of inertia.

**4      Continuous logging of torque at <1 rpm**

This would indicate the occurrence of locking torque at zero speed. In practice, for safety reasons, this test was carried out at reduced voltage (66 $V_{rms}$) and the shaft turned slowly by hand, at a fraction of an rpm. By logging data continuously for a 30 seconds time interval, a scatter plot would indicate the minimum and maximum values of torque and thus illustrate the peak-to-peak values of synchronous locking torques at standstill.

The tests were performed at Danfoss Compressors GmbH motor measurement laboratory, using a test bench with compensated bearing losses and electronic data logging via a Norma D6100 power analyzer. Fig. A2.6 shows the motor test bench and data logging equipment.
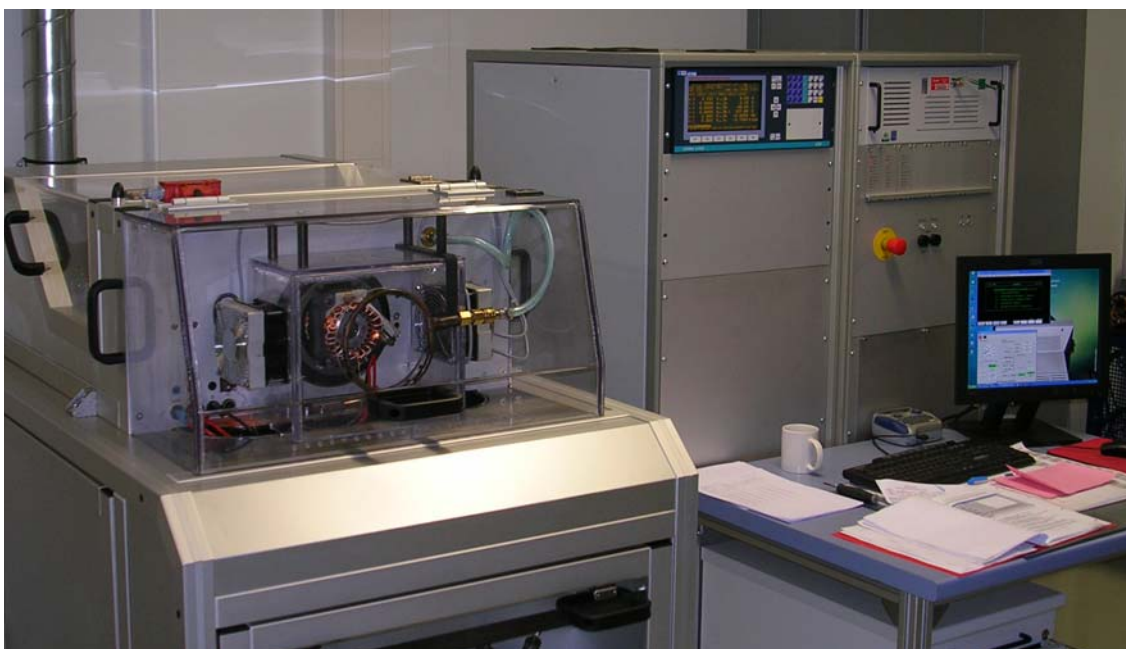


*Fig. A2.6 Motor test facility (Danfoss facility)*

Appendix 2: Quasi-steady-state torque measurement

Some key parameters of the test equipment can be found in table A2.1

|  | Force Transducer HTM S2 50N | Power Analyzer Norma D6100 Wide Band |
|---|---|---|
| Accuracy | 0,05% | 0,05% |
| Band width | < 50 Hz | DC – 1 MHz (3Mhz claimed) |

*Table A2.1*

## A2.3 Test results

In the following sections, the results from the four different tests described in A2.2 are given.

**1. Efficiency curves**

Fig. A2.7 shows an average for the five rotors of each type, where efficiency against load torque is plotted. 18 slot unskewed variant is red, 24 slot unskewed variant is green and 28 slot skewed variant is blue. Test conditions were 220 V / 50 Hz and run capacitor of 3.5 µF.
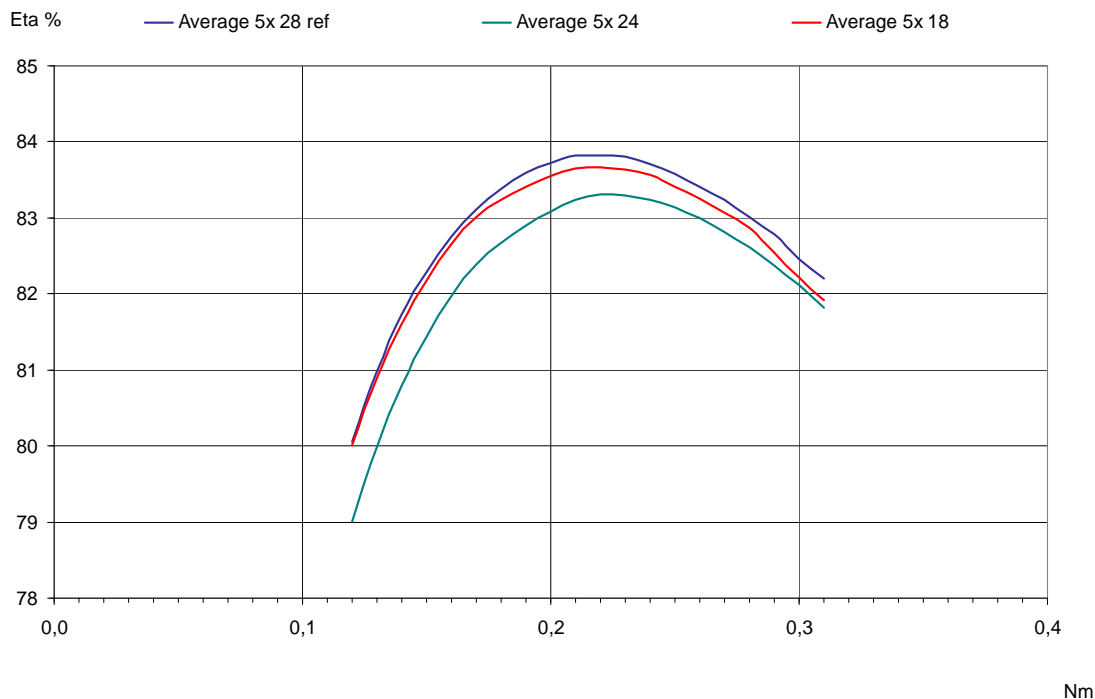


*Fig. A2.7 Efficiency against torque plot for different rotors (blue – 28 bar rotor, red – 24 bar rotor and green – 18 bar rotor)*

**2. Torque-speed curves**

Fig. A2.8 shows the torque-speed relationship for all fifteen rotors in the test series, plotted in the same graph. Each rotor type uses a separate colour: the 18 slot unskewed rotor is red, the 24 slot unskewed rotor is green and the 28 slot skewed reference rotor is blue. Test conditions

were 198 V, 50 Hz and used a run capacitor of 3.5 µF (198 V is commonly used to test pull-out torque, since this is the lower tolerance voltage of a 220 V supply system).

Torque = f(Rpm)

P.Scavenius ; TLX8,7KK4 ; Stator=117L7261-2 ; U=198V/50Hz ; R=0V/A ; T=80°C ; C=3,5µF ; (27.09.2006)
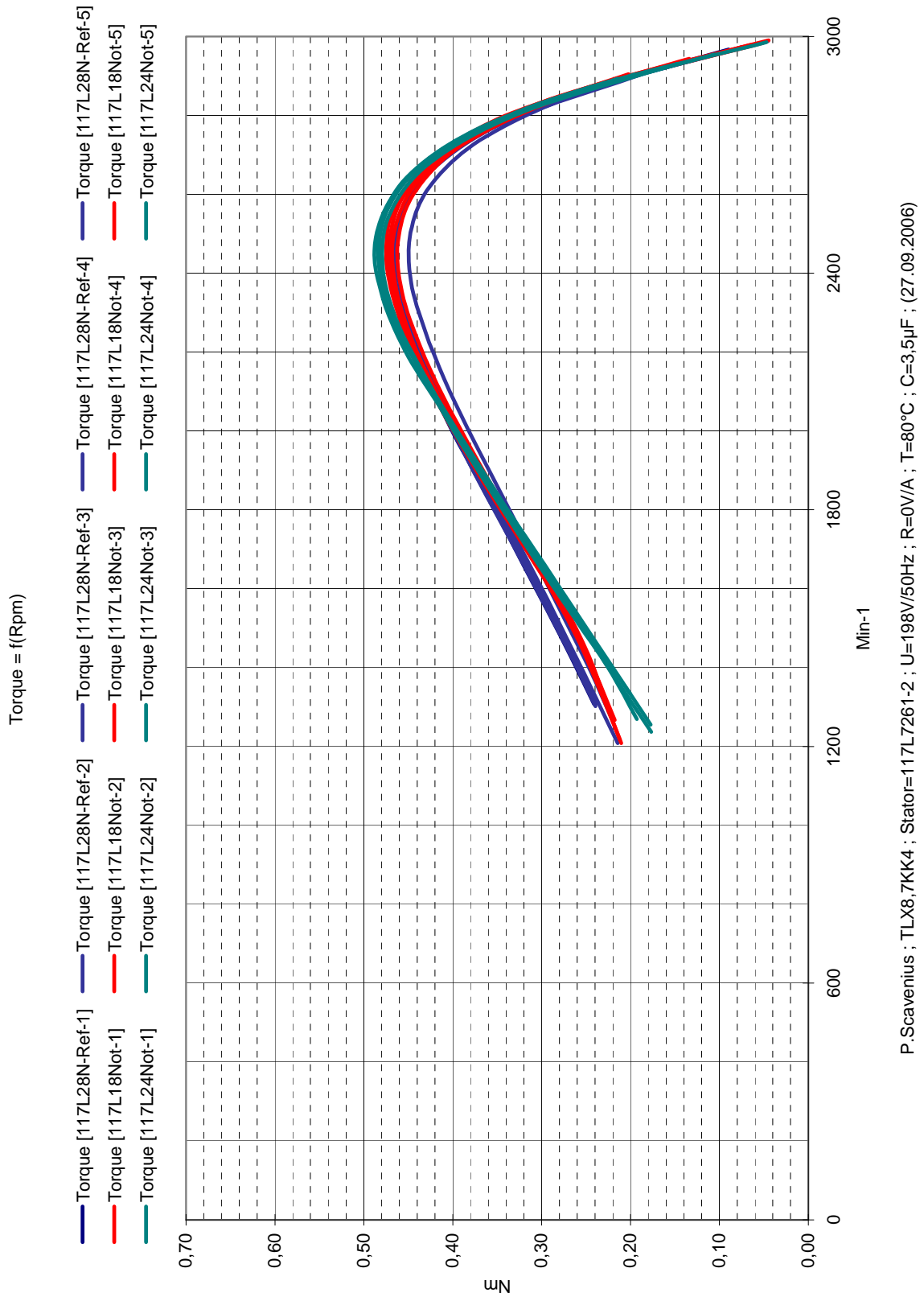
*Fig. A2.8 Torque-speed curves for different rotors*

## 3. Deceleration at slow rate

Figs. A2.9, A2.10 and A2.11 show the torque vs. speed plots from 500 to 0 rpm for the 18, 24 and skewed 28 slot rotors. Five rotors of the same type are plotted in each graph. Test conditions were 198 V/50 Hz with an auxiliary resistance of 25 Ω (start condition).
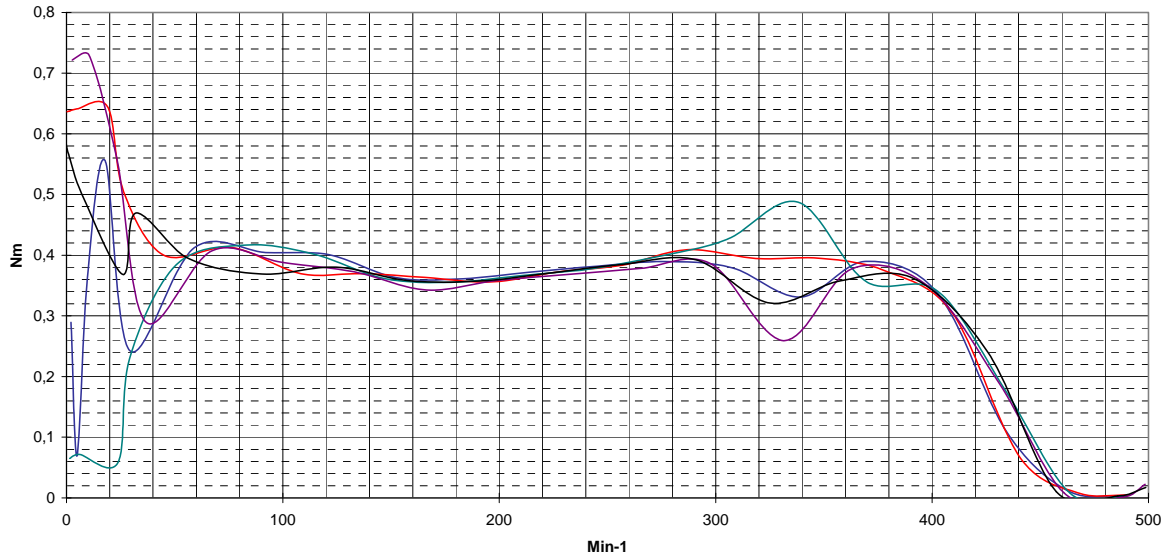


*Fig. A2.9 Deceleration test for18 bar rotor (500 rpm down to 0 rpm)*
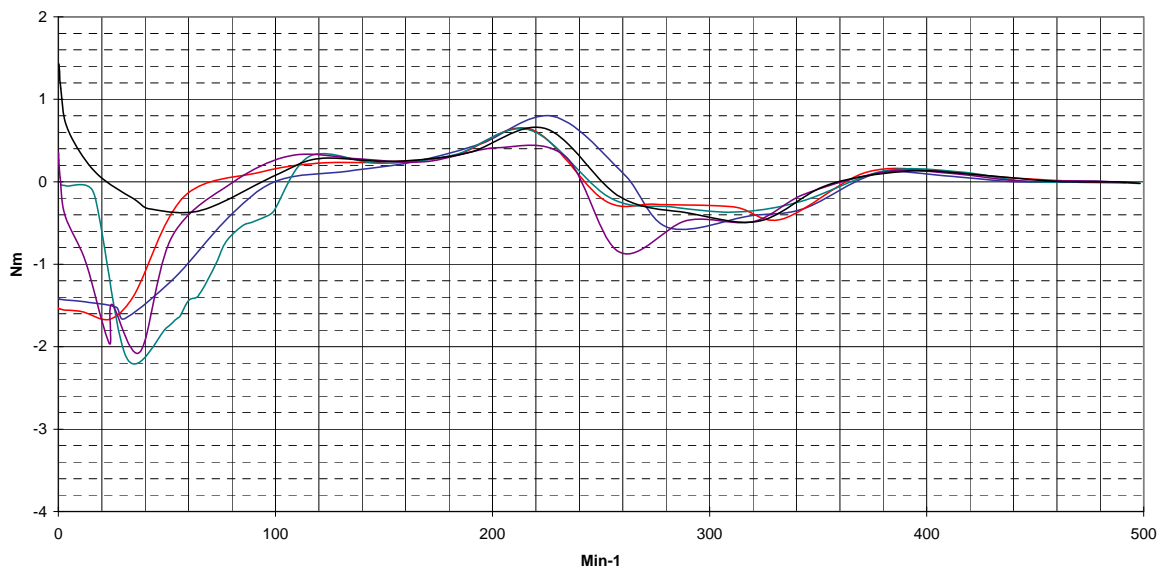


*Fig. A2.10 Deceleration test for24 bar rotor (500 rpm down to 0 rpm)*

Appendix 2: Quasi-steady-state torque measurement
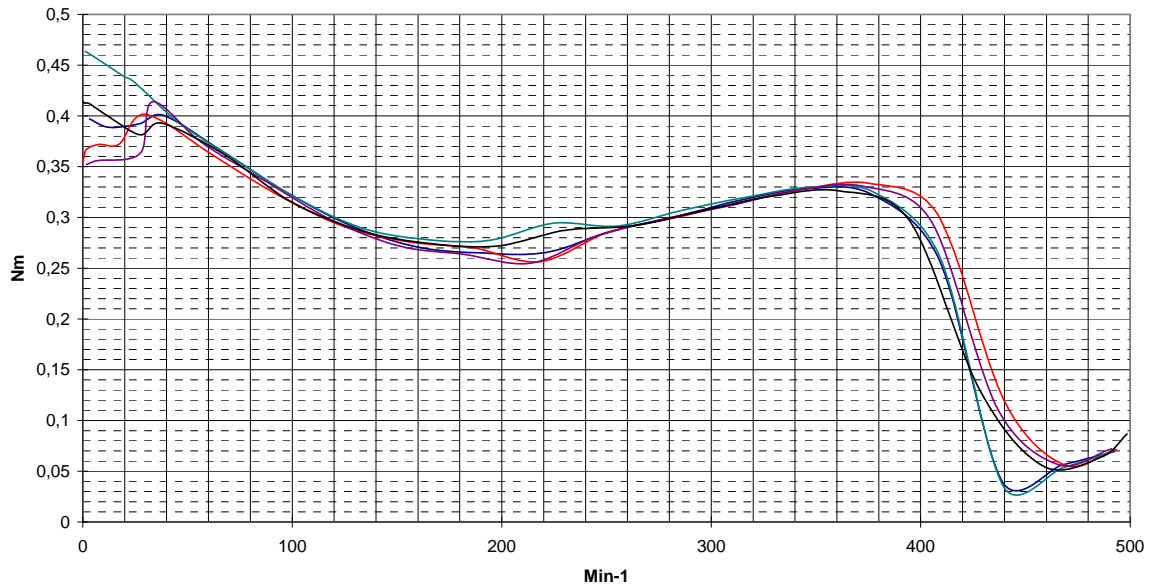


*Fig. A2.11 Deceleration test for28 bar rotor (500 rpm down to 0 rpm)*

The "average" torque values, i.e. when ignoring perturbations in figs. A2.9 – A2.11, are seen to be not comparable to true steady state values. This is because the test equipment has a pre-programmed friction toque correction curve, which presupposes a certain acceleration rate. Deviations from this acceleration rate results in values being off-set; however, in this case only the perturbations and not the mean values themselves are of interest.

**4. Torque pulsation at fractional rpm**

Figs. A2.12, A2.13 and A2.14 show the torque values at a sample frequency of 2 Hz by very slow manual rotation of the 18, 24 and skewed 28 slot rotors as described in point 4 in A2.2. Only one rotor of each type is plotted in each graph. Test conditions are 66 V/50 Hz with an auxiliary resistance is 25 Ω (start condition).
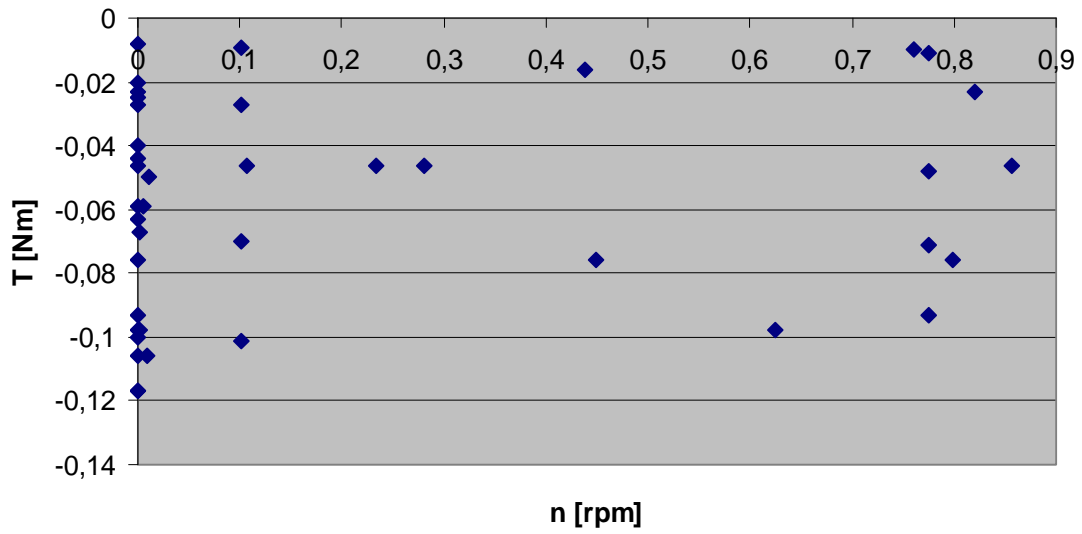
## 18 slots



*Fig. A2.12 Synchronous torque measurements for 18 slot machine*

## 24 slots
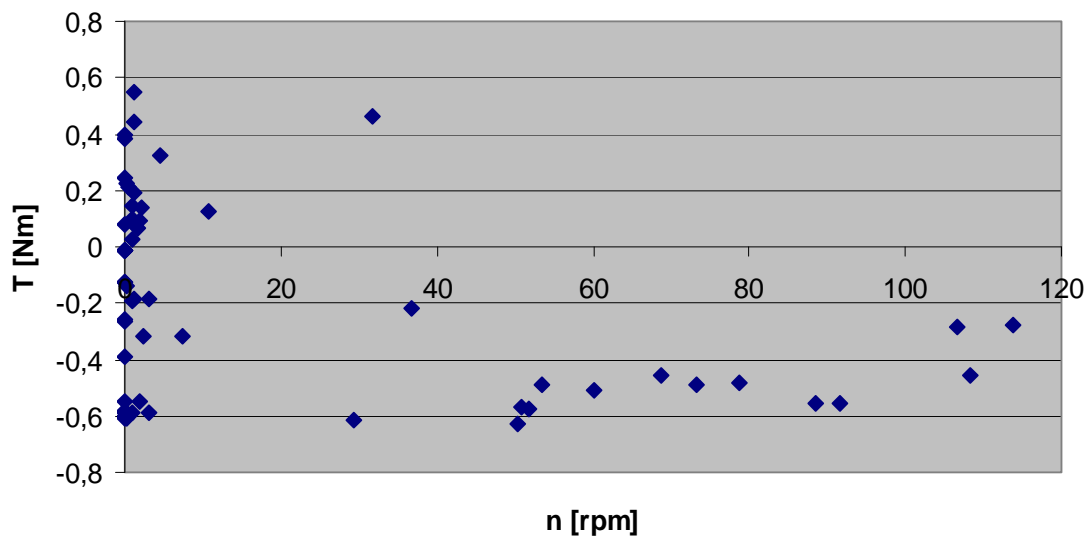


*Fig. A2.13 Synchronous torque measurements for 24 slot machine*

**28 slots skewed (ref)**
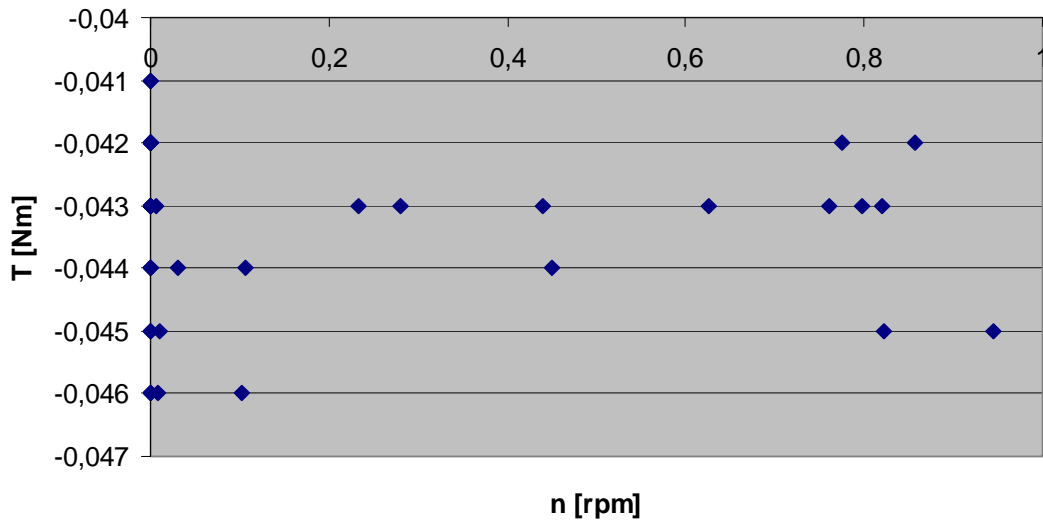


*Fig. A2.14 Synchronous torque measurements for 28 slot machine*

These values can be scaled to the voltage at which the other measurements were made by multiplying with a factor (198 $V_{rms}$/66 $V_{rms}$)$^2$ = 9. This is valid since the model can be assumed linear, due to the low flux density levels of the motor during operation. The iron losses would be under predicted, but are not relevant for this analysis, since the iron losses at locked rotor is only a very small fraction of the power being absorbed by the machine. Figs. A.15 to A.17 show the scatter plots of torque values, rescaled to 198 V.

**18 slots**
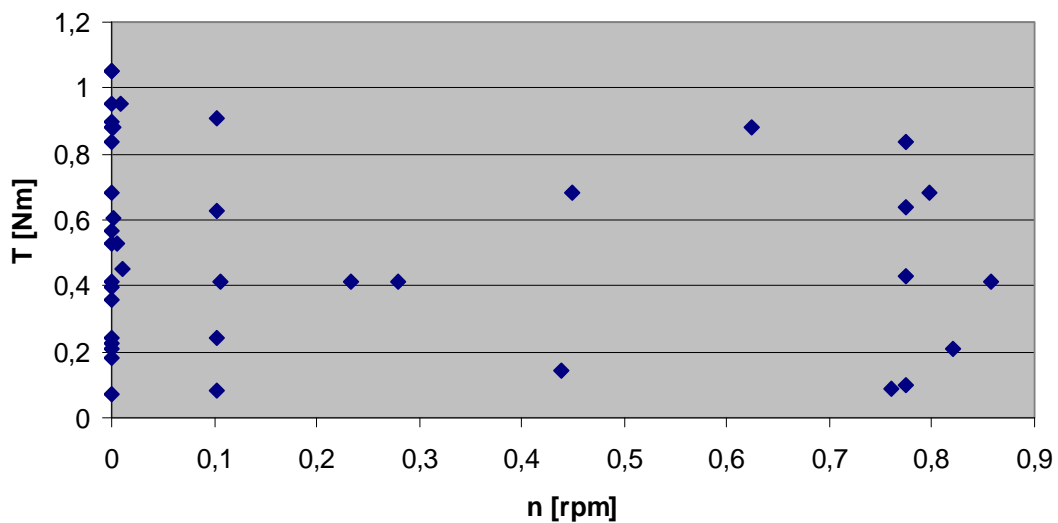


*Fig. A2.15 Synchronous torque measurements for 18 slot machine (rescaled to 198 V)*

**24 slots**
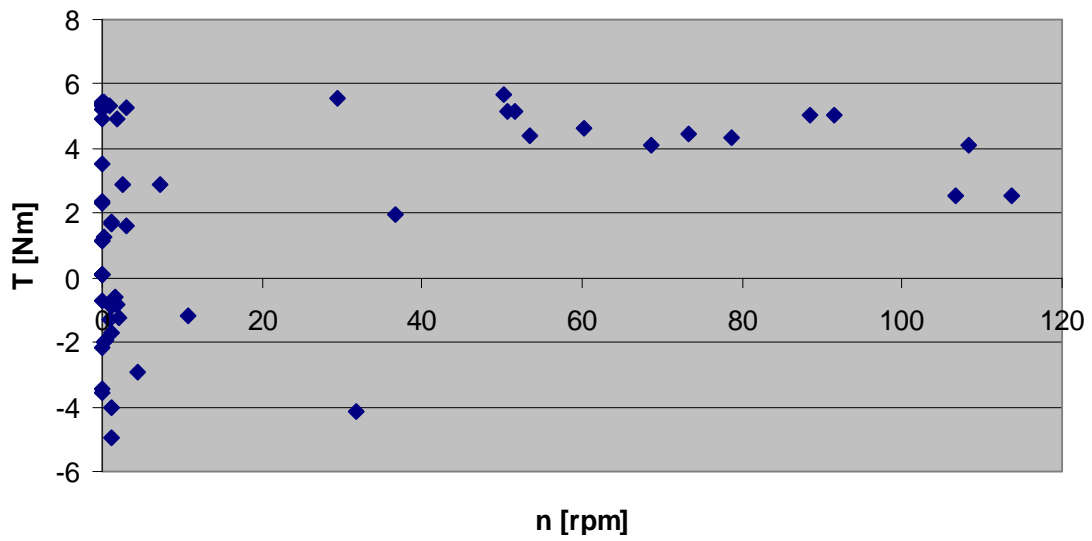


*Fig. A2.16 Synchronous torque measurements for 24 slot machine (rescaled to 198 V)*

**28 slots skewed (ref)**
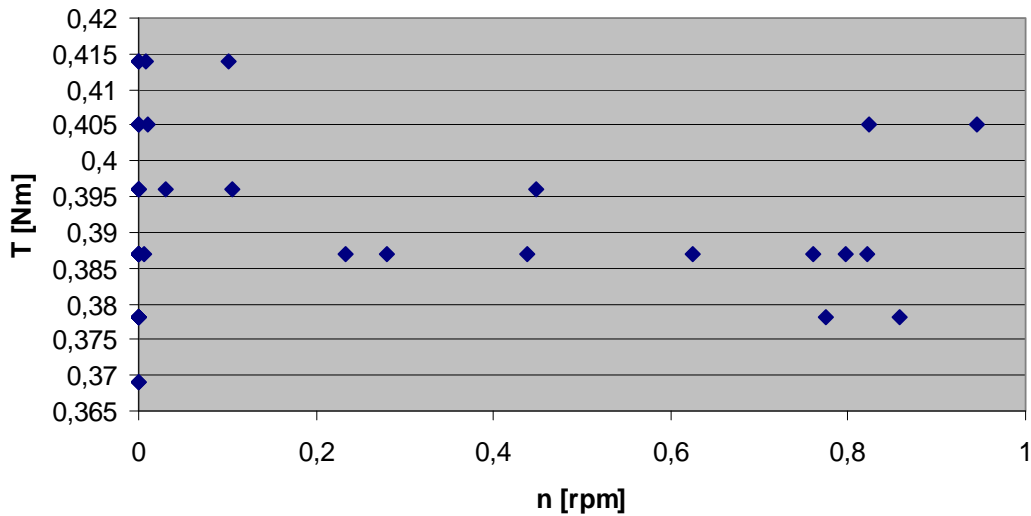


*Fig. A2.17 Synchronous torque measurements for 28 slot machine (rescaled to 198 V)*

## *A2.4 Conclusions*

By inspection of Fig. A2.7 it can be seen that operation with an unskewed rotor does not have a beneficial impact on the motor efficiency; whereas it can be seen from Fig. A2.8 that the maximum torque is increased by a few percent when the rotor is unskewed. From Fig. A2.8 it is also evident that while the 18 (unskewed) slot and 28 (skewed) slot rotors results in broadly identical steady-state torque vs. speed graphs, the 24 slot variant deviates significantly from

these, although the rotor resistances should be the same. Furthermore, at low speed, the 24 slot rotor causes the motor to exhibit large torque variations.

When decelerating slowly from 500 to 0 rpm, the 18 slot unskewed rotor exhibits locking tendencies at 330 rpm, indicated by the positive and negative deviations from the idealised line. The 24 slot rotor exhibits severe pulsations at around 260 rpm. Even the 28 slot skewed rotor shows pulsations at around 220 rpm.

When rotating the rotor slowly at a fraction of an rpm and logging the torque continuously, the measurements become confined to within a band, whose height is an indicator for the locking torque at standstill.

The 18 slot unskewed rotor is seen to have approximately ten times larger locking torque at standstill when compared to the 28 slot skewed rotor. The locking torque of the 24 slot unskewed rotor is much more severe, the magnitude being around ten times larger than that of the 18 slot variant. The conclusions are discussed further in Section 6.4.

# Appendix 3

# Specifications of simulation and test machines

In this appendix a set of data for the motors used in the thesis is put forward for comparing measurements and model predictions. They are listed in order of appearance with a reference to the section in which they are described. All units are in mm when not otherwise specified.

## *Section 3.6: 220V, 50 Hz RSCR motor*

| *Mechanical properties* | | | *Winding properties* | |
|---|---|---|---|---|
| Stator outer radius (eq) | 56.5 | | Main winding distribution (Quarter winding) | 0-46-76-110-118-118 |
| Bore radius | 31.52 | | Main wire diameter | 0.65 |
| Rotor radius | 31.23 | | Aux winding distribution (Quarter winding) | 85-85-79-65-0-0 |
| Shaft radius | 8 | | Aux wire diameter | 0.45 |
| Stator stack length | 48.5 | | Start / Run equipment | 25 $\Omega$ / 4 $\mu$F |
| Rotor stack length | 49 | | Stator number of slots | 24 |
| Axial rotor end ring length | 12 | | Rotor number of slots | 28 |
| Stator tooth width | 3.56 | | Stator slot opening | 2,1 |
| Rotor tooth width | 2,9 | | Rotor bridge depth | 0.2 |
| Stator yoke (eq) | 13 | | Stator slot depth (Quarter winding) | 9, 0-11, 6-14, 6-15, 7-14, 6-14, 6 |
| Rotor yoke | 11.7 | | Rotor bar area | $2.3 \times 10^{-5}$ m$^2$ |
| Steel grade | 3.4 W/kg | | Rotor skew | 1 stator slot pitch |

## *Section 3.6 and 7.1: 115V, 60 Hz RSIR motor*

| *Mechanical properties* | | | *Winding properties* | |
|---|---|---|---|---|
| Stator outer radius (eq) | 56.5 | | Main winding distribution (Quarter winding) | 0-0-33-53-55-55 |
| Bore radius | 28.02 | | Main wire diameter | 0.82 (equivalent) |
| Rotor radius | 27.65 | | Aux winding distribution (Quarter winding) | 25-25-31-0-0-0 (net) 40-40-31-0-0-0 (tot) |
| Shaft radius | 8.5 | | Aux wire diameter | 0.475 |
| Stator stack length | 40 | | Start / Run equipment | 5 $\Omega$ / 50 k$\Omega$ |
| Rotor stack length | 41 | | Stator number of slots | 24 |
| Axial rotor end ring length | 10 | | Rotor number of slots | 28 |
| Stator tooth width | 3.56 | | Stator slot opening | 1.63 |
| Rotor tooth width | 2.5 | | Rotor bridge depth | 0,2 |
| Stator yoke (eq) | 12.5 | | Stator slot depth (Quarter winding) | 9, 0-11, 6-14, 6-15, 7-14, 6-14, 6 |
| Rotor yoke | 10.5 | | Rotor bar area | $1.9 \times 10^{-5}$ m$^2$ |
| Steel grade | 8.0 W/kg | | Rotor skew | 1 stator slot pitch |

Appendix 3: Specifications of simulation and test machines

*Section 5.3: 220V, 50 Hz RSCR motor*

| Mechanical properties | | | Winding properties | |
|---|---|---|---|---|
| Stator outer radius (eq) | 56.5 | | Main winding distribution (Quarter winding) | 0-46-76-110-118-118 |
| Bore radius | 31.52 | | Main wire diameter | 0.65 |
| Rotor radius | 31.23 | | Aux winding distribution (Quarter winding) | 85-85-79-65-0-0 |
| Shaft radius | 8 | | Aux wire diameter | 0,45 |
| Stator stack length | 48.5 | | Start / Run equipment | 25 Ω / 4 µF |
| Rotor stack length | 49 | | Stator number of slots | 24 |
| Axial rotor end ring length | 12 | | Rotor number of slots | [10-12-...-40] |
| Stator tooth width | 3.56 | | Stator slot opening | 2.1 |
| Rotor tooth width | 2.9 | | Rotor bridge depth | 0.2 |
| Stator yoke (eq) | 13 | | Stator slot depth (Quarter winding) | 9, 0-11, 6-14, 6-15, 7-14, 6-14, 6 |
| Rotor yoke | 11.7 | | Rotor bar area | $6.6 \times 10^{-4}$ m$^2$ / [10-12-...-40] |
| Steel grade | 3.4 W/kg | | Rotor skew | 0 |

*Section 5.3: 115V, 60 Hz RSIR motor*

| Mechanical properties | | | Winding properties | |
|---|---|---|---|---|
| Stator outer radius (eq) | 56,5 | | Main winding distribution (Quarter winding) | 0-0-33-53-55-55 |
| Bore radius | 28,02 | | Main wire diameter | 0,82 (eq.) |
| Rotor radius | 27,65 | | Aux winding distribution (Quarter winding) | 25-25-31-0-0-0 (net) 40-40-31-0-0-0 (tot) |
| Shaft radius | 8,5 | | Aux wire diameter | 0,475 |
| Stator stack length | 40 | | Start / Run equipment | 5Ω / 50kΩ |
| Rotor stack length | 41 | | Stator number of slots | 24 |
| Axial rotor end ring length | 10 | | Rotor number of slots | [10-12-...-40] |
| Stator tooth width | 3,56 | | Stator slot opening | 1,63 |
| Rotor tooth width | 2,5 | | Rotor bridge depth | 0,2 |
| Stator yoke (eq) | 12,5 | | Stator slot depth (Quarter winding) | 9,0-11,6-14,6-15,7-14,6-14,6 |
| Rotor yoke | 10,5 | | Rotor bar area | $5.3 \times 10^{-4}$ m$^2$ / [10-12-...-40] |
| Steel grade | 8,0 W/kg | | Rotor skew | 0 |

### Section 5.3: 220V, 50 Hz RSCR motor (variant)

| Mechanical properties | | | Winding properties | |
|---|---|---|---|---|
| Stator outer radius (eq) | 56.5 | | Main winding distribution (Quarter winding) | 0-0-96-96-126-126 |
| Bore radius | 31.52 | | Main wire diameter | 0.65 |
| Rotor radius | 31.23 | | Aux winding distribution (Quarter winding) | 92-92-70-70-0-0 |
| Shaft radius | 8 | | Aux wire diameter | 0.45 |
| Stator stack length | 48.5 | | Start / Run equipment | 25 Ω / 4 μF |
| Rotor stack length | 49 | | Stator number of slots | 24 |
| Axial rotor end ring length | 12 | | Rotor number of slots | [10-12-...-40] |
| Stator tooth width | 3.56 | | Stator slot opening | 2.1 |
| Rotor tooth width | 2.9 | | Rotor bridge depth | 0.2 |
| Stator yoke (eq) | 13 | | Stator slot depth (Quarter winding) | 9, 0-11, 6-14, 6-15, 7-14, 6-14, 6 |
| Rotor yoke | 11.7 | | Rotor bar area | $6.6 \times 10^{-4}$ m$^2$ / [10-12-...-40] |
| Steel grade | 3.4 W/kg | | Rotor skew | 0 |

### Chapter 6 and Section 7.2: 230V, 50 Hz RSCR motor

| Mechanical properties | | | Winding properties | |
|---|---|---|---|---|
| Stator outer radius (eq) | 56.5 | | Main winding distribution (Quarter winding) | 0-57-96-124-148-148 |
| Bore radius | 31.52 | | Main wire diameter | 0.56 |
| Rotor radius | 31.22 | | Aux winding distribution (Quarter winding) | 78-72-67-46-0-0 |
| Shaft radius | 7.5 | | Aux wire diameter | 0.45 |
| Stator stack length | 40 | | Start / Run equipment | 25Ω / 3.5μF |
| Rotor stack length | 41 | | Stator number of slots | 24 |
| Axial rotor end ring length | 12 | | Rotor number of slots | [10-12-...-40] |
| Stator tooth width | 3.56 | | Stator slot opening | 2.1 |
| Rotor tooth width | 2.9 | | Rotor bridge depth | 0,2 |
| Stator yoke (eq) | 12.5 | | Stator slot depth (Quarter winding) | 9, 0-11, 6-14, 6-15, 7-14, 6-14, 6 |
| Rotor yoke | 11.7 | | Rotor bar area | $6.6 \times 10^{-4}$ m$^2$ / [10-12-...-40] |
| Steel grade | 3.4 W/kg | | Rotor skew | 0 |

### Section 7.1: 115V, 60 Hz RSIR motor identical to the one in section 3.6

### Section 7.2: 230V, 50 Hz RSCR motor identical to the one in chapter 6

# Appendix 4

# Published papers

As part of this research, two papers were published. They are:

P. Scavenius Andersen and D. G Dorrell,

"Modelling of Split-Phase Induction Machine using Rotating Field Theory", International

Conference on Electrical Machines ICEM 2006,

September 2-5, Crete, Greece.

P. Scavenius Andersen, D. G. Dorrell, N. C. Weihrauch and P. E. Hansen,

"Analysis of the Synchronous Torques in a Split Phase Induction Motor",

IEEE Power electronics Drives and systems Conference PEDS,

December 2007, Bangkok, Thailand.

The papers are given in full in the following pages.

# Modeling of Split-Phase Induction Machine using Rotating Field Theory

Peter Scavenius Andersen and David G Dorrell

*Abstract*—**This paper puts forward an analysis method for a split-phase induction motor using surface integrals and an equivalent circuit. It can account for forwards and backwards rotating air-gap fields as well as MMF harmonics. The algorithm is implemented and a set of results obtained to illustrate the simulation technique.**

*Index Terms*—**Single phase, split phase, induction motor, asynchronous torque**

## I. INTRODUCTION

SPLIT phase motor analysis (where there is a main winding and an auxiliary winding that are orthogonal to each other but are not identical) usually assume a sinusoidal winding so that only the fundamental forwards and backwards rotating MMFs need to be modelled. The usual way to analyze these machines uses the cross-field or revolving field techniques. These two methods are well documented by Veinott [1]. For a two-phase machine the 5th MMF harmonic asynchronous torque rotates forwards and the 7th backwards, etc, (whereas for a three-phase machine the 5th rotates backwards and the 7th rotates forwards), and there may also be a substantial a 3rd MMF harmonic asynchronous torque dip [2]. In a split phase machine, the phase imbalance leads to both forwards and backwards rotating fields for each harmonic. This was investigated in [3] using an impedance matrix method; however in this paper, a more classical equivalent circuit method is used. A machine model will be adopted and results will be put forward.

The effects of the asynchronous torques was addressed experimentally in [4]. This illustrated that the winding harmonics do have a substantial influence on the torque characteristic and hence why manufacturers do strive to manufacture machines with sinusoidal, or close to sinusoidal, MMF distribution in the stator winding, in which case the revolving field analysis, as described in [5], is perfectly valid.

These machines are essentially single phase machines with the main winding directly fed from the supply. The auxiliary

P. Scavenius Andersen is with Danfoss Compressors GmbH, Motor R&D, Mads Clausen Str. 7, D-24939 Flensburg, Germany (email: p.scavenius@danfoss.de).

D. G. Dorrell is with The Department of Electronics and Electrical Engineering, University of Glasgow, Glasgow, G12 8LT, UK (e-mail: d.dorrell@elec.gla.ac.uk).

winding, which is usually in quadrature to the main winding (though not necessarily so if the slot number is inconvenient [6]), and connected in parallel. The auxiliary may also have a capacitor or resistor, or combination of the two, connected in series with it to produce a phase difference in the main and auxiliary winding currents and hence help generate a revolving MMF rather than a pulsating MMF. Some split phase machines may only use the auxiliary during the starting period. It is then switched out at a point somewhere around 75 % of the synchronous speed. Other machines may keep the auxiliary winding connected in circuit during steady-state operation. If this is the case, there is still likely to be some sort of switching during run up (at about 75 % full speed) because the starting and running requirements for the auxiliary winding (resistance and/or capacitor) will be very different and require different components. The switching can be done in several different ways, i.e., using a centrifugal switch or a *PTC* (Positive Temperature Coefficient) thermistor.

The outcome from this discussion is that the spit phase machine is not a straightforward machine to simulate, however the literature is still remarkably sparse. This paper will outline a study into a model that can be applied generally. It uses rotating field theory and equivalent circuits with spatial MMF harmonics to describe the machine. These are more generally applied to multiphase machines but are equally valid here.

## II. ANALYSIS

The paper will first derive an algorithm and equivalent circuit that can be used to simulate the machine.

### A. Winding Distribution and MMF

First, we have to consider the winding distribution of the stator windings. The total numbers of turns in the main and auxiliary phases are $N_M$ and $N_A$ - so that, in terms of the distribution around the inner bore of the stator, they can be represented as:

$$N_M^m(\theta) = \frac{N_M^m}{2}\cos(\theta) \tag{1}$$

$$N_A^m(\theta) = \frac{N_A^m}{2}\sin(\theta) \tag{2}$$

where we are considering the fundamental winding harmonic. The winding coefficients can be obtained from standard winding Fourier decomposition of the winding distribution. If the main winding is excited by a sine-varying current, an MMF will be created on the stator surface, which pulsates in

time and is sinusoidally distributed in space. Considering the main MMF to be sinusoidal:

$$F_S^M(t,\theta) = \frac{N_m}{2}\cos(\theta)I_M\sin(\omega t)$$

$$= \frac{N_M I_m}{4}\left(\sin(\omega t - \theta) + \sin(\omega t + \theta)\right) \quad (3)$$

MMF rotation = forward + backward waves

This represents two rotating components of MMF (in terms of ampere-turns). The ampere-turns are of equal magnitude, but rotate in opposite directions at the angular velocity $\omega$. This means that the stator winding can be split into halves: one which creates the forward rotating field and one which creates the backwards rotating field. The rotational speed of the rotor is determined by $\omega$, the voltage, the slip, the supply frequency and the number of poles however the angular velocity of the MMF waves is simply a function of the supply frequency and pole number, if we replace (3) with a general $p$ pole-pair wave and harmonic $m$:

$$F_S(t,\theta) = \sum_m \frac{N_M^m}{2}\cos(mp\theta)I_m\sin(\omega t)$$

$$= \sum_m \frac{N_M^m I_m}{4}\left(\sin(\omega t - mp\theta) + \sin(\omega t + mp\theta)\right) \quad (4)$$

### B. Induced EMF and Magnetizing Reactance

If we assume an air-gap flux density distribution

$$b_S^m(t,\theta) = \frac{B_S^m}{2}\left(\cos(\omega t - mp\theta) - \cos(\omega t + mp\theta)\right) \quad (5)$$

The air-gap electric field is

$$e_S^m(t,\theta) = \frac{d}{dt}rL\int b_S^m(t,\theta)d\theta$$

$$e_S^m(t,\theta) = \frac{rLB_S^m}{2}\frac{\int \cos(\omega t - mp\theta) - \cos(\omega t + mp\theta)d\theta}{dt} \quad (6)$$

$$e_S^m(t,\theta) = -\frac{\omega rLB_S^m}{2mp}\left(\cos(\omega t - mp\theta) + \cos(\omega t + mp\theta)\right)$$

From (6) and (1) the voltage induced in the main winding can be found by integrating round half the machine to obtain the flux linkage with the winding so that

$$E_S^m(t) = \int_0^\pi -e_S^m(t,\theta)N_M^m(\theta)d\theta$$

$$E_S^m(t) = \int_0^\pi \frac{\omega rLB_S^m}{2mp}\left(\cos(\omega t - mp\theta) + \cos(\omega t + mp\theta)\right)$$

$$\times \frac{N_M^m}{2}\cos(mp\theta)d\theta \quad (7)$$

$$E_S^m(t) = \int_0^\pi \frac{\omega rLN_M^m B_S^m}{4mp}\left(\begin{array}{c}\cos(\omega t) + \cos(\omega t - 2mp\theta) \\ +\cos(\omega t + 2mp\theta) + \cos(\omega t)\end{array}\right)d\theta$$

$$E_S^m(t) = \frac{\pi\omega rLN_M^m B_S^m}{2mp}\cos(\omega t)$$

where $L$ is tha axial length and $r$ is the average air-gap radius. We can express the air-gap flux density in terms of the current where

$$b_S^m(t,\theta) = \int \mu_o \frac{F_S^m(t,\theta)}{g}d\theta$$

$$= \int \mu_o \frac{N_M^m I_m\left(\sin(\omega t - mp\theta) + \sin(\omega t + mp\theta)\right)}{4g}d\theta \quad (8)$$

$$= \frac{\mu_o N_M^m I_m}{4gmp}\left(\cos(\omega t - mp\theta) - \cos(\omega t + mp\theta)\right)$$

Putting (7) and (8) together leads to an expression for the magnetizing reactance where:

$$E_S^m(t) = \frac{\mu_o\pi\omega rL\left(N_M^m\right)^2 I_m}{4g\left(mp\right)^2}\cos(\omega t) \quad (9)$$

It can be seen that the voltage leads the current by 90 elec deg, therefore, from (9) we can obtain the main magnetizing reactance for the $m^{th}$ harmonic:

$$X_M^m = \frac{X_{Mf}^m}{2} + \frac{X_{Mb}^m}{2} = \frac{\mu_o\pi\omega rL\left(N_M^m\right)^2}{4g\left(mp\right)^2} \quad (10)$$

The magnetizing reactance from (6), can be seen to be split evenly between the forwards-rotating field and the backwards-rotating field. The auxiliary winding will also have a similar reactance $X_{ma}$.

### C. Rotor Forwards and Backwards Fields and Electric Field

The air-gap fields, with respect to the stator, rotate at

$$b_S^m(t,\theta) = \frac{B_S^m}{2}\left(\cos(\omega t - mp\theta) - \cos(\omega t + mp\theta)\right) \quad (11)$$

However, with respect to the rotor, the frequencies are

$$\omega_f^m = \left(1 - m(1-s)\right)\omega$$
$$\omega_b^m = \left(1 + m(1-s)\right)\omega \quad (12)$$

so that

$$b_S^m(t,\theta') = \frac{B_S^m}{2}\left(\begin{array}{c}\cos\left((1-m(1-s))\omega t - mp\theta'\right) \\ -\cos\left((1+m(1-s))\omega t + mp\theta'\right)\end{array}\right) \quad (13)$$

The stator electric field in rotor co-ordinates is then

$$e_S^m(t,\theta') = -\frac{\omega rLB_S^m}{2mp}\left(\begin{array}{c}\cos\left((1-m(1-s))\omega t - mp\theta'\right) \\ +\cos\left((1+m(1-s))\omega t + mp\theta'\right)\end{array}\right) \quad (14)$$

### D. Rotor-Stator Linkage

The electric field in (14) will induce an emf into the rotor case. If we assume that the rotor has a surface impedance, and we consider a thin section $d\theta$, then the electric field induces a voltage into the rotor. Therefore the resulting voltage along the length of the rotor stack is the difference across the element $d\theta$. If the direction out of the paper plane in Fig. 1 is chosen positive, the resulting electric field becomes

$$e_S^m(t,\theta) - e_S^m(t,\theta + d\theta) = -de_S^m(t,\theta) \quad (15)$$

Modifying (7), the resulting voltage in the rotor conductor is (in terms of the forwards and backward rotating field):

$$-dE_S^m(t,\theta) = rL\frac{d}{dt}\left(\frac{dB_{Sf}^m(t,\theta)}{d\theta} + \frac{dB_{Sb}^m(t,\theta)}{d\theta}\right)d\theta \quad (16)$$

The current at angle $\theta$ in the conducting path defined by $d\theta$ is driven by the resulting voltage and limited by the impedance, which is likewise defined by the area of the path:

$$i_r^m(t,\theta)d\theta = \frac{-dE_S^m(t,\theta)}{\overline{Z}_{f,b}^m \big/ d\theta} = \frac{-dE_S^m(t,\theta)d\theta}{\overline{Z}_{f,b}^m}$$

$$i_r^m(t,\theta) = \frac{-dE_S^m(t,\theta)}{\overline{Z}_{f,b}^m} = \frac{1}{\overline{Z}_{f,b}^m}rL\frac{d}{dt}\left(\frac{dB_{Sf}^m(t,\theta)}{d\theta} + \frac{dB_{Sb}^m(t,\theta)}{d\theta}\right) \quad (17)$$

Concentrating on the fundamental forwards-rotating field, and moving to phasor notation:

$$\overline{I}_{Sf}^1 = \frac{1}{\overline{Z}_f^m}js\omega(-j)\overline{B}_{Sf}^1 rL = \frac{1}{\overline{Z}_f^m}s\omega rL\overline{B}_{Sf}^1 \quad (18)$$

and for the backwards-rotating field:

$$\overline{I}_{Sb}^1(t,\theta) = \frac{1}{\overline{Z}_b^m}(2-s)\omega rL\overline{B}_{Sb}^1 \quad (19)$$

This illustrates the linkage between the rotor and the stator. Higher harmonics produce a similar linkage. Further combination of (18) and (19) with (7) will produce an expression for the emf induced in the stator winding due to the rotor current.
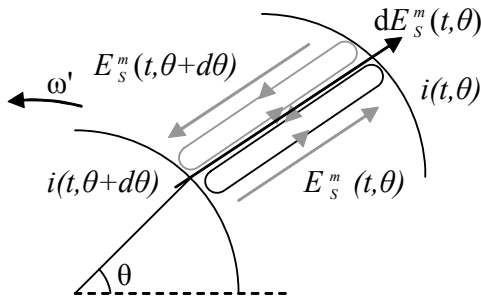


Fig. 1 Rotor surface conventions

### E. Rotor Impedance

In (17), $\overline{Z}_{f,b}^m/d\theta$ is the impedance of the path defined by the angle $d\theta$. This impedance is hardly measurable; however it can be expressed in terms of a measurable/calculable impedance of a section of the rotor, defined by the angle $\alpha$. This impedance $\overline{Z}_{\alpha(f,b)}^m$ is the parallel impedance of an infinitely large number of $\overline{Z}_{f,b}^m/d\theta$ sections so that

$$\frac{1}{\overline{Z}_{\alpha(f,b)}^m} = \left(\frac{d\theta}{\overline{Z}_{f,b}^m} + \frac{d\theta}{\overline{Z}_{f,b}^m} + \cdots\right) = \int_0^\alpha \frac{1}{\overline{Z}_{f,b}^m}d\theta$$

$$\overline{Z}_{f,b}^m = \alpha m \overline{Z}_{\alpha(f,b)}^m = \alpha m\left(R_\alpha^m + jX_{\alpha(f,b)}^m\right) \quad (20)$$

$$= R_r^m + jX_{r(f,b)}^m$$

First, considering the resistive component using the definitions in Fig. 2:

$$R_r^m = R_{\alpha(bar)} + 2R_{\alpha(end-ring)}^m$$

$$= mp\alpha\rho\frac{L_B}{A_B(\alpha)} + 2\frac{(mp\alpha)^2}{4\sin^2\left(mp\pi\big/N_b\right)}\frac{\rho}{L_E}\left(\frac{1}{\ln(r_o)-\ln(r_i)}\right) \quad (21)$$

and similarly for leakage (and this will have separate forwards and backwards rotating components):

$$X_{r(f,b)}^m = X_{\alpha(bar)}^m + 2X_{\alpha(end-ring)}^m \quad (22)$$

This will account for the bar and end-ring leakage as well as the differential leakage. Skew can also be incorporated at this point.
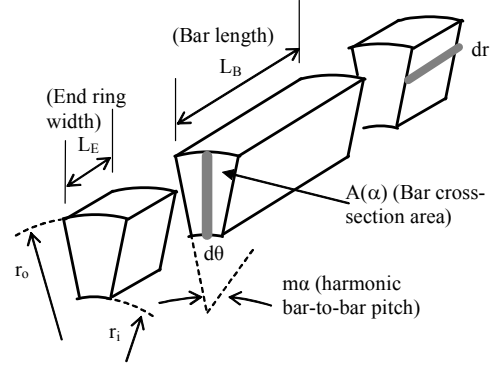


Fig. 2 Bar and end-ring conventions

### F. Characteristic Voltage Equations

Using the relationships put forward above, and after some manipulation, the main and auxiliary voltage equations can be obtained for each harmonic where:

$$\overline{E}_{Mf1} = \frac{-\frac{1}{2}\left(\frac{N_M^1}{2mp}\right)^2 rL_B\omega\pi\mu_0}{g\left[j - \left(\frac{\mu_0}{g}\cdot\frac{1}{\overline{Z}_{\alpha f}^1}s\omega rL_B\right)\right]}\overline{I}_m$$

$$+\frac{1}{\beta^1}\frac{j\frac{1}{2}\left(\frac{N_A^1}{2mp}\right)^2 rL_B\omega\pi\mu_0}{g\left[j - \left(\frac{\mu_0}{g}\cdot\frac{1}{\overline{Z}_{\alpha f}^1}s\omega rL_B\right)\right]}\overline{I}_a \quad (23)$$

and

$$\overline{E}_{Af1} = \frac{-\frac{1}{2}\left(\frac{N_A}{2mp}\right)^2 rL_B\omega\pi\mu_0}{g\left[j - \left(\frac{\mu_0}{g}\cdot\frac{1}{\overline{Z}_{\alpha(a)f}^1}s\omega rL_B\right)\right]}\overline{I}_a$$

$$+j\beta^1\frac{-\frac{1}{2}\left(\frac{N_M}{2mp}\right)^2 rL_B\omega\pi\mu_0}{g\left[j - \left(\frac{\mu_0}{g}\cdot\frac{1}{\overline{Z}_{\alpha(a)f}^1}s\omega rL_B\right)\right]}\overline{I}_m \quad (24)$$

where

$$\beta^1 = \frac{N_A^1}{N_M^1} \quad (25)$$

Similar equations exist for the backwards rotating field and also for the higher MMF harmonics. This leads to the familiar equations for a parallel combination of the magnetizing reactance and rotor impedance. If $\beta_1 = 1$, i.e., the main and auxiliary windings have the same distribution with a 90 elec deg spatial phase rotation, then when $\overline{I}_a = j\overline{I}_m$ (e.g., when it is operating as a true 2-phase machine), (23) simplifies to
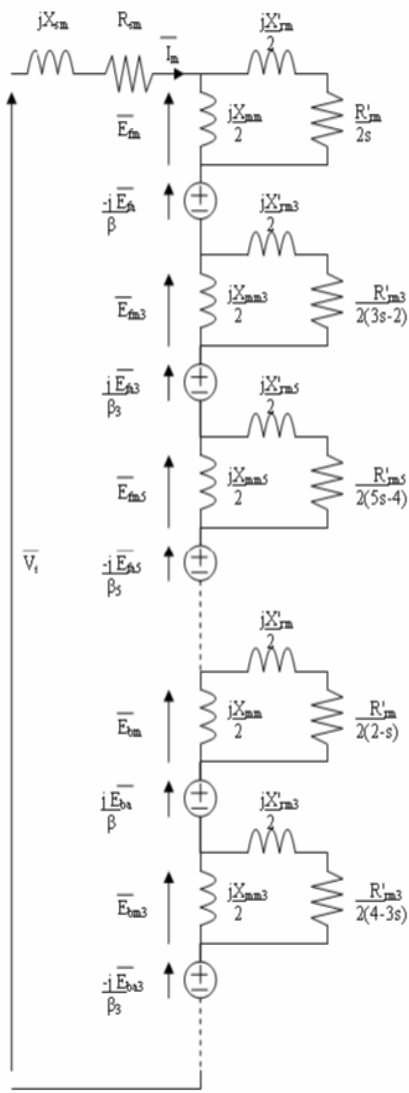
Fig.3 Main winding equivalent Circuit
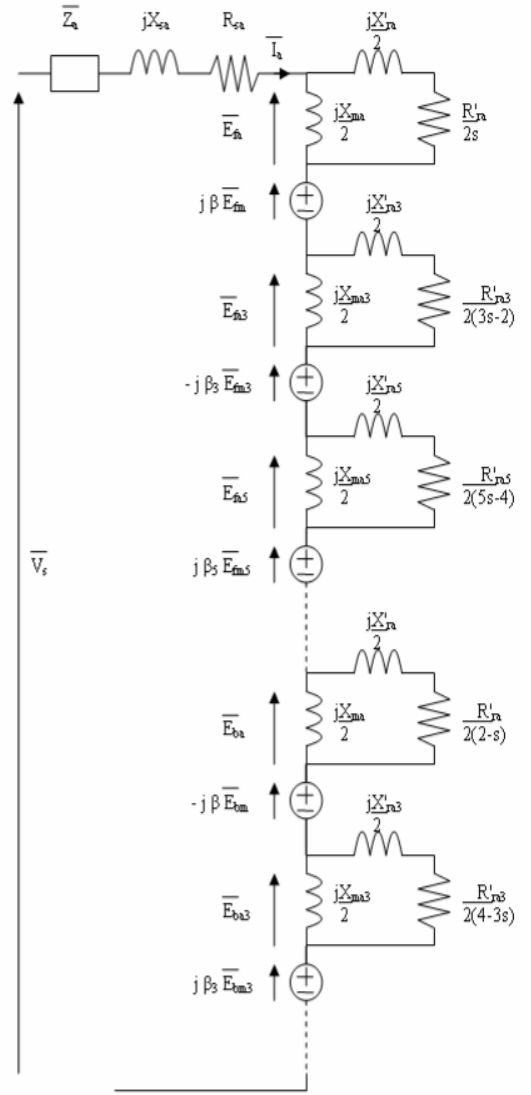


Fig. 4 Auxiliary winding equivalent circuit

$$\overline{E}_{Mf1} = 2 \times \frac{-\dfrac{1}{2}\left(\dfrac{N_M^1}{2mp}\right)^2 rL_B \omega \pi \mu_0}{g\left[ j - \left(\dfrac{\mu_0}{g} \cdot \dfrac{1}{\overline{Z}_{\alpha f}^1} s\omega rL_B\right)\right]} \overline{I}_m \qquad (26)$$

and (24) simplifies to

$$\overline{E}_{Af1} = 2 \times \frac{-\dfrac{1}{2}\left(\dfrac{N_M}{2mp}\right)^2 rL_B \omega \pi \mu_0}{g\left[ j - \left(\dfrac{\mu_0}{g} \cdot \dfrac{1}{\overline{Z}_{\alpha f}^1} s\omega rL_B\right)\right]} \overline{I}_a \qquad (27)$$

which illustrates a balanced machine. In addition, $\overline{E}_{Mb1} = \overline{E}_{Ab1} = 0$ under these conditions which shows that the pulsating MMF becomes a rotating MMF.. The voltages can be connected in series to obtain the series voltage equation for each phase. The voltages for the main and auxiliary windings in terms of the fundamental forwards-rotating MMF wave are:

$$\overline{E}_{Mf1} = \left[\frac{jX_{Mf}^1}{2} \,\|\, \frac{\dfrac{R_{Mr}^{/1}}{s} + jX_{Mfr}^{/1}}{2}\right] \cdot \overline{I}_m$$

$$+ \frac{-j}{\beta^1}\left[\frac{jX_{Af}^1}{2} \,\|\, \frac{\dfrac{R_{Ar}^{/1}}{s} + jX_{Afr}^{/1}}{2}\right] \cdot \overline{I}_a \qquad (28)$$

and

$$\overline{E}_{Af1} = \left[\frac{jX_{Af}^1}{2} \,\|\, \frac{\dfrac{R_{Afr}^{/1}}{s} + jX_{Afr}^{/1}}{2}\right] \cdot \overline{I}_a$$

$$+ j\beta^1\left[\frac{jX_{Mf}^1}{2} \,\|\, \frac{\dfrac{R_{Mfr}^{/1}}{s} + jX_{Mfr}^{/1}}{2}\right] \cdot \overline{I}_m \qquad (29)$$

## G. Equivalent Circuit

Figs. 3 and 4 show the equivalent circuit for the machine. These are obtained from equations (28) and (29) when implemented for all the forwards and backwards-rotating MMF waves. They consist of a main winding circuit and the auxiliary winding circuit that are connected in parallel across the supply. Additional impedance can be added in series to the auxiliary to account for a start or run capacitor and also a start resistor. Cross coupling between the circuits is incorporated via the voltage controlled voltage sources. The voltage sources are set by the magnetizing reactance voltage drops. These circuits account for both forwards and backwards air-gap MMF waves as well as higher harmonics, including the $3^{rd}$ harmonics. This circuit can be programmed to resolve the main and auxiliary currents for an applied voltage and slip.

## H. Torque Calculation

The torque can be obtained from the following equation for each winding harmonic:

$$
T_{Mf}^1 = \mathrm{Re}\left(\left[\frac{\overline{E}_{Mf}^1}{\omega} + \frac{\frac{-j}{\beta_m}\overline{E}_{Af}^1}{\omega}\right]\overline{I}_{Mrf}^{\prime 1\,*}\right)
$$
$$
+ \mathrm{Re}\left(\left[\frac{\overline{E}_{Af}^1}{\omega} + \frac{j\beta_m\overline{E}_{Mf}^1}{\omega}\right]\overline{I}_{Arf}^{\prime 1\,*}\right)
\tag{27}
$$

$$
T_{Mb}^1 = \mathrm{Re}\left(\left[\frac{\overline{E}_{Mb}^1}{\omega} + \frac{\frac{-j}{\beta_1}\overline{E}_{Ab}^1}{\omega}\right]\overline{I}_{Mrb}^{\prime 1\,*}\right)
$$
$$
+ \mathrm{Re}\left(\left[\frac{\overline{E}_{Ab}^1}{\omega} + \frac{j\beta_1\overline{E}_{Mb}^1}{\omega}\right]\overline{I}_{Arb}^{\prime 1\,*}\right)
\tag{28}
$$

These equations are for the fundamental forwards and backwards rotating mmf torques. Superposition of all the MMF torque harmonics lead to the total torque.

## III. SIMULATION AND RESULTS

The algorithm was tested using a model of a 2-pole split-phase induction motor. The main machine specification and results are given below. To illustrate the harmonic effects then the simulation used an unskewed rotor.

### A. Machine Model

The machine cross section is shown in Fig. 5. The basic machine parameters are listed below:

| | |
|---|---|
| Airgap-length | 0.29 mm |
| Rotor Radius | 31.2 mm |
| Axial length | 48.5 mm |
| Rated voltage | 220 V |
| Frequency | 50 Hz |
| Auxiliary winding series impedance | 4 Ω (resistive) |

The main winding has 10 coils while the auxiliary has 8 coils. The main winding is shown in Fig. 6. The phase belt coils has the coil-turns of: 46, 76, 100, 118, 118, 118, 118, 100, 76, 46. The Auxiliary winding is shown in Fig. 7. The phase belt coils has the coil-turns of: 55, 79, 85, 85, 85, 85, 79, 55. Additional resistance and reactance terms (such as the stator winding resistances and leakages and rotor bar and end-ring leakages) were obtained from *SPEED*'s PC-IMD (as are the diagrammatical representations in Figs. 5 to 7).
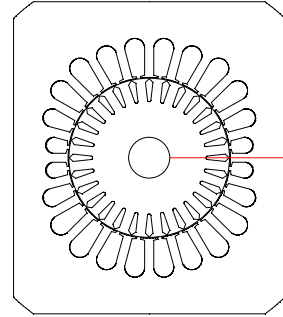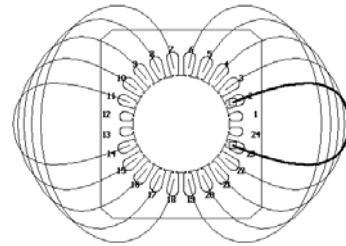


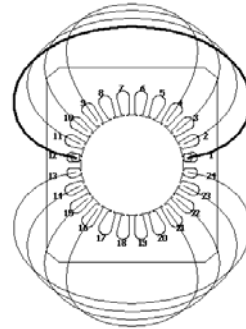Fig. 5 Machine model cross section



Fig. 6 Main winding layout



Fig. 7 Auxiliary winding layout

### B. Simulation Results

Figs. 8 to 11 show the torque speed curves obtained from the simulation program at rated voltage.
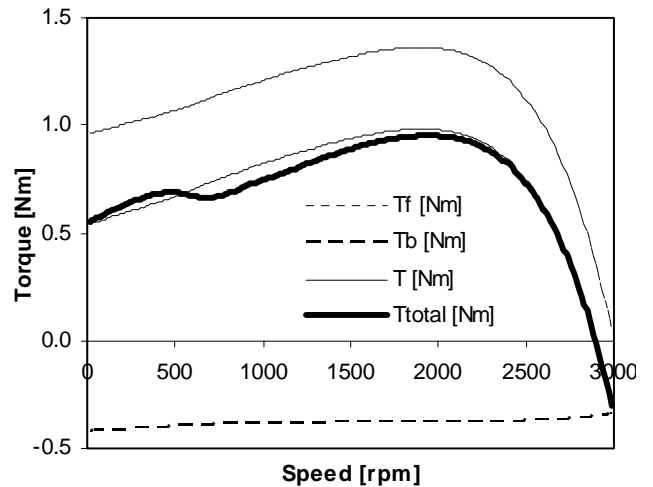


Fig. 8 Torque-speed curve - total curve plus fundamental forwards and backwards-rotating curves
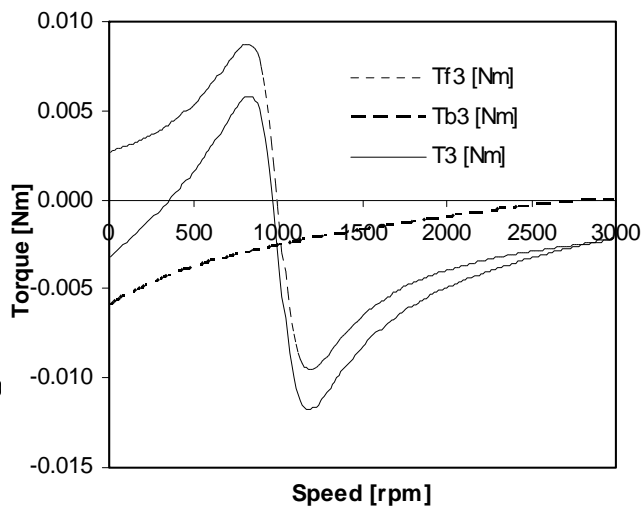
Fig. 9 Torque-speed curve - total 3rd harmonic curve plus 3rd harmonic forwards and backwards-rotating curves
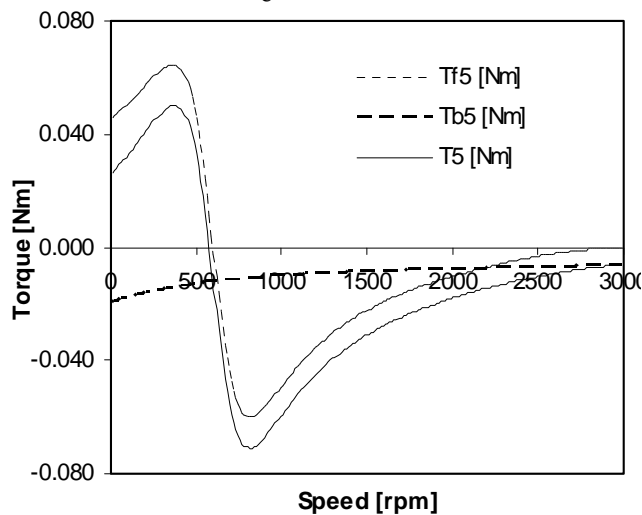


Fig. 10 Torque-speed curve - total 5th harmonic curve plus 5th harmonic forwards and backwards-rotating curves
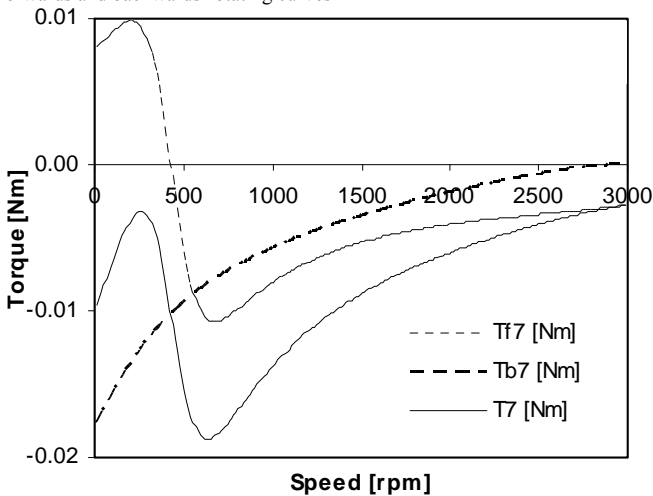


Fig. 11 Torque-speed curve - total 7th harmonic curve plus 7th harmonic forwards and backwards-rotating curves

## C. Discussion

The results in the previous section illustrate that the split phase induction motor can be modelled using standard rotating-field induction motor theory. The machine modelled here is a typical example of such a machine (although with no skew). It can be seem that even with a graded winding which is close to sinusoidal then asynchronous torques can occur if there is no skew. Unlike a balanced a 3-phase winding, a split phase machine can have asynchronous torques of 3rd, 5th, 7th, 9th, etc, harmonic that rotate in both directions as illustrated here as well as in [3]. Care needs to be taken to ensure that a winding does not produce one of these harmonics.

In Fig. 5, it can be seen that the slot sizes are graded so that a sinusoidal main winding can be realized without producing slots with poor fill factors that leaves the coils lose with poor conductive cooling. The auxiliary winding tends to have less turns and often fewer coils (if the machine is capacitor-run there will still be less than 25 % power flowing into the machine via the auxiliary winding). Designing a suitable winding with a reasonable distribution, without designing in asynchronous torques, is not a trivial matter. Skewing the rotor does aid the prevention of the asynchronous torques but may not fully suppress them.

## IV. CONCLUSION

This paper puts forward a rotating-field analysis technique for analyzing a split phase induction motor which is generally applicable to machines that are capacitor or resistor start and possibly capacitor-run if necessary. There is little literature on this subject even though designing a suitable winding for good operation of these machines is not straightforward. The algorithm was applied to a design example to illustrate the capability of the method. The paper also illustrates that asynchronous torques can exist even in a machine with a good winding.

REFERENCES

[1] C. G. Veinott, *Theory and Design of Small Induction Motors*, McGraw-Hill Book Company, 1959.
[2] P. L. Alger, *Induction Machines, Their Behavior and Uses*, Gordon and Breach Publishers, Third Edition, 1995, ISBN 2-88449-199-6.
[3] D. G. Dorrell "Analysis of split-phase induction motors using an impedance matrix", *IEE Power Electronics Machines and Drives Conference PEMD*, Edinburgh, March 2004 (on CD).
[4] R. W. Fei, J. D..Lloyd and M. C. Dierkes, "An experimental study of single-phase induction motor starting performance and its dependency on winding harmonics" *Thirtieth IEEE IAS Annual Meeting*, Vol. 1, pp 571 – 578, 8-12 Oct. 1995.
[5] C. B. Rasmussen and TJE Miller, "Revolving-field polygon technique for performance prediction of single-phase induction motors", *IEEE Trans on Industry Applications*, Vol. 39, No. 5, Sept. - Oct. 2003, pp 1300 – 1306.
[6] T. A. Walls and S. D. Sudhoff "Analysis of a single-phase induction machine with a shifted auxiliary winding" *IEEE Transactions on Energy Conversion*, Vol. 11, No. 4, Dec. 1996, pp 681 – 686.

# Analysis of the Synchronous Torques in a Split Phase Induction Motor

P. Scavenius Andersen*, D. G. Dorrell**, N. C. Weihrauch* and P. E. Hansen*

*Danfoss Compressors GmbH, Flensburg, Germany
**University of Glasgow, Glasgow, UK

*Abstract*—**This paper puts forward a method for calculating the synchronous torque dips in a split-phase induction machine. First it derives the equivalent circuits so that the torque speed/curve can be obtained over a full speed range (including asynchronous torque oscillations). When the currents are resolved these are used to calculate the synchronous torques from a set of interactions between the machine MMFs and the slot permeances. This gives the synchronous torques (speed and magnitude) which can be superimposed onto the torque/speed curve. The method is tested experimentally and found to give reasonable results.**

*Index Terms*—**Split phase induction motors, asynchronous torques, synchronous torques.**

## I. Introduction

The split phase motor, where there is a single phase main winding and an orthogonal auxiliary winding which is connected in parallel with the main winding (often with a series resistor or capacitor) is the preferred drive for a vast array of water and chemical pumping application as well as refrigeration applications, in a range possibly up to a few kW. They are cheap and relatively efficient and do not require a 3-phase supply.

Many analysis techniques still assume a sinusoidal winding so that only the fundamental forwards and backwards rotating MMFs are modelled. The usual ways to analyze these machines use the cross-field or revolving field techniques. These two methods are well documented by Veinott [1]. For a balanced two-phase machine the 5th MMF harmonic asynchronous torque rotates forwards and the 7th backwards, etc, (whereas for a three-phase machine the 5th rotates backwards and the 7th rotates forwards) For a split-phase machine, there may also be a substantial a 3rd harmonic MMF asynchronous torque dip as well as other odd harmonics that rotate both forwards and backwards [2].

Recently, with the drive for energy efficiency, and also design improvement, the operation and simulation of the split phase motor has attracted more detailed interest [3]-[6]. These address the issues of asynchronous torque dips as mentioned above and also inter-bar rotor currents. Here, we will investigate the issue of synchronous torque spikes.

## II. Analysis

The analysis builds on the theory put forward in [4] and [6]. The permeance waves due to the slotting are described in the Appendix. First, it is illustrated how the permeance harmonics due to slotting can interact with the MMF to produce flux waves of the correct pole number to interact with other MMF waves (or iven the souce MMF) which rotate at different rotational velocities. At certain rotor speeds the MMF and permeance-sourced flux waves will rotate at the same speeds to generate constant torque. Therefore a synchronous locking torque is a pulsating torque where at certain speeds the frequency of the oscillation is zero. Then the paper goes on to examine explicit cases.

### A. Interaction of MMF and permeance waves

The machine MMF will interact with the slot permeance coefficient:

$$B = F_m \times P \tag{1}$$

where the MMF $F_m$ of order $m$ is rotating. Consider a general permeance coefficient and a $p^{th}$ harmonic forward-rotating component of MMF so that

$$B(t,\theta) = F_{fp}\cos(\omega t - p\theta) \times P_x \cos(x\theta - y\omega_r t)$$
$$= \frac{F_{fp}P_x}{2}\left[\begin{array}{l}\cos((\omega + y\omega_r)t - (p+x)\theta) \\ + \cos((\omega - y\omega_r)t - (p-x)\theta)\end{array}\right] \tag{2}$$

Where, for different MMF and permeance harmonics:

Term 1:  $y = 0$  $x = 0$
Term 2:  $y = 0$  $x = m N_s$
Term 3:  $y = n N_r$  $x = n N_r$
Term 4:  $y = -n N_r$  $x = m N_s - n N_r$
Term 5:  $y = nN_r$  $x = m N_s + n N_r$

and the stator slot number is $N_s$ and the rotor slot number is $N_r$. It can be seen that the air-gap has two resulting rotating fields in (2) per Term, whose number of pole-pairs and rotational speeds are given by

$$n_{f1} = p + x \qquad n_{f2} = p - x$$

$$\omega_{f1} = \frac{\omega + y\omega_r}{p + x} \qquad \omega_{f2} = \frac{\omega - y\omega_r}{p - x}$$

If the pole-pair number is negative this corresponds to the reverse direction. $\omega_{f1}$ and $\omega_{f2}$ are the rotational speeds of the fields. They create net torque with rotor MMFs of same pole number when their speeds coincide, i.e., when

$$\omega_{r1} = \frac{\omega_{f1}(p + x) - \omega}{y} \text{ with } \omega_{f1} = \pm\frac{\omega}{n_{f1}} \tag{3}$$

In the same way, the interaction of the $p^{th}$ harmonic backwards-rotating MMF with the various permeance coefficient terms will result in a field set given by

$$B(t,\theta) = F_{bp}\cos(\omega t + p\theta) \times P_x \cos(x\theta - y\omega_r t)$$

$$= \frac{F_{bp}P_x}{2}\begin{bmatrix} \cos((\omega + y\omega_r)t + (p-x)\theta) \\ + \cos((\omega - y\omega_r)t + (p+x)\theta) \end{bmatrix} \quad (4)$$

which is also composed of two rotating fields per Term, whose number of pole-pairs and rotational speeds are given by

$$n_{b1} = p - x \qquad \omega_{b1} = -\frac{\omega + y\,\omega_r}{p - x} = \frac{\omega + y\,\omega_r}{x - p}$$

$$n_{b2} = p + x \qquad \omega_{b2} = \frac{\omega - y\omega_r}{-x - p}$$

with $p$ = MMF harmonic under consideration. In summary:

- The forward and backward magnetizing MMF with $p$ pole-pairs each interact with the general permeance term with $x$ pole pairs. (In total, 2 MMFs per harmonic)
- For each interaction, two counter rotating flux densities with
  $$n_b = (p+x) \text{ or } (p-x) \quad (5)$$
  pole pairs are created. (In total, 4 flux densities per harmonic [$p,m,n$])
- The rotational speed of each flux density is determined by the rotor speed. Each flux density may produce average torque with either the forward or the backward rotor MMF of same pole number when their speeds coincide, i.e. at either positive or negative synchronous speed of the rotor MMF. (8 speeds per harmonic [$p,m,n$])

This means, that for each harmonic component of winding MMF, eight components of synchronous locking torque need to be considered (i.e., Terms 4 and 5 for (2) and (4) – Term 2 is the main torque-producing field that is un-modulated by the permeance and Terms 2 and 3 produce field harmonics that are too high to interact and produce synchronous torques).

*B. MMF, permeance and torque*

The synchronous torque components arise as a combination of MMFs interacting with flux densities of various harmonic orders. In order to calculate the magnitude of the torque components a detailed knowledge of harmonic magnetization as well as rotor MMFs and permeances is required.
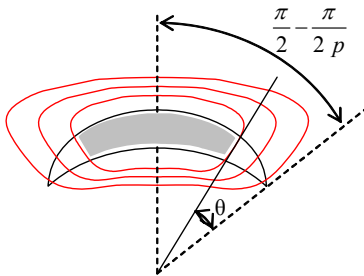


Fig. 1. Harmonic pitch definition.

*C. Magnetizing MMF of the $p^{th}$ harmonic winding*

The magnitude of the forward revolving, $p^{th}$ harmonic magnetizing (or resulting) MMF can be calculated from[6]:

$$F_{\text{mag } p} = \int_0^{\pi/p} \frac{pN_{p\text{ main}}}{4}\sqrt{2}\,\overline{I}_{\text{mag p main}}\sin(p\theta)d\theta$$

$$+ \int_0^{\pi/p} \frac{pN_{p\text{ main}}}{4}\frac{-j\beta_p}{\sin\left(\frac{p\pi}{2}\right)}\sqrt{2}\,\overline{I}_{\text{mag p aux}}\sin(p\theta)d\theta \quad (6)$$

$$= \left| \frac{N_{p\text{ main}}}{\sqrt{2}}\left( \overline{I}_{\text{mag p main}} + \frac{-j\beta_p}{\sin\left(\frac{p\pi}{2}\right)}\overline{I}_{\text{mag p aux}} \right) \right|$$

where $pN_{p\text{ main}}/4$ is the winding amplitude of half of the $p^{th}$ harmonic winding. (the total winding number is $N_p$). In addition there is the harmonic winding ratio $\beta_p$, which is defined by

$$\beta_p = \frac{N_{p\text{ aux}}}{N_{p\text{ main}}} \quad (6)$$

And the current is solved for the winding harmonics as given in [4] (the focus of this paper is the solution of the synchronous torques rather than the main torque and current components).

Having established an expression for resulting MMFs, the flux density component (with $p \pm x$ pole-pairs) can be calculated from the permeance. Therefore an expression for the actual permeances is needed

*D. Permeance and permeance coefficient*

The air-gap flux of one pole pitch from the $p^{th}$ harmonic winding is considered. Firstly, this can be expressed by magnetizing MMF and air-gap permeance *Perm* as

$$\Phi_p = \frac{2}{\pi}F_p\,Perm$$

$$= \frac{2I}{\pi}\int_0^{\pi/p} N_p\sin(p\theta)d\theta\,Perm \quad (8)$$

$$= \frac{4IN_p}{\pi p}\,Perm$$

The factor $2/\pi$ takes into account the sinusoidal distribution of the flux, since it represents the ratio between the areas of a sine function and a rectangular function with equal amplitude.

Secondly, a relationship between the flux linkage and the total flux of one pole pitch of the $p^{th}$ harmonic winding must be found. Fig. 1 shows a pole pitch of a $p^{th}$ harmonic, sinusoidally distributed winding. At angle $\theta$, the shaded area of the coil is linked by a number of flux lines, as shown in red. At angle $\theta$, the linked winding number is

$$N_{linked}(\theta) = 2\int_\theta^{\frac{\pi}{2}} N_p\sin(p\theta)d\theta = \frac{2\,N_p}{p}\cos(p\theta) \quad (9)$$

and the total flux is

$$\Phi(\theta) = \Phi_p \sin(p\theta) \qquad (10)$$

Observing a small section with width $d\theta$ at angle $\theta$, the flux linkage is

$$dΨ(\theta) = \frac{d}{d\theta} N_{linked}(\theta) \cdot \frac{d}{d\theta} \Phi(\theta) d\theta$$
$$= -2\hat{N}_p \sin(p\theta) \cdot p\Phi_p \cos(p\theta) \qquad (11)$$

From this, the total flux linkage of one pole pitch can be found by integrating over the entire pole pitch, i.e.:

$$Ψ_p = \int_{\frac{\pi}{2}-\frac{\pi}{p2}}^{\frac{\pi}{2}} dΨ(\theta) = -2pN_p\Phi_p \int_{\frac{\pi}{2}-\frac{\pi}{p2}}^{\frac{\pi}{2}} \sin(p\theta)\cos(p\theta)d\theta$$

$$= -pN_p\Phi_p \int_{\frac{\pi}{2}-\frac{\pi}{p2}}^{\frac{\pi}{2}} \sin(2p\theta) d\theta$$

$$= \frac{N_p\Phi_p}{2}\left[\cos(p\pi) - \cos(p\pi - \pi)\right]$$

$$= \frac{N_p\Phi_p}{2}\left[2\sin\left(\pi\left(\frac{2p-1}{2}\right)\right)\sin\left(-\frac{\pi}{2}\right)\right]$$

$$= N_p\Phi_p \qquad (12)$$

Solving for the pitch flux, and introducing the relationship between flux linkage, current and inductance gives

$$\Phi_p = \frac{Ψ_p}{N_p} = \frac{X_{p,mag}}{N_p\omega} I = \frac{r L_{stk} \pi \mu_0 \left(\frac{N_p}{p}\right)^2}{N_p l_{gap}} I \qquad (13)$$

Solving for *Perm* yields

$$\frac{4I\hat{N}_p}{p\pi} Perm = I \frac{rL_{stk}\pi\mu_0\hat{N}_p}{p^2 l_{gap}} \quad \Rightarrow$$

$$Perm = \frac{rL_{stk}\pi^2\mu_0}{4p l_{gap}} \qquad (14)$$

This expression relates to the flux rather than the flux density, which is sought here. Therefore, the relationship between permeance and permeance coefficient is the same as that between flux and flux density *for one pole pitch*, i.e.:

$$\frac{\Phi}{p} = \int BdA = rL_{stk}\int_0^{\pi/p} B\sin(p\theta)d\theta = \frac{rL_{stk}2B}{p} = \alpha B \quad (15)$$

In order to obtain an expression for the permeance coefficient, the following comparisons are made. The flux is given by

$$\Phi_p = F \times Perm = \alpha B \qquad (16)$$

and the flux density is given by

$$B_p = F \times P \qquad (17)$$

Dividing (16) by (17) yields

$$\frac{\Phi_p}{B_p} = \frac{Perm}{P} = \alpha \qquad (18)$$

from which

$$P = \frac{Perm}{\alpha} = \frac{\pi^2 \mu_0}{8 l_{gap}} \qquad (19)$$

where $l_{gap}$ is the amplitude of the harmonic gap lengths.

### E. Rotor MMF calculation

The rotor MMF is expressed in terms of its referred value, since only referred currents are present in the equivalent circuit (Fig. 2). Hence

$$F_{Rn_b} = \int_0^{\pi/n_b} \frac{n_b N_{n_b\,main}}{4} \sqrt{2}\,\bar{I}'_{Rn_b\,main} \sin(n_b\theta)d\theta$$

$$+ \int_0^{\pi/n_b} \frac{pN_{n_b\,main}}{4} \frac{-j\beta n_b}{\sin\left(\frac{n_b\pi}{2}\right)} \sqrt{2}\,\bar{I}'_{Rn_b\,aux} \sin(n_b\theta)d\theta \quad (20)$$

$$= \left| \frac{N_{n_b\,main}}{\sqrt{2}} \left( \bar{I}'_{Rn_b\,main} + \frac{-j\beta_{n_b}}{\sin\left(\frac{n_b\pi}{2}\right)} \bar{I}'_{Rn_b\,aux} \right) \right|$$

Where $n_b$ is given by (5). The relationship between MMF and current distribution amplitude is given by

$$\hat{I}_{Rn_b} = \frac{n_b F_{Rn_b}}{2}$$

$$= \left| \frac{n_b N_{n_b main}}{2\sqrt{2}} \left( \bar{I}_{Rn_b\,main} + \frac{-j\beta_{n_b}}{\sin\left(\frac{n_b\pi}{2}\right)} \bar{I}_{Rn_b\,aux} \right) \right| \qquad (22)$$

Where $N_{n_b\,main}$ is the total winding number of one pole pitch of the $n_b{}^{th}$ harmonic winding.

### F. Torque calculation

From (22) and (1) the magnitudes of the locking torques can be determined. The maximum value of locking torque occurs when the flux density and the current distribution are in phase, and the minimum value occurs when they are in anti-phase. The magnitude is given by

$$T_{sync\,p} = \pm rL \int_0^{2\pi} \hat{I}_{R\,p} \sin(p\theta)\hat{B}_p \sin(p\theta)d\theta$$

$$= \pm rL\hat{I}_{R\,p}\hat{B}_p\pi \qquad (23)$$

### G. Calculation synchronous locking torques

As mentioned in the previous sections, several independent synchronous locking torques can be calculated from the $p^{th}$ magnetizing MMF, which interacts with each permeance term to create flux density of harmonic order $n_b$. The torque arises from the rotor MMF of the same harmonic order $n_b$. The magnitude of the torque presupposes that the magnitudes of the various flux densities and MMFs are known. Hence it is necessary to obtain realistic values for these.

This method can be applied to several methods of calculation as a post-processing method of assessing the synchronous torques.

## III. SIMULATIONS

The equivalent circuit including winding harmonics is used to simulate the machine. This includes four separate winding harmonics of both forward and backwards rotation. This gives a system of twenty equations when considering both main and auxiliary windings. The fundamental and third winding harmonic variables are always considered, since these, or at least the fundamental, will dictate the line current drawn from the supply. In addition, the winding harmonics of order $p$ (which is the one that interacts with the permeance harmonic to produce flux) and $n_b$ (which is the winding harmonic of the same order as the resulting flux) are considered in order to obtain the values needed for torque calculation. This is illustrated in Fig. 2, where the sub-circuits representing four forward harmonic windings of the main winding are shown. In the full circuit used for calculation, four backwards windings are also included and the auxiliary winding circuit.



Fig. 2. Equivalent circuit for the main winding and forwards-rotating flux waves (and two backwards-rotating waves together with linkages with the auxiliary windings).

### A. Simulation models

Several machines with different types of rotor were simulated and verified experimentally. In the simulations, four machines were investigated. These were a 220 V 50 Hz machine with 20 and 24 bar rotors (unskewed) and a 115 V 60 Hz machine with 18 and 24 bar rotors (unskewed).

For experimental verification a set of rotors were constructed which had 18 rotor bars (unskewed), 24 rotor bars (unskewed) and 28 bar rotors with 1 slot skew. These are put forward in Section IV.

The synchronous locking torques were calculated after the solution of the torque-speed curve and solution of the main and auxiliary winding currents. These are used to obtain the different components of the synchronous locking torques which are summed (since several occur at the same speed) and superimposed on the torque-speed curves.

### B. 220 V machine 20 and 24 bar rotor simulations

This motor is designed for run capacitor operation. A resistor is used in series with the auxiliary during the Start mode. The number of stator slots is 24 and the mechanical air gap is 0.28 mm. Fig. 3 shows the synchronous locking torques superimposed on the steady state torque/speed curves for 20 rotor slots, which results in limited synchronous locking torque, as well as for 24 rotor slots (equal to stator slot number) which results in severe locking at standstill.



Fig. 3. Synchronous torque simulations with 20 rotor bars (top) and 24 rotor bars (bottom) – 220 V machine (start mode).

## C. 115 V machine with 18 and 24 bar rotor simulations

This motor is a 115 V 60 Hz motor designed for single phase run operation. A series resistor is used with the auxiliary winding during starting . The number of stator slots is 24 and the mechanical air gap is 0.36 mm. Fig. 4 shows the synchronous locking torques superimposed on the steady state torque/speed curves for 18 rotor slots, which results in synchronous locking torque, as well as for 24 rotor slots (equal to stator slot number) which results in severe locking at standstill. The steady-state torques themselves show considerable asynchronous torque dips.
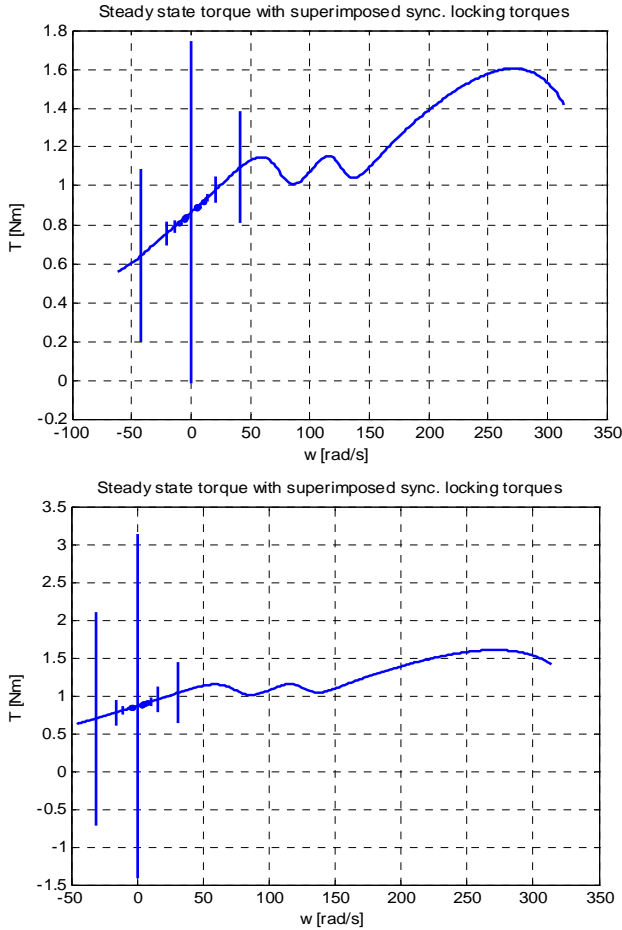




Fig. 4. Synchronous torque simulations with 18 rotor bars (top) and 24 rotor bars (bottom) – 115 V machine (start mode).

## IV. EXPERIMENTAL RESULTS – 18, 24 AND 28 BAR ROTOR MACHINES

The simulation technique was verified experimentally as shown in Fig. 5. This is for a 230 V 50 Hz machine with an 18 rotor bar machine. Five nominally identical 18 bar unskewed rotors were constructed for this machine as well as five 24 bar unskewed rotors. Five similar production machines with 28 bar rotors and skew were also tested. Space constraints prevent a full description of the methods of testing for synchronous torques and this will be reported at a later date. The averages across the rotors are shown in the results here.
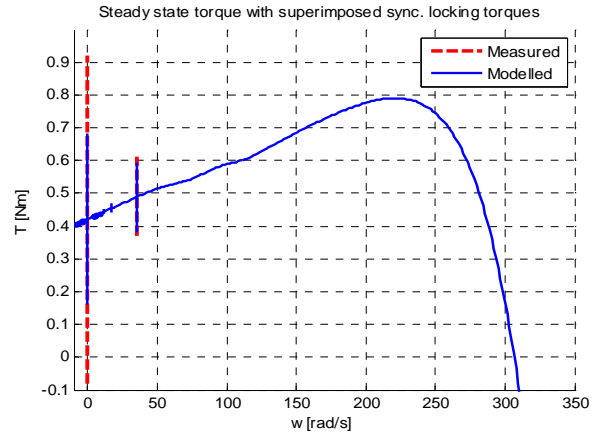


Fig. 5. Synchronous torque simulations for 18 slot experimental machine.

The results of the simulations when compared to the measurements are shown for the 18 and 24 bar rotors in Fig. 6. It can be seen that there are locking torques at zero speed and 27 rad/sec (258 rpm) for the 24 bar rotor and 35 rad/sec (335 rpm) for the 18 bar rotor. There is experimental error in these and the experimental results are higher than the simulation predictions.
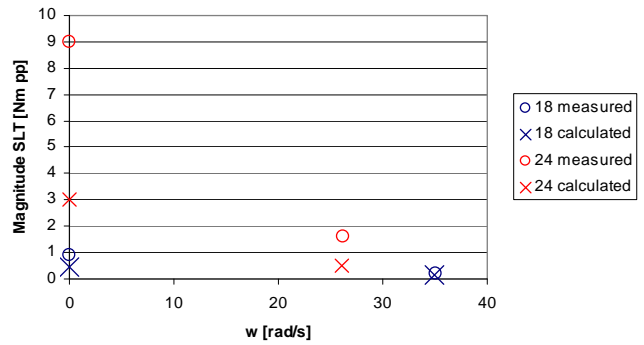


Fig. 6. Synchronous torque simulations and measurements for 18 and 24 bar rotor machines.

Deceleration torque/speed tests were carried out on the different rotors. Fig. 7 shows the deceleration tests for the 18 bar rotors from 500 rpm (right) down to 0 rpm. It can be seen that there are synchronous torques around 335 rpm as well as the locking torques at zero speed. Fig. 8 shows the deceleration tests for the 24 bar rotors. This shows the synchronous torques at about 258 rpm (the speed axis is 0 to 500 rpm). However the torque is from -4 Nm to 2 Nm which illustrates the large synchronous locking torque at zero speed due to slot cogging.
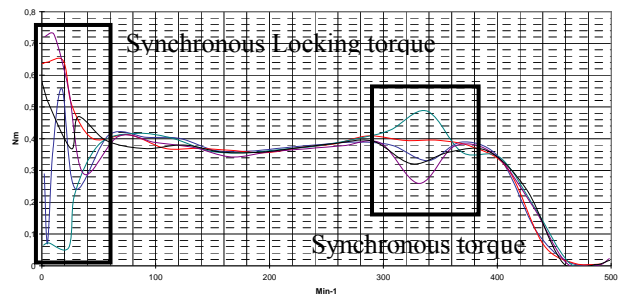


Fig. 7. Deceleration tests for 18 bar rotors – the y axis is torque 0 to 0.8 Nm and max speed (right) is 500 rpm.
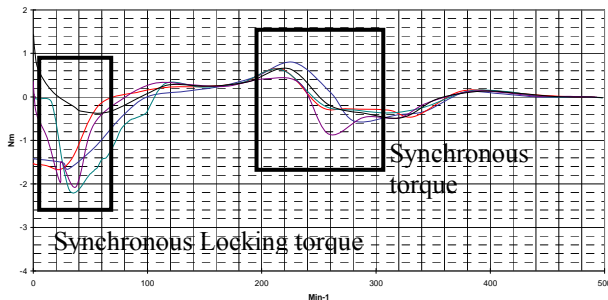
Fig. 8. Deceleration tests for 24 bar rotors – the y axis is torque -4 to 2 Nm and max speed (right) is 500 rpm.

Fig. 9 shows the deceleration test for the production machine with 28 skewed bars. It can be seen here that both the synchronous locking torque, and the characteristic synchronous torque at about 220 rpm are much reduced compared to the unskewed rotors, hence illustrating the importance of rotor skew.
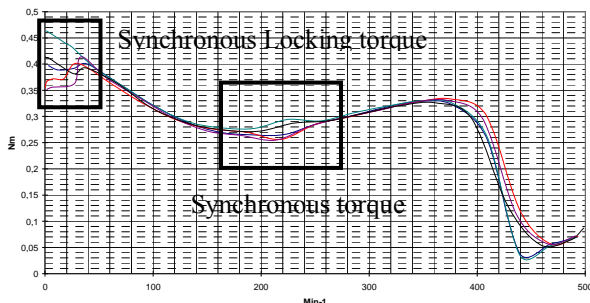


Fig. 9. Deceleration tests for 28 skewed bar rotors – the y axis is torque -0 to 0.5 Nm and max speed (right) is 500 rpm.

## V. CONCLUSIONS

The paper puts forward an analytical method for modelling split phase induction motors that includes the calculation of synchronous torque spikes and dips from permeance harmonic considerations. This will be an aid to motor designers when assessing a design, and in particular the stator/rotor slot number combination. The methods are verified experimentally using rotors with varying bar numbers.

## REFERENCES

[1] C. G. Veinott, *Theory and Design of Small Induction Motors*, McGraw-Hill Book Company, 1959.
[2] P. L. Alger, *Induction Machines, Their Behavior and Uses*, Gordon and Breach Publishers, Third Edition, 1995, ISBN 2-88449-199-6.
[3] D. G. Dorrell "Analysis of split-phase induction motors using an impedance matrix", *IEE Power Electronics Machines and Drives Conference PEMD*, Edinburgh, March 2004 (on CD).
[4] P. Scavenius Andersen and D. G. Dorrell, "Modelling of Split-Phase Induction Machine using Rotating Field Theory", ICEM 2006, Crete, September 2007
[5] S. Williamson and C. Y. Poh, "The effect of interbar currents in a permanent split capacitor motor", IEEE Transactions on Industry Applications, Volume 42, Issue 2, March-April 2006 pp 423 – 428.
[6] P. Scavenius Andersen, *Modelling and Analysis of Asynchronous and Synchronous Torques in Split-Phase Induction Machines*, PhD thesis, University of Glasgow, 2007.
[7] F. W. Carter, "A Note on Airgap and Interpolar Induction", JIEE, No. 29, pp 925, 1900.
[8] F. W. Carter, "The Magnetic Field of the Dynamo-Electric Machine", JIEE, No. 64, pp 100, 1926.
[9] B. Heller and V. Hamata, *Harmonic Field Effects in Induction Machines*, Elsevier Scientific Publishing Company, 1977.

## APPENDIX

F.W. Carter described a relationship between the mechanical air-gap and the equivalent air gap which takes stator and rotor slots into account [7][8]. Here, the air-gap as seen by the electromagnetic field is investigated in a little more detail.

### A. Air-gap length harmonics

In order to asses the variation of the air-gap magnetic field, a 2D finite element model is created which has an actual stator geometry but assumes a non-slotted rotor. This is shown in Fig. A.1. The red slots carry a uniform current density of opposite magnitude, whereas the grey slots carry no current. Hence, a quasi-square wave MMF is created.
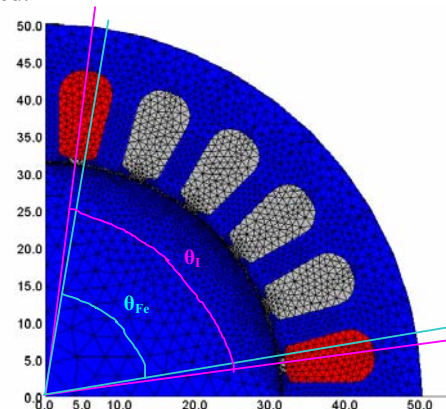


Fig. A.1. 2D finite element analysis of machine with smooth rotor-definition of $\theta_I$ and $\theta_{Fe}$

A static analysis of this model results in an air-gap flux density versus angle for a single tooth pitch as given in Fig. A.2.
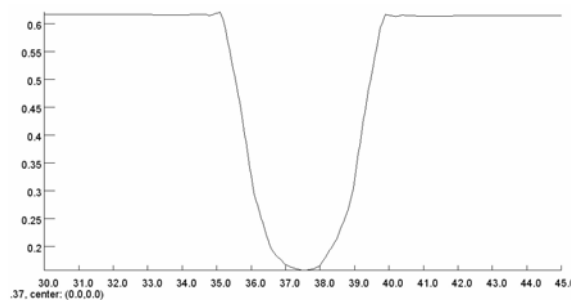


Fig. A.2. Air-gap flux density from FEA (y-axis is in Tesla)

From this flux density variation, the radial air gap length can be extracted from Ámpere's law using

$$l_g(\theta) = \frac{\theta_I}{\theta_{Fe}} \frac{\mu_0\, I_{tot}}{2\, B_g(\theta)} \tag{A.1}$$

The angles $\theta_I$ and $\theta_{Fe}$ are defined in Fig. A.1 and the ratio takes into account the concentration of flux due to the slotting, since the angular span of the MMF is larger than the span of the flux due to the slot openings.

Extracting the corresponding air-gap length from Fig. A.2 and performing a harmonic analysis of the resulting function results in a spectrum of harmonic air-gap lengths as given by Fig. A.3.
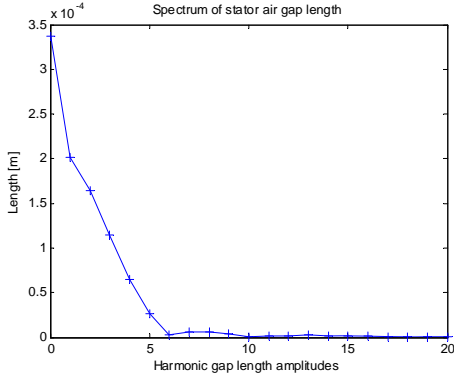

Fig. A.3. Harmonic air-gap lengths.

For the analysis, it is necessary to express the air-gap length variation mathematically. From Fig. A.2, a suitable approximation is indicated by the dotted blue line in Fig. A.4.
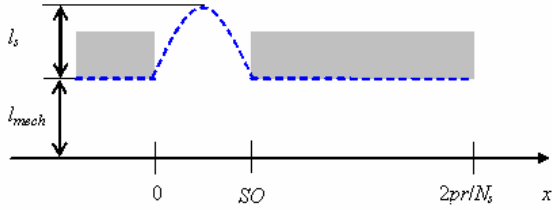

Fig. A.4. Air gap length approximation.

A suitable mathematic expression over the span $0 < x < SO$ is

$$f(x) = l_{mech} + l_s \sin\left(\frac{\pi}{SO} x\right) \tag{A.2}$$

And for $SO \le x \le 2\pi r/N_s$:

$$f(x) = l_{mech} \tag{A.3}$$

where $l_{mech}$ is the mechanical air-gap and $l_s$ is the effective air-gap as determined using the Carter factor. This actually corresponds to a constant term, i.e., the zero order harmonic of Fig. A.3.

Performing a Fourier analysis of the periodic function described by (A.2) and (A.3) will result in a spectrum which can be directly compared with the one in Fig. A.3 (as obtained from the finite element analysis). Any general magnitude deviation can be accounted for by multiplying the harmonic lengths with a correction factor. In Fig. A.5, blue graph shows the spectrum of the series defined by (A.2) and (A.3) directly, whereas the red

graph shows the same spectrum, but where the harmonic coefficients have been multiplied with by a factor of 1.3.
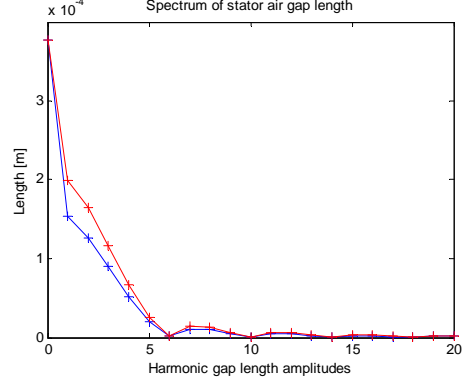

Fig. A.5. Comparison of harmonic air-gap lengths with adjustments (blue is the original harmonic magnitude and red multiplies the harmonic lengths by a factor of 1.3)

It is seen that the corrected spectrum (red graph) is in good agreement with the reference spectrum in Fig. A.3. Therefore, the mathematical functions in (A.2) and (A.3) for describing the air-gap length variation will be used in the following analysis. Generally, it can be observed from the spectra that both even and odd harmonics are present. For the lower harmonics the magnitudes are significant.

Since the spectrum shows the length variation over one tooth pitch, the fundamental value corresponds to the $N_s$'th harmonic when observing the entire air-gap where $N_s$ is the number of stator slots. Hence, for the entire air-gap, the order of the harmonic is $N_s$ times higher than shown in Fig A.5.

## B. A.2. Air-gap permeance

The reluctance variation of the air-gap is proportional to the air-gap length. The permeance is the inverse of the reluctance and it will have a similar spectrum as shown in Fig. A.5. This spectrum represents an air-gap section corresponding to one tooth pitch. For an air-gap around the whole motor air-gap circumference, the harmonic series has a fundamental of order $N_s$ (the number of stator slots) rather that unity. This is shown in Fig. A.6. This shows the air-gap permeance and the corresponding spectrum for an air-gap with 24 slots.
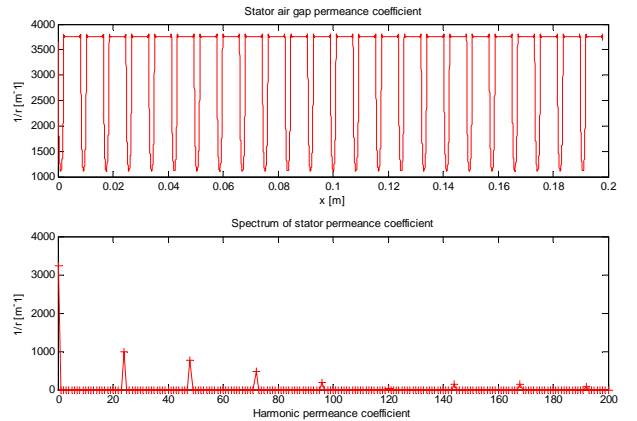

Fig. A.6. Air-gap permeance with harmonic decomposition

A similar spectrum will exist for the rotor, with a

fundamental corresponding to the number of bar slots, and the fundamental and harmonics will rotate with the rotor itself.

*C. Representation of permeance harmonics*

In the following derivation, the combined effects of stator and rotor permeance are described analytically. The approach developed by [2] is used and extended. The total air-gap reluctance is a series connection of independent reluctance terms. However, for the total air-gap permeance, the inversion process means that the stator slot, rotor slot and average permeance terms may be described by a parallel connection of individual permeances, i.e.:

$$P = \left( \frac{1}{P_r} + \frac{1}{P_s} + \frac{1}{P_g} \right)^{-1} = \frac{P_r P_s P_g}{P_s P_g + P_r P_g + P_r P_s} \qquad (A.4)$$

This type of air-gap harmonic inversion was also studied by Heller and Hamata [9]. By substitution, and for the moment ignoring higher slot harmonics:

$$P_s = P_{0s} + P_{ms} \cos(mN_s \theta) \qquad (A.5)$$

and

$$P_r = P_{0r} + P_{mr} \cos(mN_r \theta - \omega_r t) \qquad (A.6)$$

Therefore the resulting air-gap permeance will be

$$P = \frac{\left( P_{0r} + P_{mr} \cos(mN_r \theta - \omega_r t) \right) \left( P_{0s} + P_{ms} \cos(mN_s \theta) \right) P_g}{\left\{ \begin{pmatrix} P_{0s} + \\ P_{ms} \cos(mN_s \theta) \end{pmatrix} P_g + \begin{pmatrix} P_{0r} + \\ P_{mr} \cos(mN_r \theta - \omega_r t) \end{pmatrix} P_g + \\ \left( P_{0r} + P_{mr} \cos(mN_r \theta - \omega_r t) \right) \left( P_{0s} + P_{ms} \cos(mN_s \theta) \right) \right\}}$$

$$= \frac{\left\{ \begin{array}{l} P_{0r} P_{0s} P_g + P_g P_{0s} P_{mr} \cos(mN_r \theta - \omega_r t) \\ P_g P_{0r} P_{ms} \cos(mN_s \theta) + \\ P_{mr} \cos(mN_r \theta - \omega_r t) P_{ms} \cos(mN_s \theta) \end{array} \right\}}{\left\{ \begin{array}{l} P_{0s} P_g + P_{0r} P_g + P_{0r} P_{0s} + \left( P_{0r} + P_g \right) P_{ms} \cos(mN_s \theta) + \\ + \left( P_g + P_{0s} \right) P_{mr} \cos(mN_r \theta - \omega_r t) + \\ + P_{mr} \cos(mN_r \theta - \omega_r t) P_{ms} \cos(mN_s \theta) \end{array} \right\}}$$

$$(A.7)$$

Both the numerator and denominator of (A.7) contain contributions of constant and time-space-varying permeance terms. For the denominator, however, the time-space-varying permeance terms are small compared to the constant terms and are therefore ignored in the following analysis. Hence, the combined-effect air-gap permeance can be written as

$$P = P_0 \left[ 1 + \sum_{m=1}^{M} \frac{P_{Sm}}{P_0} \cos(mN_S \theta) \right] \times$$
$$\times \left[ 1 + \sum_{m=1}^{M} \frac{P_{Rm}}{P_0} \cos(mN_R (\theta - \omega_r t)) \right] \qquad (A.8)$$

The terms belonging to the stator are fixed in space, whereas the rotor terms will rotate with rotor speed. This gives rise to several terms of permeance where

$$P = P_0 + P_{S1} \cos(N_S \theta) + P_{S2} \cos(2N_S \theta) +$$
$$+ P_{S3} \cos(3N_S \theta) + \cdots$$
$$+ P_{R1} \cos(N_R (\theta - \omega_r t)) +$$
$$+ P_{R2} \cos(2N_R (\theta - \omega_r t)) + \cdots$$
$$+ \frac{P_{S1} P_{R1}}{P_0} \cos(N_S \theta) \cos(N_R (\theta - \omega_r t)) +$$
$$+ \frac{P_{S2} P_{R2}}{P_0} \cos(2N_S \theta) \cos(2N_R (\theta - \omega_r t)) + \cdots$$
$$+ \frac{P_{S1} P_{R2}}{P_0} \cos(N_S \theta) \cos(2N_R (\theta - \omega_r t)) +$$
$$+ \frac{P_{S1} P_{R3}}{P_0} \cos(N_S \theta) \cos(3N_R (\theta - \omega_r t)) + \cdots$$
$$+ \frac{P_{S2} P_{R1}}{P_0} \cos(2N_S \theta) \cos(N_R (\theta - \omega_r t)) +$$
$$+ \frac{P_{S2} P_{R3}}{P_0} \cos(2N_S \theta) \cos(3N_R (\theta - \omega_r t)) + \cdots$$
$$+ \frac{P_{S3} P_{R1}}{P_0} \cos(3N_S \theta) \cos(N_R (\theta - \omega_r t)) +$$
$$+ \frac{P_{S3} P_{R2}}{P_0} \cos(3N_S \theta) \cos(2N_R (\theta - \omega_r t)) + \cdots$$
$$+ \frac{P_{S4} P_{R1}}{P_0} \cdots$$

$$(A.9)$$

so that

$$P_{m,n} = \frac{P_{Sm} P_{Rn}}{2 P_0} \cos\left( \left[ mN_S - nN_R \right] \theta + nN_R \omega_r t \right)$$
$$+ \frac{P_{Sm} P_{Rn}}{2 P_0} \cos\left( \left[ mN_S + nN_R \right] \theta - nN_R \omega_r t \right) \qquad (A.10)$$

where *m* and *n* are stator and rotor slot harmonics. Altogether, the total air-gap permeance can be approximated using the following five terms:

$$P = P_0 + \sum_{m=1}^{M} P_{Sm} \cos(mN_S \theta) + \sum_{n=1}^{N} P_{Rn} \cos(nN_R (\theta - \omega_r t))$$
$$+ \sum_{m=1}^{M} \sum_{n=1}^{N} \frac{P_{Sm} P_{Rn}}{2 P_0} \left[ \begin{array}{l} \cos\left( \left[ mN_S - nN_R \right] \theta + nN_R \omega_r t \right) \\ + \cos\left( \left[ mN_S + nN_R \right] \theta - nN_R \omega_r t \right) \end{array} \right]$$

$$(A.11)$$

This includes the higher slot harmonics. The first term corresponds to the average air-gap permeance, calculated using the Carter factor. This is the only term which has a non-zero mean value. The second and third terms correspond to stator and rotor slot harmonics. These will have $mN_S$ and $nN_R$ pole-pairs. The fourth and fifth terms contain combinations of the stator and rotor harmonic permeances. These are permeance waves consisting of waves of $|mN_S + nN_R|$ pole pairs for the fourth term and $|mN_S - nN_R|$ pole pairs for the fifth term.